Carbide and Nitride Based Catalysts for Synthesis Gas Conversion

by

Joshua A. Schaidle

A dissertation submitted in partial fulfillment
of the requirements for the degree of
Doctor of Philosophy
(Chemical Engineering)
in The University of Michigan
2011

Doctoral Committee:

Professor Levi T. Thompson, Jr., Chair
Professor Erdogan Gulari
Professor Melanie S. Sanford
Professor Johannes W. Schwank

To my Mom and Dad, my sisters Emily and Sarah, and my fiancée Lindsay
I love all of you dearly

ACKNOWLEDGEMENTS

I would first like to thank my advisor, Dr. Levi Thompson, for his guidance and support throughout my Ph. D. research. I greatly appreciate being allowed to follow my research interests even when they did not specifically align with my project goals and objectives. Dr. Thompson has helped me grow not only as a researcher and scientist, but also as an individual. His advice will remain with me throughout my life. I would also like to thank my dissertation committee: Dr. Johannes Schwank, Dr. Erdogan Gulari, and Dr. Melanie Sanford for their helpful input and thought-provoking discussions.

In regards to the Thompson research group, I could not have asked for a better group of people to work side-by-side with over the last five years. In one way or another, every member has contributed to my development. I would specifically like to acknowledge a few individuals. First, Dr. Tim King and Dr. Worajit Setthapun helped train me on lab instruments, catalyst synthesis, and reaction experiments when I first joined the group. I appreciate their willingness to answer all of my questions and go through each step of a given procedure in detail so that I fully understood the process. Second, Dr. Chang Kim has been a great mentor and friend. He taught me to strive for excellence and work hard to answer the most difficult research questions. I appreciate his support and motivation during the early years of my research and he will remain a close friend.

Third, Adam Lausche has been a good friend and colleague over the last five years. We both joined the Thompson group in the fall of 2006 and started working on similar projects related to the sulfur tolerance of carbide-based catalysts for the water gas shift reaction and methanol steam reforming. Due to the similarity of our projects, we were constantly able to bounce ideas off of each other and put our heads together to solve problems. We worked together closely to publish two papers related to our projects. After finishing these projects, we each changed directions in our research, but we have continued to have deep discussions related to catalysis and seek out each other's input. I am grateful for having gotten the chance to work with Adam throughout my time at the University of Michigan.

Fourth, I want to acknowledge Dr. Neil Schweitzer. We collaborated extensively to understand the metal adsorption process over molybdenum carbide supports and to determine the structure of platinum particles on a molybdenum carbide support and its relationship to activity for the water gas shift reaction. Additionally, Neil and I had many thought provoking discussions which led to ideas for novel experiments and new research areas to investigate. Neil helped me become a better scientist and researcher. Moreover, I am grateful for Neil's friendship. We spent many sleepless nights collecting spectra at the beam line at the Advanced Photon Source at Argonne National Laboratory. His friendship made these long nights much more enjoyable.

I would also like to thank all of the high school and undergraduate students who have helped me along the way: Krista Blumberg, Adam Herring, Shehara Waas, Paul Rhee, Matt Goh, Leah Miller, Virgil Humes, Olabode Ajenifujah, and Ryan Moody. I could not have completed all of this work without their help.

Additionally, I would like to acknowledge the funding sources for this research, the National Science Foundation and the International Molybdenum Assosication. I have also performed a significant amount of research at the Advanced Photon Source at Argonne National Laboratory (ANL) in partnership with the Materials Research Collaborative Access Team as well as at the Electron Microbeam Analysis Laboratory (EMAL) at the University of Michigan. I would like to specifically thank Dr. Jeff Miller at ANL for all of his help regarding the fundamentals and application of X-ray absorption spectroscopy, and Dr. John Mansfield, Dr. Kai Sun, Dr. Haiping Sun, and Dr. Ying Qi for training me on the instruments at EMAL.

Finally, I want to thank my family and my fiancée Lindsay Lack for all of their support and love. I would not be where I am today without my parents. They taught me that I could achieve whatever I set my mind to. Regardless of my goals or choices in life, they always supported me and encouraged me to strive to be the best that I could be. They are my role models. I love you Mom and Dad! My sisters Emily and Sarah have always inspired me. Emily has a level of determination and persistence that is unmatched. Once she makes up her mind to do something, nothing can stop her. I make every effort to achieve this level of determination in my endeavors in life. Sarah has a unique ability to balance work and play. She understands that life is a balance and cannot be weighted to heavily on either end: work or play. I strive to reach this same type of balance. Emily and Sarah have always supported me and I will always support them. I love you Emily and Sarah! My fiancée Lindsay has always been there for me through the good times and the bad. She inspires me to be the best man that I can be. I am grateful for all of her support and love. I love you Lindsay!

TABLE OF CONTENTS

LIST OF FIGURES

Figure

LIST OF TABLES

Table

CHAPTER 1

Introduction

1.1. Motivation

The research described in this dissertation was aimed at developing catalytic materials that could be used to reduce the impact of humans on the environment. Over the last few decades, significant interest has developed in trying to understand and reduce human impacts on the environment [1, 2]. These impacts include, but are not limited to, climate change (i.e. global warming), resource depletion, fresh water availability, eutrophication, stratospheric ozone depletion, acidification of aquatic environments, biodiversity depletion, human toxicity, and aquatic toxicity [3]. Although significant advancements have been made in quantifying these impacts using methods such as life cycle assessment [3, 4], it is still difficult to fully characterize these impacts on a global scale. Moreover, these impacts are driven by multiple factors that act together to produce a compounding effect. Ehrlich and Holdren suggested using the following equation [5, 6]:

$$I = P \times A \times T \tag{1.1}$$

where I is the environmental impact, P is the human population, A is the affluence of the population, and T is technology.

This equation indicates three ways to reduce human impact on the environment. As an example, gasoline consumption (the environmental impact) in the United States due to personal transportation needs will be discussed. The first option for reducing the impact is to reduce the human population. Figure 1.1a shows the United States population

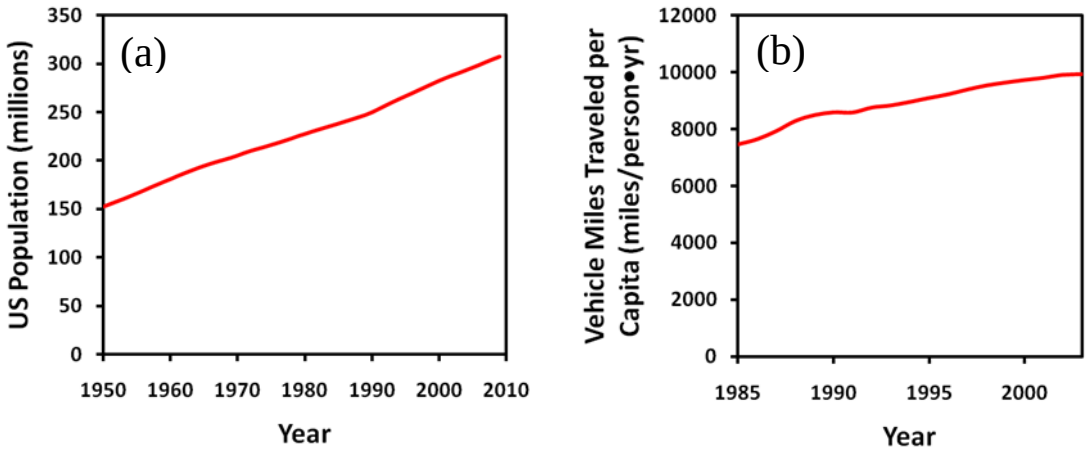

Figure 1.1: (a) Population of the United States from 1950-2010 [7] and (b) the annual vehicle miles traveled per capita in the United States from 1985-2003 [8].

over the last 60 years [7]. Over this time period, the population has been increasing at a rate of approximately 1.2% per year. Due to this increasing trend and the humanitarian issues associated with instating policies to reduce the human population, this option seems like an unrealistic way to reduce our impacts. Second, the affluence, or level of consumption, of the population could be reduced. Although this option is reasonable, it is difficult to convince individuals to reduce their standard of living in order to reduce the overall human environmental impact. The affluence in our gasoline consumption example is expressed as the annual vehicle miles traveled per person in the United States. As shown in Figure 1.1b, this parameter has been steadily increasing over the last 25 years [8]. Finally, the technology, or the processes used to obtain resources and transform them into useful goods, could be improved. In regards to our example, these technological improvements could include increasing the fuel economy of current vehicles or modifying the vehicle drivetrain to operate on other fuels. As shown in Table 1.1, the average fuel economy of vehicles in the United States improved from 13.0 miles per gallon in 1970 to 20.2 miles per gallon in 2002 [8]. This improvement helped reduce

the overall impact; however, the consumption of gasoline still increased by more than 60% from 1970 to 2002. It is clear that significant technological advancements are required to offset the effect of increasing population and affluence. Although the human impact depends on a number of factors, technological improvements appear to be the most feasible option for reducing the global human environmental impact.

Table 1.1: U.S. population, vehicle miles traveled per year per person, fuel economy, and gallons of gasoline consumed in the U.S. for 1970 and 2002, as well as the percent change in each of these values over that time period. Data taken from [8].

	Population	**Affluence**	**Technology**	**Impact**
Year	U.S. Population (million)	Vehicle Miles Traveled per Year per Person (mi/yr-per)	Fuel Economy (gal/mi)	Gallons of Gasoline Consumed (billion gallons/yr)
1970	205	5073	0.077 (13.0 miles per gallon)	80.1
2002	288	9107	0.050 (20.2 miles per gallon)	129.8
Percent Change (%)	+41	+80	−36	+62

One area where technology advancements could cause a significant reduction in environmental impact is transportation fuel production. In 2009, the United States consumed approximately 95 quadrillion Btu of energy (see Figure 1.2) [7]. More than a third of this energy was derived from petroleum, a non-renewable fossil fuel. This corresponds to the consumption of more than 18 million barrels of petroleum per day in the United States [7]. That is enough petroleum consumed in one day to cover the entire University of Michigan-Ann Arbor campus to a depth of more than 9 inches. The primary use (>70%) of the petroleum is for the production of liquid transportation fuels such as gasoline and diesel [7].

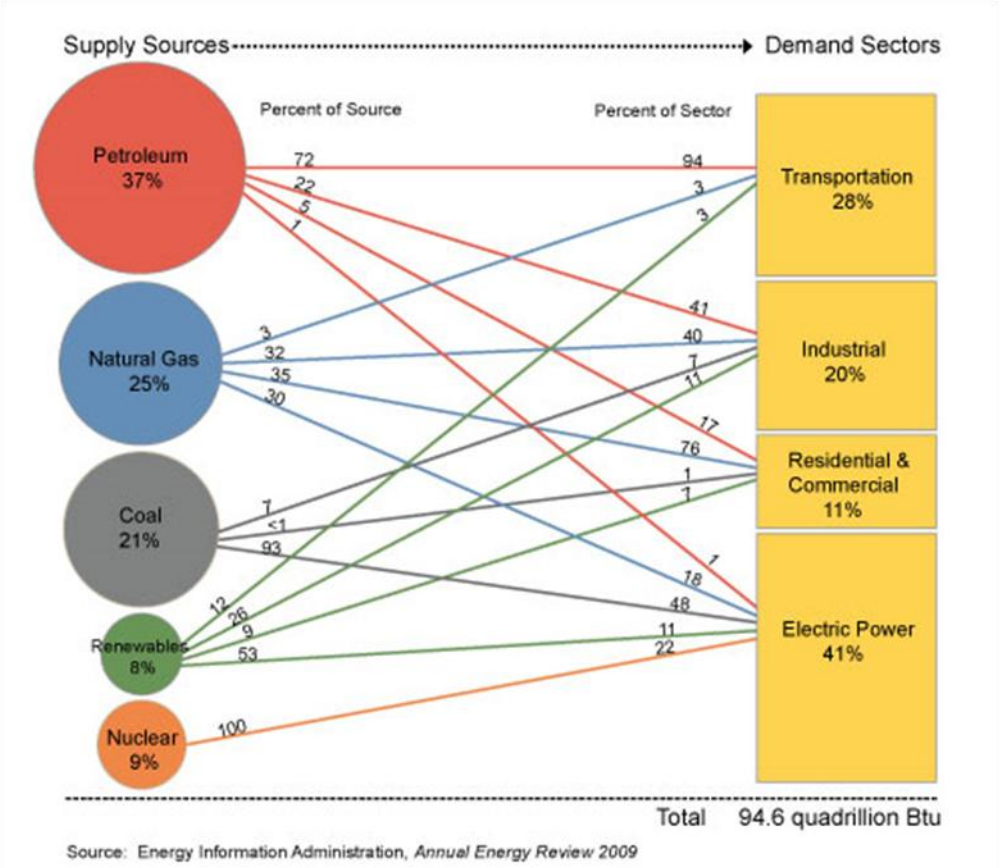

Figure 1.2: United States primary energy flow by source and sector for 2009. Taken from [7].

Utilizing petroleum as a feedstock for liquid fuel production has a number of major drawbacks. First, along with the sheer volume of consumption, the rate of consumption continues to increase as shown in Figure 1.3a [7]. This trend presents a significant problem as petroleum is a non-renewable resource and there is only a finite quantity accessible in the world. Second, the U.S. production of petroleum has steadily decreased over the last 30 years while our net imports have increased (see Figure 1.3a) [7], meaning that we are more reliant on foreign nations for our energy needs. Third, there has been high variability in the price of petroleum over the last 5 to 6 years (see Figure 1.3b) [9]. In 2003, transportation was the second largest expenditure for the

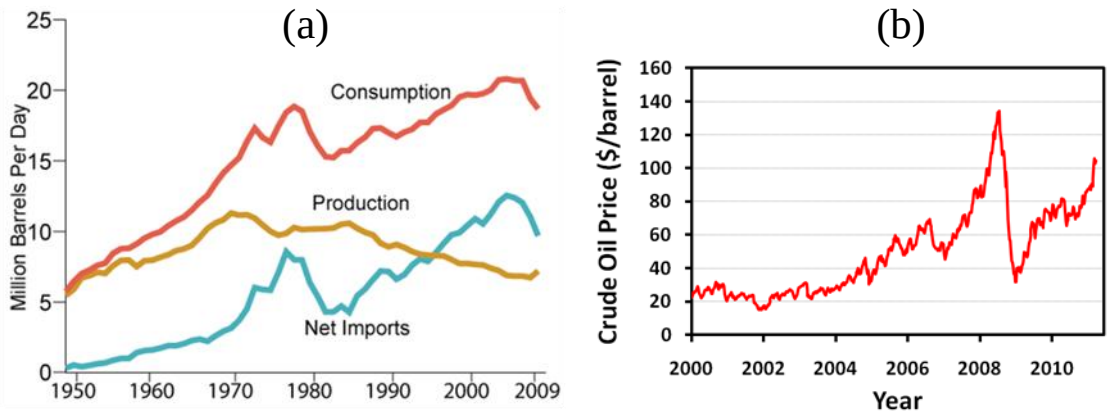

Figure 1.3: (a) United States petroleum consumption, production, and net imports from 1950-2009. Taken from [7]. (b) Crude oil price from January 2000 – January 2011 [9].

average U.S. household [8]. As such, this variability in petroleum price makes it difficult for some households to make ends meet financially. Additionally, transportation is a key step in the delivery of most consumer products, therefore increases in petroleum prices also cause increases in most goods and services. Fourth, burning fuels derived from petroleum releases carbon dioxide, a major contributor to global warming, and other harmful pollutants such as sulfur dioxide into the atmosphere. For the United States to reach long-term energy sustainability, petroleum needs to be replaced by a diverse portfolio of renewable feedstocks for the production of liquid transportation fuels.

To address this issue, the United States government created the Renewable Fuel Standard (RFS) as part of the Energy Policy Act in 2005 [10]. As of 2007, the RFS requires more than 36 billion gallons of renewable fuels to be blended into transportation fuel by 2022. To meet this need, industrial biorefineries have been identified as the most promising route to the creation of a new domestic bio-based industry [11]. Similar to a petroleum refinery, a biorefinery is a facility that produces fuels, power, and chemicals from biomass [11]. There are a number of viable routes for the production of liquid

transportation fuels from biomass (see [12] and [13] and the references cited therein). Typically, these routes fall into two broad categories based on the method of conversion: biochemical or thermochemical. The three routes that currently show the most potential are alcohol (typically ethanol) production via fermentation, biodiesel production via transesterification of oils, and thermochemical catalytic conversion of biomass into fuels.

Ethanol production via fermentation involves the conversion of the carbohydrate portion of the biomass feedstock (hemicellulose and cellulose) into sugars, which are then fermented into ethanol [14-16]. This process has four main steps. First, the biomass is pretreated (heat combined with acid or base) to break down the tough, fibrous cell walls. Next, enzymes break apart the pretreated material to release the sugars through hydrolysis. Third, the sugars are fermented into ethanol through the use of microorganisms. Finally, the ethanol is recovered from the mixture via distillation. The key areas that need to be improved in order for this process to become commercialized on a large scale are more efficient enzymes for hydrolysis and microorganisms for fermentation [14-16]. In particular, the objectives are to develop enzymes with higher efficiencies for extracting the sugars from cellulose and hemicellulose and to design microorganisms that can ferment five- and six-carbon sugars at the same time [14-16].

Biodiesel production involves the conversion of triglycerides present in vegetable oils, animal fats, or even algae into fatty acid methyl esters [15-17]. First, the oils are pretreated to remove water and other contaminants. Then, an alcohol (e.g. methanol) and a catalyst (e.g. sodium hydroxide or potassium hydroxide) are reacted with the oils. This step, called transesterification, converts the oils (triglycerides) into methyl esters and glycerin. Lastly, these products are separated and the crude biodiesel (methyl esters) is

purified. Research is ongoing to achieve cost reductions via modifying the transesterification step, while still achieving high yields (>99%) and meeting desired quality standards [16].

Thermocatalytic conversion of biomass into fuels involves the initial conversion of biomass into synthesis gas (mixture of H_2 and CO) via gasification with high temperatures and either oxygen or steam [18, 19]. Following gasification, the synthesis gas is cleaned to reduce the concentration of impurities, such as sulfur and nitrogen containing compounds, to an acceptable level. Additionally, the H_2/CO ratio is often adjusted to a more optimal value (~2) using the water gas shift reaction. Then, the synthesis gas can be converted into either alcohols via alcohol synthesis or long-chain hydrocarbons (gasoline, diesel, etc) via Fischer-Tropsch Synthesis. Key research areas for improving this process include advanced gasification techniques to minimize char production and reduce energy input, and developing catalysts for water gas shift, Fischer-Tropsch Synthesis, and alcohol synthesis with improved sulfur tolerance, selectivities, and lifetimes [18, 19].

Based on the current technology and ongoing research and development regarding these routes for liquid fuel production from biomass, there is no clear commercial or technical advantage between the biochemical and thermochemical pathways [16]. However, the thermochemical production of fuels via Fischer-Tropsch Synthesis faces the least number of technical hurdles with regards to commercialization as a majority of the technology is already proven. Fischer-Tropsch Synthesis plants operating with either coal or natural gas as a feedstock have been in operation for more than 50 years in South Africa [20-23]. Additionally, Fischer-Tropsch Synthesis allows for the production of

fungible fuels (gasoline and diesel), whereas alcohols (i.e. methanol and ethanol) produced either thermochemically or biochemically may require vehicle modifications. These fuels produced via Fischer-Tropsch Synthesis are also of a high quality due to very low aromaticity and zero sulfur content. Finally, due to the long chain hydrocarbons produced via Fischer-Tropsch Synthesis, fuels for marine or aviation applications can be produced. Given these advantages, thermochemical biomass conversion to hydrocarbon fuels via gasification, water gas shift, and Fischer-Tropsch Synthesis will likely play a critical role in the production of renewable liquid transportation fuels in the future. The next sections will describe in detail the water gas shift and Fischer-Tropsch Synthesis reactions as well as discuss the properties of early transition metal carbide and nitride materials.

1.2. Water Gas Shift Reaction

The water gas shift reaction (WGS) involves the production of H_2 and CO_2 from CO and H_2O (Equation 1.2) [20]:

$$CO + H_2O \leftrightarrow CO_2 + H_2 \quad (1.2)$$

WGS plays a critical role in the production of hydrogen via hydrocarbon reforming as well as the production of liquid transportation fuels via Fischer-Tropsch Synthesis. For coal-derived or biomass-derived synthesis gas, the H_2/CO ratio (0.7-1) is typically below the optimal range for Fischer-Tropsch Synthesis (~2). Therefore, WGS is employed to shift this ratio into a more usable regime.

Due to thermodynamic limitations (ΔH^0_{WGS} = −41 kJ/mol), WGS is typically carried out over two different temperature ranges: high temperature shift (300-450°C) and low temperature shift (200-270°C) [20]. A diagram illustrating the operating regimes

for high and low temperature shift is shown in Figure 1.4. Industrially, high temperature shift is carried out over a Fe-Cr catalyst and low temperature shift is carried out over a Cu/Zn/Al catalyst [20]. Although these catalysts are used industrially, they still have a number of limitations, specifically with regards to the sulfur intolerance of the Cu/Zn/Al

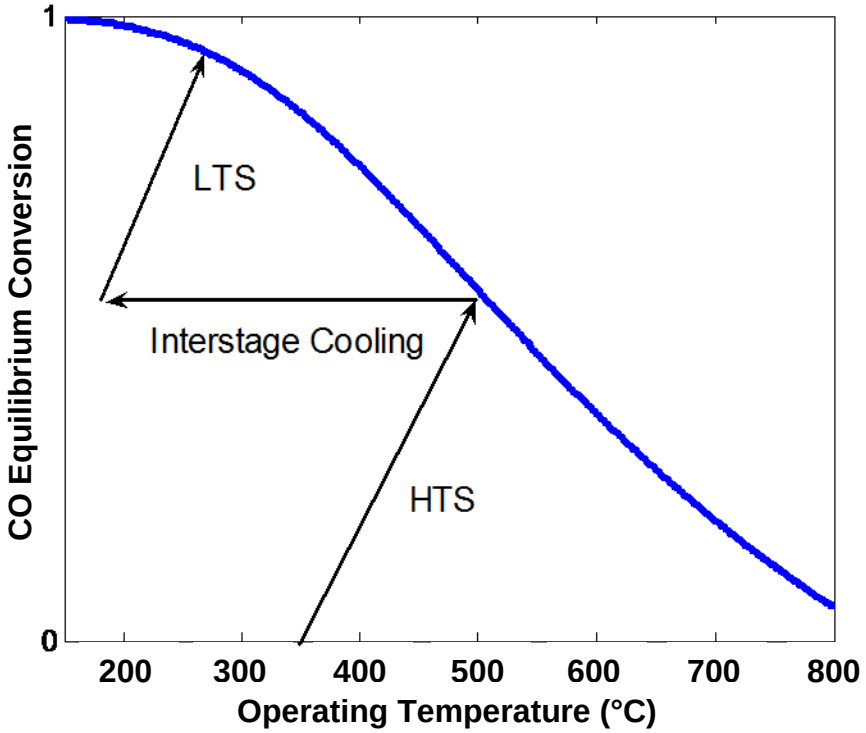

Figure 1.4: Water gas shift equilibrium CO conversion as a function of reaction temperature. Sample adiabatic operating ranges are shown indicating high temperature shift (HTS) and low temperature shift (LTS).

catalyst. The Cu/Zn/Al catalyst has been reported to lose a significant portion of its WGS activity in the presence of <1 ppm of H_2S or COS [24].

Due to the sulfur impurities present in feedstocks such as coal and biomass, a WGS catalyst that meets or exceeds the activity of the commercial Cu/Zn/Al catalyst as well as exhibits tolerance to sulfur compounds is needed. Previous research in our group has shown that early transition metal carbide and nitride based materials, specifically Mo_2C and Pt/Mo_2C, are highly active for WGS (discussed in detail in Section 1.5) [25-

28]. Additionally, these materials have been reported to be sulfur tolerant for certain reactions (discussed in detail in Section 1.4). For these reasons, early transition metal carbide and nitride based catalysts were investigated in the research described in this dissertation.

1.3. Fischer-Tropsch Synthesis

Fischer-Tropsch Synthesis (FTS) is the conversion of synthesis gas into a mixture of hydrocarbons and oxygenated products and water [29]. The primary products are linear paraffins and olefins as shown in Equations 1.3 and 1.4:

$$(2n+1)H_2 + nCO \rightarrow C_nH_{2n+2} + nH_2O \quad (1.3)$$

$$2nH_2 + nCO \rightarrow C_nH_{2n} + nH_2O \quad (1.4)$$

where n is a positive integer. Side reactions include the water gas shift reaction and alcohol synthesis (Equation 1.5):

$$2nH_2 + nCO \rightarrow C_nH_{2n+2}O + (n-1)H_2O \quad (1.5)$$

Under typical FTS reaction conditions, these reactions occur concurrently to produce a complex multi-component mixture.

The FTS process was first developed in the early 1900's and was used by Germany during the 1930's and 1940's to produce liquid fuels from coal-derived synthesis gas [12, 30]. Since that time, interest in FTS has waxed and waned depending upon environmental concerns, technological developments, and fossil fuel price and availability; however, the process has been demonstrated commercially by Sasol in South Africa [20-23] and Shell in Malaysia [31]. The first Sasol FTS plant came on line in 1955 producing fuels from coal. Currently, Sasol operates three FTS plants in South Africa producing more than 160,000 barrels of fuel per day as well as other chemicals using

both coal and natural gas as feedstocks [32, 33]. The Shell Middle Distillate Synthesis process in Malaysia produces heavy paraffins using natural gas as the feedstock [31]. These heavy paraffins can be sold as wax specialties or upgraded through hydrocracking to diesel fuel [29, 31].

Industrially, FTS is typically carried out at pressures ranging from 10-60 bar and two temperature regimes: high temperature FTS (300-350°C) and low temperature FTS (200-250°C) [34]. High temperature FTS typically yields hydrocarbons in the C_1-C_{15} range and is used primarily to produce liquid fuels as well as valuable chemicals (produced from olefins). Low temperature FTS is used primarily for the synthesis of linear long-chain hydrocarbon waxes and paraffins, which can be converted into diesel fuel through hydrocracking [34]. The H_2/CO ratio for the feed is typically much less than 2 for high temperature FTS and between 1.7 and 2.2 for low temperature FTS. Due to the strong exothermic nature of FTS and the complex multiphase, multi-component product stream, three different types of reactor designs have been used commercially: tubular fixed bed, fluidized bed (circulating and fixed), and a slurry reactor [35]. Fluidized bed reactors are typically used for high temperature FTS while low temperature FTS is typically carried out in a tubular fixed bed or slurry reactor. The choice of reactor design is based on many factors including catalyst/liquid product separation, heat transfer, pressure drop, catalyst attrition, diffusion limitations, C_5+ selectivity, and capital and operating cost [35].

Due to the number of parallel reactions, selectivity to the desired products is essential for the economical operation of large-scale FTS plants. The operating conditions for FTS offer some opportunities to control the selectivity of the reaction [29]. Table 1.2

shows the response of various product selectivities to changing specific process parameters. For example, to minimize the production of methane (a relatively undesired product), the best process conditions would be low temperature, high pressure, low H_2/CO ratio, low conversion, and high space velocity. Understanding the effects of process conditions is important as the desired products from a given FTS process vary from gasoline and diesel to waxes to chemicals (olefins and alcohols).

Table 1.2: Selectivity control in Fischer-Tropsch Synthesis by process conditions. ↑ indicates increase with increasing parameter. ↓ indicates decrease with increasing parameter. * indicates a complex relation. Adapted from [29].

Parameter	Chain Length	Chain Branching	Olefin Selectivity	Alcohol Selectivity	Carbon Deposition	Methane Selectivity
Temperature	↓	↑	*	↓	↑	↑
Pressure	↑	↓	*	↑	*	↓
H_2/CO	↓	↑	↓	↓	↓	↑
Conversion	*	*	↓	↓	↑	↑
Space Velocity	↑	*	↑	↑	↑	↓

Beyond process conditions, the product selectivity is constrained by the polymerization nature of FTS [36]. In general, the distribution of hydrocarbon chain length has been shown to follow the Anderson-Schulz-Flory (ASF) chain polymerization model [29, 37], which can be described by equation 1.6:

$$m_n = (1-\alpha)\alpha^{n-1} \tag{1.6}$$

where m_n is the mole fraction of a hydrocarbon with chain length n and α is the chain growth probability parameter. The chain growth parameter, α, is defined by:

$$\alpha = \frac{R_P}{R_P + R_T} \tag{1.7}$$

where R_P and R_T are the rates of propagation and termination of the hydrocarbon chain, respectively [29]. Figure 1.5 illustrates this chain polymerization model with the

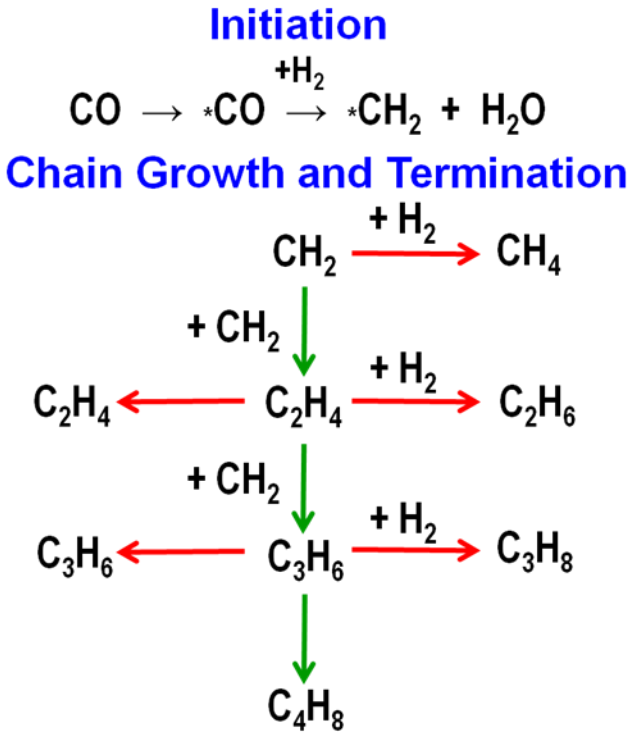

Figure 1.5: Anderson-Schulz-Flory chain polymerization diagram showing the initiation of the chain through the formation of a methylene monomer, followed by chain propagation steps (green) and chain termination steps (red).

propagation steps shown in green and the termination steps shown in red. For this example, the monomer is a methylene group ($-CH_2$). It should be noted that the ASF model does not account for reversibility of the chain propagation steps (i.e. hydrocracking or hydrogenolysis). Other models have been developed to account for reversibility and product re-adsorption [29 and the references cited therein]. The total carbon-number distribution of the FTS products is determined by α, as shown in Figure 1.6. For example, to produce the maximum weight fraction of C_{11}-C_{20} hydrocarbons, α should be around 0.85-0.9. The range of α is directly affected by not only the reaction conditions as discussed earlier, but also the catalyst type.

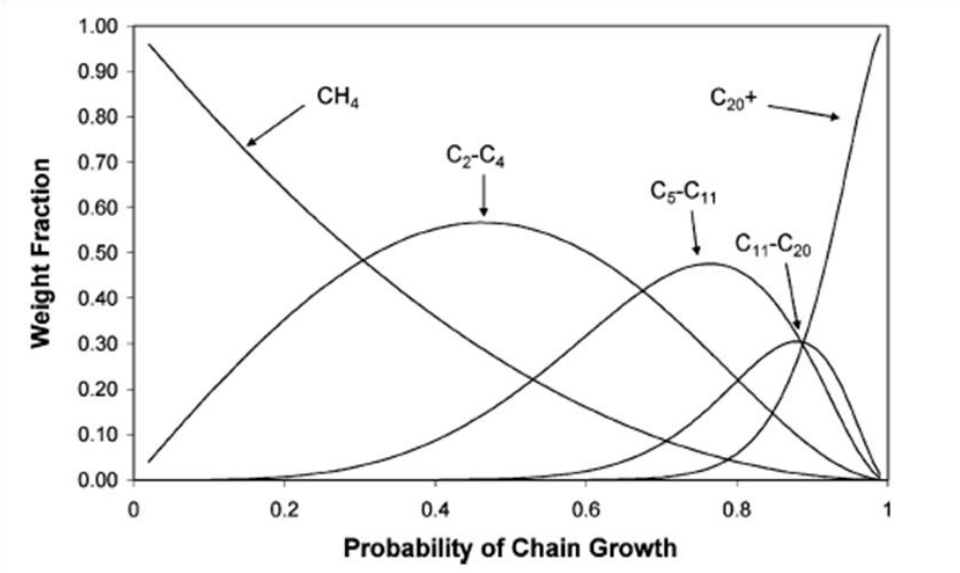

Figure 1.6: Idealized product distribution for FTS based on the Anderson-Schulz-Flory model. Taken from [12].

Due to the long history of FTS, the performance of a number of transition metals (Ru, Fe, Co, Rh, Ni, Ir, Pt, Mo) has been investigated [38-41]. However, the two primary catalysts used industrially are Co and Fe [19, 29]. These metals are typically supported on oxides such as silica (SiO_2) and alumina (Al_2O_3), and promoters are often added (Cu and K for Fe catalysts and Pt for Co catalysts). A comparison of Co and Fe catalysts is given in Table 1.3. In general, Co catalysts are highly active and demonstrate good resistance to deactivation, but are expensive and are very sensitive to changes in temperature, pressure, and H_2/CO ratio [34]. Iron catalysts are less expensive and more robust in terms of operating conditions, but are less active and less resistant to deactivation. Both catalysts are susceptible to sulfur poisoning at concentrations above 0.1 ppm [34].

For the thermochemical conversion of biomass into fuels via FTS, the catalyst needs to achieve high overall CO conversion and a high C_5+ selectivity [18, 19]. Additionally, the H_2/CO ratio of synthesis gas produced from biomass is typically between 1 and 2, and can vary during operation due to changes in the biomass feed or

other plant upsets. Ideally, the catalyst would also have a long lifetime and be tolerant to impurities such as sulfur and nitrogen containing molecules. Therefore, based on these requirements and the properties of Fe and Co catalysts given in Table 1.3, there is a need to develop a relatively inexpensive catalyst with activity and selectivity similar to Co and robustness similar to Fe towards varying operation conditions. Early transition metal carbides and nitrides have been reported to be active for CO hydrogenation (discussed in detail in Section 1.4) and have potential for meeting these requirements.

Table 1.3: Comparison of Co- and Fe-based FTS Catalysts. Adapted from [34].

Parameter	Cobalt Catalysts	Iron Catalysts
Cost	More expensive	Less expensive
Lifetime	Resistant to deactivation	Less resistant to deactivation (coking, carbon deposit, iron carbide)
Activity at low conversion	Comparable	
Productivity at high conversion	Higher; less significant effect of water on rate of carbon monoxide conversion	Lower; strong negative effect of water on the rate of carbon monoxide conversion
Maximum chain growth probability	0.94	0.95
Water gas shift reaction	Not very significant; more noticeable at high conversion	Significant
Maximum sulfur content	<0.1 ppm	<0.2 ppm
Flexibility (temperature and pressure)	Less flexible; significant influence of temperature and pressure on hydrocarbon selectivity	Flexible; methane selectivity is relatively low even at 340°C
H_2/CO ratio	~2	0.5-2.5
Attrition Resistance	Good	Not very resistant

1.4. Early Transition Metal Carbides and Nitrides

Transition metals in Groups 4-6 of the periodic table (Ti, V, Nb, Ta, Mo, W) are capable of forming stable compounds with carbon or nitrogen [42]. In these compounds,

the carbon or nitrogen occupies the interstitial spaces between the parent metal atoms. The incorporation of the carbon or nitrogen into the metal structure causes an expansion of the metal crystal lattice, which results in an increase in the metal-metal bond distance [42]. The crystal structure adopted is based on geometric and electronic factors. The geometric factor is based on the Hägg rule, which states that simple structures are formed when the ratio of the radii of nonmetal to metal is less than 0.59 [43]. The electronic factor is based on the Engel-Brewer theory of metals, which states that the structure adopted by a metal or a substitutional alloy depends on the s-p electron count [42]. As such, the mixing of the s-p orbitals of the nonmetal with the s-p-d band of the metal will affect the crystal structure of the carbide or nitride material. Typical crystal structures for early transition metal carbides and nitrides are shown in Figure 1.7.

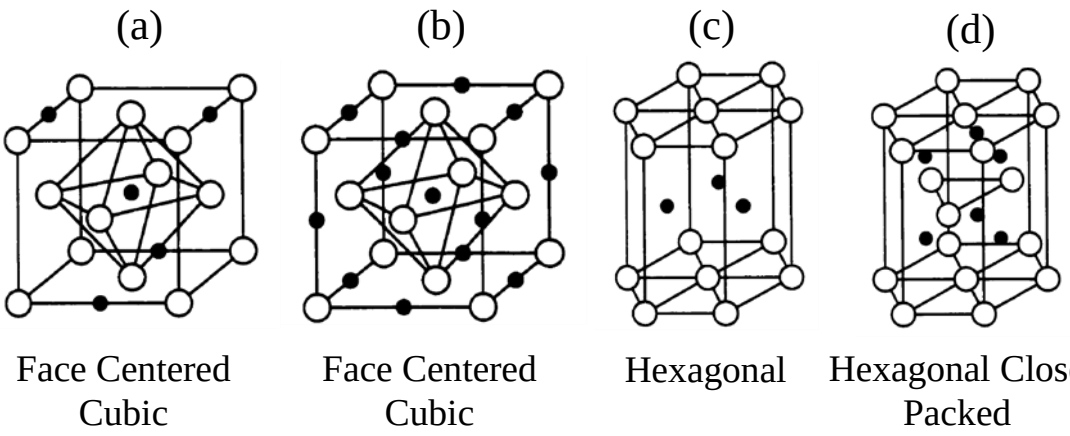

Figure 1.7: Crystal structures for Groups 4-6 transition metal carbides and nitrides. (a) Mo_2N, W_2N, MoC_{1-x}, and WC_{1-x}, (b) TiN, ZrN, HfN, VN, CrN, TiC, ZrC, HfC, VC, NbC, and TaC, (c) TaN, MoN, MoC, WC, and (d) Mo_2C and W_2C. Adapted from [44].

Along with changes in the crystal structure, the addition of carbon and nitrogen into the parent metal lattice causes the carbide or nitride material to possess physical and chemical properties that are different from the parent metal [42]. Group 4-6 transition metal carbide and nitride compounds exhibit high melting points, extreme hardness and

strength, as well as high electrical and thermal conductivities [42]. Of particular interest to the field of heterogeneous catalysis, carbides and nitrides also exhibit chemical reactivities that are quite different from the parent metal. This result was first observed by Levy and Boudart in 1973 [45]. They showed that tungsten carbide catalyzed the isomerization of 2,2-dimethylpropane to 2-methylbutane; this catalytic behavior is not exhibited by tungsten metal. Additionally, the only other metals that have been found to perform this reaction are Pt, Au, and Ir, suggesting that carbides and nitrides may possess catalytic properties similar to noble metals [45]. Since this discovery by Levy and Boudart, the catalytic behavior of early transition metal carbides and nitrides has been investigated for a variety of reactions ranging from ammonia synthesis to hydrocarbon reforming [42 and the references cited therein].

Based on their properties, early transition metal carbides and nitrides are promising materials for meeting the catalyst requirements for WGS and FTS. First, these materials have been shown to be active for CO hydrogenation [46-53]. Kojima et al. were among the first to investigate the CO hydrogenation activity of early transition metal carbides [46-48]. At atmospheric pressure, they found that carbides such as TiC, TaC, Mo_2C, WC, and W_2C primarily produced CH_4, light hydrocarbons (C_2-C_4), CO_2, and H_2O; however a small amount of higher hydrocarbons were also observed (C_5+). Additionally, they noted that the carbides continued to produce C_2+ hydrocarbons under conditions of high temperatures and high H_2/CO ratios. These conditions strongly favor the production of CH_4. For common CO hydrogenation catalysts such as Ru and Ni, the primary product under high temperatures and high H_2/CO ratios is CH_4. Ranhotra et al. compared the CO hydrogenation performance of Mo_2C and Mo_2N at atmospheric

pressure and reported that the activity for the face centered cubic (FCC) phases of Mo_2C and Mo_2N were similar [49]. Kim et al. found that supported and unsupported Mo_2C catalysts exhibited turnover rates for CO hydrogenation at atmospheric pressure similar to those for Ru metal [50]. More recent studies have also investigated the effect of higher pressure [51] and the addition of promoters such as potassium [52, 53]. Although the performance of these materials for CO hydrogenation has been explored to some extent, there are still a number of areas that need further investigation. These areas include evaluating performance under industrially relevant reaction conditions, elucidating the governing mechanisms, and improving selectivity towards C_5+ hydrocarbons.

Second, these materials have been reported to be sulfur tolerant for certain reactions [54-57] as well as moderately resistant to coking [58, 59]. Dhandapani et al. observed that Mo_2C exhibited minimal deactivation during simultaneous hydrodesulfurization, hydrodeoxygenation, and hydrodenitrogenation in the presence of up to 30 ppm of sulfur in the form of dibenzothiphene [54]. The authors proposed that the Mo_2C surface was converted to a carbosulfide in the presence of sulfur. Under similar conditions, a noble metal catalyst (Pt/Al_2O_3) deactivated immediately. Minimal deactivation was also reported by Cheekatamarla et al. for the steam reforming of tri-methyl pentane over Mo_2C at sulfur concentrations up to 100 ppm [55]. For the hydrogenation of tetralin in the presence of H_2S, Da Costa et al. reported that post-reaction characterization did not show any evidence of sulfide formation on the supported Mo_2C and W_2C catalysts [56]. However, most of these studies were performed at moderately high temperatures and pressures. The sulfur tolerance of early transition metal carbides and nitrides has not been investigated under conditions similar to those for the

low temperature water gas shift reaction (1 atm, 200-270°C). In regards to coking, Claridge et al. reported that carbon deposition was not observed using high resolution transmission electron microscopy over Mo_2C and W_2C catalysts for the reforming of methane [58]. Based on thermodynamics, Sehested et al. concluded that Mo_2C has a greater resistance to surface carbon formation than Ni-based catalysts, which often exhibit severe deactivation due to coking [59].

Third, using a temperature programmed reaction method, these materials can be synthesized with high surface areas, presenting the possibility of using these materials as supports for other metals [42]. In general, a metal oxide precursor is placed into a flowing stream of either a reductive carburizing gas (such as a CH_4/H_2 mixture) to produce the carbide or ammonia gas to produce the nitride [42, 60]. The temperature is increased in a uniform manner until some maximum temperature is reached. This method directly converts the oxide precursor into the carbide/nitride while bypassing formation of the metallic state [42]. The metallic state is the most prone to sinter and leads to the formation of carbides/nitrides with low specific surface areas (<1 m^2/g) [42]. Formation of the carbide/nitride material is often topotactic, and differences in densities between the oxide precursor and the carbide/nitride material result in the final material having a significant pore structure [42]. Carbides and nitrides with surface areas as high as 225 m^2/g have been synthesized using this method [42].

1.5. Early Transition Metal Carbide and Nitride Supported Metal Catalysts

Due to the ability to synthesize early transition metal carbide and nitride materials with high surface areas as well as their unique catalytic properties, interest has developed in using these materials as supports. Ledoux et al. investigated the effect of adding of Pt,

Ru, or Ir onto Mo_2C or WC for the isomerization of n-hexane [61]. They reported that Pt supported on Mo_2C exhibited a specific activity that was 6 times higher than that of a conventional Pt/Al_2O_3 catalyst. For methane reforming with CO_2 in a solar receiver reactor, Volter et al. observed a significant increase in activity when Rh was supported on WC [62]. For FTS, Griboval-Constant et al. explored the performance of Co or Ru supported on Mo_2C [63] and WC [64]. The Co/Mo_2C and Ru/WC catalysts exhibited increased formation of higher hydrocarbons compared to the carbide support alone. However, the surface areas of the carbides employed in these FTS studies were low (<10 m^2/g), and the metal loadings of Co and Ru were approximately 1 wt%. Assuming a site density of $1x10^{19}$ sites/m^2 and a surface area of the carbide support of 5 m^2/g, the surface loading of Co and Ru was approximately 200% and 120% of a monolayer, respectively. Due to these high surface loadings, it is probable that the improved performance exhibited by the carbide supported Co and Ru catalysts is just due to the innate activity and selectivity of the supported metal, and not due to a combination of the support and the metal. More recently, Lewandowski et al. tested the activity of a Pt-doped Mo_2C catalyst for hydrodesulfurization and hydrodenitrogenation of 4,6-dimethyldibenzothiophene and carbazole [65]. For both reactions, the Pt-doped Mo_2C catalyst was more active than Mo_2C alone. The authors attributed the improved hydrotreating activity to the improved hydrogenation activity of the modified catalyst. For all of these aforementioned studies, the supported metal was deposited onto the passivated carbide surface (carbides are typically passivated prior to exposure to air due to their pyrophoricity). Therefore, the metal precursors interacted with an oxidized surface rather than the native carbide surface.

Recently, our group developed a technique to deposit metals directly onto the native carbide or nitride surfaces using an aqueous wet impregnation method [25, 26, 66, 67]. The performance of early transition metal carbide and nitride supported metal catalysts synthesized via this method has been explored for methanol steam reforming [66, 67] and the water gas shift reaction [26]. For both reactions, the addition of the metal to the carbide or nitride surface affected the activity and selectivity of the catalyst. For WGS, the addition of Pt or Ni onto the Mo_2C surface resulted in a marked improvement in activity (see Figure 1.8). Although the rate for the Mo_2C support was less

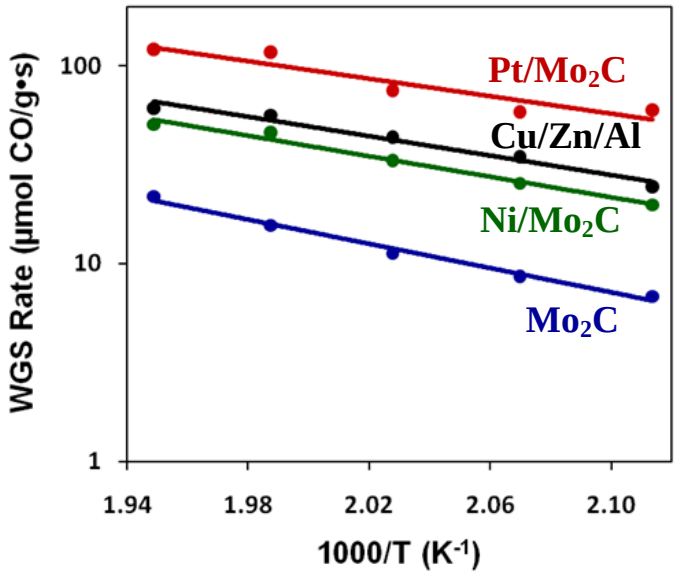

Figure 1.8: Arrhenius plots of the WGS reaction rate for Mo_2C, Ni/Mo_2C, Pt/Mo_2C, and a commercial Cu/Zn/Al catalyst.

than 50% of the rate of the Cu/Zn/Al commercial catalyst, a 4% Pt/Mo_2C catalyst exhibited a rate that was 2-3 times higher than that of Cu/Zn/Al. In comparison, a 4% Pt/Al_2O_3 catalyst exhibited negligible activity under these conditions. Additionally, it has been shown that these materials exhibit a support effect for WGS (see Figure 1.9). A support effect can be defined as an interaction of the support with the active catalytic phase, which causes a measureable change in the turnover frequency [68]. The areal rates

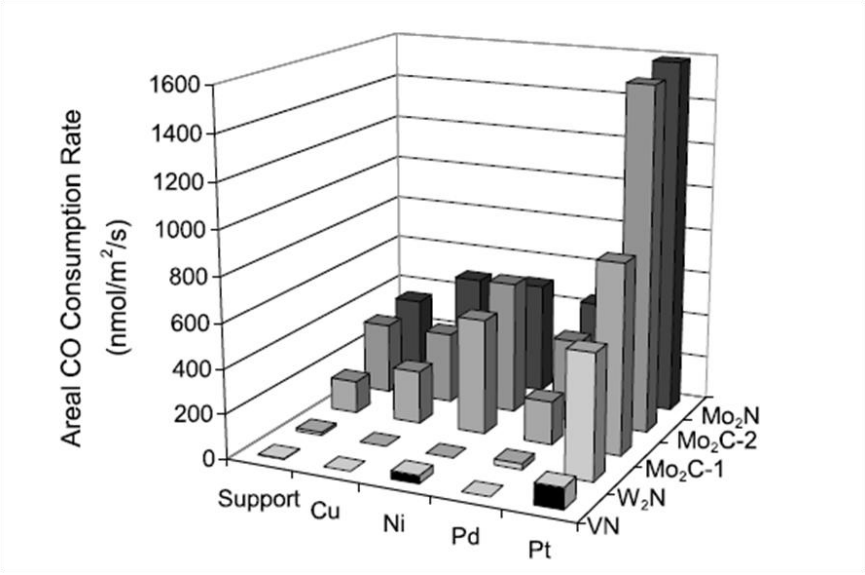

Figure 1.9: Areal CO consumption rates for WGS at 240 °C for Cu, Ni, Pd, and Pt supported on various carbide and nitride supports. Taken from [26].

shown in Figure 1.9 illustrate that the catalytic performance for a given metal changes depending upon the carbide or nitride support.

Schweitzer et al. investigated the support effect further for Pt/Mo_2C WGS catalysts and drew two key conclusions [28]. First, a strong interaction between the Pt precursor and the native Mo_2C surface occurs during wet impregnation resulting in the formation of "raft-like" Pt particles. As shown in Figure 1.10, these Pt particles have relatively low contact angles with the Mo_2C support and exhibit flatter intensity profiles than cubo-octahedral Pt particles supported on carbon. These "raft-like" particles result in high dispersion of the metal and a high density of Pt-Mo_2C interface sites, which were shown to be active for WGS. Second, the addition of the Pt onto the Mo_2C surface results in a catalyst that is bi-functional in nature. More specifically, the Pt sites appear to adsorb CO while the Mo_2C sites activate H_2O. The result of this combination (Pt/Mo_2C) is a catalyst that is more active than most other Pt-based WGS catalysts (See Figure 1.11) [28]. The conclusions from this work encouraged further investigations of interactions

between metal precursors and the native carbide surface in an attempt to exploit the bi-functional nature of these carbide and nitride supported metal catalysts for FTS.

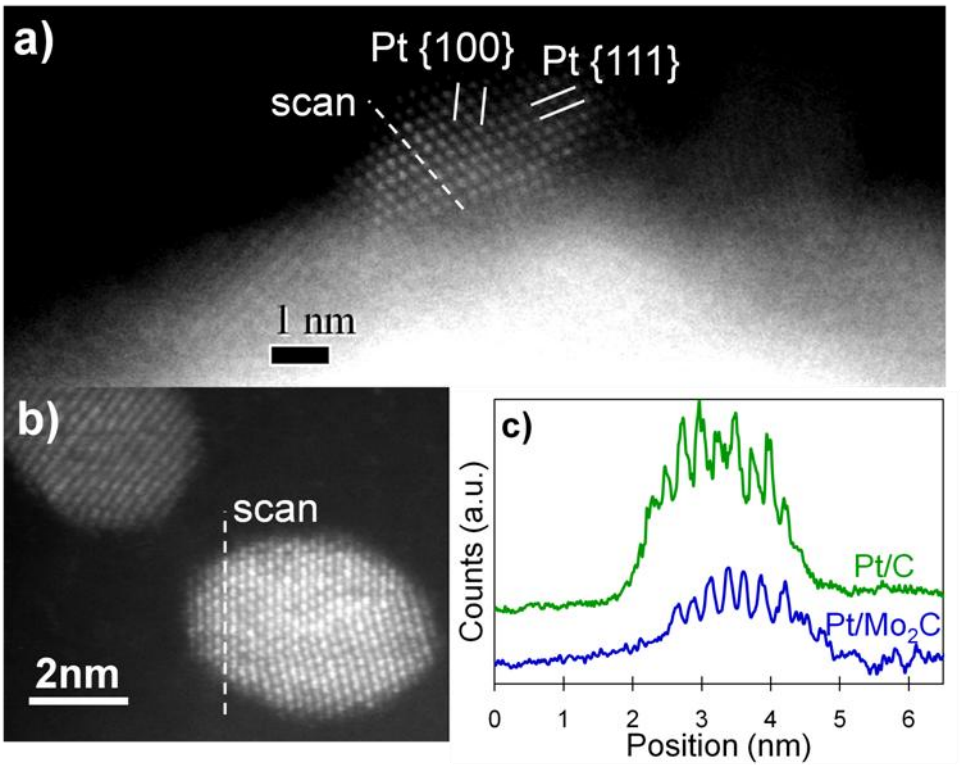

Figure 1.10: High resolution HAADF-STEM electron micrographs of (a) a Pt particle supported on Mo_2C and (b) a Pt particle (cubo-octahedral shape) supported on carbon. (c) Intensity line scans for the Pt particle supported on Mo_2C in Figure 1.9a and the Pt particle supported on carbon in Figure 1.9b. The line scans indicate that the Pt particle on the Mo_2C support has a flatter profile than the cubo-octahedral Pt particles supported on carbon. Taken from [28].

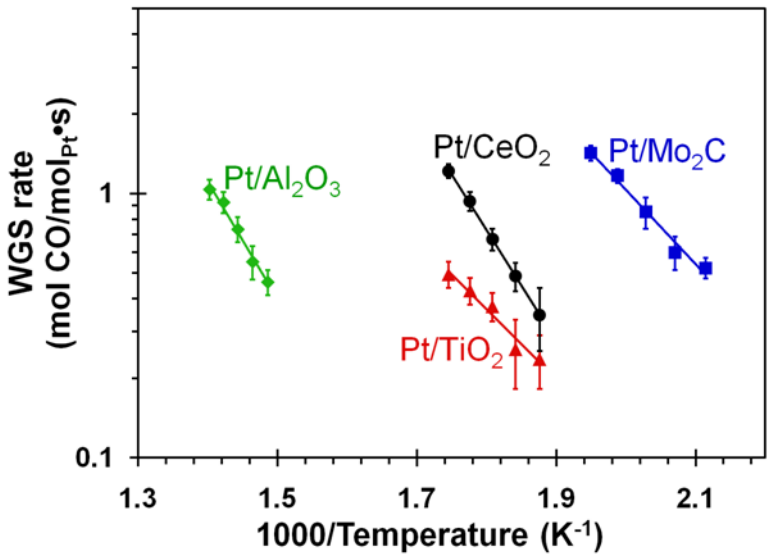

Figure 1.11: Arrhenius plots of the WGS reaction rate for Pt supported on Al_2O_3, CeO_2, TiO_2, and Mo_2C. Taken from [28].

1.6. Research Goals and Organization of the Text

There are three primary goals for research described in this dissertation: (1) investigate the effects of sulfur on the properties of Mo_2C and Pt/Mo_2C catalysts under water gas shift conditions, (2) evaluate the performance of a series of early transition metal carbide- and nitride-based catalysts for Fischer-Tropsch Synthesis and (3) develop structure-function relationships that can be used to guide future catalyst development. The specific objectives regarding these goals were to:

1. Evaluate the WGS performance of Mo_2C and Pt/Mo_2C catalysts in the presence of H_2S and characterize the materials pre- and post-reaction to determine the effect of sulfur on their surface and bulk structures.
2. Synthesize and characterize carbides and nitrides of molybdenum, tungsten, vanadium, and niobium, and evaluate their FTS performance in terms of activity, selectivity, and durability.

3. Develop relationships between FTS performance and (1) the interstitial atom (C vs. N) and (2) the interactions of specific probe molecules such as CO with the carbide/nitride surface.
4. Determine the effect on FTS performance of depositing metals onto the carbide/nitride surface. To accomplish this objective, the interactions between the metal precursors and the native carbide/nitride surface were explored during the metal loading process.

This thesis is divided into seven chapters. A brief description of the remaining chapters is given below:

Chapter 2: Effects of Sulfur on Mo_2C and Pt/Mo_2C Water Gas Shift Catalysts

This chapter discusses the effect of sulfur on the structure and water gas shift activities of Mo_2C and Pt/Mo_2C catalysts. The effect of sulfur is explored using time on stream deactivation studies and regeneration studies, thermogravimetric analysis, and bulk and surface characterization using techniques such as X-ray diffraction, X-ray photoelectron spectroscopy, and scanning electron microscopy. The catalyst deactivation due to sulfur is linked to changes to the catalyst surface.

Chapter 3: Synthesis, Characterization, and Fischer-Tropsch Synthesis Performance Evaluation of Early Transition Metal Carbide and Nitride Materials

Synthesis conditions and catalyst characterization via X-ray diffraction and CO uptake measurements are discussed. The activities and selectivities for FTS of the carbide and nitride materials are presented. Key performance differences between carbides and

nitrides are identified and are investigated in Chapter 4. The durability of these materials is assessed using time on stream deactivation studies as well as structural and surface characterization using techniques such as X-ray diffraction, X-ray photoelectron spectroscopy, and scanning electron microscopy.

Chapter 4: Fischer-Tropsch Synthesis Kinetics and Mechanisms

The effect of various process conditions (temperature, pressure, and H_2/CO ratio) on the rate and selectivity of Mo_2C for FTS is discussed. A simple power rate law for Mo_2C is developed. Elementary reaction steps and FTS mechanisms governing performance are discussed with specific focus on exploring differences between Mo_2C and Mo_2N and identifying routes for C-C coupling to produce higher hydrocarbons over the Mo_2C surface. Temperature programmed reaction and temperature programmed desorption experiments are employed. This investigation provides insight into strategies for modifying the catalysts to improve performance.

Chapter 5: Mechanistic Investigation of the Metal Adsorption Process over Mo_2C

Chapter 5 discusses the interactions between the metal precursors and the native Mo_2C surface during metal adsorption via wet impregnation. These interactions are explored using point of zero charge measurements for Mo_2C, metal concentration measurements as a function of loading time, X-ray diffraction, X-ray photoelectron spectroscopy, as well as X-ray absorption spectroscopy. The dominant mechanisms controlling the metal adsorption process are discussed and insight is provided to guide future catalyst preparation.

Chapter 6: Fischer-Tropsch Synthesis Performance of Mo_2C-Supported Metal Catalysts

The activities and selectivities of a series of Mo_2C-supported metal (Pt, Co, Cu, Fe, Ni, Ru, Rh) catalysts are presented. The catalysts are characterized using X-ray diffraction, CO chemisorptions, and H_2 temperature programmed reduction. Based on the results, catalyst leads for future investigation are identified.

Chapter 7: Summary, Conclusions, and Future Work

Chapter 7 provides an overview of the key results and conclusions from this research. Based on these conclusions, methods for improving the Fischer-Tropsch Synthesis performance of these catalysts are provided. Additionally, future research directions are suggested.

1.7. References

[1] D. Kennedy, *Science Magazine's State of the Planet 2006-2007*, Island Press, 2006.

[2] B. Lomborg, *The Skeptical Environmentalist: Measuring the Real State of the World*, Cambridge University Press, 2001.

[3] O. Jolliet, M. Margni, R. Charles, S. Humbert, J. Payet, G. Rebitzer, R. Rosenbaum, Impact 2002+: A New Life Cycle Impact Assessment Methodology, *International Journal of Life Cycle Assessment* 8 (2003) 324-330.

[4] E. G. Hertwich, Life Cycle Approaches to Sustainable Consumption: A Critical Review, *Environmental Science and Technology* 39 (2005) 4673-4684.

[5] P. R. Ehrlich, J. P. Holdren, Impact of Population Growth, *Science* 171 (1971) 1212-1217.

[6] M. R. Chertow, The IPAT Equation and Its Variants, *Journal of Industrial Ecology* 4 (2001) 13-29.

[7] Annual Energy Review 2009, U.S. Energy Information Administration (2010).

[8] S. C. Davis, S. W. Diegel, Transportation Energy Data Book: Edition 25, Oakridge National Laboratory, U.S. Department of Energy (2006).

[9] Weekly United States Spot Price FOB Weighted by Estimated Import Volume, U.S. Energy Information Administration. http://tonto.eia.gov/dnav/pet/hist/LeafHandler.ashx?n=PET&s=WTOTUSA&f=W Accessed March 2011.

[10] Renewable Fuel Standard, U.S. Environmental Protection Agency. http://www.epa.gov/otaq/fuels/renewablefuels/index.htm. Accessed March 2011.

[11] What is a Biorefinery?, Biomass Research, National Renewable Energy Laboratory, Department of Energy. http://www.nrel.gov/biomass/biorefinery.html. Accessed March 2011.

[12] G. W. Huber, S. Iborra, A. Corma, Synthesis of Transportation Fuels from Biomass: Chemistry, Catalysts, and Engineering, *Chemistry Reviews* 106 (2006) 4044-4098.

[13] G. W. Huber, Breaking the Chemical and Engineering Barriers to Lignocellulosic Biofuels: Next Generation Hydrocarbon Biorefineries, National Science Foundation. Chemical, Bioengineering, Environmental, and Transport Systems Division. Washington D.C. (2008).

[14] Using Fermentation and Catalysis to Make Fuels and Products: Biochemical Conversion, Biomass Program, Energy Efficiency and Renewable Energy, U.S. Department of Energy (2010).

[15] Biofuel Production, IEA Energy Technology Essentials, International Energy Agency (2007).

[16] R. Sims, M. Taylor, From 1st-to 2nd-Generation Biofuel Technologies: An Overview of Current Industry and RD&D Activities, International Energy Agency (2008).

[17] Biodiesel Production, Alternative Fuels & Advanced Vehicles Data Center, Energy Efficiency and Renewable Energy, U.S. Department of Energy (2010).

[18] M. J. A. Tijmensen, A. P. C. Faaij, C. N. Hamelinck, M. R. M. van Hardeveld, Exploration of the Possibilities for Production of Fischer Tropsch Liquids and Power via Biomass Gasification, *Biomass and Bioenergy* 23 (2002) 129-152.

[19] E. van Steen, M. Claeys, Review: Fischer-Tropsch Catalysts for the Biomass-to-Liquid Process, *Chemical Engineering and Technology* 31 (2008) 655-666.

[20] C. N. Satterfield, *Herogeneous Catalysis in Industrial Practice*, 2nd ed., McGraw-Hill, Inc., 1991.

[21] M. E. Dry, J. C. Hoogendoorn, Technology of the Fischer-Tropsch Process, *Catalysis Reviews: Science and Engineering* 23 (1981) 265-278.

[22] M. E. Dry, The Fischer-Tropsch Process-Commercial Aspects, *Catalysis Today* 6 (1990) 183-206.

[23] B. Jager, R. Espinoza, Advances in Low Temperature Fischer-Tropsch Synthesis, *Catalysis Today* 23 (1995) 17-28.

[24] F. M. Gottschalk, G. J. Hutchings, Cobalt Manganese Oxide: A Novel High Activity Water Gas Shift Catalyst *Journal of Chemical Society: Chemical Communications* (1988) 123-124.

[25] J. J. Patt, Carbide and Nitride Catalysts for the Water Gas Shift Reaction, Ph. D. Thesis, University of Michigan, 2003.

[26] T. E. King, Carbide and Nitride Supported Water-Gas Shift Catalysts, Ph. D. Thesis, University of Michigan, 2007.

[27] N. M Schweitzer, Evaluating the Effect of a Strong Metal-Support Interaction on the Activity of Molybdenum Carbide Supported Platinum Water-Gas Shift Catalysts, Ph. D. Thesis, University of Michigan, 2010.

[28] N. M. Schweitzer, J. A. Schaidle, O. K. Ezekoye, X. Pan, S. Linic, L. T. Thompson, High Activity Carbide Supported Catalysts for Water Gas Shift, *Journal of the American Chemical Society* 133 (2011) 2378-2381.

[29] G. P. Van Der Laan, A. A. C. M. Beenackers, Kinetics and Selectivity of the Fischer-Tropsch Synthesis: A Literature Review, *Catalysis Reviews: Science and Engineering* 41 (1999) 255-318.

[30] F. Fischer and H. Tropsch, *Brennst. Chem.* 4 (1923) 276-285.

[31] S. T. Sie, M. M. G. Senden, H. M. H. Van Wechem, *Catalysis Today* 8 (1991) 371-394.

[32] Unlocking the Potential Wealth of Coal: Introducing Sasol's Unique Coal-to-Liquids Technology, Sasol.

http://www.sasol.com/sasol_internet/downloads/CTL_Brochure_1125921891488.pdf. Accessed March 2011.

[33] Reaching New Energy Frontiers Through Competitive GTL Technology, Sasol. http://www.sasol.com/sasol_internet/downloads/GTL_brochure12_6_1150180264478.pdf. Accessed March 2011.

[34] A. Y. Khodakov, W. Chu, P. Fongarland, Advances in the Development of Novel Cobalt Fischer-Tropsch Catalysts for Synthesis of Long-Chain Hydrocarbons and Clean Fuels, *Chemical Reviews* 107 (2007) 1692-1744.

[35] G. P. Van Der Laan, Kinetics, Selectivity and Scale Up of the Fischer-Tropsch Synthesis, Ph. D. Thesis, University of Groningen, 1999.

[36] H. Schulz, Short History and Present Trends of Fischer-Tropsch Synthesis, *Applied Catalysis A: General* 186 (1999) 3-12.

[37] R. B. Anderson, *Catalysts for the Fischer-Tropsch Synthesis*, Van Nostrand Reinhold, New York, 1956. Vol. 4.

[38] M. A. Vannice, Catalytic Synthesis of Hydrocarbons from Hydrogen-Carbon Monoxide Mixtures over the Group VIII metals. I. Specific Activities and Product Distributions of Supported Metals, *Journal of Catalysis* 37 (1975) 449-461.

[39] M. A. Vannice, Catalytic Synthesis of Hydrocarbons from Hydrogen-Carbon Monoxide Mixtures over the Group VIII metals. II. Kinetics of the Methanation Reaction over Supported Metals, *Journal of Catalysis* 37 (1975) 462-473.

[40] M. A. Vannice, Catalytic Synthesis of Hydrocarbons from Hydrogen-Carbon Monoxide Mixtures over the Group VIII metals. III. Metal-Support Effects with Platinum and Palladium Catalysts, *Journal of Catalyis* 40 (1975) 129-134.

[41] D. F. Ollis, M. A. Vannice, Catalytic Synthesis of Hydrocarbons from Hydrogen/Carbon Monoxide Mixtures over the Group VIII Metals, *Journal of Catalysis* 38 (1975) 514-515.

[42] S. T. Oyama, Preparation and Catalytic Properties of Transition Metal Carbides and Nitrides, *Catalysis Today* 15 (1992) 179-200.

[43] G. Hagg, Regularity in Crystal Structures in Hydrides, Borides, Carbides and Nitrides of Transition Elements, *Z. Phys. Chem.* 12 (1931) 33-56.

[44] C. A. Bennett, Influence of Nanostructure and Composition on the Catalytic Properties of Mono and Bimetallic Nitrides, Ph. D. Thesis, University of Michigan, 2002.

[45] R. B. Levy, M. Boudart, Platinum-Like Behavior of Tungsten Carbide in Surface Catalysis, *Science* 181 (1973) 547-549.

[46] I. Kojima, E. Miyazaki, I. Yasumori, Synthesis of Hydrocarbons from CO and H_2 over Metal Carbide Catalysts, *Journal of Chemical Society-Chemical Communications* (1980) 573-574.

[47] I. Kojima, E. Miyazaki, Catalysis by Transition Metal Carbides. V. Kinetic Measurements of Hydrogenation of CO over TaC, TiC, and Mo_2C Catalysts, *Journal of Catalysis* 89 (1984) 168-171.

[48] I. Kojima, E. Miyazaki, Y. Inoue, I. Yasumori, Catalysis by Transition Metal Carbides. VI. Hydrogenation of Carbon Monoxide over WC, W_2C, and W Powder Catalysts, *Bulletin of the Chemical Society of Japan*, 58 (1985) 611-617.

[49] G. S. Ranhotra, A. T. Bell, J. A. Reimer, Catalysis over Molybdenum Carbides and Nitrides. II. Studies of CO Hydrogenation and C_2H_6 Hydrogenolysis, *Journal of Catalysis* 108 (1987) 40-49.

[50] H.-G. Kim, K. H. Lee, J. S. Lee, Carbon Monoxide Hydrogenation over Molybdenum Carbide Catalysts, *Research on Chemical Intermediates* 26 (2000) 427-443.

[51] P. M. Patterson, T. K. Das, B. H. Davis, Carbon Monoxide Hydrogenation over Molybdenum and Tungsten Carbides, *Applied Catalysis A: General* 251 (2003) 449-455.

[52] H. C. Woo, K. Y. Park, Y. G. Kim, I.-S. Nam, J. S. Chung, J. S. Lee, Mixed Alcohol Synthesis from Carbon Monoxide and Dihydrogen over Potassium-Promoted Molybdenum Carbide Catalysts, *Applied Catalysis* 75 (1991) 267-280.

[53] M. Xiang, D. Li, W. Li, B. Zhong, Y. Sun, Performances of Mixed Alcohols Synthesis over Potassium Promoted Molybdenum Carbides, *Fuel* 85 (2006) 2662-2665.

[54] B. Dhandapani, T. St. Clair, S. T. Oyama, Simultaneous Hydrodesulfurization, Hydrodeoxygenation, and Hydrogenation with Molybdenum Carbide, Applied *Catalysis A: General* 168 (1998) 219-228.

[55] P. K. Cheekatamarla, W. J. Thomson, Poisoning Effect of Thiophene on the Catalytic Activity of Molybdenum Carbide during Tri-Methyl Pentane Reforming for Hydrogen Generation, *Applied Catalysis A: General* 287 (2005) 176-182.

[56] P. Da Costa, J.-L. Lemberton, C. Potvin, J.-M. Manoli, G. Perot, M. Breysse, G. Djega-Mariadassou, Tetralin Hydrogenation Catalyzed by Mo_2C/Al_2O_3 and WC/Al_2O_3 in the Presence of H_2S, *Catalysis Today* 65 (2001) 195-200.

[57] S. T. Oyama, C. C. Yu, S. Ramanathan, Transition Metal Bimetallic Oxycarbides: Synthesis, Characterization, and Activity Studies, *Journal of Catalysis* 184 (1999) 535-549.

[58] J. B. Claridge, A. P. E. York, A. J. Brungs, C. Marquez-Alvarez, J. Sloan, S. C. Tsang, M. L. H. Green, New Catalysts for the Conversion of Methane to Synthesis Gas: Molybdenum and Tungsten Carbide, *Journal of Catalysis* 180 (1998) 85-100.

[59] J. Sehested, C. J. H. Jacobsen, S. Rokni, J. R. Rostrup-Nielsen, Activity and Stability of Molybdenum Carbide as a Catalyst for CO_2 Reforming, *Journal of Catalysis* 201 (2001) 206-212.

[60] J. B. Claridge, A. P. E. York, A. J. Brungs, M. L. H. Green, Study of the Temperature-Programmed Reaction Synthesis of Early Transition Metal Carbide and Nitride Catalyst Materials from Oxide Precursors, *Chemistry of Materials* 12 (2000) 132-142.

[61] M. J. Ledoux, C. P. Huu, J. Guille, H. Dunlop, Compared Activities of Platinum and High Specific Surface Area Mo_2C and WC Catalysts for Reforming Reactions. I. Catalyst Activation and Stabilization: Reaction of n-Hexane, *Journal of Catalysis* 134 (1992) 383-398.

[62] J. Volter, H. Berndt, G. Lietz, H. Preiss, R. Tamme, Rhodium on Tungsten Carbide. A New Catalyst for Methane Reforming with Carbon Dioxide, *Chemie-Ingenieur-Technik* 69 (1997) 83-87.

[63] A. Griboval-Constant, J.-M. Giraudon, G. Leclercq, L. Leclercq, Catalytic Behaviour of Cobalt and Ruthenium Supported Molybdenum Carbide Catalysts for FT Reaction, *Applied Catalysis A: General* 260 (2004) 35-45.

[64] A. Griboval-Constant, J.-M. Giraudon, I. Twagishema, G. Leclercq, M. E. Rivas, J. Alvarez, M. J. Perez-Zurita, M. R. Goldwasser, Characterization of New Co and Ru on α-WC Catalysts for Fischer-Tropsch Reaction: Influence of the Carbide Surface State, *Journal of Molecular Catalysis A: Chemical* 259 (2006) 187-196.

[65] M. Lewandowski, A. Szymanska-Kolasa, P. Da Costa, C. Sayag, Catalytic Performances of Platinum Doped Molybdenum Carbide for Simultaneous Hydrodenitrogenation and Hydrodesulfuization, *Catalysis Today* 119 (2007) 31-34.

[66] W. Setthapun, S. K. Bej, L. T. Thompson, Carbide and Nitride Supported Methanol Steam Reforming Catalysts: Parallel Synthesis and High Throughput Screening, *Topics in Catalysis* 49 (2008) 73-80.

[67] W. Sethapun, Carbide and Nitride Supported Methanol Steam Reforming Catalysts, Ph. D. Thesis, University of Michigan, 2007.

[68] C. H. Bartholomew, R. J. Farrauto, *Fundamentals of Industrial Catalytic Processes*, 2nd ed. John Wiley and Sons, Inc. 2006.

CHAPTER 2

Effects of Sulfur on Mo_2C and Pt/Mo_2C Water Gas Shift Catalysts

2.1. Introduction

Sulfur is a contaminant in fossil fuels including crude oil and coal, and often remains in products derived from fossil fuels [1]. Sulfur can also be present in biomass-derived products. For example, Robinson et al. reported that depending on the type of biomass, the sulfur content varied from ~14 to 2200 ppm [2]. Sulfur severely and irreversibly deactivates most catalytic materials, and typically has to be removed upstream of the reactor. For some reactions, early transition metal carbides and nitrides have been reported to be sulfur tolerant, in particular at high temperatures and/or pressures [3, 4, 5]. For example, DaCosta et al. [4] reported that tetralin hydrogenation activities for Mo_2C/Al_2O_3 and WC/Al_2O_3 catalysts were not significantly impacted by the presence of 200 ppm H_2S at 300 °C and 4 MPa.

Previous research in our group has demonstrated that carbide-based catalysts, specifically Mo_2C and Pt/Mo_2C, are active for the water gas shift reaction (WGS) [6-8]. For example, a 4% Pt/Mo_2C catalyst has been reported to be more active than a commercial $Cu/Zn/Al_2O_3$ WGS catalyst as well as other Pt-based catalysts [7, 8]. Research described in this chapter investigated the tolerance of Mo_2C and Pt/Mo_2C catalysts to sulfur exposure during the WGS reaction (Equation 2.1).

$$CO + H_2O \leftrightarrow CO_2 + H_2 \qquad \Delta H° = -41.1 \text{ kJ/mol} \qquad (2.1)$$

This reaction is a critical step in the conversion of hydrocarbon and alcohol feedstocks into reformate or syngas [9] as well as the production of synthetic fuels via Fischer-Tropsch Synthesis. Due to the sensitivity of most WGS catalysts, sulfur concentrations in the feed typically have to be reduced to ppb levels [1]. The effects of H_2S exposure on the WGS activities of Mo_2C and Pt/Mo_2C catalysts were evaluated, and the materials were characterized to define any associated changes in catalyst structure and composition. Hydrogen sulfide was used as the sulfur species because it is often present in process streams [10]. Results presented in this chapter were determined at more moderate temperatures and pressures than those used in most prior investigations [3, 4, 5] and provide new insights into the effects of sulfur on the catalytic properties of Mo_2C-based catalysts.

2.2. Experimental Setup

2.2.1. Catalyst Preparation

The Mo_2C catalyst was synthesized using a temperature programmed reaction procedure [11]. Approximately 1.3 g of ammonia paramolybdate (AM, $(NH_4)_6Mo_7O_{24}•4H_2O$, 81-83% MoO_3, Alpha-Aesar) was loaded into a quartz tube reactor on top of a quartz wool plug, and placed in a vertical furnace. A diagram of the reactor system is shown in Figure 2.1. In order to maintain consistent catalyst properties, the AM was sieved to 125-250 μm prior to carburization. The AM was reduced in H_2 at 375 mL/min as the temperature was increased from room temperature (RT) to 350 °C (heating rate of 278 °C/h), and then held at this temperature for 12 h. The reactant gas was then switched from H_2 to a 15% CH_4/H_2 mixture and the temperature was increased from 350 °C to 590 °C at a rate of 160 °C/h. The final temperature was maintained for 2 h prior to

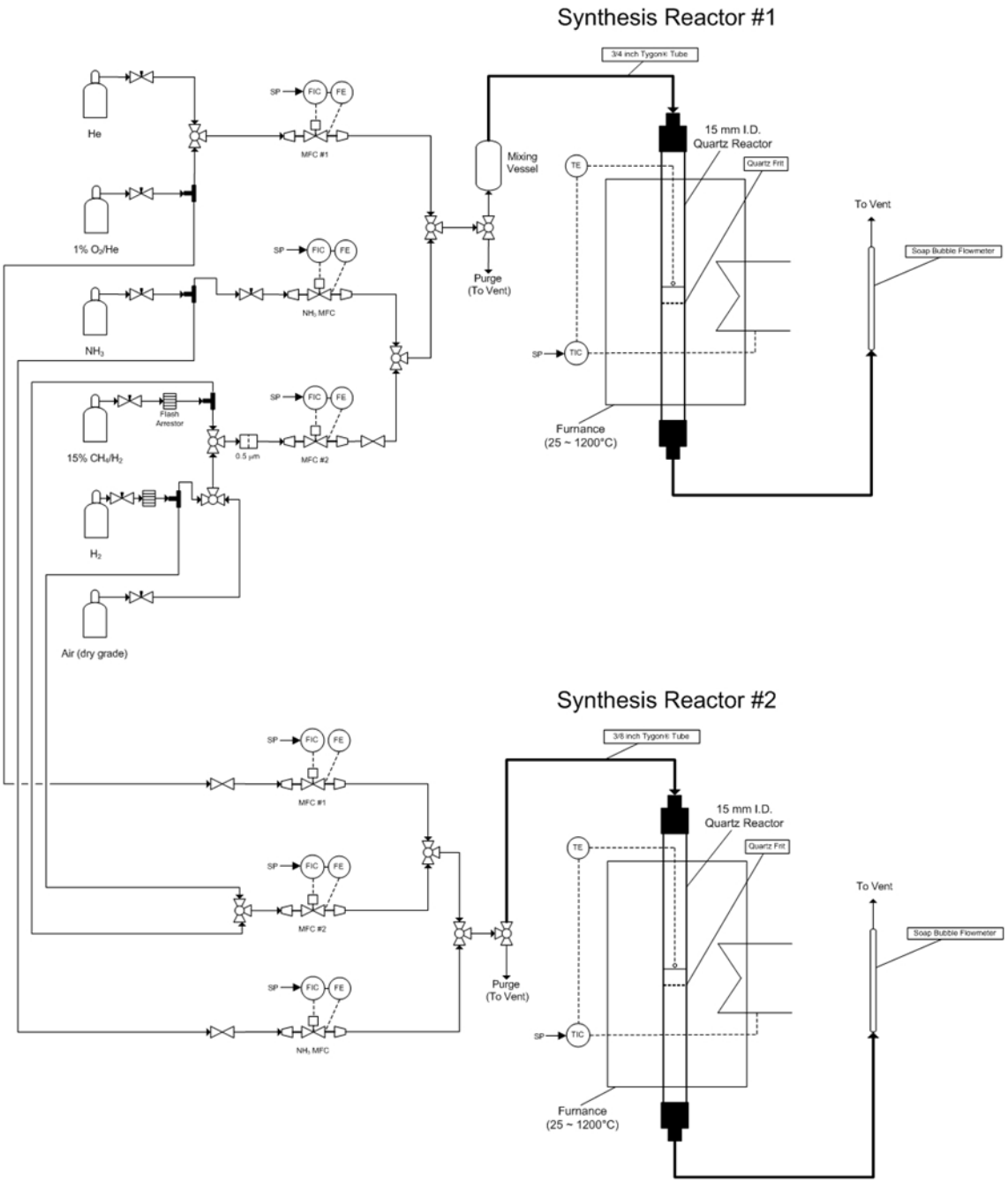

Figure 2.1: Schematic of the reactor system used in the synthesis of Mo_2C via the temperature-programmed reaction method. Taken from [6].

quenching the material to RT. Depending upon the gas hourly space velocity used during synthesis, this procedure has been shown to produce β-Mo_2C [12]. The resulting material was passivated using a 1% O_2/He mixture at 20 mL/min for at least 5 h.

The Mo_2C-supported Pt catalyst was prepared via wet impregnation of the unpassivated Mo_2C with a deaerated aqueous solution containing 1.3 mg/mL of dihydrogen hexachloriplatinate hexahydrate ($H_2PtCl_6 \cdot 6H_2O$, 99.95% metal basis, Alfa Aesar). After decanting the excess solution, the material was loaded into a quartz reactor and dried in H_2 at 375 mL/min for 3 h at RT. Subsequently, the temperature was increased to 110 °C in ~1 h and held there for 2 h. The temperature was then increased to 450 °C at a rate of 340 °C/h and held for 4 h. Finally, the material was quenched to room temperature and passivated in a 1% O_2/He mixture at 20 mL/min for at least 5 h.

In addition to the Mo_2C and Pt/Mo_2C catalysts, a commercial $Cu/Zn/Al_2O_3$ catalyst was also obtained from industry and used as a benchmark catalyst for comparison.

2.2.2. Catalyst Characterization

X-ray diffraction analysis was performed using a Rigaku Miniflex diffractometer with Cu Kα radiation and a Ni filter (λ = 1.540 Å). The range ($10° < 2\theta < 90°$) was scanned at a rate of 5°/min with a 0.02° step size. The BET surface areas were determined via N_2 physisorption using a Micromeritics ASAP 2010 analyzer. Prior to these measurements, the catalysts were degassed at 300 °C for 4 h. Pulse chemisorption experiments were performed using a Micromeritics AutoChem 2910 Chemisorption Analyzer equipped with a thermal conductivity detector and mass spectrometer. A schematic of the chemisorption analyzer is shown in Figure 2.2. Prior to analysis, the Mo_2C and Pt/Mo_2C catalysts were pretreated in 15% CH_4/H_2 for 4 h at 590 °C. The catalysts were then degassed in flowing He for 1 h. After cooling to RT, the catalysts were repeatedly dosed with 5 mL of 5% CO/He until saturation was achieved. The

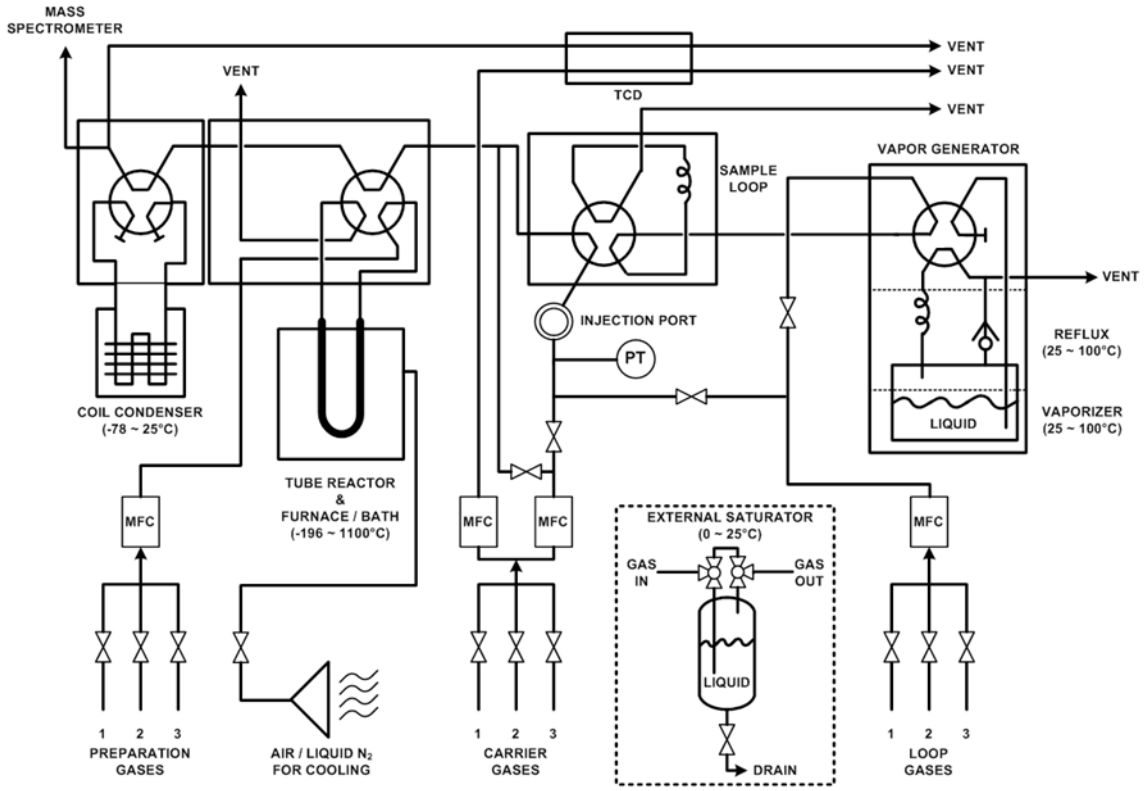

Figure 2.2: Schematic of the Micromeritics 2910 AutoChem Chemisorption analyzer. Taken from [6].

$Cu/Zn/Al_2O_3$ catalyst was reduced in flowing 4% H_2/N_2 at 200 °C based on the instructions from the supplier. The sample was then degassed in flowing He for 1 h and cooled to 60 °C. The gas flow was then switched to N_2O for 1.5h. The N_2O flow was then replaced with He and the sample was cooled to RT. N_2O titration was used to probe the number of exposed Cu atoms as N_2O decomposes on the Cu surface at 60°C resulting in the formation of Cu_2O (Cu:O stoichiometry of 2:1). The N_2O uptake was determined by performing a H_2 temperature programmed reduction and measuring the H_2 consumption (removal of O in the form of H_2O). This method was based on the one proposed by Bond and Namijo [13].

The catalyst compositions were determined by inductively coupled plasma optical emission spectroscopy (ICP-OES) using a Varian 720-ES analyzer. The materials were

dissolved in aqua regia (3 parts HCl to 1 part HNO_3) and the emission spectra of dissolved species were compared to those for a series of standard solutions of known concentrations. The surface morphologies of the fresh and spent catalysts were characterized using scanning electron microscopy (SEM) with a Phillips XL30 FEG SEM operating at an accelerating voltage of 15-25 kV and a nominal resolution of 2-5 nm. Prior to analysis, the materials were sputter coated with Pd-Au to mitigate charging effects. Sulfur adsorption/incorporation experiments were performed using the microbalance on a TA Instruments Q50 Thermogravimetric Analyzer. These experiments characterized interactions of the catalyst with H_2S at different concentrations. The flow rate to catalyst ratio and temperatures were similar to those used during the reaction rate measurements.

The fresh and spent catalysts were characterized using x-ray photoelectron spectroscopy (XPS) to determine the compositions and oxidation states of species on the surfaces. The XPS experiments were performed using a Kratos Axis Ultra x-ray photoelectron spectrometer with an Al anode (K_α radiation at 1486.6 eV) operating at 10 mA and 14 kV. The spectrometer was equipped with an *in situ* XPS reaction chamber. However, due to the difficulty of removal, sulfur was not used in the XPS reaction chamber. The spectra were deconvoluted using a nonlinear least squares method employing a combination of Gaussian (80%) and Lorentzian (20%) distributions and CasaXPS, a commercially available XPS analysis program. The goodness-of-fit of the peak envelope to the spectral data was evaluated by the residual standard deviation (STD). The peak parameters were set to minimize the residual STD. Parameter constraints were imposed during deconvolution of the Mo, Pt, and S spectra. The Mo 3d

spectra were fit using doublets with a splitting of 3.2 eV between the $3d_{5/2}$ and $3d_{3/2}$ peaks and an intensity ratio of 3:2. The Pt 4f spectra were fit using doublets with a splitting of 3.3 eV between the $4f_{7/2}$ and $4f_{5/2}$ peaks and an intensity ratio of 4:3. The S 2p spectra were fit using doublets with a splitting of 1.2 eV between the $2p_{3/2}$ and $2p_{1/2}$ peaks and an intensity ratio of 2:1. For all spectra, the peak widths (FWHM) for the doublets were constrained to be similar. Shirley backgrounds were used for the Mo 3d, Pt 4f, and S 2p spectra, while a linear background was used for the C 1s and O 1s spectra. The peak areas were normalized using the appropriate atomic sensitivity factors. This allowed comparison of the relative atomic fractions of each species on the catalyst surfaces.

2.2.3. Water Gas Shift Rate Measurements

The WGS rates were measured using a 4 mm I.D. quartz U-tube in which 20-30 mg of catalyst was supported on a quartz wool plug. A diagram of the WGS reactor system is shown in Figure 2.3. As necessary, the catalysts were diluted with inert, low surface area (<1 m^2/g) silica (particle size 125-250μm) to prevent channeling, avoid problems with axial dispersion, and minimize temperature gradients in the bed. Prior to the reaction rate measurements, the catalysts were pretreated at 590 °C for 4 h in a mixture of 15% CH_4/H_2 [6]. The effluent gas was passed through an ice-bathed condenser to remove most of the H_2O, and the composition was analyzed using a SRI 8610C gas chromatograph (GC) equipped with a Supelco Carboxen-1000 column and thermal conductivity detector. The GC sampled the effluent gas every 30 min. To ensure that there was no residual sulfur, the reactor system (reactor and lines) was heated to 500 °C in flowing H_2 for 12 h in between runs. This treatment was sufficient to reproduce the sulfur-free WGS rate for a commercial $Cu/Zn/Al_2O_3$ benchmark catalyst.

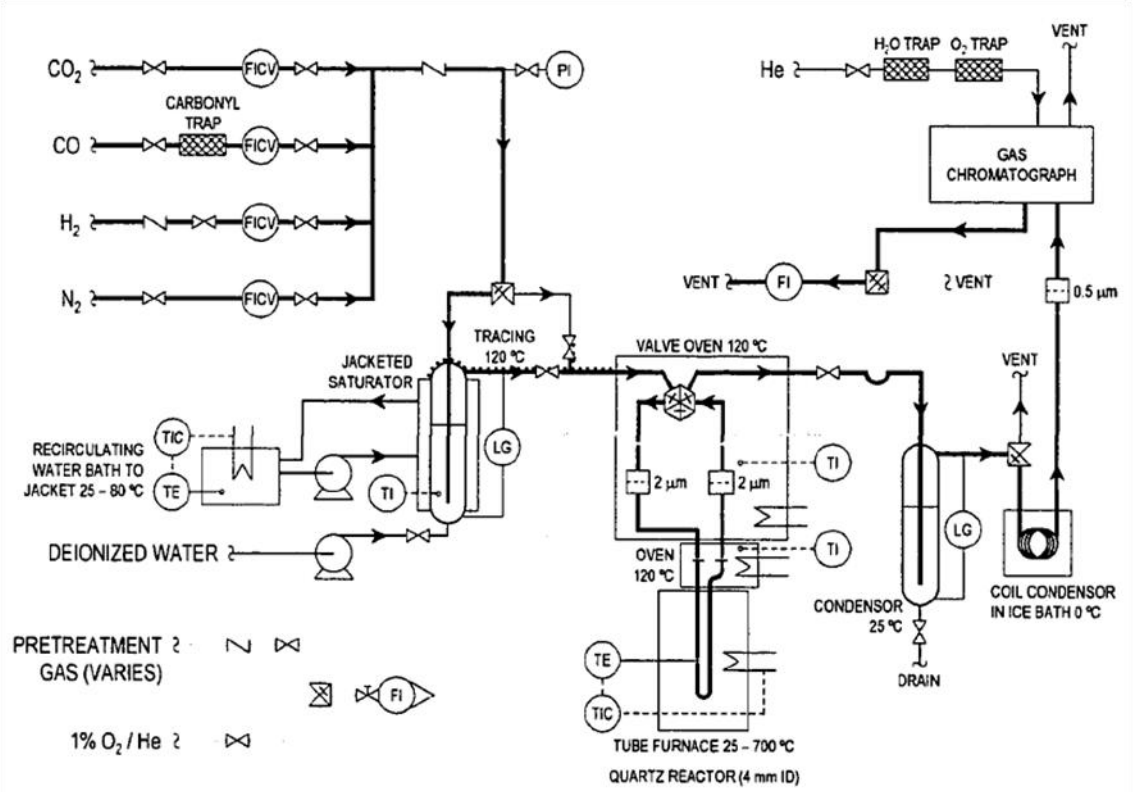

Figure 2.3: Schematic of the water gas shift reactor system. Taken from [11].

The rates were measured under differential conditions (conversion ≤ 10%) at atmospheric pressure over a temperature range of 200-240°C. Operating under differential conditions ensures that the reaction is in the reaction-limited regime (not limited by mass transfer), thus measurements of the intrinsic rates of the material can be performed. The equilibrium WGS conversion under conditions used in the experiments would be greater than 90%. The dry reactant simulated the effluent stream from a partial oxidation reformer and consisted of 13% CO, 56% H_2, 8% CO_2, and balance N_2. The dry reactant was passed through a H_2O saturator maintained at 69.4 ± 0.4 °C resulting in a wet reactant containing 30% H_2O. The flow rate of the reactant was 262 mL/min corresponding to a gas hourly space velocity of 125,000 h^{-1}. Hydrogen production (CO consumption) rates and conversions were determined by monitoring the concentration of

CO in the product stream. Features attributable to H_2 were present in the chromatograms but could not be quantified because He was used as the carrier gas. No products other than CO_2 and H_2 were observed in the effluent.

For measurements including sulfur, the catalysts were initially allowed to achieve pseudo steady-state rates at 240 °C in the sulfur-free reactant stream. Subsequently, H_2S was added to the reactant stream to produce concentrations ranging up to 50 ppmv. In order to maintain the same gas hourly space velocity, the N_2 balance gas flow rate was adjusted to account for the addition of H_2S. The regenerability of the catalysts was investigated by treating the spent materials in 15% CH_4/H_2 for 4 h at 590 °C. After this treatment, the catalysts were again exposed to the sulfur-free feed at 240 °C to determine the recovered rate.

2.3. Results

2.3.1. Pre-Reaction Characterization

Diffraction patterns for the Mo_2C and Pt/Mo_2C catalysts (Figure 2.4) contained peaks for β-Mo_2C [14] and α-MoC_{1-x} [15]. The relative peak areas suggested similar amounts of each. These phases have Mo:C ratios near two, therefore, we will refer to this material as Mo_2C. No peaks were observed for MoO_2 [16] or MoO_3 [17], indicating that synthesis achieved complete bulk carburization. There were no clearly discernable Pt peaks for the Pt/Mo_2C catalyst [18], indicating that crystallites, if present, were below the detection limit of the x-ray diffractometer (particle diameter of <5nm). Results from catalyst characterization are given in Table 2.1. The reduced surface area for the Pt/Mo_2C catalyst compared to the Mo_2C catalyst may be due to pore blocking by Pt nanoparticles. Interestingly, the addition of Pt decreased the CO uptake as compared to Mo_2C.

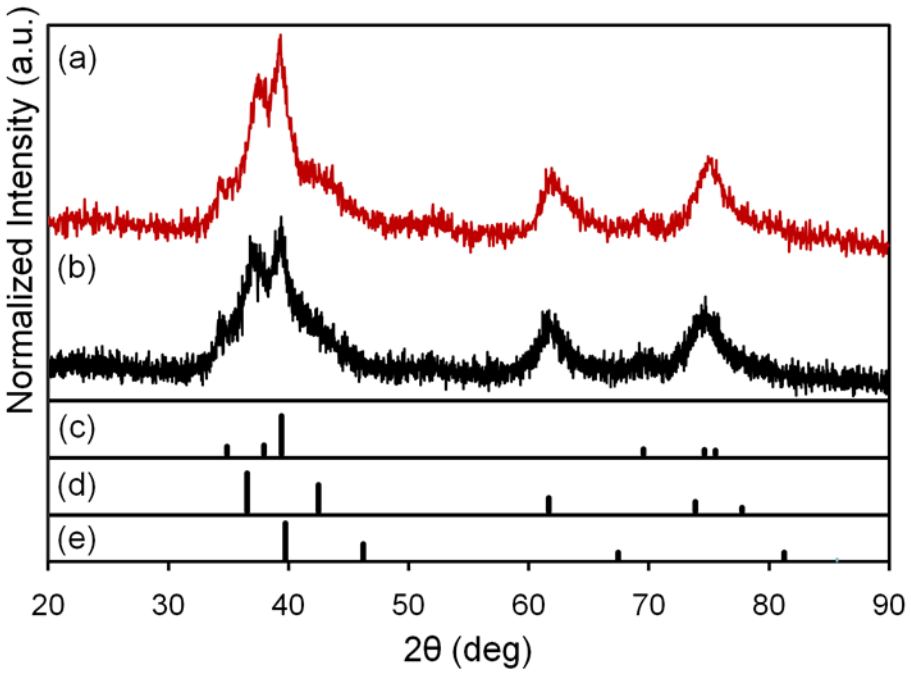

Figure 2.4: X-ray diffraction patterns for the (a) Pt/Mo_2C and (b) Mo_2C catalysts, and peak positions for polycrystalline (c) β-Mo_2C [14], (d) α-MoC_{1-x} [15], and (e) Pt [18] reference materials.

Table 2.1: BET surface areas, N_2O uptakes, CO uptakes, site densities, Pt loadings, and TOFs for Mo_2C, Pt/Mo_2C, $Cu/Zn/Al_2O_3$, and Pt/oxide catalysts.

Catalyst	BET Surface Area (m^2/g)	N_2O Uptake (μmol/g)	CO Uptake (μmol/g)	Site Density[1] (sites/m^2 x 10^{18})	Pt Loading (wt%)	TOF (s^{-1})
Mo_2C	98	--	268	1.65	--	0.08[3]
Pt/Mo_2C	70	--	151	1.30	3.7[2]	0.80[3]
$Cu/Zn/Al_2O_3$	60	192	--	1.93	--	0.32[3]
Pt/Al_2O_3 [19]	180	--	91	0.31	3	0.03[4]
Pt/ZrO_2 [19]	75	--	56	0.45	3	0.20[4]
Pt/TiO_2 [19]	74	--	9	0.07	3	0.82[4]

[1] Determined from uptake and BET surface area.
[2] Determined using ICP-OES. Corresponds to a surface coverage of 12% assuming 10 Pt atoms/nm^2.
[3] Based on rates measured at 240 °C. Extrapolated TOFs for the Mo_2C, Pt/Mo_2C, and $Cu/Zn/Al_2O_3$ catalysts at 250 °C are 0.11 s^{-1}, 1.02 s^{-1}, and 0.44 s^{-1}, respectively.
[4] Based on rates measured at 250 °C.

The *in situ* XPS results tracked effects of the various treatments on the surface chemistries without exposure to air. Following treatment, the samples were purged with

N_2 then cooled to room temperature in the *in situ* XPS reaction chamber. The pressure was reduced to < 10^{-8} torr and the material was transferred into the analysis chamber. Results from deconvolution of spectra for the as-synthesized and pretreated (15% CH_4/H_2 at 590 °C for 4 h) catalysts are summarized in Table 2.2. Peaks that accounted for less than 10% of the total spectral area typically did not contribute significantly to the goodness-of-fit. Surfaces of the catalysts contained varying concentrations of species attributable to Mo_2C, Mo and Pt oxides, and carbon oxides; no chlorine residue (from the Pt precursor) was observed for the Pt/Mo_2C catalyst. The C 1s spectra for the Mo_2C and Pt/Mo_2C catalysts are shown in Figure 2.5. Peaks centered at 284.8 eV corresponded to adventitious carbon and were used to reference the other binding energies. In addition to adventious carbon, surfaces of the Mo_2C and Pt/Mo_2C catalysts contained carbidic carbon and adsorbed carbon oxides. Peaks at 283.5 ± 0.1 eV were assigned to carbidic carbon in Mo_2C [19]. The peaks at 286.6 ± 0.6 eV and 288.4 ± 0.4 eV were assigned to species containing C-O and C=O bonds, respectively [21, 22]. These could be associated with carbonates and/or formates on the catalyst surface.

The Mo 3d spectra for the Mo_2C and Pt/Mo_2C catalysts contained four doublets (see Figure 2.5). Doublets with Mo $3d_{5/2}$ peaks at 232.3 ± 0.2 eV are characteristic of Mo^{6+} and suggested the presence of MoO_3 [3, 21, 23, 24]. The peaks at 229.7 ± 0.2 eV were likely due to Mo^{4+} in MoO_2 [21, 24, 25]. The peaks at 228.5 ± 0.1 eV were assigned to Mo in the Mo_2C based on comparisons with spectra reported in the literature (values in literature range from 228.1 eV to 228.8 eV) [3, 20, 26, 27]. For most of the materials, the ratio of the normalized area for the C 1s peak at 283.5 ± 0.1 eV to the area for the Mo $3d_{5/2}$ peak at 228.5 ± 0.1 eV was consistent with the presence of Mo_2C (see

Table 2.2: Binding energies for species on surfaces of the as-synthesized and pretreated Mo_2C and Pt/Mo_2C catalysts.

Catalyst	Treatment	C 1s (eV)[1,2]			Mo $3d_{5/2}$ (eV)[1]				Pt $4f_{7/2}$ (eV)[1]		O 1s (eV)[1]		
		Mo_2C	C-O	C=O	Mo^{2+}	$Mo^{\delta+}$	Mo^{4+}	Mo^{6+}	Pt^0	Pt^{2+}	MoO_x	PtO	O^-,OH^- H_2O,O=C
Mo_2C		283.5 (22)	286.1 (26)	288.8 (13)	228.5 (15)	229.0 (16)	229.6 (19)	232.4 (50)	--	--	530.8 (64)	--	532.2 (36)
Mo_2C	CH_4/H_2[3]	283.6 (48)	287.3 (2)	--	228.5 (55)	228.8 (23)	229.6 (19)	--	--	--	530.6 (81)	--	532.2 (19)
Pt/Mo_2C		283.5 (6)	286.6 (16)	288.2 (18)	228.5 (23)	228.8 (27)	229.8 (25)	232.3 (25)	71.6 (78)	72.7 (22)	530.6 (37)	531.5 (21)	532.6 (42)
Pt/Mo_2C	CH_4/H_2[3]	283.6 (23)	286.1 (22)	--	228.5 (51)	228.8 (31)	229.9 (14)	--	71.8 (85)	73.3 (15)	530.7 (37)	531.8 (8)	532.4 (55)

[1] The number in parentheses represents the atomic percentage.
[2] Balance of atomic percentages for C 1s is adventitious carbon.
[3] Pretreated in 15% CH_4/H_2 at 590 °C for 4 h, purged with N_2 then cooled to room temperature.

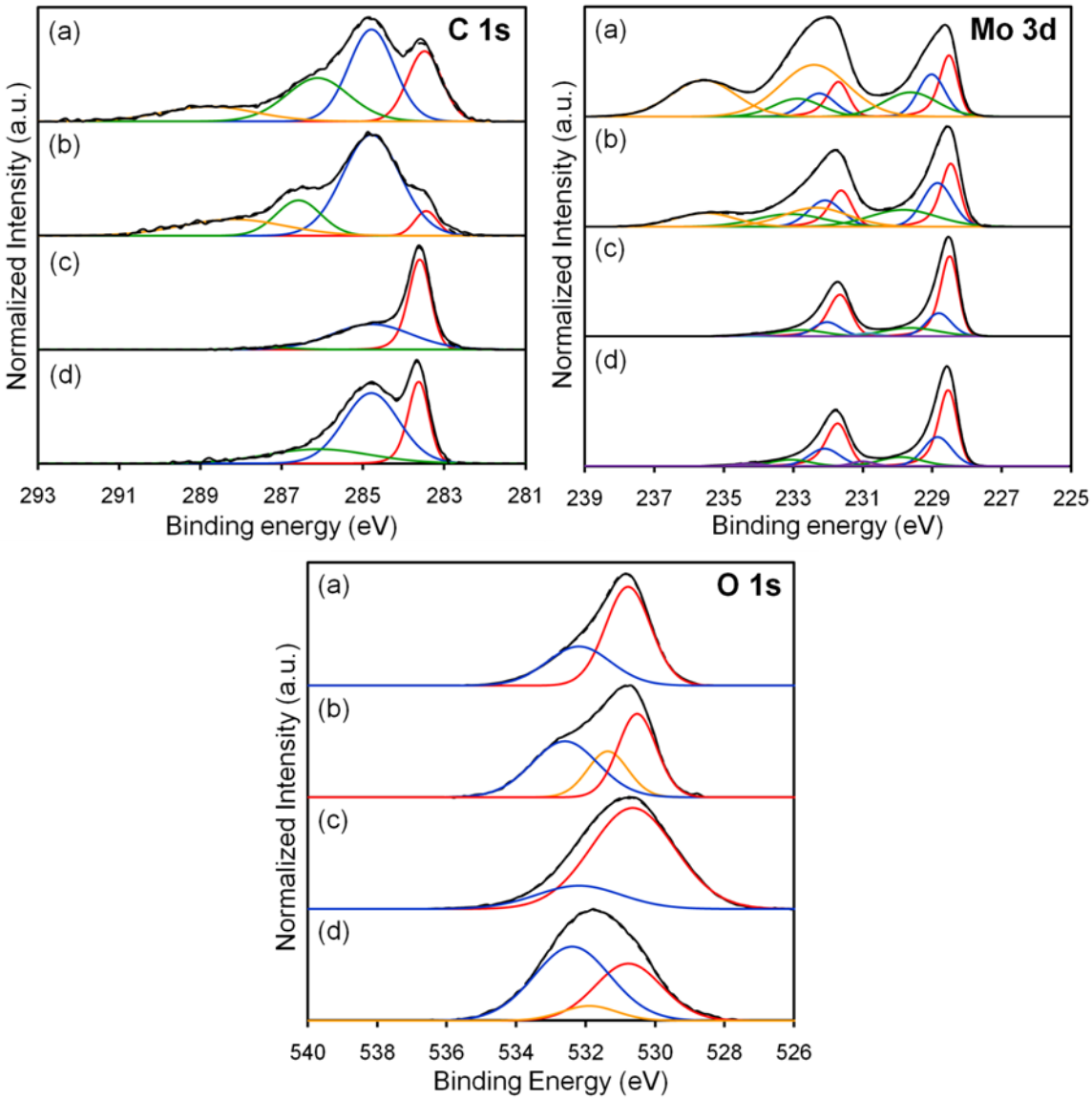

Figure 2.5: Carbon 1s, Molybdenum 3d, and Oxygen 1s XPS spectra for the (a) as-synthesized Mo_2C catalyst, (b) as-synthesized Pt/Mo_2C catalyst, (c) pretreated Mo_2C catalyst, and (d) pretreated Pt/Mo_2C catalyst. The catalysts were pretreated at 590 °C for 4 h in a mixture of 15% CH_4/H_2.

Table 2.3). The Mo $3d_{5/2}$ peak at 228.9 ± 0.1 eV was designated as $Mo^{\delta+}$ ($2<\delta<4$), perhaps in an oxycarbide [24, 28].

The O 1s spectra for the Mo_2C and Pt/Mo_2C catalysts are also shown in Figure 2.5. Two different species were present on the Mo_2C surfaces. Peaks at 530.7 ± 0.2 eV are typically assigned to oxygen in Mo oxides [20, 21, 23, 24]. Peaks at 532.4 ± 0.2 eV

are indicative of strongly bound O^-, OH^-, H_2O and/or O=C [22, 24]. Spectra for the Pt/Mo_2C catalyst contained additional peaks at 531.7 ± 0.2 eV corresponding to Pt oxide [29, 30].

Two doublets were observed in the Pt 4f XPS spectra (Figure 2.6). The dominant doublet with Pt $4f_{7/2}$ peaks at 71.7 ± 0.1 eV was assigned to Pt^0 [30, 31]. The minor component with Pt $4f_{7/2}$ peaks at 73.0 ± 0.3 eV was assigned to Pt^{2+}, most likely in the form of PtO [31].

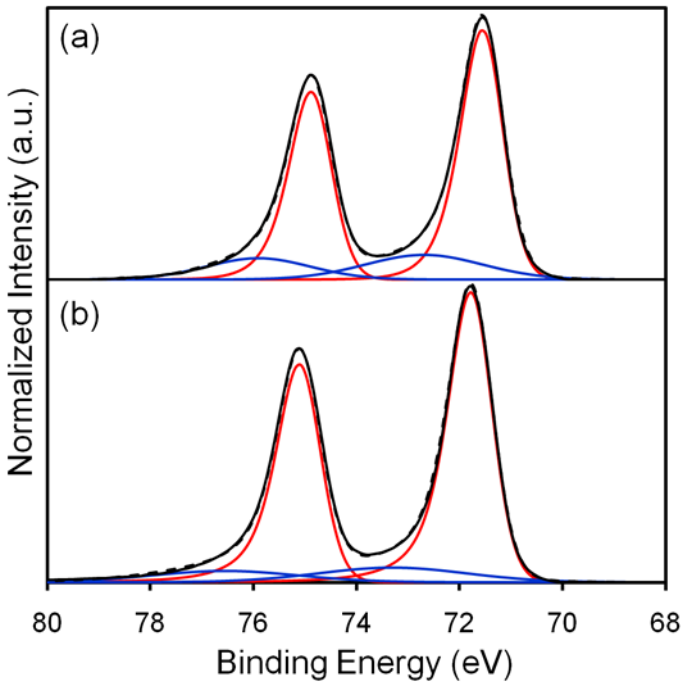

Figure 2.6: Platinum 4f XPS spectra for the (a) as-synthesized and (b) pretreated Pt/Mo_2C catalyst. The catalyst was pretreated at 590 °C for 4 h in a mixture of 15% CH_4/H_2.

Pretreatment of the as-synthesized catalysts in 15% CH_4/H_2 at 590 °C for 4 h caused a significant change in the surface chemistry. The percentage of Mo in the form of Mo_2C increased from 15-20% in the as-synthesized catalysts to more than 50% in the pretreated catalysts. Pretreatment completely reduced the Mo^{6+} concentration and caused the formation of a small amount of a species with Mo $3d_{5/2}$ peaks at 231.0 ± 0.1 eV (see

Figure 2.5). Peaks with similar binding energies have been assigned to Mo^{5+} [23, 24, 25]. Pretreatment also increased the relative amount of carbidic carbon at the surface and decreased the amount of oxygen and carbon oxides (Figure 2.5). Approximately 70% of Mo on the as-synthesized Mo_2C surface was in the form of MoO_3 and MoO_2, which is in good agreement with an O/Mo ratio of 2.6 (Table 2.3). The O/Mo ratio for the as-synthesized Pt/Mo_2C catalyst was 1.9. Pretreatment at 590 °C in 15% CH_4/H_2 resulted in a substantial reduction in the O/Mo ratio to 1.5 for Mo_2C and 1.2 for Pt/Mo_2C. While pretreatment reduces the overall O/Mo ratio for both catalysts, the presence of Pt on Pt/Mo_2C seems to facilitate the reduction of Mo oxides to a greater extent than Mo_2C alone. There was only a slight reduction in the percentage of Pt^{2+} after pretreatment with 15% CH_4/H_2 at 590 °C.

Table 2.3: Selected atomic ratios for species on surfaces of the as-synthesized and pretreated Mo_2C and Pt/Mo_2C catalysts.

Catalyst	Treatment	C^{1}/Mo^{2} Ratio	O/Mo Ratio	O^{3}/Pt^{4} Ratio
Mo_2C		1.9	2.6	--
Mo_2C	CH_4/H_2[5]	0.7	1.5	--
Pt/Mo_2C		0.5	1.9	0.8
Pt/Mo_2C	CH_4/H_2[5]	0.5	1.2	0.4

[1] Carbidic carbon.
[2] Mo in the form of Mo^{2+}.
[3] O 1s peak corresponding to PtO (531.7 ± 0.2 eV).
[4] Pt doublet corresponding to PtO (73.0 ± 0.3 eV).
[5] Pretreated in 15% CH_4/H_2 at 590 °C for 4 h, purged with N_2 then cooled to room temperature.

2.3.2. Reaction Rates

The WGS rates for the Pt/Mo_2C catalyst were almost an order of magnitude higher than those for the Mo_2C catalyst and 2-3 times higher than those for the $Cu/Zn/Al_2O_3$ catalyst in the absence of H_2S (Figure 2.7). The apparent activation energies for the Mo_2C, Pt/Mo_2C, and $Cu/Zn/Al_2O_3$ catalysts were 59, 42 and 47 kJ/mol,

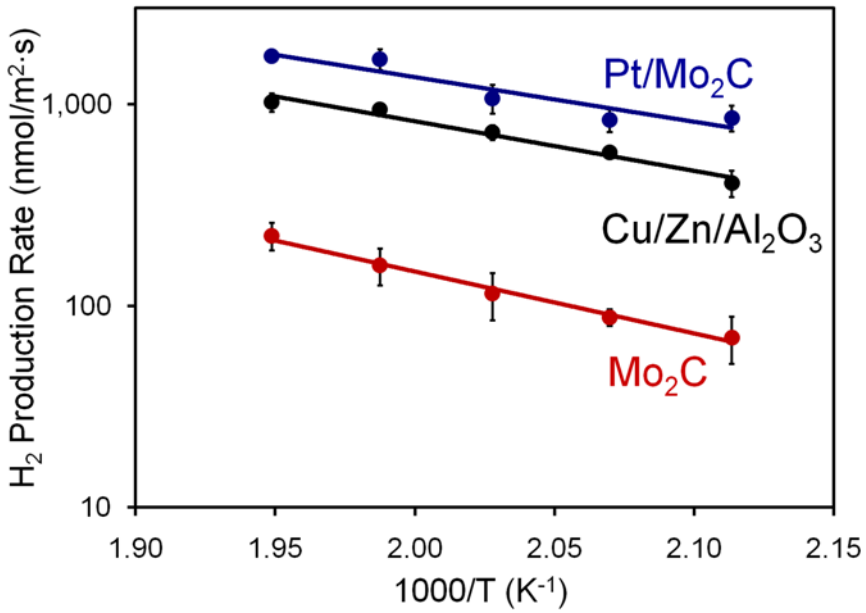

Figure 2.7: Hydrogen production rates during WGS for the Mo_2C and Pt/Mo_2C catalysts at 200-240 °C. The H_2 production rates for a commercial $Cu/Zn/Al_2O_3$ catalyst are also illustrated. The reformate feed consisted of 9% CO, 30% H_2O, 6% CO_2, 39% H_2 and 16% N_2.

respectively. These results are consistent with those reported previously [6, 11]. For example, King reported an activation energy of 45 kJ/mol for the 4% Pt/Mo_2C catalyst [6]. Turnover frequencies for the Pt/Mo_2C catalyst were higher than those for the $Cu/Zn/Al_2O_3$ catalyst and similar to those reported for the most active Pt-based catalysts (see Table 2.1).

The Mo_2C and Pt/Mo_2C catalysts deactivated during the first 10-15 h of exposure to sulfur-free reformate. Figure 2.8 shows the rates for Mo_2C and Pt/Mo_2C at 240°C as a function of time on stream (TOS). To probe the nature of this deactivation, rate decay for the Mo_2C and Pt/Mo_2C catalysts was fit to models of the form [32]:

$$-\frac{da}{dt} = k_d a(t)^m \qquad (2.2)$$

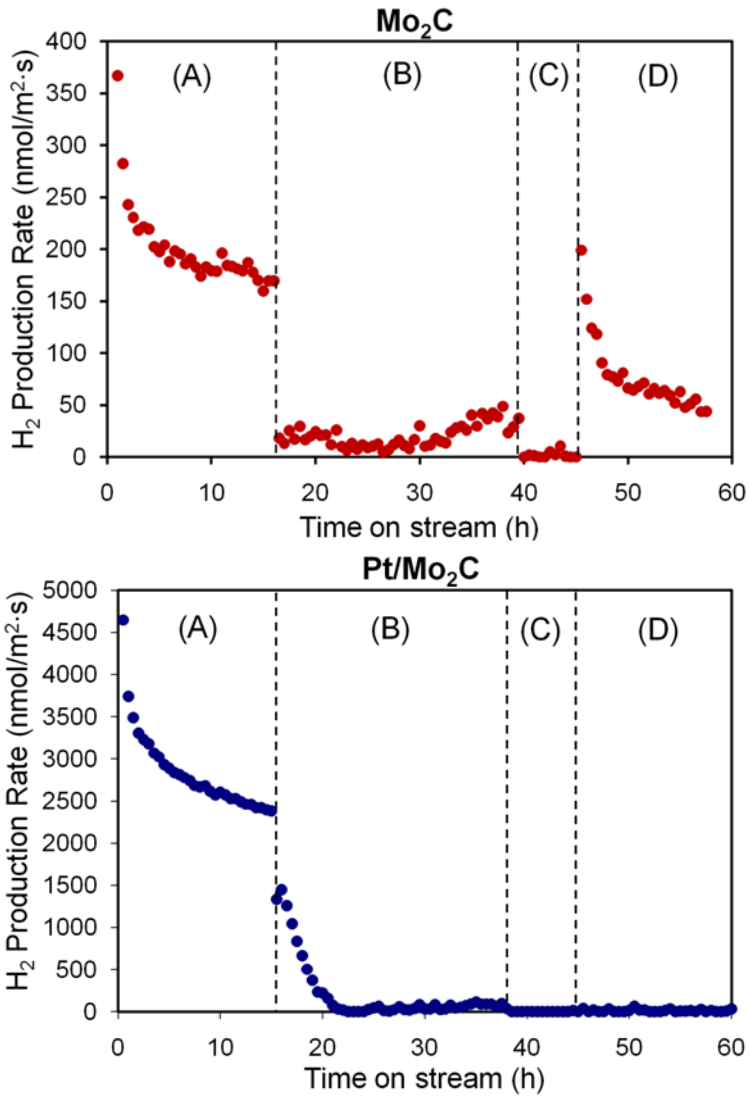

Figure 2.8: Hydrogen production rates for the Mo_2C and Pt/Mo_2C catalysts with (A) sulfur-free reformate, (B) reformate with 5 ppm H_2S, (C) sulfur-free reformate and (D) sulfur-free reformate after treatment of the catalyst at 590 °C for 4 h in a mixture of 15% CH_4/H_2. The reformate contained 9% CO, 30% H_2O, 6% CO_2, 39% H_2 and 16% N_2.

where *a(t)* is the ratio of the rate at time t to the initial rate, k_d is the specific decay constant and *t* is time on stream. Based on the F value and the R^2_{adj} value, the best-fit for the Mo_2C and Pt/Mo_2C catalysts was obtained using the reciprocal power form (Tables 2.4 and 2.5). This form is consistent with deactivation by carbon deposition [33, 34].

Table 2.4: Results from nonlinear regression of sulfur-free activity data for the Mo_2C catalyst to four empirical decay rate laws.

Type	Linear	Exponential	Hyperbolic	Reciprocal Power
Differential Form	$-\frac{da}{dt} = k_d$	$-\frac{da}{dt} = k_d a$	$-\frac{da}{dt} = k_d a^2$	$-\frac{da}{dt} = k_d A_0^{1/5} a^m$
Integral Form	$a = 1 - k_d t$	$a = e^{-k_d t}$	$a = \frac{1}{1 + k_d t}$	$a = A_0 t^{-k_d}$
k_d (h^{-1})	0.06 ± 0.01	0.18 ± 0.05	0.41 ± 0.08	0.20 ± 0.02
A_0	--	--	--	0.46 ± 0.03
R_{adj}^2	0.371	0.732	0.893	0.996
F[1]	18.3	84.7	260	4140

[1] Calculated by dividing the mean square model by the mean square error. P values for all model parameters were <0.0002.

Table 2.5: Results from nonlinear regression of sulfur-free activity data for the Pt/Mo_2C catalyst to four empirical decay rate laws.

Type	Linear	Exponential	Hyperbolic	Reciprocal Power
Differential Form	$-\frac{da}{dt} = k_d$	$-\frac{da}{dt} = k_d a$	$-\frac{da}{dt} = k_d a^2$	$-\frac{da}{dt} = k_d A_0^{1/5} a^m$
Integral Form	$a = 1 - k_d t$	$a = e^{-k_d t}$	$a = \frac{1}{1 + k_d t}$	$a = A_0 t^{-k_d}$
k_d (h^{-1})	0.045 ± 0.006	0.066 ± 0.009	0.10 ± 0.05	0.136 ± 0.007
A_0	--	--	--	0.75 ± 0.02
R_{adj}^2	0.952	0.970	0.982	0.999
F[1]	573	926	1570	60300

[1] Calculated by dividing the mean square model by the mean square error. P values for all model parameters were <0.0001.

Rates for the Mo_2C and Pt/Mo_2C catalysts also decreased on exposure to sulfur. Figure 2.8 shows the rates for Mo_2C and Pt/Mo_2C at 240 °C as a function of TOS. After the introduction of 5 ppm H_2S, the hydrogen production rate for the Mo_2C catalyst decreased by ~90% within 10 min. After ~32 h on stream, the catalyst regained some of its activity, reaching a H_2 production rate that was ~25% of its sulfur-free reactant steady-state rate. These temporal trends were reproducible. When H_2S was removed from the reactant, the rate for the Mo_2C catalyst quickly decreased to zero. Upon treating the spent Mo_2C catalyst with 15% CH_4/H_2 at 590 °C for 4 h, 25-30% of its initial rate was recovered.

General temporal trends for the Pt/Mo_2C catalyst were similar to those for the Mo_2C catalyst although the deactivation rate for the Pt/Mo_2C catalyst was much slower and occurred over a period of several hours. The Pt/Mo_2C catalyst did not regain any of its lost activity after removal of H_2S from the reactant and treatment in 15% CH_4/H_2 at 590 °C for 4 h resulted in a very slight reactivation of the catalyst to a rate similar to that for the Mo_2C catalyst.

To better understand the nature of interactions between sulfur and the Pt/Mo_2C catalyst, the H_2S concentration in the reactant was varied. The deactivation rates were strong functions of the sulfur concentration. The ratio of the rate following exposure to H_2S to the rate just before exposure to H_2S, $a_s(t)$, is plotted in Figure 2.9 as a function of TOS with 5, 25, and 50 ppm H_2S in the reactant. The activity decay was again fit to models of the form [32]:

$$-\frac{da_s}{dt} = k_{d,s} C_{H_2S,0}^{n} a_s(t)^m \tag{2.3}$$

where $k_{d,s}$ is the specific decay constant due to sulfur exposure, t is TOS after sulfur introduction, and $C_{H_2S,0}$ is the concentration of H_2S in the reactant (assumed to be constant). The best-fit was achieved for m = 1 (exponential form) and n = 0.51 ± 0.05, although the hyperbolic form was also a good fit for the data. The fit parameters for each of the models are included in Table 2.6. The exponential form is typical of deactivation caused by poisoning [35] while the hyperbolic form often indicates deactivation by sintering [32]. The half order dependence on concentration also suggests that H_2S dissociated on the Pt/Mo_2C catalyst surface [35].

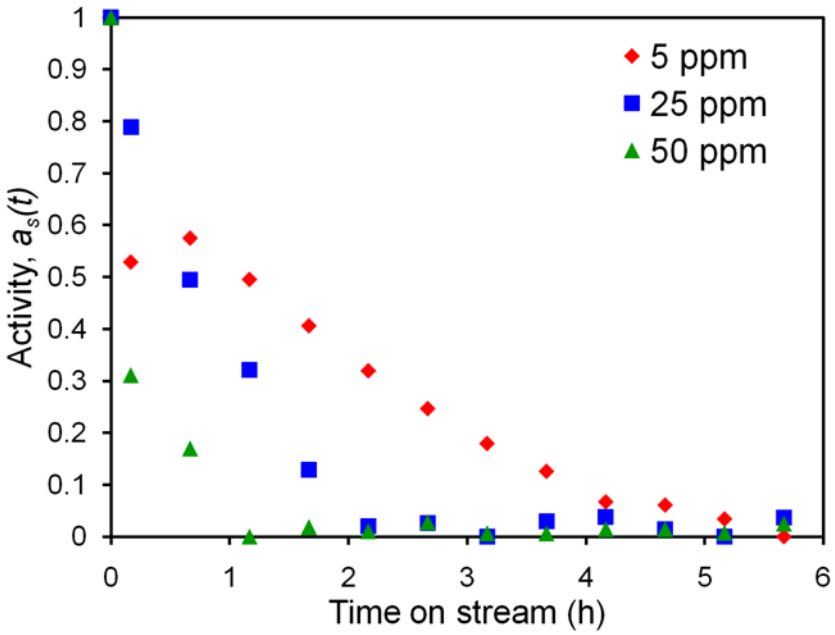

Figure 2.9: Activity, a_s(t), for the Pt/Mo_2C catalyst as a function of time on stream after the introduction of 5, 25, and 50 ppm H_2S to the reformate.

Hydrogen sulfide readily dissociates on Mo_2C at room temperature [36] and the conversion of Mo_2C and H_2S to MoS_2 is thermodynamically favorable with a ΔG_f of -264 kJ/mol at 240°C [37]. Furthermore, it has been reported that H_2S dissociates on Pt at temperatures as low as 100°C [38]. The formation of PtS from Pt and H_2S is also thermodynamically favorable with a ΔG_f of -32 kJ/mol at 240°C.

Table 2.6: Results from nonlinear regression of activity data for the Pt/Mo_2C catalyst to four empirical decay rate laws. The WGS rates were measured using reformate containing 5, 25 and 50 ppm H_2S.

Type	Linear	Exponential	Hyperbolic	Reciprocal Power
Differential Form	$-\frac{da_s}{dt} = k_{d,s} C_{H_2S,0}^n$	$-\frac{da_s}{dt} = k_{d,s} C_{H_2S,0}^n a_s$	$-\frac{da_s}{dt} = k_{d,s} C_{H_2S,0}^n a_s^{\,2}$	$-\frac{da_s}{dt} = k_{d,s} C_{H_2S,0}^n A_0^{1/5} a_s^{\,m}$
Integral Form	$a_s = 1 - k_{d,s} C_{H_2S,0}^n t$	$a_s = e^{-k_{d,s} C_{H_2S,0}^n t}$	$a_s = \frac{1}{1 + k_{d,s} C_{H_2S,0}^n t}$	$a_s = A_0 t^{-k_{d,s} C_{H_2S,0}^n}$
n	0.38 ± 0.06	0.51 ± 0.05	0.6 ± 0.1	0.1 ± 0.3
$k_{d,s}$ ($ppm^{-n}\ h^{-1}$)	0.12 ± 0.02	0.25 ± 0.03	0.5 ± 0.1	0.6 ± 0.5
A_0	--	--	--	0.31 ± 0.04
R_{adj}^2	0.781	0.986	0.965	0.737
F[1]	39.7	777	304	18.4

[1] Calculated by dividing the mean square model by the mean square error. P value for all model parameters were <0.0001.

2.3.3. *In Situ* Characterization

Prior to collection of the *in situ* XPS spectra, the materials were pretreated in 15% CH_4/H_2 at 590 °C for 4 h, exposed to a reformate containing 9% CO, 30% H_2O, 6% CO_2, 39% H_2 in N_2 at 240 °C for 4 h, purged with N_2 then cooled to room temperature in the XPS reaction chamber. After reducing the pressure to < 10^{-8} torr, the material was transferred into the analysis chamber. Compared to the pretreated sample, the C 1s spectrum (Figure 2.10) for Mo_2C presented peaks associated with C-O and C=O, in addition to a prominent carbidic carbon peak. The resulting Mo spectra for the Mo_2C catalyst (Figure 2.10) were similar to that for the pretreated catalyst. However, the oxygen spectra were different (Figure 2.10). In addition to peaks at 530.7 ± 0.2 and 532.4 ± 0.2 eV (also observed for the pretreated materials), a peak at 533.7 ± 0.2 eV was observed (Table 2.7). This peak is believed to correspond to oxygen in adsorbed carbon oxides [22]. Under reaction conditions, the O/Mo ratio for the Mo_2C catalyst was 5.7 compared to a O/Mo ratio of 1.5 for the pretreated material. This increase in O/Mo ratio was due to an increase in the density of adsorbed O^-, OH^- and/or H_2O, and not to an increase in Mo oxides.

For the Pt/Mo_2C catalyst, the C and Mo spectra (Figure 2.10) resembled those after pretreatment, except for an additional C 1s peak that was attributed to C=O. As observed for the Mo_2C catalyst, the oxygen spectra included an additional peak at 533.7 ± 0.2 eV that we attributed to adsorbed carbon oxides. The O/Mo ratio for the Pt/Mo_2C catalyst increased to 4.2 under reaction conditions from a value of 1.2 after pretreatment. This increase was primarily due to increases in the concentrations of O^-, OH^-, and/or H_2O.

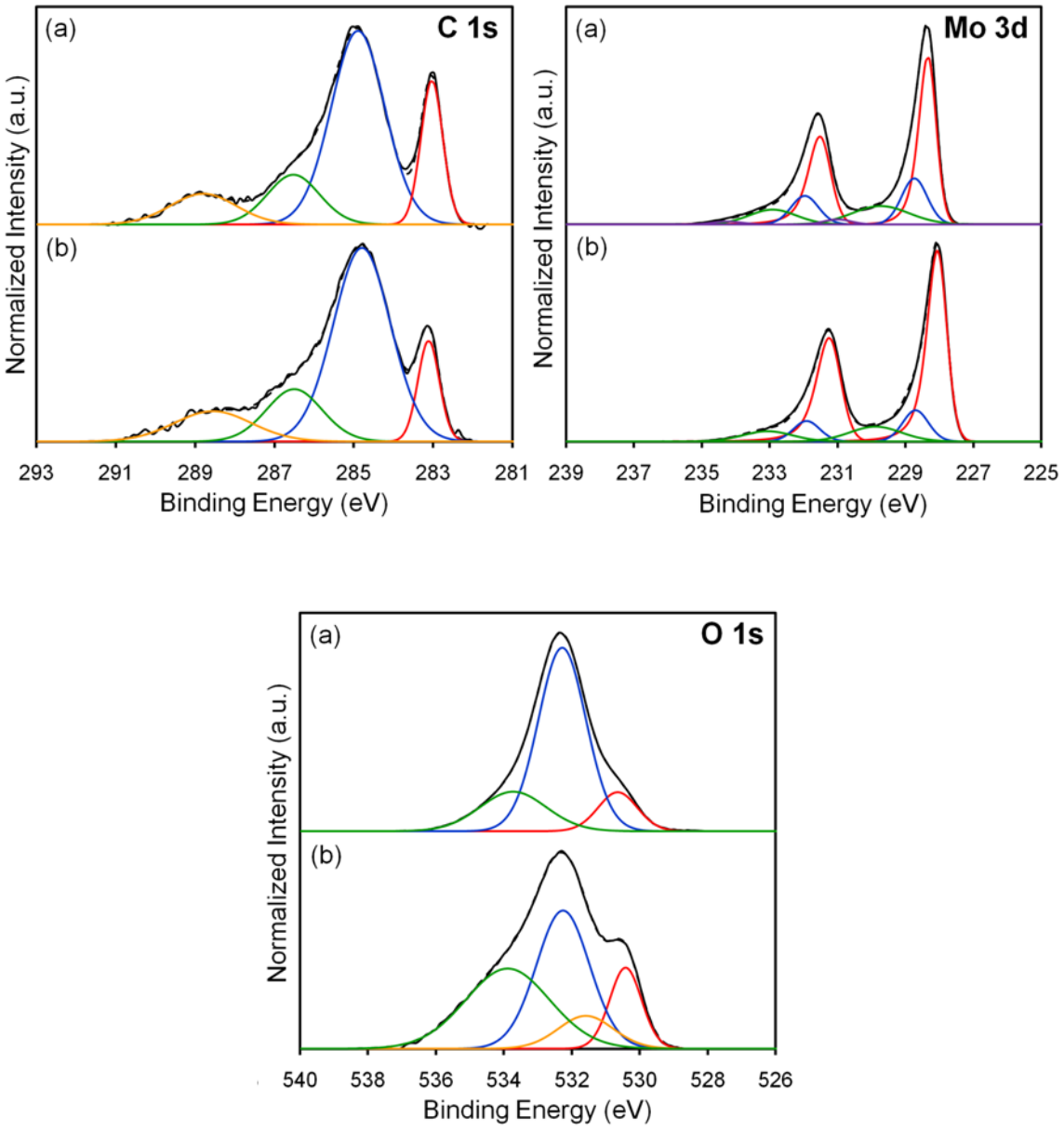

Figure 2.10: Carbon 1s, Molybdenum 3d, and Oxygen 1s XPS spectra for the (a) Mo_2C and (b) Pt/Mo_2C catalysts following pretreatment in 15% CH_4/H_2 at 590 °C for 4 h and exposure to reformate containing 9% CO, 30% H_2O, 6% CO_2, 39% H_2 and 16% N_2 at 240 °C in the *in situ* XPS reaction chamber.

Table 2.7: Binding energies from *in situ* spectra for species on surfaces of the Mo_2C and Pt/Mo_2C catalysts following pretreatment in 15% CH_4/H_2 at 590 °C for 4 h, exposure to reformate containing 9% CO, 30% H_2O, 6% CO_2, 39% H_2 in N_2 at 240 °C for 4 h, purge with N_2 then cooling to room temperature.

Catalyst	C 1s (eV)[1,2]		Mo $3d_{5/2}$ (eV)[1]			Pt $4f_{7/2}$ (eV)[1]		O 1s (eV)[1]		
	Mo_2C	C-O	Mo^{2+}	$Mo^{\delta+}$	Mo^{4+}	Pt^0	Pt^{2+}	MoO_x	O^-, OH^-, H_2O, O=C	O-C
Mo_2C	283.1 (18)	286.5 (14)	228.3 (55)	228.7 (23)	229.7 (20)	--	--	530.7 (12)	532.3 (68)	533.7 (20)
Pt/Mo_2C	283.2 (11)	286.5 (16)	228.2 (69)	228.7 (16)	229.9 (15)	71.6 (83)	73.3 (17)	530.5 (14)	532.3 (40)	533.9 (36)

[1] The number in parentheses represents the atomic percentage.
[2] Balance of atomic percentages for C 1s is adventitious carbon.

Temporal changes in the catalyst weight during exposure to H_2S provided insight regarding the nature of interactions between the catalysts and sulfur. Prior to these measurements, the catalysts were pretreated at 590 °C for 4 h in the CH_4/H_2 mixture then degassed in He at 240 °C for 1 h. Changes in weight were assumed to be due to the adsorption onto and/or incorporation of sulfur into the catalysts. During the first 10 minutes at 240 °C in a 5 ppm H_2S/He mixture, there was a rapid weight gain (Figure 2.11). Subsequently, the rate of weight gain decreased, but remained somewhat steady

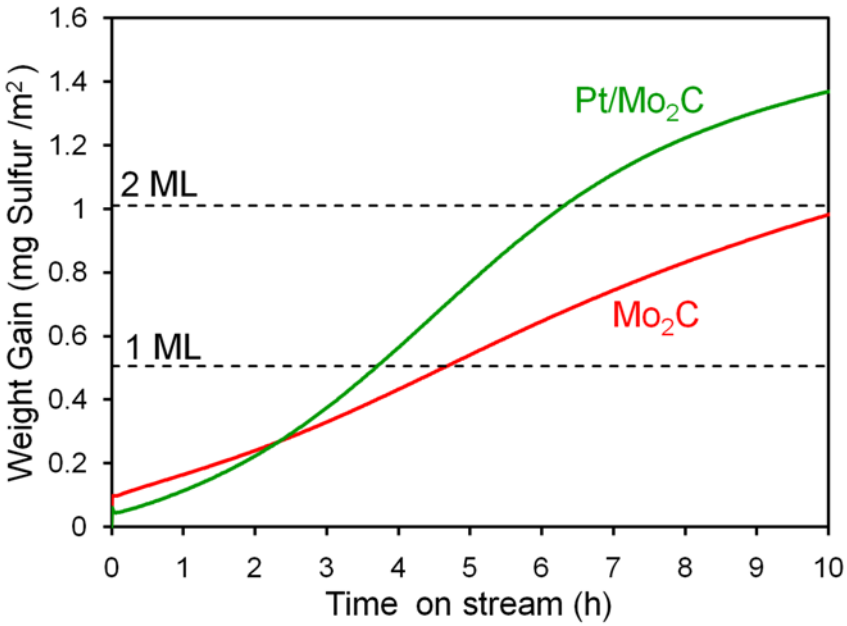

Figure 2.11: Weight gain during exposure of the Mo_2C and Pt/Mo_2C catalysts to 5 ppm H_2S in He at 240 °C. The dashed lines indicate the weight gains corresponding to 1 ML and 2 ML of sulfur coverage assuming a material with 98 m^2/g.

until reaching a weight gain equivalent to ~2 monolayers (ML) of sulfur, based on a site density of 10 sites/nm^2 and 1 sulfur atom/site. After the adsorption or incorporation of ~2 ML of sulfur, the rate of weight gain slowed then leveled off. The overall rate of sulfur uptake was slightly higher for the Pt/Mo_2C catalyst than for the Mo_2C catalyst, and

shapes of the curves were different suggesting that the presence of Pt caused a change in the mechanism for sulfur incorporation.

2.3.4. Post Reaction *Ex Situ* Characterization

Bulk crystalline structures for the Mo_2C and Pt/Mo_2C catalysts did not change on exposure to reformate without or with 5 ppm H_2S at 240 °C, as evident from the XRD patterns (Figure 2.12). The sharper peaks were due to the SiO_2 that was used as a diluent

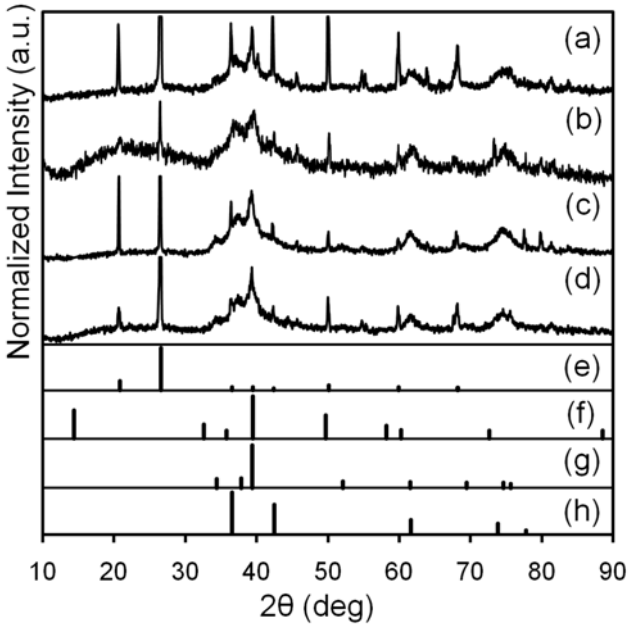

Figure 2.12: X-ray diffraction patterns for the (a) Mo_2C catalyst after WGS without H_2S, (b) Pt/Mo_2C catalyst after WGS without H_2S, (c) Mo_2C catalyst after WGS with 5 ppm H_2S and (d) Pt/Mo_2C catalyst after WGS with 5 ppm H_2S. Peak positions for polycrystalline (e) SiO_2 [39], (f) MoS_2 [40], (g) β-Mo_2C [14], and (h) α-MoC_{1-x} [15] reference materials are also illustrated. The SiO_2 was used as a catalyst diluent during the reaction rate measurements.

during the reaction rate measurements. The absence of a peak at $2\theta \sim 14$ ° indicated that MoS_2 crystallites, if present, were below the detection limit of the x-ray diffractometer. Micrographs of the fresh and spent catalysts (see for example Figure 2.13) were very

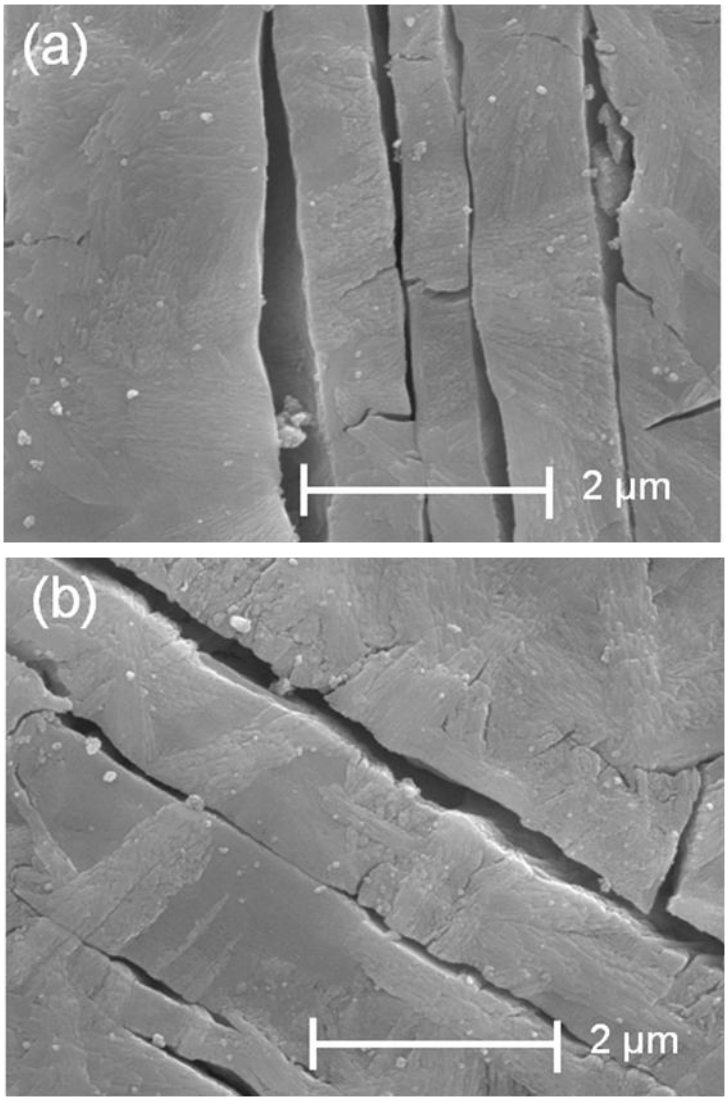

Figure 2.13: Scanning electron micrographs of the (a) as-synthesized and (b) spent (WGS with 5 ppm H_2S at 240 °C) Mo_2C catalysts. Images were collected at 15 kV accelerating voltage, 3.0 spot size, and 18,000 magnification.

similar indicating that there were no significant changes in the surface morphology. Although sulfidation of Mo_2C and Pt is thermodynamically favorable, these materials are reported to be moderately resistant to bulk sulfidation, possibly because the diffusion of sulfur into the sub-surface is slow due to its size [3, 37, 41, 42]. Surface areas for the spent catalysts both in sulfur-free and sulfur-containing reactants were ~5-15% lower than those for the fresh catalysts. For example, surface areas for the spent Mo_2C catalysts

were 86 ± 4 (without sulfur) and 93 ± 4 m^2/g (with sulfur) compared to a surface area of 98 ± 5 m^2/g for the as-synthesized catalyst. These results confirm that the deactivation caused by exposure to H_2S was not due to surface area loss or sintering.

Due to the difficulty of ensuring the complete removal of sulfur, experiments involving sulfur could not be carried out in the XPS reaction system. Instead, catalysts exposed to reformate in the catalytic reactor were cooled to room temperature, quickly transferred in air to a desiccator, and stored under vacuum until being transferred to the spectrometer and collection of the *ex situ* spectra. A comparison of the *in situ* (Figure 2.10) and *ex situ* (Figure 2.14) Mo spectra for materials exposed to the reformate suggests that this brief exposure to air caused partial oxidation of Mo_2C at the surface to MoO_3. As shown in Figure 2.12, however, the catalysts did not undergo bulk oxidation to MoO_2 or MoO_3 upon exposure to air. Nevertheless, an examination of major changes in the *ex situ* spectra provided insight regarding the significant effects of sulfur on the Mo_2C and Pt/Mo_2C catalysts. Results from deconvolution of the *ex situ* spectra are summarized in Table 2.8 for catalysts subjected to the following treatments (also see Figure 2.8):

(A) sulfur-free reformate at 240 °C for 16 h;

(B) reformate with 5 ppm H_2S at 240 °C for 22 h;

(C) sulfur-free reformate at 240 °C for 5 h;

(D) sulfur-free reformate after treatment of the catalyst at 590 °C in CH_4/H_2 for 4h

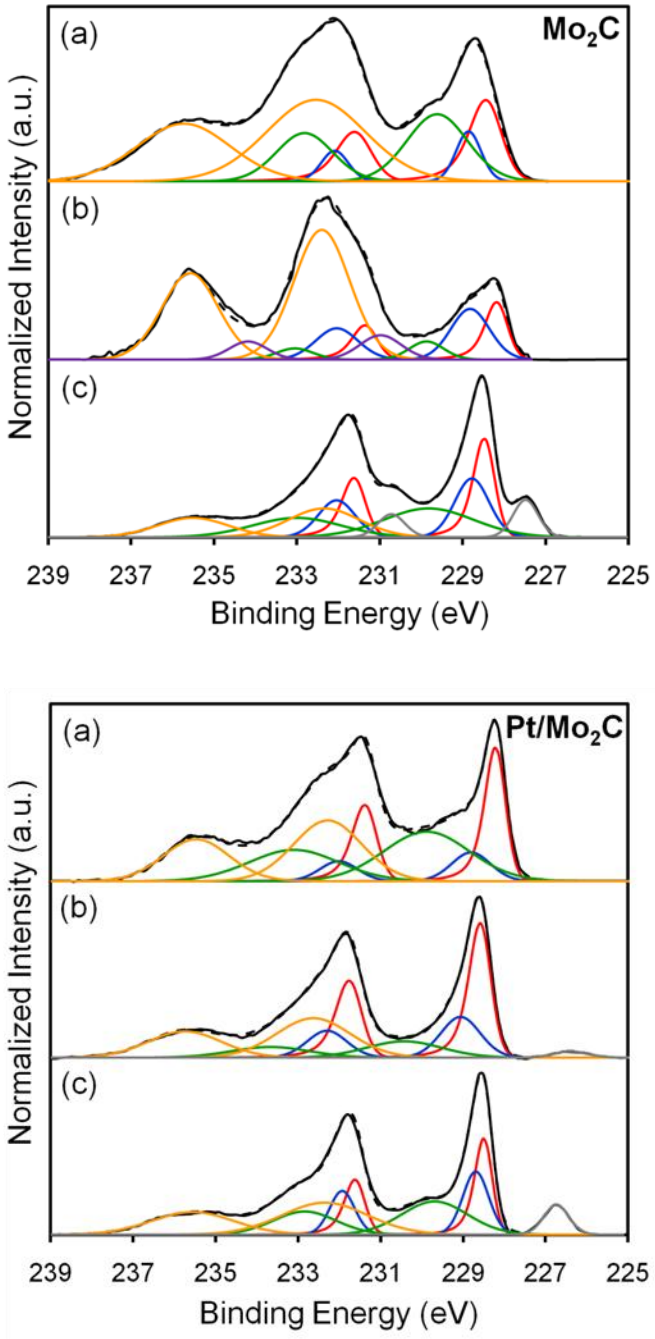

Figure 2.14 Molybdenum 3d XPS spectra for the Mo_2C and Pt/Mo_2C catalysts (a) after WGS without H_2S, (b) after WGS with 5 ppm H_2S, and (c) after WGS with 5 ppm H_2S, treatment in 15% CH_4/H_2 at 590 °C for 4 h, and WGS without H_2S.

Table 2.8: Binding energies from *ex situ* spectra for species on the surfaces of the Mo_2C and Pt/Mo_2C catalysts following measurement of the reaction rates (see Figure 2.8).

Catalyst	Treatment[1]	C 1s (eV)[2,3]		Mo $3d_{5/2}$ (eV)[2]				Pt $4f_{7/2}$ (eV)[2]			O 1s (eV)[2]			S 2p (eV)[2]					S 2s (eV)[2]
		Mo_2C	C-O	Mo^{2+}	$Mo^{\delta+}$	Mo^{4+}	Mo^{6+}	Pt*	Pt^0	Pt^{2+}	MoO_x	O^-,OH^- H_2O,O=C	O-C	MoS_xC_y	S-Mo	MoS_2/ PtS	S_2^{2-}	SO_4^{2-}	
Mo_2C	A	283.3 (10)	286.6 (35)	228.4 (15)	228.8 (8)	229.6 (26)	232.5 (51)	--	--	--	530.6 (30)	532.6 (39)	533.8 (31)	--	--	--	--	--	--
Mo_2C	ABC	--	285.8 (36)	228.2 (10)	228.8 (16)	229.9 (5)	232.4 (60)	--	--	--	530.6 (9)	532.8 (80)	533.7 (11)	--	--	--	163.1 (100)	--	--
Mo_2C	ABCD	283.6 (27)	286.3 (22)	228.5 (21)	228.8 (21)	229.8 (27)	232.3 (21)	--	--	--	530.7 (62)	532.4 (30)	533.5 (8)	160.7 (18)	161.7 (37)	162.3 (45)	--	--	--
Pt/Mo_2C	A	283.1 (35)	286.7 (7)	228.2 (22)	228.8 (9)	229.9 (35)	232.3 (34)	69.7 (26)	71.5 (71)	73.3 (3)	530.6 (64)	532.2 (29)	533.8 (3)	--	--	--	--	--	---
Pt/Mo_2C	ABC	283.6 (22)	286.4 (22)	228.6 (33)	229.0 (19)	230.4 (14)	232.6 (34)	--	71.9 (71)	72.7 (29)	530.8 (55)	532.1 (31)	533.7 (2)	--	161.9 (23)	162.5 (59)	--	168.8 (18)	226.4
Pt/Mo_2C	ABCD	283.6 (17)	286.4 (20)	228.5 (19)	228.7 (20)	229.7 (27)	232.4 (34)	70.5 (24)	72.0 (73)	73.4 (3)	530.8 (49)	532.1 (43)	533.6 (2)	160.3 (11)	161.9 (14)	162.4 (58)	--	168.9 (17)	226.7

[1] Treatments correspond to sections of Figure 2.8.
[2] The number in parentheses represents the atomic percentage.
[3] Balance of atomic percentages for C 1s is adventitious carbon.

With the exception of the S 2p spectra, spectra for the Mo_2C catalyst prior to and after exposure to sulfur were similar. Exposure to reformate with 5 ppm H_2S resulted in a doublet with S $2p_{3/2}$ peak at 163.1 ± 0.2 eV (Figure 2.15). This binding energy is consistent with the presence of S_2^{2-} in MoS_3 or SH groups [3, 43].

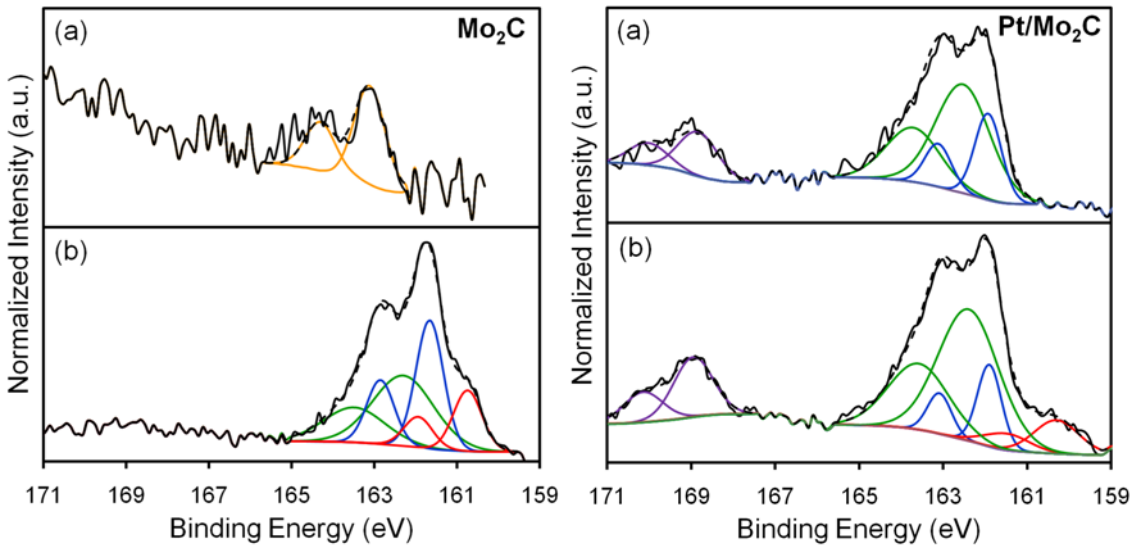

Figure 2.15: Sulfur 2p XPS spectra for the Mo_2C and Pt/Mo_2C catalysts (a) after WGS with 5 ppm H_2S for 22 h and (b) after WGS with 5 ppm H_2S, treatment in 15% CH_4/H_2 at 590 °C for 4 h, and WGS without H_2S.

Treatment of the sulfur deactivated Mo_2C catalyst in 15% CH_4/H_2 at 590 °C for 4 h caused an increase in the relative amounts of Mo that we attributed to Mo_2C and MoS_2 [3, 26] (Figure 2.14) and emergence of a small doublet with Mo $3d_{5/2}$ peak at 227.5 ± 0.1 eV. This doublet is consistent with the presence of Mo^0 [44]. Three doublets were resolved in the S 2p spectra (Figure 2.15). The doublet with S $2p_{3/2}$ peak at 161.8 ± 0.2 eV has been assigned to atomic sulfur strongly adsorbed to Mo [45, 46]. The peak at 162.4 ± 0.2 eV corresponds to S^{2-} species, likely in the form of MoS_2 [3, 23, 42]. The peak at 160.5 ± 0.2 eV has been tentatively attributed to a Mo sulfidocarbide [41, 47, 48] based on the position.

Exposure of the Pt/Mo_2C catalyst to sulfur significantly affected the associated XPS spectra. Spectra following exposure to sulfur-free reformate contained a doublet with Pt $4f_{7/2}$ peak at 70.1 ± 0.4 eV (Figure 2.16), in addition to peaks attributable to Pt^0

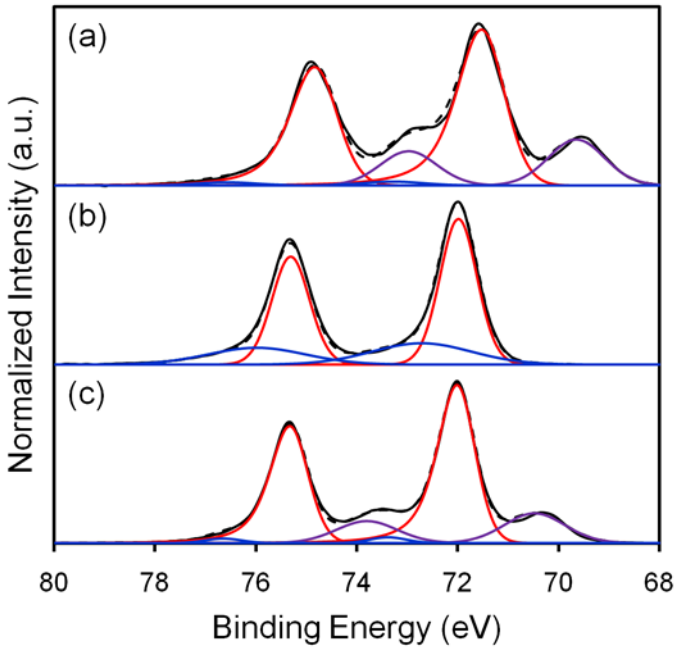

Figure 2.16: Platinum 4f XPS spectra for the Pt/Mo_2C catalyst (a) after WGS without H_2S, (b) after WGS with 5 ppm H_2S, and (c) after WGS with 5 ppm H_2S, treatment in 15% CH_4/H_2 at 590 °C for 4 h, and WGS without H_2S.

and PtO. This binding energy does not match those of any previously reported Pt species, but the shift relative to Pt^0 is consistent with the presence of anionic Pt. Exposure to sulfur eliminated this highly reduced Pt species. The relative amount of Mo_2C increased following exposure to reformate containing 5 ppm H_2S. Three doublets were resolved in the S 2p spectra for the Pt/Mo_2C catalyst after exposure to reformate with 5 ppm H_2S at 240 °C (Figure 2.15). The doublet with S $2p_{3/2}$ peak at 161.8 ± 0.2 eV corresponds to sulfur strongly adsorbed to Mo. The doublet with S $2p_{3/2}$ peak at 162.4 ± 0.2 eV corresponds to S^{2-} species, possibly in the form of MoS_2 or PtS [3, 23, 42, 49, 50]. The doublet with S $2p_{3/2}$ peak at 168.8 ± 0.2 eV is consistent with the presence of sulfate

species (S^{6+}) [26, 51, 52]. Oxygen in the sulfate might have been introduced from the subsurface or exposure to air. Treatment of the sulfur deactivated Pt/Mo_2C catalyst in 15% CH_4/H_2 at 590 °C for 4 h caused reemergence of peaks that we attributed to anionic Pt and Mo sulfidocarbide, a slight decrease in the amount of Mo_2C and a slight increase in the amount of MoS_2.

2.4. Discussion

The focus of this chapter was to assess the effects of sulfur, in the form of H_2S, on the WGS activities and structures of Mo_2C and Pt/Mo_2C catalysts. It is important to understand these effects as sulfur is a common impurity in fossil-fuel derived feed streams. Catalysts with a high tolerance to sulfur are desired. In general, sulfur tolerance can be manifested in two ways. The most attractive form of tolerance is when the catalyst maintains its rate during exposure to sulfur. Another form is when the catalytic activity can be restored via modest treatment of the spent material. Results described in this chapter indicate that the Mo_2C and Pt/Mo_2C catalysts possessed some degree of sulfur tolerance. The Mo_2C catalyst was significantly deactivated during exposure to sulfur but maintained a modest rate, and some of the initial performance could be restored via treatment in CH_4/H_2 mixtures. The Pt/Mo_2C catalyst behaved in a similar manner with the exception that the extent of reactivation was much lower than that for the Mo_2C catalyst. This discussion section will explore changes in the surface chemistry that correlate with deactivation of the catalysts.

The Mo_2C and Pt/Mo_2C catalysts deactivated during the first 10-15 h of exposure to sulfur-free reformate (Figure 2.8). Rate decay equations for the Mo_2C and Pt/Mo_2C catalysts during the first 10-15 h of exposure to sulfur-free reformate suggested that the

deactivation was caused by carbon deposition. This result is in agreement with the XPS results. Comparison of XPS spectra from pretreated and in-situ WGS exposed samples revealed an increase in carbon oxide groups (C-O and C=O) as well as surface oxygen. Formation of carbonate or formate groups may have caused blockage of active sites, as this behavior has been reported for other WGS catalysts [53]. Formation of surface oxides could reduce the number of active Mo_2C sites.

Deactivation of the Mo_2C catalyst by H_2S appeared to occur in three stages. The reaction rate decreased significantly during the first 10 minutes of exposure to sulfur. In a similar time frame, the sulfur adsorption and/or incorporation rate increased dramatically. We believe these responses were interrelated and that highly active Mo_2C sites were quickly poisoned during this stage. Subsequently, the WGS rate decreased and the sulfur content increased more gradually. During the final stage, the activity increased slightly. This increase in activity appeared to correspond with the adsorption and/or incorporation of ~2 ML of sulfur on the Mo_2C catalyst surface. When sulfur was removed from the reactant, the activity decreased suggesting that it was associated with MoS_2 nanoparticles. Molybdenum sulfide is known to be active for the WGS in the presence of H_2S, and in fact, requires sulfur in the feed to maintain its activity [54]. A fraction of the Mo_2C sites could be restored via treatment in 15% CH_4/H_2 at 590 °C for 4 h, however, based on the XPS results, MoS_2 sites persisted. Therefore, we have concluded that the sulfur tolerance exhibited by the Mo_2C catalyst was associated with MoS_2 nanoparticles produced via sulfidation of Mo_2C, and the regenerability of highly active Mo_2C-based sites poisoned during initial exposure to sulfur.

In comparison to the Mo_2C catalyst, the Pt/Mo_2C catalyst exhibited a much slower deactivation rate suggesting that most of the activity was associated with the presence of Pt. The results are consistent with two types of sites on the Pt/Mo_2C catalyst: sites on the Pt nanoparticles or at the Pt nanoparticle-Mo_2C support interface, and sites on the Mo_2C support. The high activity Pt-based sites were severely and irreversibly deactivated, we believe, as a consequence of the conversion of Pt into inactive PtS. Sites associated with the Mo_2C support could be partially reactivated in a manner similar to that observed for the Mo_2C catalyst.

Finally, we note that surface oxygen may have played a role in the interactions of sulfur with the Mo_2C and Pt/Mo_2C catalysts. Oxygen has been reported to facilitate the sulfidation of early transition metal carbides and nitrides [23]. After exposure to WGS conditions, there was a high concentration of oxygen on the surface of the Mo_2C and Pt/Mo_2C catalysts, as indicated by the O/Mo atomic ratios determined from XPS (5.7 and 4.2, respectively). This oxygen was present in the form of strongly adsorbed O-, OH- and/or H_2O. Upon exposure to H_2S, these surface oxygen species may have facilitated the formation of MoS_2 domains. Using XPS, MoS_2 was confirmed to be present on the catalyst surface.

2.5. Summary

The effects of H_2S on the WGS activities, structures and compositions of Mo_2C and Pt/Mo_2C catalysts have been investigated. These catalysts were severely deactivated on exposure to H_2S but could be partially regenerated. Characterization of the spent catalysts suggested that deactivation of the Mo_2C catalyst was primarily due to the adsorption of sulfur on Mo_2C sites and the formation of surface MoS_2. The MoS_2 sites

were active in the presence of sulfur. Deactivation of the Pt/Mo_2C catalyst appeared to be primarily due to the irreversible sulfidation of Pt nanoparticles. Other features for this catalyst were similar to those for the Mo_2C catalyst. Under reaction conditions, the Mo_2C and Pt/Mo_2C surfaces also possessed high concentrations of oxygen, which may have facilitated formation of the Mo sulfide. Although Pt improved the activity of the Mo_2C catalyst, it also altered the interaction of sulfur with the catalyst surface resulting in an increased susceptibility to sulfur poisoning. These results suggest that the Mo_2C and Pt/Mo_2C catalysts were partially tolerant to sulfur during WGS.

2.6. References

[1] C. N. Satterfield, Heterogeneous Catalysis in Industrial Practice, 2nd ed., McGraw-Hill, 1991.

[2] J. M. Robinson, S. R. Barrett, K. Nhoy, R. K. Pandey, J. Phillips, O. M. Ramirez, R. I. Rodriguez, Energy Dispersive X-ray Fluorescence Analysis of Sulfur in Biomass *Energy Fuels* 23 (2009) 2235-2241.

[3] P. K. Cheekatamarla, W. J. Thomson, Poisoning Effect of Thiophene on the Catalytic Activity of Molybdenum Carbide during Tri-Methyl Pentane Reforming for Hydrogen Generation *Applied Catalysis A: General* 287 (2005) 176-182.

[4] P. Da Costa, J.-L. Lemberton, C. Potvin, J.-M. Manoli, G. Perot, M. Breysse, D. Djega- Mariadassou, Tetralin Hydrogenation Catalyzed by Mo_2C/Al_2O_3 and WC/Al_2O_3 in the Presence of H_2S *Catalysis Today* 65 (2001) 195-200.

[5] P. A. Aegerter, W. W. C. Quigley, G. J. Simpson, D. D. Ziegler, J. W. Logan, K. R. McCrea, S. Glazier, M. E. Bussell, Thiophene Hydrodesulfurization over Alumina-Supported Molybdenum Carbide and Nitride Catalysts: Adsorption Sites, Catalytic Activities, and Nature of the Active Surface *Journal of Catalysis* 164 (1996) 109-121.

[6] T. E. King, Carbide and Nitride Supported Water-Gas Shift Catalysts, Ph. D. Thesis, University of Michigan, 2007.

[7] N. M Schweitzer, Evaluating the Effect of a Strong Metal-Support Interaction on the Activity of Molybdenum Carbide Supported Platinum Water-Gas Shift Catalysts, Ph. D. Thesis, University of Michigan, 2010.

[8] N. M. Schweitzer, J. A. Schaidle, O. K. Ezekoye, X. Pan, S. Linic, L. T. Thompson, High Activity Carbide Supported Catalysts for Water Gas Shift, *Journal of the American Chemical Society* 133 (2011) 2378-2381.

[9] Q. Ming, T. Healey, L. Allen, P. Irving, Steam Reforming of Hydrocarbon Fuels *Catalysis Today* 77 (2002) 51-64.

[10] Y.-M. Wu, *Oil and Gas Journal* 92 (1994) 38.

[11] J. J. Patt, Carbide and Nitride Catalysts for the Water Gas Shift Reaction, Ph. D. Thesis, University of Michigan, 2003.

[12] J. Patt, D. J. Moon, C. Phillips, L. Thompson, Molybdenum Carbide Catalysts for Water-Gas Shift *Catalysis Letters* 65 (2000) 193-195.

[13] G. C. Bond, S. N. Namijo, An improved procedure for estimating the metal surface area of supported copper catalysts, *Journal of Catalysis* 118 (1989) 507-510.

[14] S. Nagakura, M. Kikuchi, S. Oketani, Electron Diffraction Determination of the Ionization of the Carbon Atom in β-Mo_2C Crystal *Acta Crystallographica* 21 (1966) 1009-1010.

[15] J. C. Schuster, H. Nowotny, Molybdenum Carbides and Molybdenum Tungsten Carbides in the Temperature Range of 600-1600°C *Monatshefte fuer Chemie* 110 (1979) 321-333.

[16] M. Ghedira, C. Do-Dinh, M. Marezio, J. Mercier, The Crystal Structure of Molybdenum Titanium Oxide ($Mo_{0.975}Ti_{0.025}O_2$) between 24 and 900°C *Journal of Solid State Chemistry* 59 (1985) 159-167.

[17] J. D. Hanawalt, H. W. Rinn, L. K. Frevel, Chemical Analysis by X-ray Diffraction. Classification and Use of X-ray Diffraction Patterns *Industrial and Engineering Chemistry: Analytical Edition* 10 (1938) 457-512.

[18] C. A. Vanderborgh, Y. K. Vohra, H. Xia, A. L. Ruoff, Lead at 109 GPa: Diffraction Studies to 208 GPa *Physical Review B: Condensed Matter and Materials Physics* 41 (1990) 7338-7340.

[19] H. Iida, A. Igarashi, Characterization of a Pt/TiO_2 (rutile) Catalyst for Water Gas Shift Reaction at Low-Temperature *Applied Catalysis A: General* 298 (2006) 152-160.

[20] T. P. St. Clair, S. T. Oyama, D. F. Cox, S. Otani, Y. Ishizawa, R.-L. Lo, K.-I. Fukui, Y. Iwasawa, Surface Characterization of α-Mo_2C (0001) *Surface Science* 426 (1999) 187-198.

[21] P. Delporte, F. Meunier, C. Pham-Huu, P. Vennegues, M. J. Ledoux, J. Guille, Physical Characterization of Molybdenum Oxycarbide Catalyst: TEM, XRD, and XPS *Catalysis Today* 23 (1995) 251-267.

[22] M. Buo, J. M. Martin, T. Le Mogne, L. Vovelle, Chemistry of the Interface between Aluminum and Polyethylene Terephthalate by XPS *Applied Surface Science* 47 (1991) 149-161.

[23] Z. B. Zhaobin Wei, P. Grange, B. Delmon, XPS and XRD Studies of Fresh and Sulfided Mo_2N *Applied Surface Science* 135 (1998) 107-114.

[24] J.-G. Choi, L. T. Thompson, XPS Study of As-prepared and Reduced Molybdenum Oxides *Applied Surface Science* 93 (1996) 143-149.

[25] A. Katrib, P. Leflaive, L. Hilaire, G. Maire, Molybdenum Based Catalysts: I. MoO_2 as the Active Species in the Reforming of Hydrocarbons *Catalysis Letters* 38 (1996) 95-99.

[26] A. S. Mamede, J.-M. Giraudon, A. Lofberg, L. Leclercq, G. Leclercq, Hydrogenation of Toluene over β-Mo_2C in the Presence of Thiophene *Applied Catalysis A: General* 227 (2002) 73-82.

[27] M. J. Ledoux, C. P. Huu, J. Guille, H. Dunlop, Compared Activities of Platinum and High Specific Surface Area Molybdenum Carbide (Mo_2C) and Tungsten Carbide (WC) Catalysts for Reforming Reactions. I. Catalyst Activation and Stabilization: Reaction of n-hexane *Journal of Catalysis* 134 (1992) 383-398.

[28] P. Perez-Romo, C. Potvin, J.-M. Manoli, M. M. Chehimi, G. Djega-Mariadassou, Phosphorus-Doped Molybdenum Oxynitrides and Oxygen-Modified Molybdenum Carbides: Synthesis, Characterization, and Determination of Turnover Rates for Propene Hydrogenation *Journal of Catalysis* 208 (2002) 187-196.

[29] J. L. G. Fierro, J. M. Palacios, F. Tomas, An Analytical SEM and XPS Study of Platinum-Rhodium Gauzes Used in High Pressure Ammonia Burners *Surface and Interface Analysis* 13 (1988) 25-32.

[30] J. P. Contour, G. Mouvier, M. Hoogewys, C. Leclere, X-ray Photoelectron Spectroscopy and Electron Microscopy of Platinum-Rhodium Gauzes Used for Catalytic Oxidation *Journal of Catalysis* 48 (1977) 217-228.

[31] G. M. Bancroft, I. Adams, L. L. Coatsworth, C. D. Bennewitz, J. D. Brown, W. D. Westwood, ESCA Study of Sputtered Platinum Films *Analytical Chemistry* 47 (1975) 586-588.

[32] H.S. Fogler, Elements of Chemical Reaction Engineering, 3rd Ed., Prentice Hall, New Jersey, 1999, p. 643.

[33] A, Voorhies, Jr., C Formation in Catalytic Cracking *Journal of Industrial and Engineering Chemistry* 37 (1945) 318-322.

[34] C. G. Rudershausen, C. C. Watson, Variables Affecting Activity of Molybdena-Alumina Hydroforming Catalyst in Aromatization of Cyclohexane *Chemical Engineering Science* 3 (1954) 110-121.

[35] C. H. Bartholomew, R. J. Farrauto, Fundamentals of Industrial Catalytic Processes, 2nd Ed., John Wiley & Sons, 2006.

[36] J. A. Rodriguez, J. Dvorak, T. Jirsak, Chemistry of SO_2, H_2S, and CH_3SH on Carbide-Modified Mo(110) and Mo_2C Powders: Photoemission and XANES Studies *Journal of Physical Chemistry B* 104 (2000) 11515-11521.

[37] E. Furimsky, Metal Carbides and Nitrides as Potential Catalysts for Hydroprocessing *Applied Catalysis A: General* 240 (2003) 1-28.

[38] M. V. Mathieu, M. Primet, Sulfurization and Regeneration of Platinum *Applied Catalysis* 9 (1984) 361-370.

[39] V. I. Pakhomov, A. V. Goryunov, P. V. Pakhomov, N. T. Chibiskova, Stucture of a Quartz Crystal Containing Iron (3+) Impurities *Zhunal Neorganicheskoi Khimii* 38 (1993) 44-50.

[40] V. Petkov, S. J. L. Billinge, P. Larson, S. D. Mahanti, T. Vogt, K. K. Rangan, M. G. Kanatzidis, Structure of Nanocrystalline Materials Using Atomic Pair Distribution Function Analysis: Study of $LiMoS_2$ *Physical Review B: Condensed Matter and Materials Physics* 65 (2002) 1-4.

[41] E. J. Markel, J. W. Van Zee, Catalytic Hydrodesulfurization by Molybdenum Nitride *Journal of Catalysis* 126 (1990) 643-657.

[42] Z. Paal, P. Tetenyi, M. Muhler, U. Wild, J.-M. Manoli, C. Potvin, Bulk and Surface Analysis of a Supported Pt-MoO_x-Al_2O_3 Model System in the Fresh and Sulfided State *Journal of the Chemical Society, Faraday Transactions* 94 (1998) 459-466.

[43] Th. Weber, J. C. Muijsers, J. W. Niemantsverdriet, Structure of Amorphous MoS_3 *Journal of Physical Chemistry* 99 (1995) 9194-9200.

[44] J. E. De Vries, H. C. Yao, R. J. Baird, H. S. Gandhi, Characterization of Molybdenum-Platinum Catalysts Supported on γ-Al_2O_3 by X-ray Photoelectron Spectroscopy *Journal of Catalysis* 84 (1983) 8-14.

[45] J. T. Roberts, C. M. Friend, Desulfurization of Ethylene Sulfide on Molybdenum(110). The Roles of Ring Size and Strain in Adsorbate Reaction Selectivity *Surface Science* 202 (1988) 405-432.

[46] J. A. Rodriguez, S. Y. Li, J. Hrbek, H. H. Huang, G.-Q. Xu, Chemical Properties of Zn/S/Mo(110) and Co/S/Mo(110) Surfaces: Reaction with Hydrogen and Formation of Hydrogen Sulfide *Journal of Physical Chemistry* 100 (1996) 14476-14484.

[47] P. Liu, J. A. Rodriguez, J. T. Muckerman, Sulfur Adsorption and Sulfidation of Transition Metal Carbides as Hydrotreating Catalysts *Journal of Molecular Catalysis A: Chemical* 239 (2005) 116-124.

[48] S. P. Kelty, G. Berhault, R. R. Chianelli, The Role of Carbon in Catalytically Stabilized Transition Metal Sulfides *Applied Catalysis A: General* 322 (2007) 9-15.

[49] M. Muhler, Z. Paal, Sulfided Platinum Black by XPS *Surface Science Spectra* 4 (1997) 125-129.

[50] J. Dembowski, L. Marosi, M. Essig, Platinum Sulfide by XPS *Surface Science Spectra* 2 (1993) 104-108.

[51] M.-D. Appay, J.-M. Manoli, C. Potvin, M. Muhler, U. Wild, O. Pozdnyakova, Z. Paal, High-Resolution Electron Microscopic, Spectroscopic, and Catalytic Studies of Intentionally Sulfided Pt/ZrO_2-SO_4 Catalysts *Journal of Catalysis* 222 (2004) 419-428.

[52] B. J. Lindberg, K. Hamrin, G. Johansson, U. Gelius, A. Fahlman, C. Nordling, K. Siegbahn, Molecular Spectroscopy by Means of ESCA. II. Sulfur Compounds. Correlation of Electron Binding Energy with Structure *Physica Scripta* 1 (1970) 286-298.

[53] C. H. Kim, L. T. Thompson, Deactivation of Au/CeO_x Water Gas Shift Catalysts *Journal of Catalysis* 230 (2005) 66-74.

[54] P. Hou, D. Meeker, H. Wise, Kinetic Studies with a Sulfur-Tolerant Water Gas Shift Catalyst *Journal of Catalysis* 80 (1983) 280-285.

CHAPTER 3

Synthesis, Characterization, and Fischer-Tropsch Synthesis Performance Evaluation of Early Transition Metal Carbide and Nitride Materials

3.1. Introduction

The focus of research described in this chapter was to evaluate the performance of carbide and nitride materials of molybdenum, tungsten, vanadium, and niobium for Fischer-Tropsch Synthesis (FTS). FTS performance was assessed via three figures-of-merit: activity, selectivity, and durability. The activity of these materials was probed using reaction rate measurements in a fixed bed reactor under realistic FTS conditions. In an attempt to evaluate the intrinsic activity of the catalytic sites on the surface, the reaction rates were normalized by the material's CO uptake. For a reaction such as FTS where a variety of compounds are produced, selectivity to the desired products is also important. In general, the desired products are long chain hydrocarbons and the undesired products are CH_4 and CO_2. Alcohols and olefins are also desired products as these compounds are precursors for the production of organic chemicals. Selectivities for the carbide and nitride materials included their total product selectivities, hydrocarbon-only selectivities, olefin/paraffin molar ratios, and chain growth probability factors, α (based on the Anderson-Schulz-Flory model [1, 2]).

The durability of these materials was assessed based on time on stream deactivation and regeneration studies as well as surface and bulk characterization. For FTS, catalyst durability is often evaluated based on resistance to coking/carbon

deposition, changes in feed gas composition, sintering, and crystal structure/phase changes due to oxidation or carburization [3, 4]. For example, metallic Fe and Co particles can be converted to the oxide or carbide phases under FTS reaction conditions, thus altering their performance characteristics [3, 4]. Although there have been a number of studies of early transition metal carbides and nitrides for CO hydrogenation [5-12], very few have explored the durability of these materials. Ranhotra et al. reported that the bulk crystal structure of Mo_2C and Mo_2N remained unchanged after exposure to synthesis gas for 24 h at 300°C at atmospheric pressure [8]. However, there was clear evidence of carbon and oxygen accumulation from elemental analysis [8].

The results discussed in this chapter were used as a guide for the mechanistic investigations described in Chapter 4 and the design of carbide/nitride supported metal catalysts described in Chapters 5 and 6.

3.2. Experimental Setup

3.2.1. Catalyst Synthesis and Pretreatment

High surface area carbide and nitride materials were synthesized using a temperature programmed reaction procedure. First, the oxide precursors were sieved to a particle size of 125-250μm. The powder was then supported in a tubular quartz reactor with quartz wool, and placed in a vertical furnace. A diagram of the reactor system was shown in Chapter 2 (Figure 2.1). The synthesis conditions for the Mo, W, V, and Nb carbides and nitrides are outlined in Table 3.1. These parent metals were chosen because they form stable carbide and nitride structures, can be synthesized at temperatures below 1000°C, and can achieve moderately high surface areas. The table includes the metal oxide precursor, precursor weight, synthesis gas and flow rate, as well as the temperature

Table 3.1: Synthesis parameters for carbides and nitrides of Mo, W, V, and Nb.

Catalyst	Precursor	Precursor Amount (g)	Synthesis Gas	Synthesis Gas Flow Rate (mL/min)	T1[3] (°C)	Ramp Time1 (hr:min)	Soak Time1 (hr:min)	T2 (°C)	Ramp Time2 (hr:min)	Soak Time2 (hr:min)	T3 (°C)	Ramp Time3 (hr:min)	Soak Time3 (hr:min)
Mo_2C	AM[1]	1.3	H_2 and 15% CH_4/H_2[2]	400	350	1:10	12:00	590	1:30	2:00			
Mo_2N	AM[1]	1.05	NH_3	400	350	0:33	0:00	450	2:30	0:00	700	2:30	1:00
W_2C	WO_3	1.1	15% CH_4/H_2	250	200	0:17	0:00	650	7:30	5:00			
W_2N	WO_3	1.3	NH_3	360	270	0:20	0:00	560	9:40	0:15			
VC	V_2O_5	0.4	15% CH_4/H_2	800	900	1:28	2:00						
VN	V_2O_5	1.0	NH_3	600	800	12:55	3:00						
NbC	Nb_2O_5	0.4	15% CH_4/H_2	800	900	1:28	2:00						
NbN	Nb_2O_5	1.0	NH_3	600	800	12:55	3:00						

[1] AM represents ammonium paramolybdate, $((NH_4)_6Mo_7O_{24}\cdot 4H_2O)$, containing 81-83% MoO_3.
[2] The 1st step for Mo_2C synthesis is in flowing H_2. The second step is in flowing 15% CH_4/H_2.
[3] The initial temperature for all catalysts was room temperature.

program for each material. These synthesis conditions were developed based on previous research in our group [13-17] and other references [18].

Once the samples were placed inside the furnace, the synthesis gas was passed over the powder at a specified flow rate. The carburization gas consisted of 15% CH_4 with balance H_2 and the nitridation gas was NH_3. The flow rate of the gas was controlled by Omega mass flow controllers and the temperature was controlled by an Omega programmable PID controller. The temperature of the bed was monitored using a K-type thermocouple that was placed in contact with the sample. Upon completion of the temperature program (listed in Table 3.1), the quartz reactor was removed from the furnace and quenched to room temperature, while the synthesis gas remained flowing. The final material was then exposed to a 1% O_2/He mixture flowing at 20 mL/min for 6 h to passivate the surface of the catalyst. This passivation step is required to prevent bulk oxidation of the catalyst upon exposure to air due to the pyrophoric nature of these materials.

Due to this passivation step, the carbide and nitride catalysts were pretreated prior to FTS reaction rate measurements and chemisorption experiments. The catalysts were pretreated at atmospheric pressure in the gas used during synthesis flowing at 200 mL/min for 4 h at the maximum temperature used during synthesis (see Table 3.1). For example, Mo_2C was pretreated at 590°C in 15% CH_4/H_2. These conditions were chosen to remove the oxygen deposited during the passivation step and return the catalyst to its as-synthesized state.

3.2.2. Catalyst Characterization

The bulk crystal structures of the oxide precursors and the fresh and spent carbide and nitride catalysts were characterized using X-ray diffraction (XRD). XRD was performed using a Rigaku miniflex X-ray diffractometer with a Cu-Kα (λ = 1.54nm) radiation source and a Ni filter. A range of $20° < 2\theta < 90°$ was scanned at a rate of 5°/min with a 0.02° step size.

Surface area measurements and CO pulse chemisorptions were carried out in a Micromeritics 2910 AutoChem Chemisorption analyzer. A schematic of the chemisorption analyzer was shown in Chapter 2 (Figure 2.2). For surface area measurements, the catalysts were first pretreated as described above, degassed in flowing He at a temperature slightly higher than the pretreatment temperature to remove any adsorbed H_2, and then cooled to room temperature. The samples were then exposed to a 30% N_2/He mixture and the temperature was reduced to 77K using a liquid nitrogen bath. BET surface areas were calculated from single point N_2 desorption peaks recorded with a thermal conductivity detector (TCD). For the CO pulse chemisorption experiments, the samples were again pretreated. Then, the gas flow was switched to He and the samples were degassed and cooled to room temperature. The samples were then repeatedly dosed with pulses containing 5% CO/He until complete saturation was achieved. Saturation was achieved when the CO peak areas recorded with the TCD were no longer changing (areas were within 1%). CO uptakes were determined from peak areas recorded with the TCD.

The surface morphologies of the fresh and spent catalysts were characterized using scanning electron microscopy (SEM). SEM images were collected using a Phillips XL30 Field Emission Gun SEM operating at an accelerating voltage of 15-25 kV and a

nominal resolution of 2-5 nm. Prior to analysis, the materials were sputter coated with Pd-Au to mitigate charging effects.

The fresh and spent catalysts were also characterized using X-ray photoelectron spectroscopy (XPS) to determine the compositions and oxidation states of species on the surfaces. The XPS experiments were performed using a Kratos Axis Ultra X-ray photoelectron spectrometer with an Al anode (Kα radiation at 1486.6 eV) operating at 10mA and 14 kV. The spectrometer was equipped with an *in situ* XPS reaction chamber. The spectra were deconvoluted using a nonlinear least squares method employing a combination of Gaussian (80%) and Lorentzian (20%) distributions and CasaXPS, a commercially available XPS analysis program. Parameter constraints were imposed during deconvolution of the Mo spectra. The Mo 3d spectra were fit using doublets with a splitting of 3.2 eV between the $3d_{5/2}$ and $3d_{3/2}$ peaks and an intensity ratio of 3:2. For all spectra, the peak widths (Full Width at Half Max, FWHM) for the doublets were constrained to be similar. Shirley backgrounds were used for the Mo 3d spectra while linear backgrounds were used for the C 1s and O 1s spectra. The peak areas were normalized using the appropriate atomic sensitivity factors. This allowed comparison of the relative atomic fractions of each species on the catalyst surfaces. The adventitious carbon peak (284.8 eV) was used to reference the other binding energies.

Coking experiments were performed using the microbalance on a TA Instruments Q600 Thermogravimetric Analyzer. By monitoring the catalyst weight as a function of temperature, carbon deposition/incorporation was studied by exposing the samples to H_2-CO mixtures with varying concentrations.

3.2.3. Fischer-Tropsch Synthesis Experiments

The FTS rate and selectivity measurements were carried out in a 4.6 mm I.D. stainless steel U-tube fixed bed reactor. The catalyst samples (40-200mg) were supported on a quartz wool plug inside the reactor. Typical reactions conditions were 25 bar, H_2/CO = 2, gas hourly space velocity of 9600-42,000 h^{-1}, and two temperature ranges: 200-250°C and 270-320°C. The two temperature ranges were selected to cover the typical temperatures used industrially for FTS, allow for adequate control of the temperature, and maintain the reaction under differential conditions. Due to the exothermic nature of FTS, high conversion requires significant heat removal and makes it difficult to operate the reactor isothermally. The amount of sample used was adjusted to maintain CO conversions below 10% (differential conditions). The samples were diluted with low surface area SiO_2 (<1m^2/g, particle size: 125-250 μm) to maintain a constant bed height and volume as well as to prevent channeling, avoid problems with axial dispersion, and minimize temperature gradients in the bed.

The feed gases, H_2, CO, and N_2 (internal standard), were introduced into the reactor using Teledyne Hastings mass flow controllers (rated to a maximum inlet pressure of 500psi). The feed lines to the reactor were heated to 150°C. The pressure of the system was set using a back pressure regulator located downstream of the reactor. All effluent lines were maintained at 200°C to ensure that the reaction products remained in the gas phase. Hydrocarbon products containing up to 10 or 11 carbon atoms should remain in the gas phase at this temperature. For example, the boiling point of decane ($C_{10}H_{22}$) is 174°C. Any products that remained as liquids were condensed out in a trap. After a typical 40 h run, no liquids were observed in the trap. The concentrations of reactants and

products in the effluent gas were analyzed using a Varian 3800 gas chromatograph equipped with two thermal conductivity detectors and a flame ionization detector. The GC sampled the effluent gas every 45 min.

Prior to the reaction rate measurements, the catalysts were pretreated at atmospheric pressure as described at the end of Section 3.2.1. The temperature was then reduced to 150°C and the catalysts were exposed to 100% N_2. The pressure of the system was then increased to the reaction pressure (typically 25 bar). The H_2 flow was then introduced. The temperature was then increased to the reaction temperature and the CO flow was introduced. The catalysts were allowed to stabilize for 8 hours before steady-state rate measurements were recorded. To construct the Arrhenius plots shown in the results section, the rates were recorded at each temperature for 4 h, allowing for 6 samples to be taken by the GC at each temperature. The initial temperature was revisited to evaluate catalyst deactivation with time on stream. An example of the rate data as a function of time on stream for Mo_2C over the temperature range of 200-250°C is shown in Figure 3.1.

The activities and selectivities of the carbide and nitride catalysts for FTS were compared in a number of ways. The product formation rate on a C_1 basis was calculated using Equation 3.1:

$$r = \left(\frac{F_{exit}}{W_{cat}} \right) \sum_i C_i Z_i \qquad (3.1)$$

where F_{exit} is the flow rate of the effluent gas from the reactor, W_{cat} is the weight of catalyst in the reactor, C_i is the molar concentration of component *i* in the effluent stream determined from GC analysis, and Z_i is the carbon number of component *i*. The components are the products of the reaction (hydrocarbons, alcohols, and CO_2). The

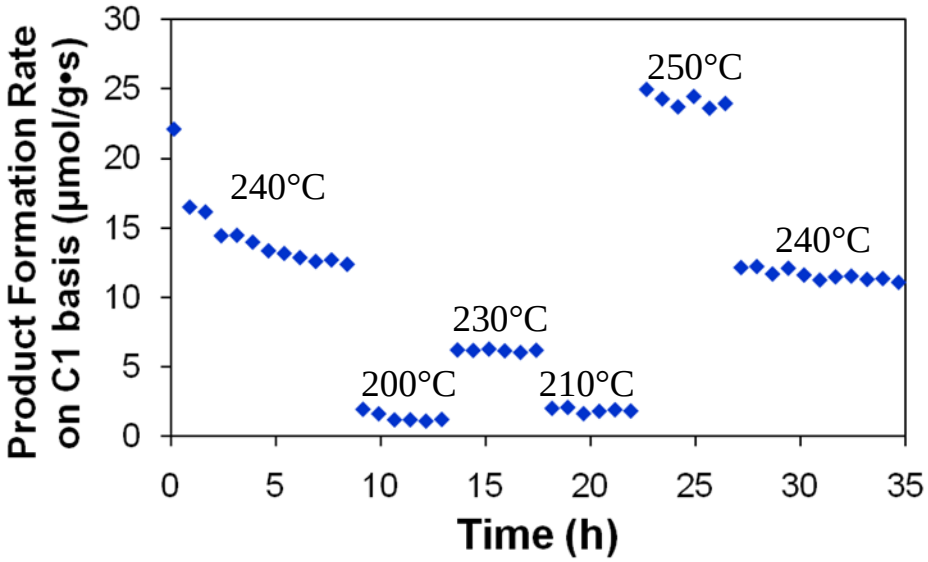

Figure 3.1: Product formation rate on C1 basis as a function of time on stream for Mo_2C under the following reaction conditions: 25 bar, H_2/CO = 2, and 200-250°C.

product formation rate was calculated including and excluding the by-product CO_2. For all experiments, the carbon balance closed within 5%.

The total selectivity (including CO_2) on a C_1 basis was determined using Equation 3.2:

$$S_j = \frac{C_j Z_j}{\sum_i C_i Z_i} \tag{3.2}$$

where S_j is the total selectivity to component(s) j. Component(s) j can be 1 compound such as CH_4 or can be a series of compounds such as C_2-C_4 hydrocarbons, C_5+ hydrocarbons, or alcohols. The hydrocarbon only selectivity was calculated in a similar fashion except the concentrations of CO_2 and alcohols were removed from the denominator. The olefin selectivity was calculated as the molar ratio of olefins to paraffins for a given carbon number as shown in Equation 3.3:

$$R_n = \frac{C_{o,n}}{C_{p,n}} \tag{3.3}$$

where R_n is the molar ratio of olefin to paraffin for carbon number n, $C_{o,n}$ is the molar concentration in the effluent stream of olefin with carbon number n, and $C_{p,n}$ is the molar concentration in the effluent stream of paraffin with carbon number n.

Lastly, based on the Anderson-Schulz-Flory model [1, 2] discussed in Chapter 1, the distribution for hydrocarbons can be described by Equation 3.4:

$$m_n = (1-\alpha)\alpha^{n-1} \tag{3.4}$$

where m_n is the mole fraction of a hydrocarbon with chain length n and α is the chain growth probability factor. By taking the natural log of Equation 3.4, equation 3.5 is formed:

$$\ln m_n = \ln(1-\alpha) + (n-1)\ln\alpha \tag{3.5}$$

By plotting ln m_n vs. n for a given catalyst, α was determined from the slope of the line.

3.3. Results

3.3.1. Catalyst Characterization

X-ray diffraction patterns for the oxide precursors and the as-synthesized carbide and nitride catalysts are shown in Figures 3.2 - 3.5. Peaks related to the oxide precursors were not observed for the carbide and nitride catalysts, suggesting that complete bulk carburization or nitridation of the starting materials was achieved. Except for Mo_2C and W_2C, all of the carbide and nitride catalysts had face centered cubic (FCC) crystal structures. For NbN, the small peaks at 2θ of ~31°, ~46°, and ~62° correspond to the hexagonal phase of NbN that can be formed under similar conditions [19]. The W_2C catalyst had an orthorhombic (distorted hexagonal close packed) structure while the crystalline structure of Mo_2C was consistent with a mixture of α-MoC_{1-x} (FCC) and β-Mo_2C (orthorhombic). This multi-phase Mo_2C material has been produced previously in

our research group [16] and was found to have a surface area twice that of β-Mo_2C [16]. Having said that, modifying synthesis conditions to maximize surface areas of the carbide and nitride materials was not a focus of this research.

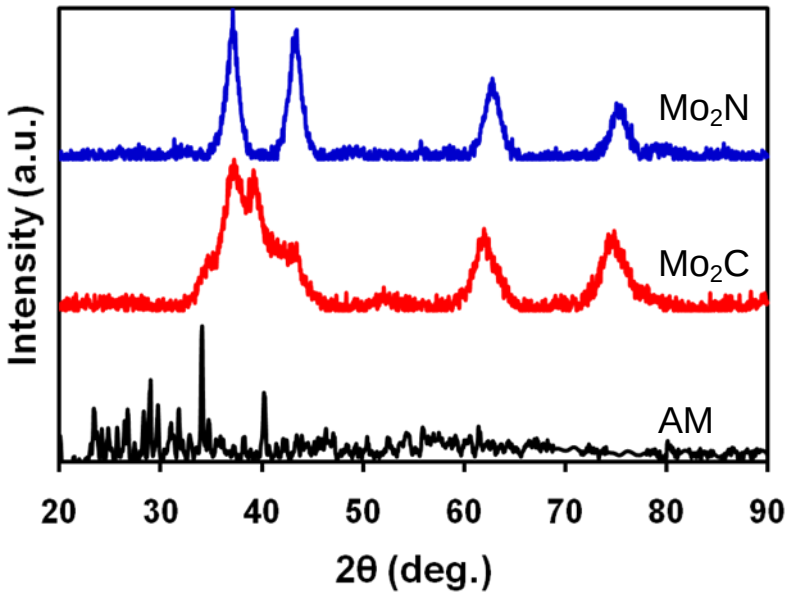

Figure 3.2: X-ray diffraction patterns for ammonium paramolybdate, AM (black), Mo_2C (red), and Mo_2N (blue).

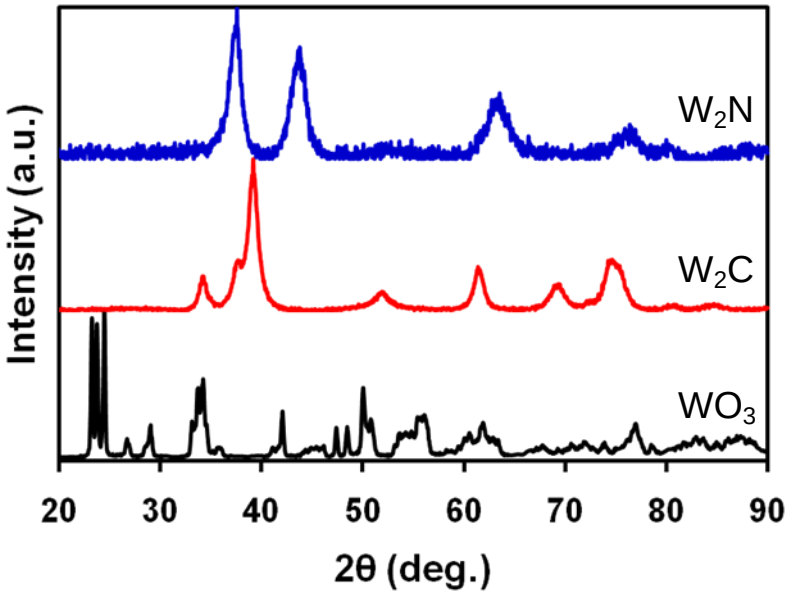

Figure 3.3: X-ray diffraction patterns for WO_3 (black), W_2C (red), and W_2N (blue).

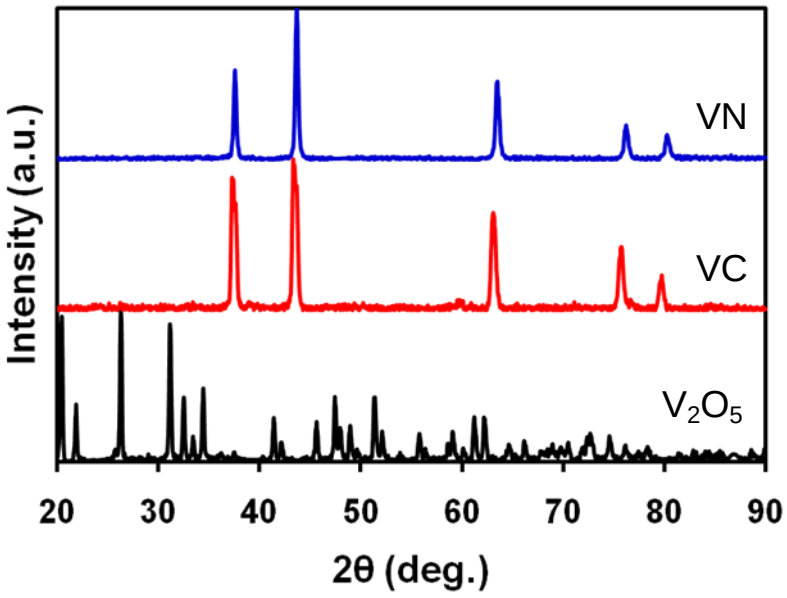

Figure 3.4: X-ray diffraction patterns for V_2O_5 (black), VC (red), and VN (blue).

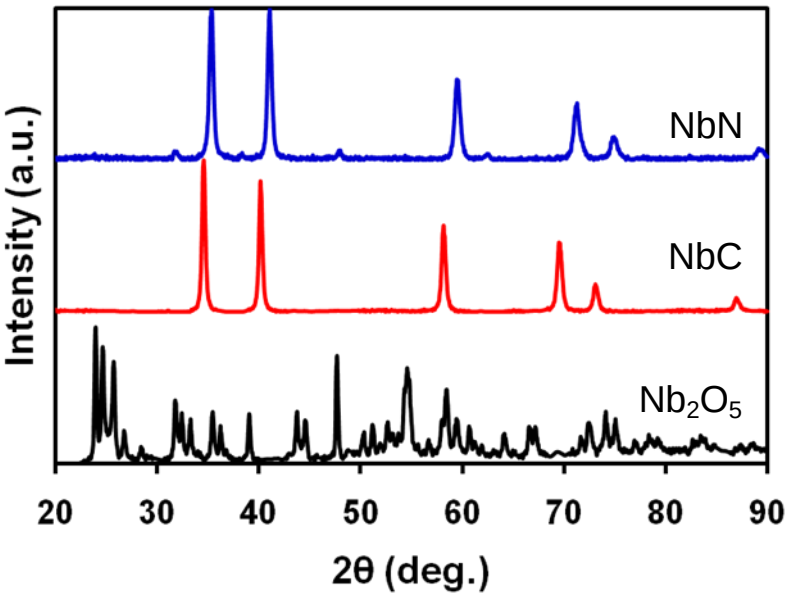

Figure 3.5: X-ray diffraction patterns for Nb_2O_5 (black), NbC (red), and NbN (blue).

The carbide and nitride catalysts were further characterized using BET surface area measurements and CO pulse chemisorption. The results from this analysis are given

in Table 3.2. The carbides and nitrides of Mo and W exhibited the highest CO uptakes and CO site densities. The VN and NbN catalysts exhibited CO site densities 4-5 times lower than those of the Mo and W carbides and nitrides. The CO uptakes for VC and NbC were below the detection limit of the instrument, thus CO site densities could not be calculated.

Table 3.2: Pretreated BET surface areas, CO uptakes, and site densities for the carbide and nitride catalysts.

Catalyst	Pretreated BET Surface Area (m^2/g)	CO Uptake[1] (μmol/g)	CO Site Density[2] (molecules/m^2 x 10^{18})
Mo_2C	106	268	1.52
Mo_2N	154	307	1.20
W_2C	36	74	1.24
W_2N	82	109	0.80
VC	9	<1	--
VN	28	8	0.27
NbC	10	<1	--
NbN	47	11	0.14

[1] CO uptake calculated from CO pulse chemisorptions performed at room temperature.
[2] CO site density calculated from pretreated BET surface area and CO uptake.

3.3.2. Fischer-Tropsch Synthesis Performance

3.3.2.1.Activity

Arrhenius plots of the gravimetric FTS product formation rates for the carbide and nitride catalysts are shown in Figure 3.6. The reaction rates and selectivities were measured at 25 bar and $H_2/CO = 2$. Two separate temperature ranges were tested: 200-250°C and 270-320°C. The two temperature ranges were required to maintain the CO conversions below 10% (differential conditions) and allow for accurate temperature control. The FTS is strongly exothermic, making it difficult to control the catalyst bed temperature at higher CO conversions. For the lower temperature range, only Mo_2C and W_2C exhibited measureable product formation rates. On a gravimetric basis, the most active catalyst was Mo_2C. This result is not surprising as Mo_2C was capable of high CO

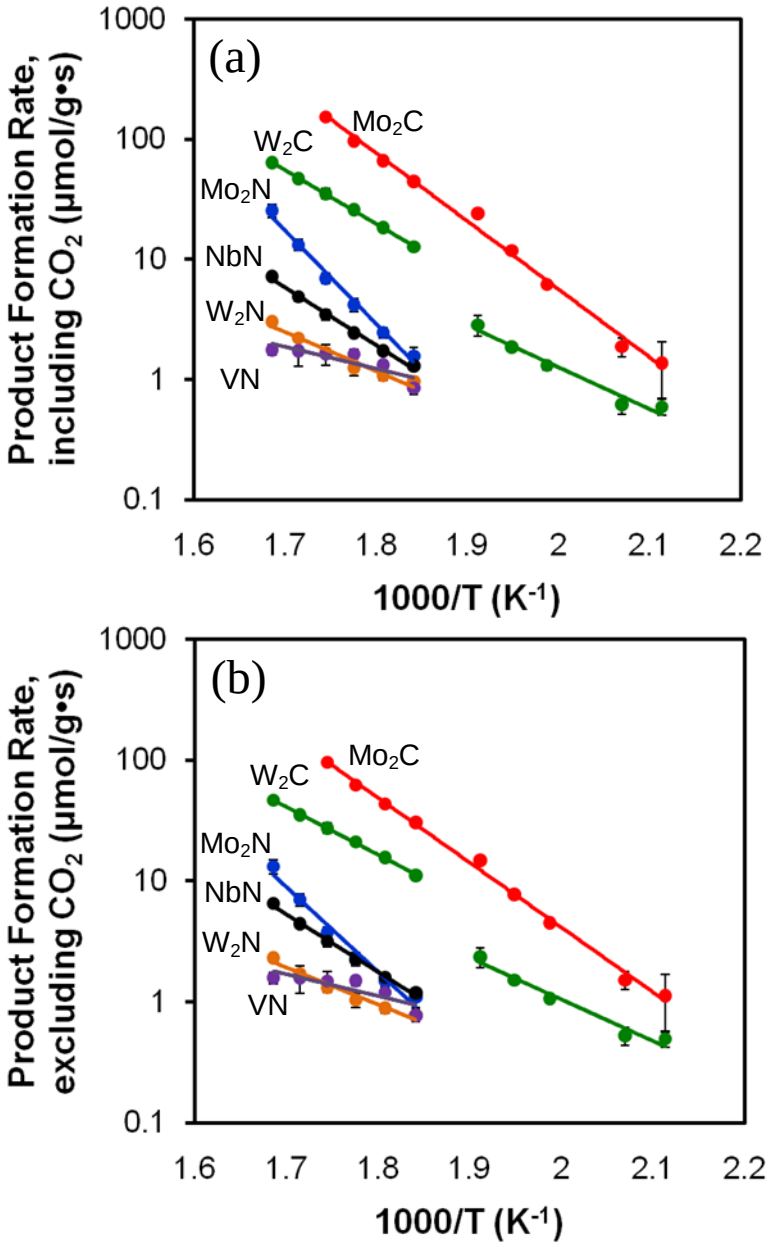

Figure 3.6: Arrhenius plots of the gravimetric product formation rates (a) including CO_2 and (b) exluding CO_2 for the carbide and nitride catalysts. Reaction conditions: 25 bar, H_2/CO = 2, 200-320°C, and GHSV = 9600-42000h^{-1}. Error bars correspond to 95% confidence interval.

uptakes, indicating that there is a high density of sites for CO to adsorb and react. Mo_2C was not tested at temperatures above 300°C as it became very difficult to maintain control of the reaction temperature. The VC and NbC catalysts were the least active

catalysts tested as they did not exhibit any measureable CO conversion under these reaction conditions.

As a measure of the intrinsic activity of the catalysts, the product formation rates were normalized by the CO uptakes (see Figure 3.7). On a normalized basis, Mo_2C, W_2C, VN, and NbN exhibited similar product formation rates. Rates for the Mo_2N and W_2N catalysts were more than an order of magnitude lower. The activity trend for these materials is as follows: Mo_2C ~ W_2C ~ VN ~ NbN > Mo_2N, W_2N >> VC, NbC. Based on these results, there appears to be a significant difference in FTS activity for the carbides and nitrides of the same metal.

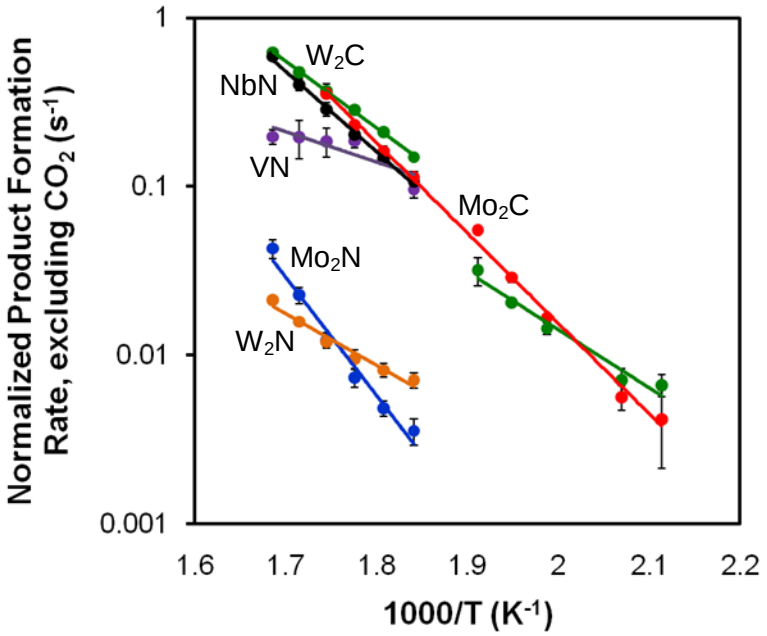

Figure 3.7: Arrhenius plots of the normalized product formation rates exluding CO_2 for the carbide and nitride catalysts. Reaction conditions: 25 bar, H_2/CO = 2, 200-320°C, and GHSV = 9600-42000h^{-1}. Error bars correspond to 95% confidence interval.

Using the normalized rates shown in Figure 3.7, the activity of the carbides and nitrides can be compared to typical Fischer-Tropsch catalysts such as Co. Based on a review by Ribeiro et al., the average CO hydrogenation turnover frequency for a series of supported Co catalysts was 0.017 ± 0.014 s^{-1} at 200°C, 10 atm, and H_2/CO = 2 [20]. At

200°C, the normalized rate for Mo_2C was 0.004 ± 0.002 s^{-1}. Although the rate for Mo_2C was below the average for the Co catalysts, it was within the range reported.

The apparent activation energies ($E_{a,app}$) for the carbide and nitride catalysts are given in Table 3.3. These values were calculated from the slope of the lines in the Arrhenius plots. For the temperature range 270-320°C, Mo_2N exhibited the highest $E_{a,app}$ of 134 kJ/mol, while W_2C and W_2N exhibited the lowest values, 76 kJ/mol and 59 kJ/mol, respectively. Griboval-Constant et al. reported apparent activation energies in the range of 120-170 kJ/mol for Mo_2C depending upon the reaction conditions [21]. For CO hydrogenation over Mo_2C and Mo_2N at atmospheric pressure, Ranhotra et al. reported $E_{a,app}$ values ranging from 60-130 kJ/mol depending upon the product [8]. The $E_{a,app}$ values for Mo_2C and Mo_2N in this study were within these reported ranges.

Table 3.3: FTS apparent activation energies for the carbide and nitride catalysts.

	$E_{a,app}$[1,2] (kJ/mol)	
	Temperature Ranges	
Catalyst	**200-250°C**	**270-320°C**
Mo_2C	107 ± 22	98 ± 19
Mo_2N	--	134 ± 28
W_2C	66 ± 22	76 ± 4
W_2N	--	59 ± 15
VN	--	85[3]
NbN	--	91 ± 7

[1] Calculated from product formation rates excluding CO_2.
[2] Error corresponds to 95% confidence interval.
[3] $E_{a,app}$ for VN was calculated for rates from 270-290°C. Due to only three points, the 95% confidence interval was large.

As shown in Figure 3.7, the product formation rate over VN does not increase linearly with respect to 1/*T* above a temperature of 290°C. The rate remains fairly constant between 300°C and 320°C. This result could be due to a change in the catalyst's functional ability (deactivation, reaction pathway, kinetics) or diffusion limitations. To check that the FTS reaction over VN was not diffusion limited at temperatures above

290°C, the Weiss-Prater criterion was evaluated [22]. The Weiss-Prater criterion is a dimensionless number that compares the rate of pore diffusion to the rate of reaction and is given by Equation 3.6 [22]:

$$N_{W-P} = \frac{\Re R_p^2}{C_s D_{eff}} \tag{3.6}$$

where $\Re$ is the observed reaction rate, R_p is the radius of the catalyst particle, C_s is the limiting reactant concentration at the catalyst surface (assumed to be the concentration of the limiting reactant in the gas phase), and D_{eff} is the effective diffusivity of the limiting reactant. For the reaction to not be diffusion limited, N_{W-P} should be less than 0.3 [22]. For VN, the maximum particle radius was 125μm (particles were sieved to a size of 125-250μm), the average pore radius was 8 nm, the FTS reaction rate at 320°C was 1.7 μmol/g•s, and the gas phase concentration of CO and H_2 was 0.16 mol/L and 0.32 mol/L, respectively. D_{eff} consists of two resistances in series: Knudsen diffusion (collisions between gas molecules and pore walls are dominant) and bulk diffusion (collisions between gas molecules in the free space are dominant) [22, 23]. D_{eff} was calculated using Equation 3.7:

$$\frac{1}{D_{eff}} = \frac{1}{D_{K,eff}} + \frac{1}{D_{b,eff}} \tag{3.7}$$

where $D_{k,eff}$ is the effective diffusivity for Knudsen diffusion and $D_{b,eff}$ is the effective diffusivity for bulk gas molecule diffusion. The $D_{k,eff}$ values used in the calculation were 1.72 x 10^{-2} cm^2/s and 6.43 x 10^{-2} cm^2/s for CO and H_2, respectively. The $D_{b,eff}$ values were 5.03 x 10^{-2} cm^2/s and 1.65 x 10^{-1} cm^2/s for CO and H_2, respectively. Assuming either CO or H_2 as the limiting reactant, N_{W-P} for VN at 320°C was always less than 1 x

10^{-3}, which is much less than 0.3 indicating that the reaction is not diffusion limited under these conditions.

3.3.2.2.Selectivity

The selectivities of the carbide and nitride catalysts are compared at 290°C in Figure 3.8. The gravimetric product formation rates on a C1 basis at 290°C are also given in Table 3.4. At this temperature, the CO conversions for all catalysts were similar, allowing for an equitable comparison as the extent of conversion can affect selectivity [2]. The primary products for the carbide and nitride catalysts were hydrocarbons and CO_2. Only a small percentage of alcohols were produced; however, it should be noted that higher temperatures do not favor alcohol formation. The only alcohols produced were methanol and ethanol, with ethanol being the more favored product at 290°C. VN and NbN exhibited the highest selectivities to hydrocarbons while Mo_2C and Mo_2N exhibited the lowest selectivities to hydrocarbons.

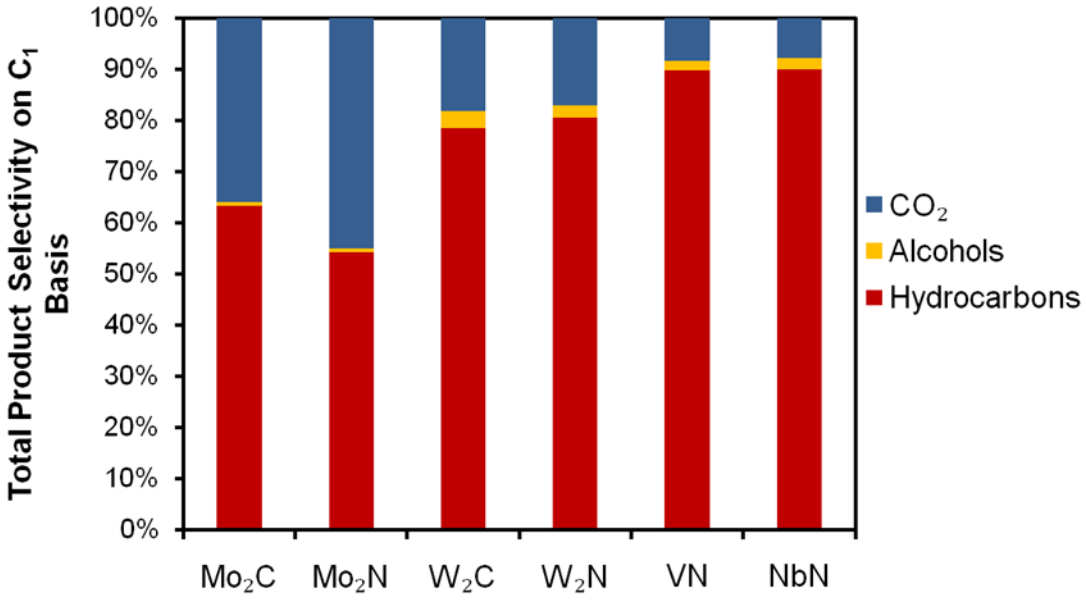

Figure 3.8: Total product selectivity for the carbide and nitride catalysts. Reaction conditions: 290°C, 25 bar, $H_2/CO = 2$.

Table 3.4: Gravimetric product formation rates on a C1 basis for the carbide and nitride catalysts. Reaction conditions: 290°C, 25 bar, $H_2/CO = 2$.

	Product Formation Rate on C1 basis (μmol/g•s)				
Catalyst	**CO_2**	**CH_4**	**C_2-C_4**	**C_5+**	**Alcohols**
Mo_2C	34.9	34.0	25.7	1.63	0.66
Mo_2N	1.89	1.36	0.87	0.07	0.03
W_2C	4.69	10.7	8.60	0.94	0.84
W_2N	0.21	0.65	0.31	0.05	0.03
VN	0.14	0.95	0.47	0.04	0.03
NbN	0.19	1.60	0.56	0.03	0.05

Based on the observed CO_2 production, all catalysts appeared to be active for the water gas shift (WGS) reaction (Equation 3.8):

$$CO + H_2O \leftrightarrow CO_2 + H_2 \tag{3.8}$$

The trend in terms of CO_2 selectivity was as follows: $Mo_2C \sim Mo_2N > W_2C \sim W_2N > VN \sim NbN$. A similar trend for WGS activity was reported by King [16]. The H_2O that participates in WGS was likely produced from the FTS reactions. Assuming that all of the CO_2 produced comes from the WGS, the percentage of the H_2O produced via FTS that is consumed by WGS can be calculated by Equation 3.9:

$$\frac{\text{mols of } CO_2 \text{ produced}}{\text{mols of } H_2O \text{ produced from FTS}} \times 100 \tag{3.9}$$

These percentages are given in Table 3.5. For Mo_2C and Mo_2N, greater than 50% of the H_2O produced via FTS was consumed by WGS. For VN and NbN, this value is approximately 10%.

Table 3.5: Percentage of H_2O produced via FTS that was consumed by WGS. Reaction conditions: 290°C, 25 bar, $H_2/CO = 2$.

Catalyst	**H_2O consumed during WGS (%)**
Mo_2C	56 ± 2
Mo_2N	79 ± 11
W_2C	23 ± 3
W_2N	21 ± 6
VN	11 ± 6
NbN	9 ± 2

The hydrocarbon selectivity is shown in Figure 3.9. In general, the carbide and nitride catalysts favored the production of CH_4 and light hydrocarbons (C_2-C_4). At 290°C, the selectivity to higher hydrocarbons (C_5+) for these catalysts was between 2% and 5%. The olefin selectivity represented as the molar ratio of olefin to paraffin for a given carbon number, R_n, is shown in Figure 3.10. In general, R_n followed the same trend as a function of carbon number for all of the catalysts. The ratios were typically lowest for C_2 and highest for C_3. W_2N exhibited the highest R_n while Mo_2C exhibited the lowest R_n. It is not surprising that Mo_2C favored saturated hydrocarbons as it has been reported to be a good hydrogenation catalyst [24-26].

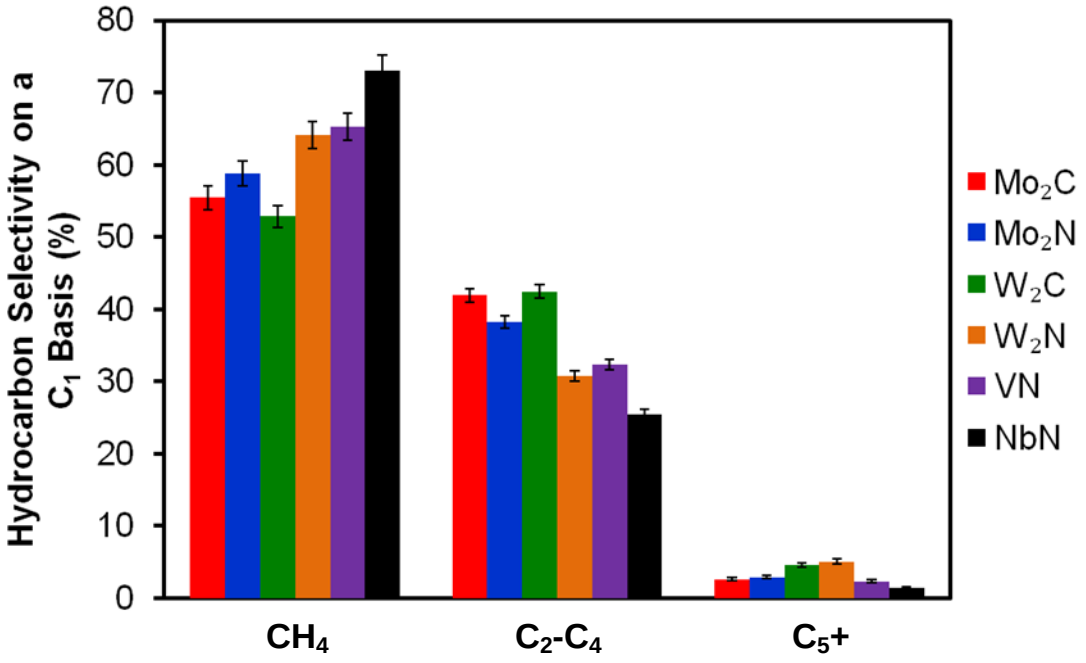

Figure 3.9: Hydrocarbon selectivity for the carbide and nitride catalysts. Reaction conditions: 290°C, 25 bar, $H_2/CO = 2$.

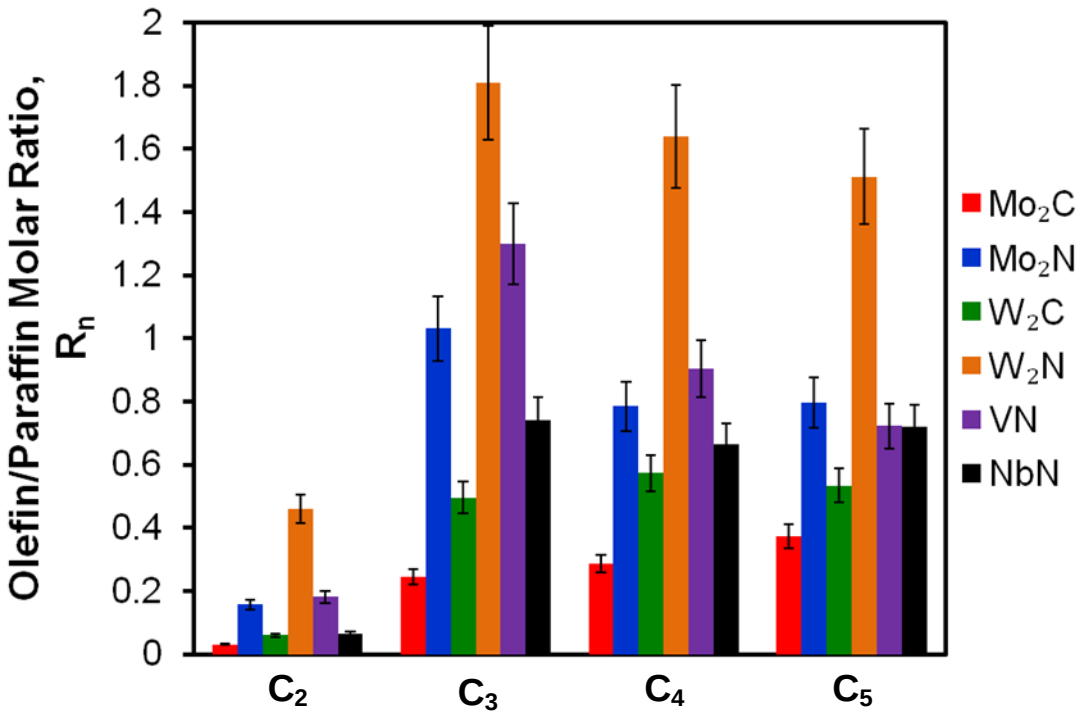

Figure 3.10: Olefin/Paraffin molar ratio for the carbide and nitride catalysts. Reaction conditions: 290°C, 25 bar, $H_2/CO = 2$.

Based on the Anderson-Schulz-Flory (ASF) model [1, 2], the chain growth probability factor, α, was determined for the carbide and nitride catalysts by plotting the natural log of hydrocarbon mole percent vs. carbon number (see Figure 3.11). The results suggest that chain growth for the carbides and nitrides followed the ASF model. The α values are listed in Table 3.6. At 290°C, the highest α (0.43) was observed for W_2N and the lowest α (0.31) was observed for NbN and Mo_2C. The α values for the other catalysts were all within error of each other. A higher α value indicates that there is a higher probability of increasing the chain length.

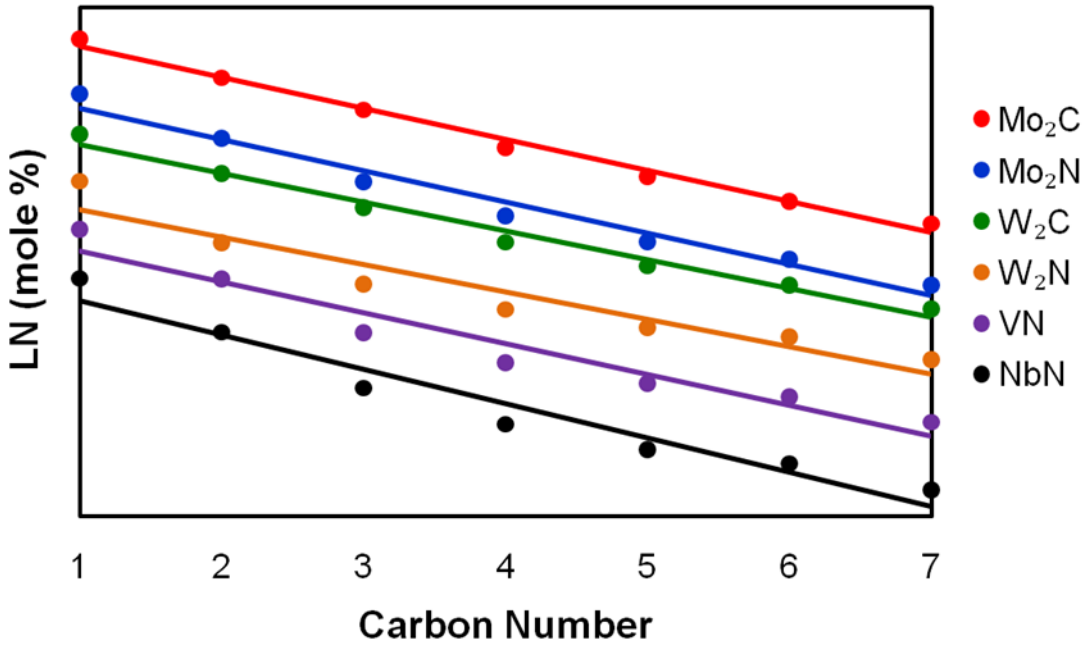

Figure 3.11: Anderson-Schulz-Flory plots of the hydrocarbon distribution for the carbide and nitride catalysts. Reaction conditions: 290°C, 25 bar, H_2/CO = 2.

Table 3.6: ASF α values for carbide and nitride catalysts. Reaction conditions: 290°C, 25 bar, H_2/CO = 2.

Catalyst	ASF α[1]
Mo_2C	0.31 ± 0.02
Mo_2N	0.33 ± 0.03
W_2C	0.35 ± 0.02
W_2N	0.43 ± 0.04
VN	0.35 ± 0.04
NbN	0.31 ± 0.04

[1] Error calculated from linear regression of fits shown in Figure 3.11.

3.3.3. Catalyst Durability

Upon exposure to the synthesis gas mixture, the carbide and nitride catalysts deactivated. This deactivation behavior will be discussed for Mo_2C, but all catalysts showed similar trends. The gravimetric FTS product formation rates including CO_2 for Mo_2C at 240°C are shown in Figure 3.12 as a function of time on stream (TOS).

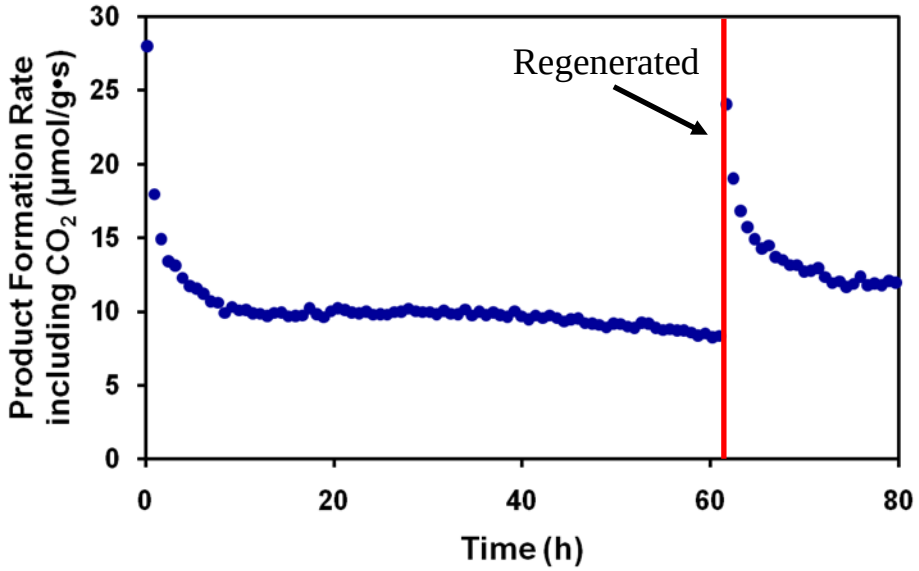

Figure 3.12: Product formation rates including CO_2 for Mo_2C as a function of time on stream. Reaction conditions: 240°C, 25 bar, H_2/CO = 2. Regeneration conditions: 15% CH_4/H_2 at 590°C for 4 h.

In the first 10 h, the reaction rate decreased rapidly, reaching a pseudo steady state rate that was approximately 35% of the initial rate. For the remaining 50 h of the run, the rate decreased more slowly. The catalyst deactivation does not appear to be due to consumption of carbon in Mo_2C. After 10 h TOS, the total amount of carbon contained in the reaction products was ~56,000 µmol. The amount of carbon present in the Mo_2C catalyst loaded into the reactor was ~1000 µmol. After regeneration in 15% CH_4/H_2 at 590°C for 4 h (same as the pretreatment conditions for Mo_2C), the Mo_2C catalyst recovered its lost activity.

The activity of the Mo_2C catalyst, *a(t)*, is plotted as a function of TOS in Figure 3.13. The activity *a(t)* is calculated by Equation 3.10.

$$a(t) = \frac{r(t)}{r_0} \tag{3.10}$$

where *r(t)* is the FTS product formation rate at time *t* after exposure to the feed gas and r_0 is the initial FTS product formation rate. The activity decay for Mo_2C during the first 20

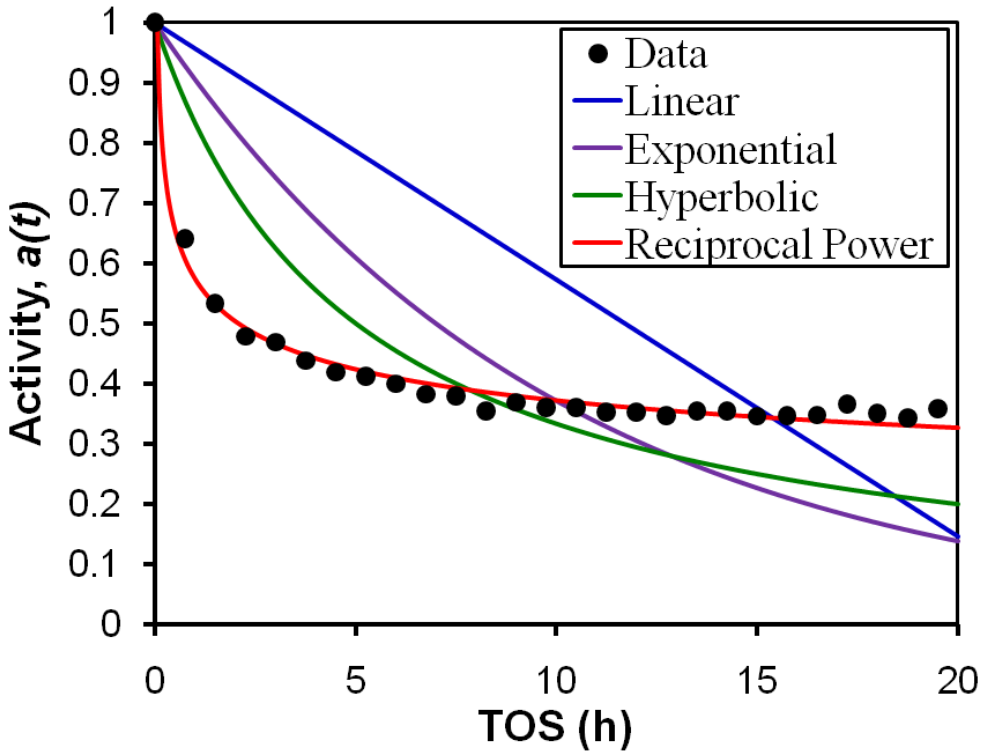

Figure 3.13: Activity *a(t)* for Mo_2C as a function of time on stream. The best-fit activity models are also displayed. Reaction conditions: 240°C, 25 bar, $H_2/CO = 2$.

h TOS was fit using non-linear regression to models of the form shown in Equation 3.11 [27]:

$$-\frac{da}{dt} = k_d a(t)^m \qquad (3.11)$$

where k_d is the specific decay rate constant and *t* is the TOS. As shown in Figure 3.13, the best fit for the Mo_2C catalyst was obtained using the reciprocal power form. This form is consistent with deactivation by carbon deposition [28, 29].

Table 3.7: Results from nonlinear regression of activity data for Mo_2C catalyst to four empirical decay rate laws. Reaction conditions: 240°C, 25 bar, H_2/CO = 2.

Type	Linear	Exponential	Hyperbolic	Reciprocal Power
Differential Form	$-\frac{da}{dt} = k_d$	$-\frac{da}{dt} = k_d a$	$-\frac{da}{dt} = k_d a^2$	$-\frac{da}{dt} = k_d A_0^{1/5} a^m$
Integral Form	$a = 1 - k_d t$	$a = e^{-k_d t}$	$a = \frac{1}{1 + k_d t}$	$a = A_0 t^{-k_d}$
k_d (h^{-1})	0.046 ± 0.004	0.10 ± 0.01	0.20 ± 0.02	0.187 ± 0.009
A_0	--	--	--	0.57 ± 0.01
R_{adj}^2	0.654	0.831	0.924	0.998

As process conditions can have a significant effect on catalyst deactivation, the activity decay of Mo_2C at 240°C was investigated for various H_2/CO ratios (see Figure 3.14). For all H_2/CO ratios tested, the deactivation trends were similar. This observed stability under varying H_2/CO ratios may be due to the intrinsic water gas shift activity of the Mo_2C catalyst. It should also be noted that the FTS product formation rates for the

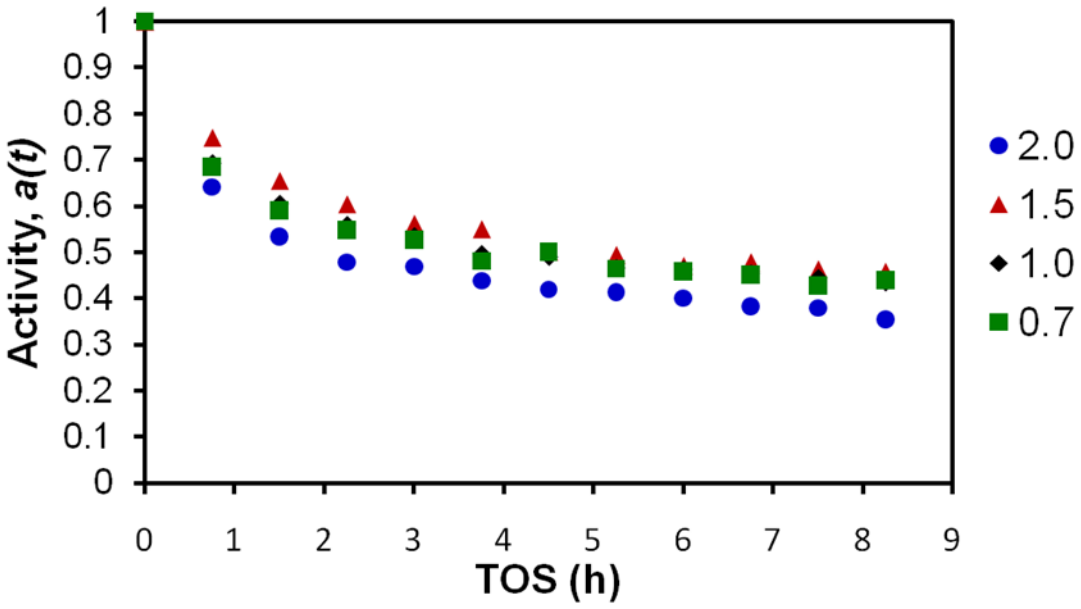

Figure 3.14: Activity *a(t)* for Mo_2C as a function of time on stream for H_2/CO ratios of 2.0, 1.5, 1.0, and 0.7. Reaction conditions: 240°C and 25 bar.

Mo_2C catalyst were different for the different H_2/CO ratios. The variation in catalyst activity with varying process parameters will be discussed in Chapter 4.

The product selectivity also changed as a function of TOS. Figures 3.15 and 3.16 show the total product selectivity and the olefin/paraffin molar ratio for Mo_2C as a function of TOS. The selectivity towards CH_4 increased over time while the selectivity towards C_2+ hydrocarbons decreased. This result suggests that changes to the catalyst surface over time reduced its ability to perform C-C coupling. Additionally, the

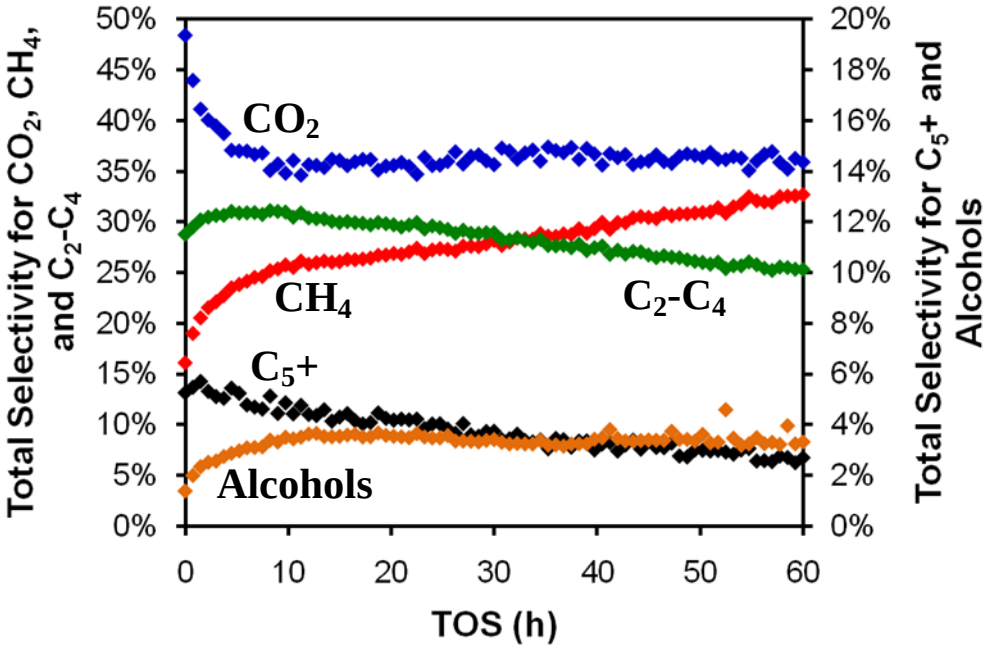

Figure 3.15: Total product selectivity for Mo_2C as a function of time on stream. Reaction conditions: 240°C, 25 bar, $H_2/CO = 2$.

selectivity towards alcohols increased slightly. This result may be due to an increase in the oxygen concentration on the Mo_2C surface. The CO_2 selectivity decreased during the first 10 h TOS, but then remained fairly constant. The R_n also changed significantly as a function of TOS. In general, R_n increased during the first 10 h TOS, and then decreased

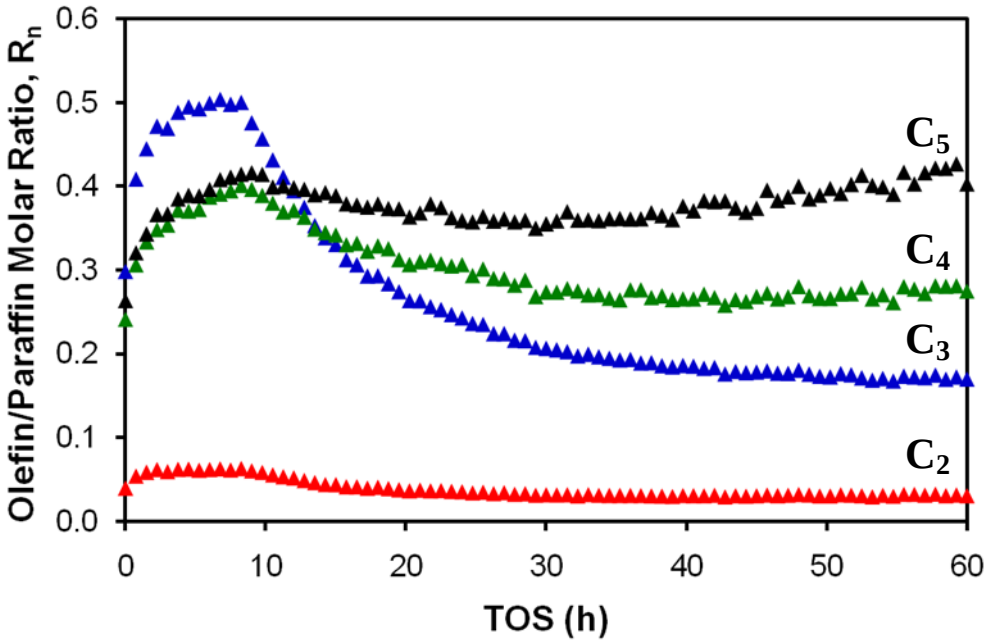

Figure 3.16: Olefin/Paraffin molar ratio for Mo_2C as a function of time on stream. Reaction conditions: 240°C, 25 bar, $H_2/CO = 2$.

steadily. A TOS of 10 h was also when the Mo_2C activity stabilized (Figure 3.13). The other carbide and nitride catalysts showed similar behavior.

To further assess durability, the catalysts were characterized using X-ray diffraction (XRD), X-ray photoelectron spectroscopy (XPS), and scanning electron microscopy (SEM). Figures 3.17 and 3.18 show the diffraction patterns of the spent carbide and nitride catalysts, respectively. The spent catalysts had been exposed to FTS reaction conditions (270-320°C, 25 bar, $H_2/CO = 2$), purged with an inert gas at 270°C, cooled to room temperature in the inert gas, and then passivated with a 1% O_2/He mixture for 6 h. For all of the carbides and nitrides, the diffraction patterns for the spent catalysts resembled those of the fresh catalysts (Figures 3.2-3.5). The additional peaks in the patterns correspond to the SiO_2 used as a diluent for the FTS experiments. These results suggest that the bulk crystal structures of the carbides and nitrides were stable under FTS reaction conditions.

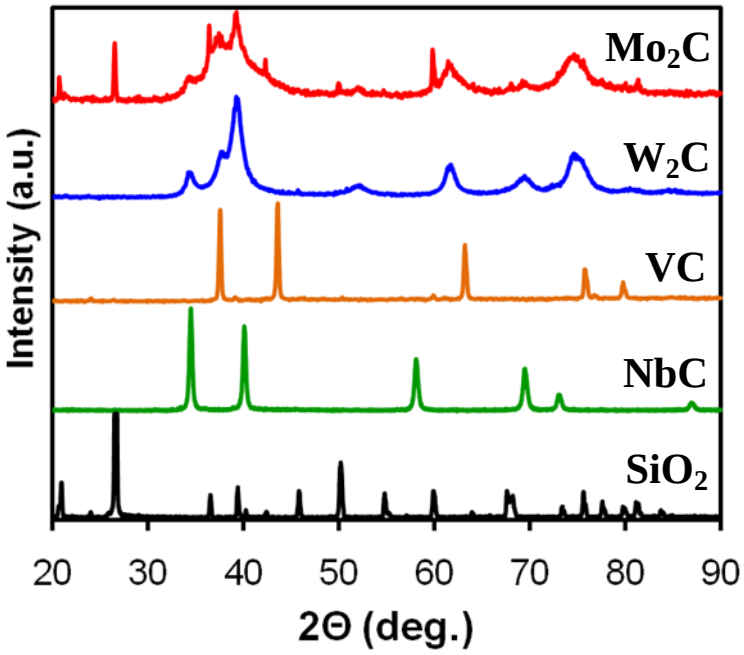

Figure 3.17: XRD patterns of the spent carbide catalysts as well as the SiO_2 diluent.

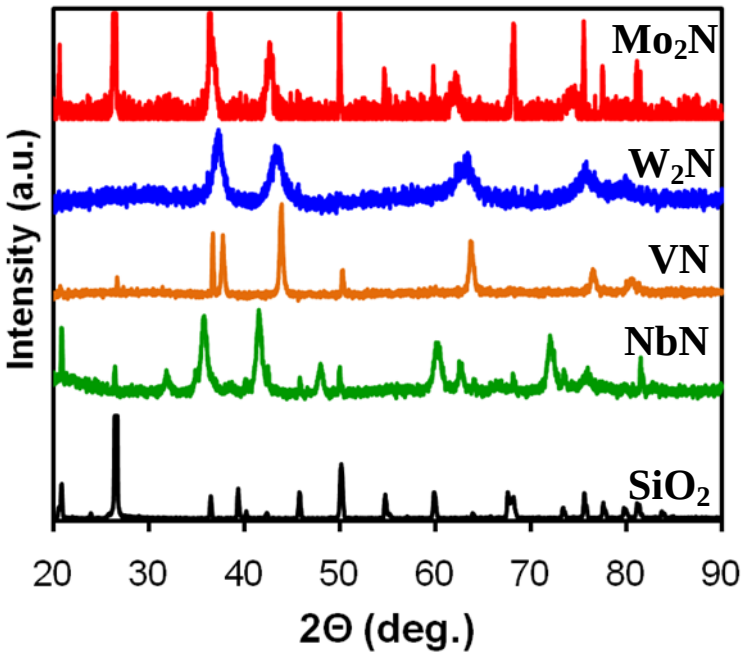

Figure 3.18: XRD patterns of the spent nitride catalysts as well as the SiO_2 diluent.

The FTS reaction conditions are carburizing, and it is possible that nitride materials were converted to carbides. Based on the diffraction patterns, there was no evidence of conversion of the bulk nitride structures to carbide; however it would be

difficult to see this conversion via XRD. XPS was used to determine if the nitride surfaces were converted to carbide surfaces under reaction conditions. Figure 3.19 shows the C 1s XPS spectra for the spent nitride catalysts. The peaks at approximately 284.8 eV correspond to adventitious carbon, carbon typically present in the form of hydrocarbons [30]. Carbidic carbon (carbon present in the carbide structure) peaks are typically located at 283.0 ± 0.5 eV [31]. As shown in Figure 3.19, the spent nitride catalysts did not exhibit carbide peaks, suggesting that the nitride surfaces were not carburized under FTS reaction conditions.

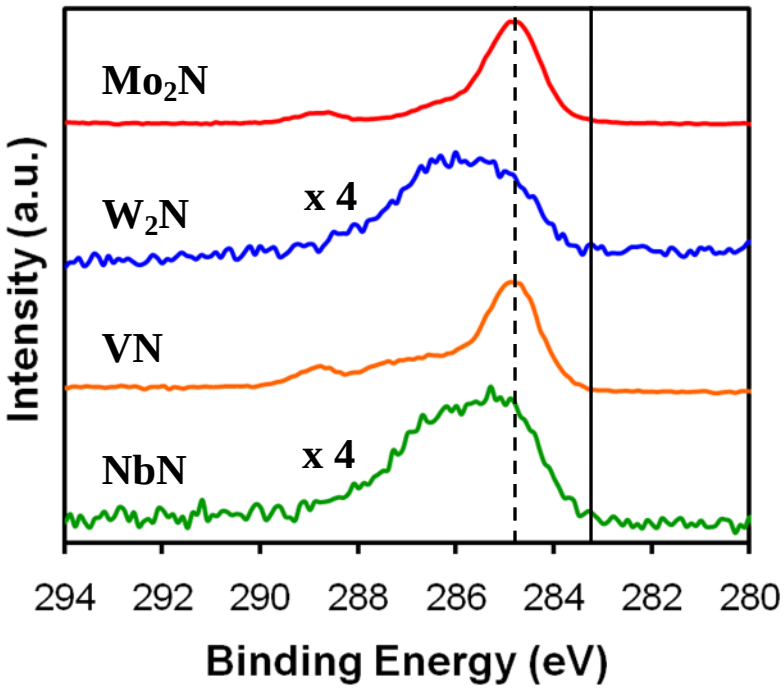

Figure 3.19: C 1s XPS spectra of the spent nitride catalysts. Dashed line indicates peak position for adventitious carbon. Solid line indicates peak position for carbidic carbon.

SEM micrographs of the fresh and spent Mo_2C surfaces are shown in Figure 3.20. The micrographs of the spent catalysts show the formation of layers with wax-like appearance on the Mo_2C surface. These layers likely covered active sites on the catalyst surface, resulting in deactivation. These layers were not formed by product condensation

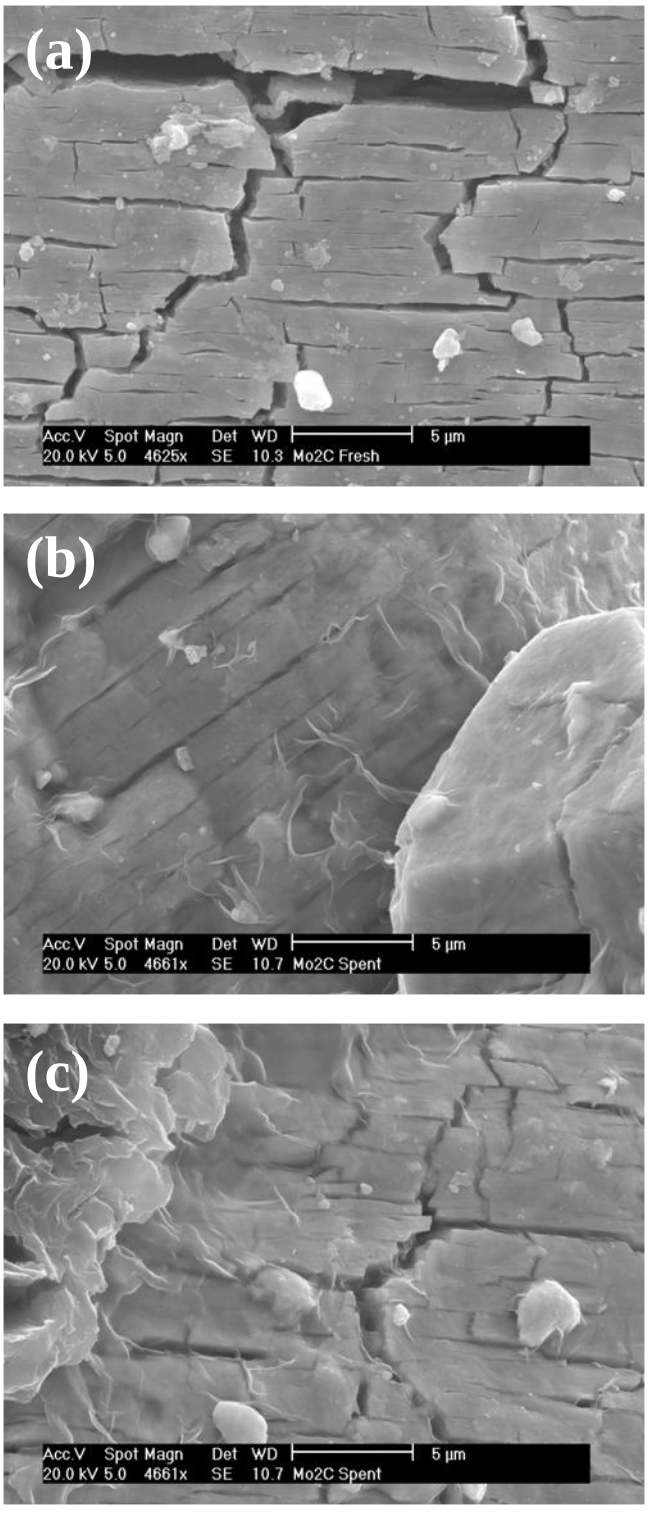

Figure 3.20: SEM micrographs of (a) the fresh Mo_2C catalyst and (b-c) the spent Mo_2C catalyst after exposure to FTS reaction conditions.

during cooling, as the sample was first purged in inert gas at reaction temperature for 1 h prior to cooling. XPS spectra of the fresh and spent Mo_2C catalyst are shown in Figure 3.21. The spectrum for the fresh Mo_2C catalyst exhibited peaks corresponding to carbidic carbon (283.5 eV) [31], adventitious carbon (284.8 eV) [30], and species containing C-O bonds (286.2 eV) [32, 33] and C=O bonds (288.8 eV) [32, 33]. The spent Mo_2C catalyst

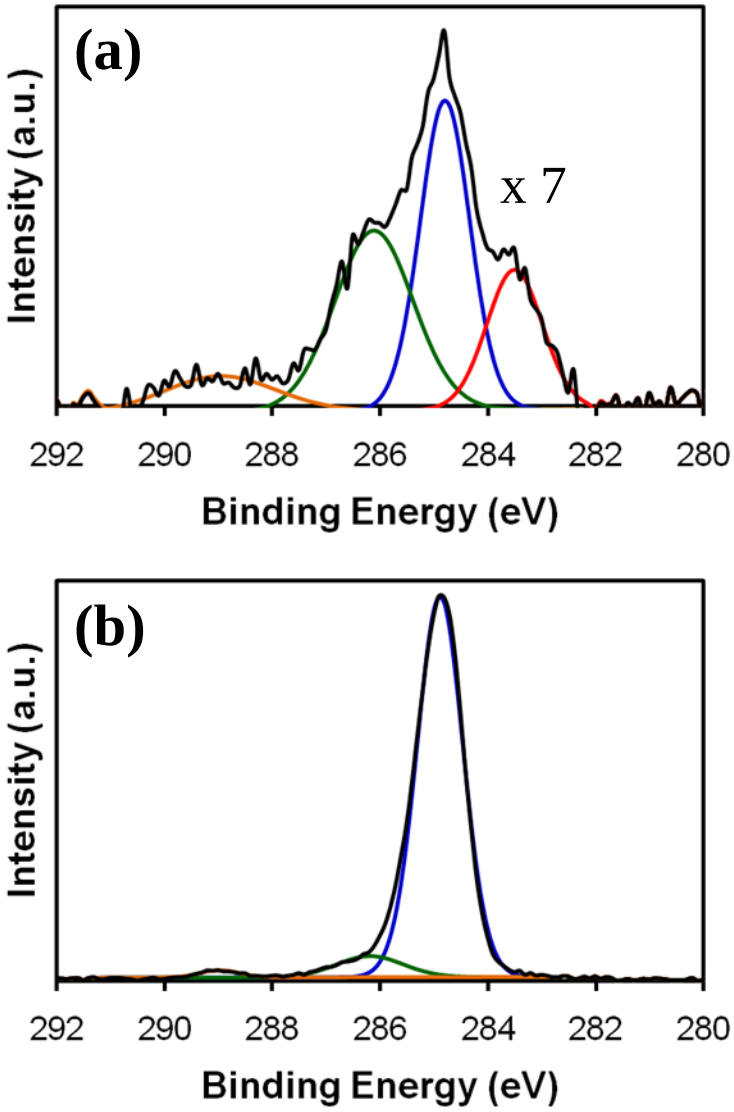

Figure 3.21: C 1s XPS spectra of (a) the fresh Mo_2C catalyst and (b) the spent Mo_2C catalyst after exposure to FTS reaction conditions. The intensity of the C 1s spectrum for the fresh Mo_2C catalyst was multiplied by 7 to put it on the same scale as the spectrum for the spent Mo_2C catalyst.

spectrum exhibited peaks for adventitious carbon and adsorbed carbon oxides (C-O and C=O). The dominant peak in the spent spectrum was for adventitious carbon. The intensity for the spent Mo_2C C 1s spectrum was approximately seven times higher than that for the fresh Mo_2C spectrum. The C/Mo atomic ratios for the fresh and spent Mo_2C catalysts were 1.4 and 84, respectively. Based on these results, carbon, most likely in the form of hydrocarbons, accumulated on the Mo_2C surface under FTS reaction conditions.

To further investigate the basis for deactivation, Mo_2C was first pretreated in 15% CH_4/H_2 at 590°C for 4 h, cooled to 200°C, purged with N_2, then exposed to a 1:1 mixture of H_2 and CO in a thermogravimetric analyzer. The temperature was then linearly increased at 1°C/min to a final temperature of 500°C while recording the weight of the catalyst. The 1:1 mixture of H_2 and CO was chosen because lower H_2/CO ratios are more likely to cause carbon deposition. The weight change as a function of temperature is shown in Figure 3.22. The weight initially decreased until reaching a temperature of approximately 375°C, at which time the weight percent increased rapidly. SEM micrographs of the catalyst following this treatment are shown in Figure 3.23. The SEM micrographs revealed the buildup of carbon deposits that covered the Mo_2C surface (presence of excess carbon was confirmed using energy dispersive x-ray spectroscopy). The extent of deposition was much more severe than that observed previously for the spent Mo_2C catalyst after a FTS experiment (270-320°C, 25 bar, $H_2/CO = 2$, $X_{CO} < 10\%$). These results suggest that the onset temperature for coking over Mo_2C in a 1:1 H_2:CO mixture was approximately 375°C and that coking was not occurring during the FTS experiments.

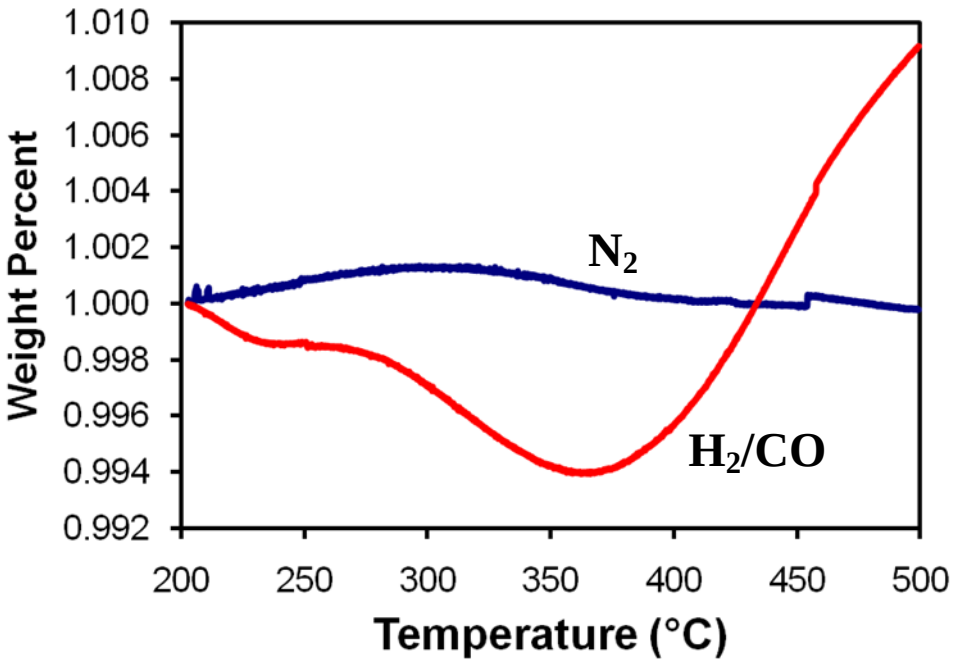

Figure 3.22: Weight change of the Mo_2C catalyst as a function of temperature during exposure to a 1:1 H_2:CO mixture in a thermogravimetric analyzer. The temperature ramp rate was 1°C/min. A blank is also shown in which the catalyst was exposed to N_2 only, instead of the H_2:CO mixture.

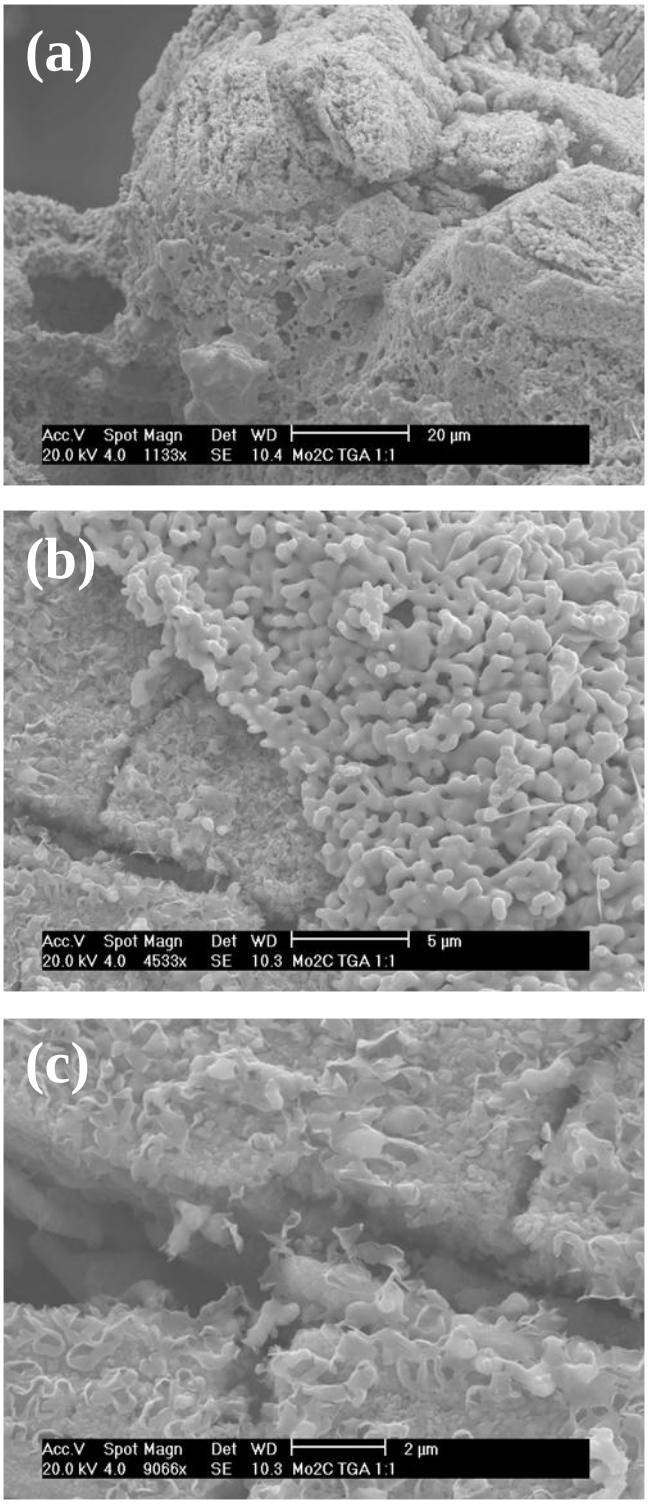

Figure 3.23: SEM micrographs of Mo_2C after exposure to a 1:1 H_2:CO mixture in the thermogravimetric analyzer at a magnification of (a) 1100 (b) 4500, and (c) 9000.

3.4. Discussion

In this chapter, the FTS activities, selectivities, and durabilities of Groups 5 and 6 transition metal carbides and nitrides were investigated. Based on the normalized FTS product formation rates (Figure 3.7), the following activity trend was developed: Mo_2C ~ W_2C ~ VN ~ NbN > Mo_2N, W_2N >> VC, NbC. This trend indicates that carbides and nitrides of the same metal exhibit significantly different FTS rates. For example, the normalized rate for Mo_2C at 300°C was 0.36 s^{-1} while the rate for Mo_2N was only 0.04 s^{-1} although these materials exhibited similar surface areas, CO uptakes, and CO site densities. Additionally, the apparent activation energy was much higher for Mo_2N than Mo_2C (Table 3.3). Performance differences for carbides and nitrides of the same metal have also been reported for other reactions [17, 34].

These differences could be explained in two ways. First, the electronegativity difference between N (3.0) and C (2.5) results in a greater charge transfer from the metal to the non-metal atoms for the nitrides compared to the carbides [35]. This charge transfer affects the bonding of the reactant, intermediates and products to the surface [35]. Second, these observed rate differences could be explained by the difference in the d-band center of the carbide and nitride [36-38]. Based on the model developed by Bjork Hammer and Jens Norskov, the d-band center of a transition metal has been shown to be a good descriptor of the material's reactivity towards adsorbates [39-43]. Liu and Rodriguez reported that the d-band center relative to the Fermi level for Mo in the surface of γ-MoC(001) and δ-MoN(001) was −1.61 and −1.86, respectively [36]. However, it should be mentioned that development of a modified d-band model to more fully explain the reactivity of early transition metal carbides and nitrides has been the focus of recent

work [38]. The observed performance difference between Mo_2C and Mo_2N will be investigated in Chapter 4 by exploring the interactions between the catalyst surface and adsorbates such as CO and H_2.

Additionally, it was observed that Mo_2C, W_2C, VN, and NbN exhibited similar normalized FTS rates, suggesting that the sites on the catalyst surfaces were similar. This finding is different than that reported for butane dehydrogenation, hydrogenolysis, and isomerization, in which Group 6 (Mo, W) transition metal carbides and nitrides were intrinsically more active than those from Group 5 (V, Nb) [17]. The similar rates for Mo_2C, W_2C, VN, and NbN can be explained in context of Sabatier's principle. Sabatier stated that the optimal catalyst would not bind adorbates too strongly such that they poisoned the surface or too weakly such that there is a large activation barrier. This principle is the basis for volcano plots observed in catalysis. A volcano plot for CO hydrogenation as a function of dissociative CO adsorption energy is shown in Figure 3.24 [44]. The dissociative CO adsorption energy for different transition metals is a good descriptor of their CO hydrogenation activity. The most active catalysts (Ru, Co) have intermediate dissociative CO adsorption energies.

As shown in Figure 3.25, the dissociative CO adsorption energy decreases moving from right to left on the periodic table. For metals on the right, CO is bound too weakly and for metals on the left bind CO is bound too strongly. Mo and W are on the left and bind CO too strongly. Since V and Nb are to the left of Mo and W on the periodic table, these metals would also bind CO too strongly. Thus, in order for the carbides and nitrides of these metals to be catalytically active for CO hydrogenation (FTS), they would have to interact less strongly with CO. In order to interact less strongly

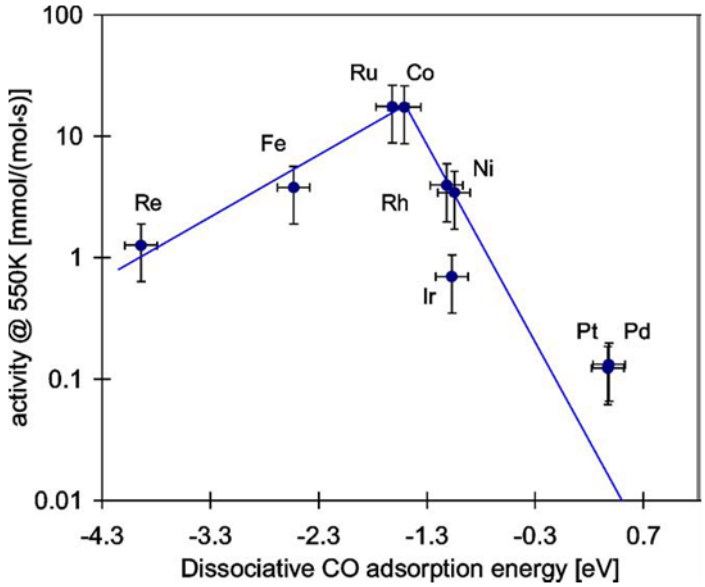

Figure 3.24: CO hydrogenation activities of different supported transition metals as a function of the reaction energy for dissociative CO chemisorption. Taken from [44].

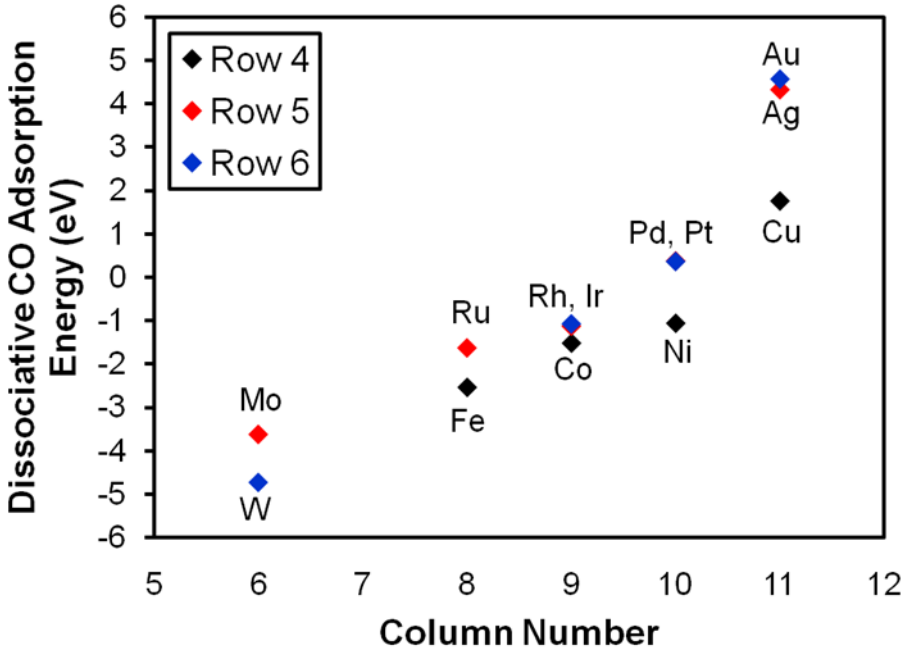

Figure 3.25: Dissociative CO adsorption energy calculated by density functional theory for a series of transition metals plotted as a function of column number in the periodic table. Values taken from [44].

with an adsorbate such as CO, the d-band center of the carbide or nitride would have to be at a lower energy compared to the Fermi level than the parent metal. Liu and

Rodriguez reported that the d-band center for MoC and MoN compared to Mo metal was shifted by −0.30 eV and −0.55 eV, respectively [36]. The nitride resulted in the largest shift to lower energy for the d-band center. If the same trend is assumed for W, V, and Nb, it is plausible that the nitrides of V and Nb and the carbides of Mo and W could have similar d-band centers and similar dissociative CO adsorption energies. An illustration of this concept is shown in Figure 3.26.

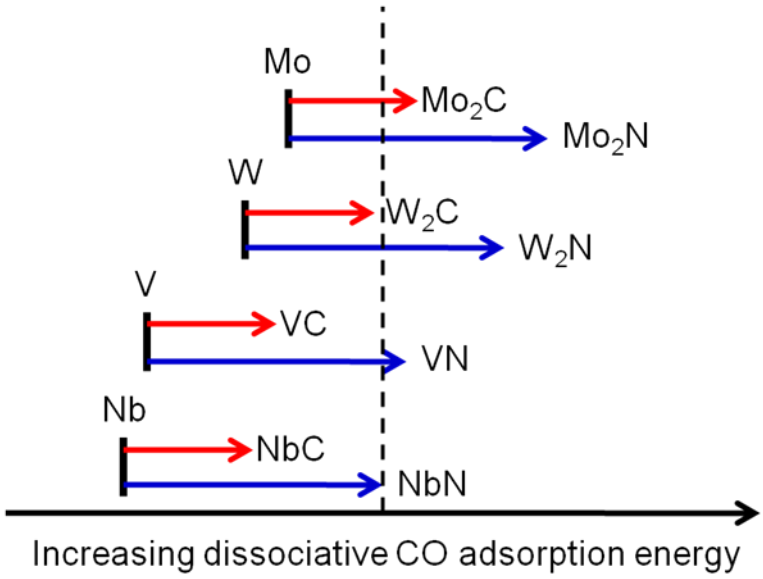

Figure 3.26: Illustration showing shifts in dissociative CO adsorption energy for carbides (red) and nitrides (blue) compared to parent metals for Mo, W, V, and Nb. This illustration is just an example of a concept; exact values have not been determined.

In addition to hydrocarbons, the carbide and nitride materials, especially Mo_2C and Mo_2N, produced CO_2 most likely via the water gas shift reaction (Figure 3.8). In general, the water gas shift reaction is undesirable as it results in the loss of carbon as CO_2 instead of incorporating it into hydrocarbons. However, for situations where the feed gas has a low H_2/CO ratio (0.7 – 1.5), the water gas shift reaction can be beneficial because it shifts the H_2/CO ratio into a more desirable range (~2). For Mo_2C, its observed WGS activity may be a reason that the catalyst deactivation for H_2/CO ratios varying

from 0.7 – 2 was similar (Figure 3.14). Due to WGS, the H_2/CO ratio at the catalyst surface may be higher than that of the bulk gas phase, resulting in a greater resistance to carbon deposition.

Regarding selectivity, all of the carbides and nitrides favored light hydrocarbons, C_1-C_4 (Figure 3.9). At 290°C, the C_1-C_4 hydrocarbon selectivity was greater than 90% for all materials. To compare these materials to commercial catalysts, Fe/SiO_2 and Co/Al_2O_3 catalysts were obtained from industry and tested in the fixed bed FTS reactor. The pretreatment conditions and reaction conditions were selected based off of the supplier's recommendations. At 230°C, 25 bar, H_2/CO = 2, and X_{CO} < 10%, the hydrocarbon selectivity on a C_1 basis to C_5+ hydrocarbons was 37% and 41% for Fe/SiO_2 and Co/Al_2O_3, respectively. Under the same conditions, the C_5+ hydrocarbon selectivity for Mo_2C was ~10%. The ASF α values for these materials were 0.65, 0.66, and 0.43 for Fe/SiO_2, Co/Al_2O_3, and Mo_2C, respectively. These results indicate that C-C coupling occurs much more readily over the Fe and Co based catalysts than it does over Mo_2C. C-C coupling is affected by a number of factors: reaction pathway (FTS mechanism), carbon mobility on the catalyst surface, and CO, H_2 and CH_x coverages under reaction conditions [45-47]. In Chapter 4, the mechanism for C-C coupling over the Mo_2C surface will be investigated.

Overall, the carbides and nitrides favored the production of C_1-C_4 hydrocarbons, exhibited activity for water gas shift, and produced some alcohols. Compared to typical CO hydrogenation catalysts, the selectivities of the carbides and nitrides lie in between that of Ni (favors methane) and Fe (favors long-chain hydrocarbons, but also produces CO_2 and alcohols).

With regards to durability, the bulk crystal structures of the carbides and nitrides were stable under FTS conditions. The carburizing conditions during FTS did not cause the carburization of the bulk or surface of the nitride catalysts. However, the catalysts did exhibit deactivation as a function of time on stream. Based on the deactivation studies and the characterization of the spent catalysts, there appeared to be two stages of deactivation for Mo_2C.

The initial stage, during the first 10 h TOS, resulted in a rapid loss of activity. FTS rates for the Mo_2C catalyst decreased by more than 50% during the first 2 h. Additionally, the selectivity towards alcohols (Figure 3.15) and olefins (Figure 3.16) increased during this initial stage. The best fit rate model for this initial decay was the reciprocal power model, which suggests that this deactivation was due to carbon deposition [28, 29]. Using XPS, Schweitzer observed that the carbon concentration on the Mo_2C surface increased after exposure to water gas shift conditions at 240°C for 4 h (CO, H_2, CO_2, H_2O, N_2) [48]. Additionally, the oxygen concentration on the catalyst surface also increased. During FTS, the Mo_2C surface would be exposed to similar conditions (H_2 and CO are reactants and CO_2 and H_2O are products), thus it is reasonable to assume that the carbon and oxygen concentration on the Mo_2C surface also increased during FTS. Based on these findings, the deactivation was likely caused by the formation of surface oxides or carbonate/formate species. This conclusion is in agreement with the increase in selectivity towards alcohols, as an increase in surface oxygen concentration would likely result in an increase in oxygen-containing products such as alcohols. Once the concentration of oxygen on the catalyst surface stabilizes, the production of alcohols would stabilize, as was observed in Figure 3.15. This result is also in agreement with

literature. For the conversion of synthesis gas, Muramatsu et al. reported that MoO_2 favored the production of alcohols over hydrocarbons [49].

The second deactivation stage resulted in a slow steady loss of activity over long time periods. Based on SEM (Figure 3.20) and XPS (Figure 3.21) results, this second stage was primarily due to the buildup of carbon species on the catalyst surface. These species are likely long-chain hydrocarbon waxes that block the active catalytic sites. This carbon buildup affected C-C coupling, as evidenced by the decrease in C_2+ hydrocarbon selectivity and increase in CH_4 selectivity over time (Figure 3.15). It is proposed that the carbon buildup limited the mobility of carbon and CH_x species on the catalyst surface, thus decreasing C-C coupling. Future work to further probe the effects of this carbon deposition could include post-reaction surface area and CO uptake measurements.

3.5. Summary

The activities, selectivities, and durabilities of carbides and nitrides of Mo, W, V, and Nb were investigated for Fischer-Tropsch Synthesis. On a CO uptake normalized rate basis, the most active catalysts were Mo_2C, W_2C, VN, and NbN. Carbides and nitrides of the same parent metal exhibited significantly different rates, which is likely due to differences in their electronic structures (d-band center) which governs the strength of interactions with adsorbates. These interactions will be explored further in Chapter 4.

All of the carbides and nitrides were active for the water gas shift reaction, indicating that they may be potential catalysts for conversion of CO-rich syngas feed streams. These materials favored the production of light hydrocarbons (C_1-C_4) compared to commercial Fe and Co catalysts. The mechanism for C-C coupling will be explored in Chapter 4. The bulk crystal structures of these materials were stable under reaction

conditions; however, changes to the catalyst surface resulted in deactivation and changes in product selectivity. These changes to the catalyst surface included an increase in oxygen and carbon species initially, as well as the deposition of waxy hydrocarbon species.

3.6. References

[1] R. B. Anderson, *Catalysts for the Fischer-Tropsch Synthesis*, Van Nostrand Reinhold, New York, 1956. Vol. 4.

[2] G. P. Van Der Laan, A. A. C. M. Beenackers, Kinetics and Selectivity of the Fischer-Tropsch Synthesis: A Literature Review, *Catalysis Reviews: Science and Engineering* 41 (1999) 255-318.

[3] D. de Smit, B. M. Weckhuysen, The Renaissance of Iron-Based Fischer-Tropsch Synthesis: On the Multifaceted Catalyst Deactivation Behaviour, *Chemical Society Reviews* 37 (2008) 2758-2781.

[4] A. Y. Khodakov, W. Chu, P. Fongarland, Advances in the Development of Novel Cobalt Fischer-Tropsch Catalysts for Synthesis of Long-Chain Hydrocarbons and Clean Fuels, *Chemical Reviews* 107 (2007) 1692-1744.

[5] I. Kojima, E. Miyazaki, I. Yasumori, Synthesis of Hydrocarbons from CO and H_2 over Metal Carbide Catalysts, *Journal of Chemical Society-Chemical Communications* (1980) 573-574.

[6] I. Kojima, E. Miyazaki, Catalysis by Transition Metal Carbides. V. Kinetic Measurements of Hydrogenation of CO over TaC, TiC, and Mo_2C Catalysts, *Journal of Catalysis* 89 (1984) 168-171.

[7] I. Kojima, E. Miyazaki, Y. Inoue, I. Yasumori, Catalysis by Transition Metal Carbides. VI. Hydrogenation of Carbon Monoxide over WC, W_2C, and W Powder Catalysts, *Bulletin of the Chemical Society of Japan*, 58 (1985) 611-617.

[8] G. S. Ranhotra, A. T. Bell, J. A. Reimer, Catalysis over Molybdenum Carbides and Nitrides. II. Studies of CO Hydrogenation and C_2H_6 Hydrogenolysis, *Journal of Catalysis* 108 (1987) 40-49.

[9] H.-G. Kim, K. H. Lee, J. S. Lee, Carbon Monoxide Hydrogenation over Molybdenum Carbide Catalysts, *Research on Chemical Intermediates* 26 (2000) 427-443.

[10] P. M. Patterson, T. K. Das, B. H. Davis, Carbon Monoxide Hydrogenation over Molybdenum and Tungsten Carbides, *Applied Catalysis A: General* 251 (2003) 449-455.

[11] H. C. Woo, K. Y. Park, Y. G. Kim, I.-S. Nam, J. S. Chung, J. S. Lee, Mixed Alcohol Synthesis from Carbon Monoxide and Dihydrogen over Potassium-Promoted Molybdenum Carbide Catalysts, *Applied Catalysis* 75 (1991) 267-280.

[12] M. Xiang, D. Li, W. Li, B. Zhong, Y. Sun, Performances of Mixed Alcohols Synthesis over Potassium Promoted Molybdenum Carbides, *Fuel* 85 (2006) 2662-2665.

[13] J.G. Choi, R.L. Curl, and L.T. Thompson, *Journal of Catalysis* 146 (1994) 218.

[14] J. J. Patt, Carbide and Nitride Catalysts for the Water Gas Shift Reaction, Ph. D. Thesis, University of Michigan, 2003.

[15] W. Setthapun, Carbide and Nitride Supported Methanol Steam Reforming Catalysts, Ph. D. Thesis, University of Michigan, 2007.

[16] T. E. King, Carbide and Nitride Supported Water-Gas Shift Catalysts, Ph. D. Thesis, University of Michigan, 2007.

[17] M.K. Neylon, S. Choi, H. Kwon, K.E. Curry, and L.T. Thompson, *Applied Catalysis A-General* 183 (1999) 253-263.

[18] J. B. Claridge, A. P. E. York, A. J. Brungs, M. L. H. Green, Study of the Temperature-Programmed Reaction Synthesis of Early Transition Metal Carbide and Nitride Catalyst Materials from Oxide Precursors, *Chemistry of Materials* 12 (2000) 132-142.

[19] H. S. Kim, C. H. Shin, G. Bugli, M. Bureau-Tardy, G. Djega-Mariadassou, Catalytic Activity of Niobium Oxynitride and Carbide I. Preparation, Characterization and Thermal Stability of Finely Divided Niobium Oxynitrides, *Applied Catalysis A: General* 119 (1994) 223-240.

[20] F. H. Ribeiro, A. E. Schach Von Wittenau, C. H. Bartholomew, G. A. Somorjai, Reproducibility of Turnover Rates in Heterogeneous Metal Catalysis: Compilation of Data and Guidelines for Data Analysis, *Catalysis Reviews* 39 (1997) 49-76.

[21] A. Griboval-Constant, J.-M. Giraudon, G. Leclercq, L. Leclercq, Catalytic Behaviour of Cobalt and Ruthenium Supported Molybdenum Carbide Catalysts for FT Reaction, *Applied Catalysis A: General* 260 (2004) 35-45.

[22] M. A. Vannice, *Kinetics of Catalytic Reactions*, Springer, New York, 2005.

[23] C. N. Satterfield, *Herogeneous Catalysis in Industrial Practice*, 2nd ed., McGraw-Hill, Inc., 1991, pg 434.

[24] J. S. Lee, M. H. Yeom, K. Y. Park, I.-S. Nam, J. S. Chung, Y. G. Kim, S. H. Moon, Preparation and Benzene Hydrogenation Activity of Supported Molybdenum Carbide Catalysts, *Journal of Catalysis* 128 (1991) 126-136.

[25] S. T. Oyama, Preparation and Catalytic Properties of Transition Metal Carbides and Nitrides, *Catalysis Today* 15 (1992) 179-200.

[26] T. P. St. Clair, B. Dhandapani, S. T. Oyama, Cumene Hydrogenation Turnover Rates on Mo_2C: CO and O_2 as Probes of the Active Site, *Catalysis Letters* 58 (1999) 169-171.

[27] H.S. Fogler, *Elements of Chemical Reaction Engineering*, 3rd ed., Prentice Hall, New Jersey, 1999.

[28] A. Voorhies Jr., *Ind. Eng. Chem.* 37 (1945) 318.

[29] C.G. Rudershausen, C.C. Watson, *Chem. Eng. Sci.* 3 (1954) 110.

[30] D. J. Miller, M. C. Biesinger, N. S. McIntyre, Interactions of CO_2 and CO at Fractional Atmosphere Pressures with Iron and Iron Oxide Surfaces: One Possible Mechanism for Surface Contamination, *Surface and Interface Analysis* 33 (2002) 299-305.

[31] T.P. St. Clair, S.T. Oyama, D.F. Cox, S. Otani, Y. Ishizawa, R.-L. Lo, K.-I. Fukui, Y. Iwasawa, *Surface Science* 426 (1999) 187.

[32] P. Delporte, F. Meunier, C. Pham-Huu, P. Vennegues, M.J. Ledoux, J. Guille, *Catalysis Today* 23 (1995) 251.

[33] M. Buo, J.M. Martin, T. Le Mogne, L. Vovelle, *Applied Surface Science* 47 (1991) 149.

[34] S. K. Bej, L. T. Thompson, Acetone Condensation over Molybdenum Nitride and Carbide Catalysts, *Applied Catalysis A: General* 264 (2004) 141-150.

[35] A. Zaoui, S. Kacimi, B. Bouhafs, A. Roula, First-Principles Study of Bonding Mechanisms in the Series of Ti, V, Cr, Mo, and their Carbides and Nitrides, *Physica B* 358 (2005) 63-71.

[36] P. Liu, J. A. Rodriguez, Catalytic Properties of Molybdenum Carbide, Nitride, and Phosphide: A Theoretical Study, *Catalysis Letters* 91 (2003) 247-252.

[37] J. R. Kitchin, J. K. Norskov, M. A. Barteau, J. G. Chen, Trends in the Chemical Properties of Early Transition Metal Carbide Surfaces: A Density Functional Study, *Catalysis Today* 105 (2005) 66-73.

[38] A. Vojvodic, A. Hellman, C. Ruberto, B. I. Lundqvist, From Electronic Structure to Catalytic Activity: A Single Descriptor for Adsorption and Reactivity on Transition-Metal Carbides, *Physical Review Letters* 103 (2009) 146103.

[39] J. K. Nørskov, Effective Medium Potentials for Molecule-Surface Interactions: H_2 on Cu and Ni Surfaces. *Journal of Chemical Physics* 90 (1989) 7461-7471.

[40] B. Hammer, J.K. Nørskov, Why Gold is the noblest of all the metals, *Nature* 376 (1995) 238-240.

[41] B. Hammer, J.K. Nørskov, Electronic Factors Determining the Reactivity of Metal Surfaces, *Surface Science* 343 (1995) 211-220.

[42] B. Hammer, Y. Morikawa, J.K. Nørskov. CO Chemisorption at Metal Surfaces and Overlayers, *Physical Review Letters* 76 (1996) 2141-2144.

[43] B. Hammer, Special Sites at Noble and Late Transition Metal Catalysts. *Topics in Catalysis* 37 (2006) 3-16.

[44] T. Bligaard, J. K. Norskov, S. Dahl, J. Matthiesen, C. H. Christensen, J. Sehested, The Bronsted-Evans-Polanyi Relation and the Volcano Curve in Heterogeneous Catalysis *Journal of Catalysis* 224 (2004) 206-217.

[45] Y. Borodko, G. A. Somorjai, Catalytic Hydrogenation of Carbon Oxides-A 10-year Perspective *Applied Catalysis A: General* 186 (1999) 355-362.

[46] J. Chen, Z.-P. Liu, Origin of Selectivity Switch in Fischer-Tropsch Synthesis over Ru and Rh from First-Principles Statitistical Mechanics Studies *Journal of American Chemical Society* 130 (2008) 7929-7937.

[47] J. Cheng, P. Hu, P. Ellis, S. French, G. Kelly, C. M. Lok, Chain Growth Mechanism in Fischer-Tropsch Synthesis: A DFT Study of C-C Coupling over Ru, Fe, Rh, and Fe Surfaces *Journal of Physical Chemistry C* 112 (2008) 6082-6086.

[48] N. M Schweitzer, Evaluating the Effect of a Strong Metal-Support Interaction on the Activity of Molybdenum Carbide Supported Platinum Water-Gas Shift Catalysts, Ph. D. Thesis, University of Michigan, 2010.

[49] A. Muramatsu, T. Tatsumi, H. Tominaga, Active Species of Molybdenum for Alcohol Synthesis from CO-H_2, *Journal of Physical Chemistry* 96 (1992) 1334-1340.

CHAPTER 4

Fischer-Tropsch Synthesis Kinetics and Mechanisms

4.1. Introduction

For a given reaction, catalyst performance is based on a number of factors including the operating conditions (temperature, pressure, feed gas concentrations) and the intrinsic properties of the catalyst. These intrinsic properties of the catalyst (electronic structure and surface structure) govern the interactions between adsorbates and the catalyst surface as well as the reaction pathway or mechanism. The focuses of this chapter are (1) investigate the effect of operating conditions on the Fischer-Tropsch Synthesis (FTS) rates and selectivities of carbide and nitride catalysts, and (2) examine the interactions between the carbide and nitride surfaces and key probe molecules such as CO and H_2, with the goal of explaining the observed FTS rates and selectivities.

Van der Laan and Beenackers have summarized the effects of temperature, pressure, H_2/CO ratio, conversion, and space velocity on FTS selectivities (see Table 1.2) [1]. These relationships were primarily developed for Fe and Co based catalysts, and have not been explicitly explored for other materials such as early transition metal carbides and nitrides. It was shown in Chapter 3 that these materials were active for FTS. To explore these relationships, FTS experiments were carried out over a Mo_2C catalyst at varying pressures, temperatures, and H_2/CO ratios. By varying the H_2/CO ratio, the reaction orders with respect to CO and H_2 were determined for Mo_2C. Additionally, the effect of different pretreatment conditions was investigated.

Recall that carbides and nitrides of the same metal exhibited significantly different normalized FTS rates (Figure 3.9). For Mo_2C and Mo_2N, the normalized rates varied by almost an order of magnitude even though the materials possessed similar surface areas and CO site densities. For FTS, the total reaction involves four principal steps: adsorption of reactants, chain initiation, chain propagation, and chain termination and desorption of products [1-3]. The elementary reactions involved in these four steps are given in Equations 4.1 – 4.12.

Adsorption of Reactants

$$H_2 + 2* \leftrightarrow 2H* \quad (4.1)$$

$$CO + * \leftrightarrow CO* \quad (4.2)$$

$$CO* + * \leftrightarrow C* + O* \quad (4.3)$$

Chain Initiation

$$C* + H* \leftrightarrow CH* + * \quad (4.4)$$

$$CH* + H* \leftrightarrow CH_2* + * \quad (4.5)$$

Chain Propagation

$$R_n* + CH_2* \leftrightarrow R_{n+1}* + * \quad (4.6)$$

Chain Termination and Desorption of Products

$$R_n* + H* \leftrightarrow P_n + 2* \quad (4.7)$$

$$R_n* \leftrightarrow O_n + H* \quad (4.8)$$

$$CH_2* + H* \leftrightarrow CH_3* + * \quad (4.9)$$

$$CH_3* + H* \leftrightarrow CH_4 + 2* \quad (4.10)$$

$$O* + H* \leftrightarrow OH* + * \quad (4.11)$$

$$OH* + H* \leftrightarrow H_2O + 2* \quad (4.12)$$

where * is a reaction site on the catalyst surface, X* is species X adsorbed to the catalyst surface, R_n is an alkyl group with carbon number n, P_n is a paraffin with carbon number n, and O_n is an olefin with carbon number n. In this example, the monomer for chain growth is assumed to be a methlylene ($-CH_2$) group. Mechanisms regarding other monomers for chain growth will be discussed shortly.

It is often reported that adsorption (Equation 4.2) and dissociation (Equation 4.3) of CO as well as hydrogenation of carbon species, Equations 4.4 and 4.5, are the rate-limiting elementary reactions [1-3]. To elucidate the observed difference in FTS rates for Mo_2C and Mo_2N, the influence of each of these elementary reactions (CO adsorption, CO dissociation, and carbon hydrogenation) was investigated using temperature programmed desorption and reaction methods.

The specific FTS mechanism for Mo_2C was also investigated. There are three primary FTS mechanisms reported in literature: the carbide mechanism, the oxygenate (enol) mechanism, and the CO insertion mechanism (Figure 4.1) [1, 4-5]. For the carbide mechanism, CO dissociates on the catalyst surface and is then hydrogenated to form a methlyene group ($-CH_2$). This group serves as the monomer for chain propagation. For the oxygenate mechanism, CO adsorbs molecularly to the catalyst surface and is hydrogenated to form an oxygenate species. These oxygenate species combine via condensation reactions. Chain growth occurs via alternating hydrogenation and condensation steps. The CO insertion mechanism involves the insertion of molecularly adsorbed CO into either a metal-H bond or a metal-alkyl bond. The chain propagates by alternating hydrogenation and CO insertion steps.

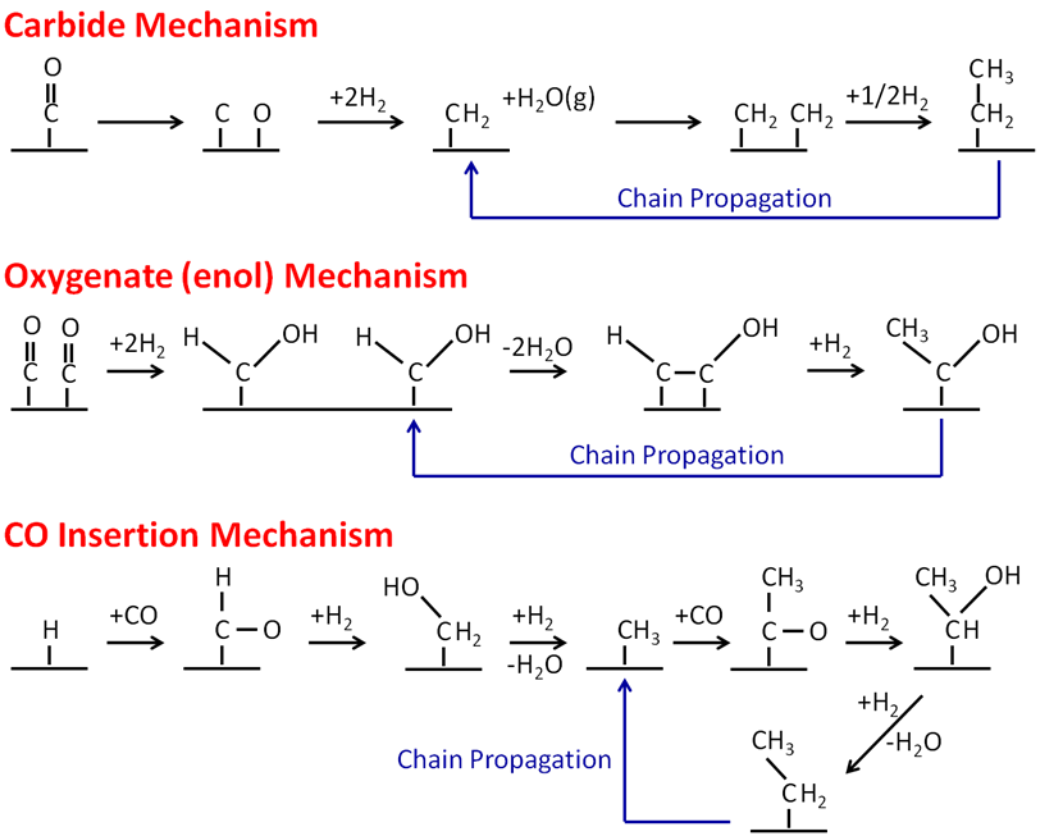

Figure 4.1: Schematic showing the 3 primary Fischer-Tropsch Synthesis mechanisms: the carbide mechanism, the oxygenate mechanism, and the CO insertion mechanism.

As shown in Figure 4.1, the carbide mechanism involves CO dissociation while the oxygenate and CO insertion mechanisms involve molecularly adsorbed CO. To investigate the FTS mechanism over Mo_2C, the effect of dissociatively adsorbed CO vs. molecularly adsorbed CO on the production of higher hydrocarbons was studied.

4.2. Experimental Setup

4.2.1. Fischer-Tropsch Synthesis Experiments

The FTS experiments were performed as described in Chapter 3. The catalyst for these experiments was Mo_2C and unless otherwise stated it was pretreated at 590°C in 15% CH_4/H_2 for 4 h prior to exposure to reaction conditions. The operating conditions varied in this study were temperature (200-250°C), pressure (1-25 bar), and H_2/CO ratio

(0.7-2). The H_2 and CO partial pressures were varied independently to determine the reaction orders for a power rate law. The form of the power rate law is shown in Equation 4.13:

$$-r_{CO} = kP_{CO}^{a}P_{H_2}^{b} \tag{4.13}$$

where r_{CO} is the rate of CO consumption, k is the rate constant, P_{CO} and P_{H_2} are the partial pressures of CO and H_2, respectively, and a and b are the reaction orders with respect to CO and H_2. The partial pressure of H_2 was varied from 5.7 – 16.3 bar. The partial pressure of CO was varied from 4.9 – 13.9 bar.

In addition to operating conditions, the effect of pretreatment conditions on FTS performance was also explored. Three different pretreatment conditions were used: N_2 at 200°C for 4 h, H_2 at 400°C for 4 h, and 15% CH_4/H_2 at 590°C for 4 h. The N_2 pretreatment should simply degas the Mo_2C surface. The H_2 reduction conditions were selected based on pretreatment procedures for Mo_2C reported in literature [6]. The 15% CH_4/H_2 conditions were chosen based on previous research in our group [7, 8].

4.2.2. Temperature Programmed Desorption and Reaction Experiments

Temperature programmed desorption (TPD) and reaction (TPRxn) experiments were carried out in a Micromeritics 2910 AutoChem Chemisorption analyzer. A schematic of the analyzer was shown in Chapter 2 (Figure 2.2). The analyzer was equipped with a thermal conductivity detector and a Balzers Instruments ThermoStar GS300 quadrupole mass spectrometer (MS) for online analysis of the effluent stream from the reactor. Approximately 100 mg of catalyst sample was loaded into a 15 mm I.D. quartz U-tube reactor and supported on a quartz wool plug. The mass of catalyst loaded was varied to achieve the same total number of CO adsorption sites (based on the CO

uptake of the materials given in Table 3.2). Prior to analysis, the Mo_2C catalyst was pretreated in 15% CH_4/H_2 at 590°C for 4 h and the Mo_2N catalyst was pretreated at 700°C in NH_3 for 4 h. These are the same pretreatment conditions used for the FTS experiments performed in Chapter 3. After pretreatment, the temperature was increased by 10°C and the catalyst sample was degassed in flowing He for 0.5 h. The catalysts were then cooled in He and were ready for analysis. It should be noted that all experiments carried out in the chemisorption analyzer were performed at atmospheric pressure. The experimental details for the various temperature programmed desorption and reaction experiments are discussed below.

For CO-H_2 pulse chemisorptions experiments, the catalyst sample was cooled to 240°C in He after pretreatment. The sample was then dosed 10 times with 5mL of a 10% CO/He mixture. The catalysts were allowed to equilibrate for 15 min between doses. Next, the catalyst sample was dosed 10 times with 5mL of a 10% H_2/He mixture. Again, the catalysts were allowed to equilibrate between doses. These two steps were then repeated twice. During these doses, the products in the effluent stream were monitored using the MS.

For the H_2/CO TPRxn experiments, the catalysts were cooled to room temperature in He following pretreatment. Next, the sample was exposed to a flowing mixture of H_2 and CO (H_2/CO = 4). The temperature was then linearly increased at a rate of 10°C/min to 450°C. The effluent stream was monitored using the MS.

The CO TPD experiments were performed by dosing the catalyst sample at room temperature with 5mL of a 5% CO/He mixture until saturation was achieved. Saturation was typically achieved within 4-8 doses. While flowing He, the temperature was then

linearly increased at 30°C/min to 800°C. The effluent stream was monitored using the MS and the TCD.

The CO adsorption energies can be determined from the CO TPD spectra (recorded at m/z = 28) using the heating rate variation method [9, 10]. The Polanyi-Wigner equation describes the rate of desorption of molecules on a catalyst surface, r_{des} (Equation 4.14) [9]:

$$r_{des} = -\frac{d\Theta}{dt} = \nu_n \exp\left(-\frac{\Delta E_{des}^{PW}}{RT}\right)\Theta^n \qquad (4.14)$$

where t is time, Θ is the surface coverage, ν_n is the frequency factor, T is temperature, R is the ideal gas constant, ΔE_{des}^{PW} is the activation energy of desorption, and n is the desorption rate order. Due to microscopic reversibility, this rate equation also describes adsorption, as a reaction must pass through exactly the same states irrespective of whether it proceeds forwards or backwards [9].

The heating rate variation method allows for determination of ΔE_{dex}^{PW} by analyzing TPD spectra obtained with different heating rates, β. β is therefore a constant and is equal to dT/dt. By substituting $dt = (1/\beta)dT$ into equation 4.14, the following equation is derived:

$$\frac{d\Theta}{dT} = -\frac{1}{\beta}\cdot\nu_n \cdot \exp\left(-\frac{\Delta E_{dex}^{PW}}{RT}\right)\cdot\Theta^n \qquad (4.15)$$

For the maximum desorption rate, which occurs at $T = T_{max}$, the following condition must be fulfilled

$$\left.\frac{dr_{des}}{dT}\right|_{T_{\max}} = 0 \qquad (4.16)$$

Therefore,

$$0 = \left.\frac{d^2\Theta}{dT^2}\right|_{T_{max}} = n\cdot\Theta^{n-1}\cdot\frac{d\Theta}{dT} + \Theta^n\cdot\frac{\Delta E_{des}}{RT_{max}^2} \tag{4.17}$$

Inserting Equation 4.15 for $d\Theta/dT$ and solving for $\Delta E_{des}/RT_{max}^2$ provides:

$$\frac{\Delta E_{des}}{RT_{max}^2} = \frac{1}{\beta}\cdot\nu_n\cdot n\cdot\Theta^{n-1}\cdot\exp\left(-\frac{\Delta E_{des}}{RT_{max}}\right) \tag{4.18}$$

Assuming first order desorption (n=1), this equation can be rearranged to produce the following:

$$\ln\frac{T_{max}^2}{\beta} = \frac{\Delta E_{des}}{RT_{max}} + \ln\frac{\Delta E_{des}}{\nu_1 R} \tag{4.19}$$

By plotting $\ln\left(T_{max}^2/\beta\right)$ vs. $1/T_{max}$ for a series of β values, ΔE_{des} can be determined from the slope of the line. This analysis was performed for Mo_2C CO TPD spectra with β values ranging from 4 to 40°C/min.

For Mo_2C, the CO TPD spectra consisted of multiple peaks; therefore the TPD spectra had to be deconvoluted. The deconvolution was performed using CasaXPS, a commercially available peak deconvolution software package that is typically used for analysis of X-ray photoelectron spectroscopy data. The spectra were deconvoluted using a non-linear least squares method employing Gaussian distributions. The primary constraint imposed during fitting was that the relative intensities of the different peaks were held constant for each spectrum.

The importance of dissociative CO adsorption and hydrogenation was investigated using the experimental sequences shown in Figure 4.2. Following pretreatment and degassing, the catalysts were cooled down in Ar to a specified

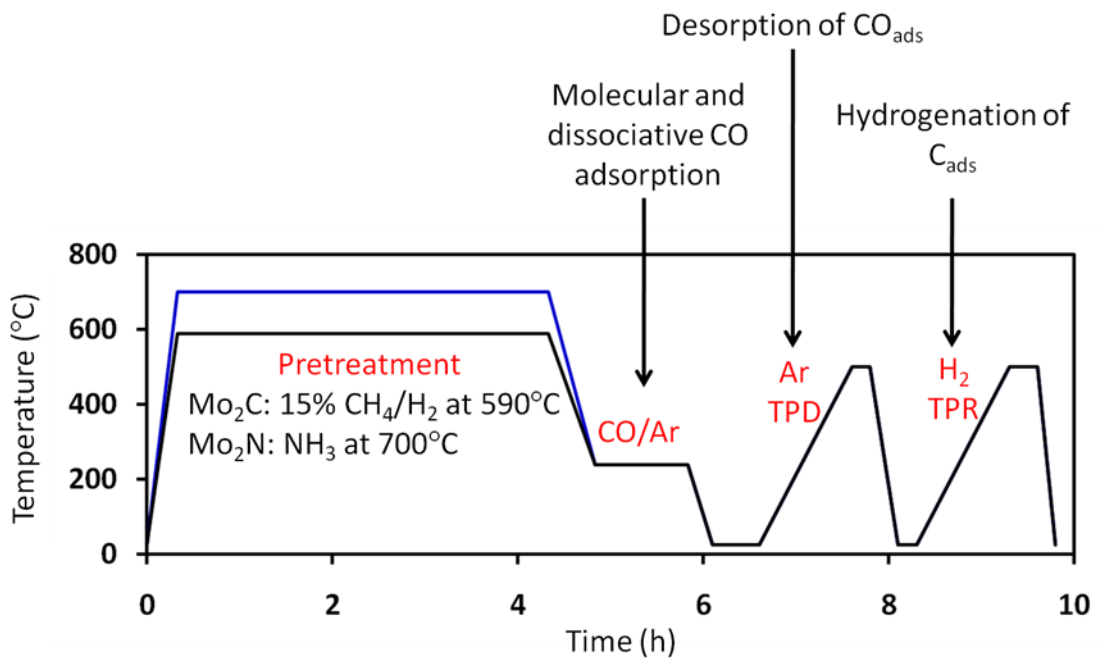

Figure 4.2: Experimental sequence employed to investigate CO dissociation and hydrogenation over Mo_2C and Mo_2N.

temperature. The temperature shown in Figure 4.2 is 240°C. The catalyst was then held at this temperature for 1 h while being exposed to a flowing mixture of 10% CO/Ar. The goal was to associatively and dissociatively adsorb CO to the catalyst surface. Blank runs were also performed in which the catalyst sample was not exposed to CO. The sample was just held at the specified temperature for 1 h in flowing Ar. After 1 h, the catalyst was cooled to room temperature in Ar. A TPD experiment was then performed in Ar with a ramp rate of 20°C/min up to 500°C. Based on the findings of St. Clair et al. [11], the maximum temperature of 500°C was chosen to ensure desorption of all molecular CO and to minimize recombination of carbon and oxygen from dissociated CO. St. Clair reported recombination of C and O over Mo_2C at temperatures above 500°C [11]. The final temperature was held for 10 min prior to cooling the sample back to room temperature. The goal of the TPD experiment was to desorb the associately adsorbed CO, leaving only adsorbed carbon and oxygen from CO dissociation on the catalyst surface.

To explore the impact of molecularly adsorbed CO, experiments were also performed in which the Ar TPD step was not performed. In this case, it is assumed that molecular CO and adsorbed carbon and oxygen remain on the catalyst surface. The sample was then exposed to a mixture of 10% H_2/Ar and the temperature was linearly increased at 20°C/min to a final temperature of 500°C. The goal was to hydrogenate the adsorbed carbon present from CO dissociation. The MS was used to monitor products in the effluent stream during the TPD and H_2 TPRxn steps.

4.3. Results

4.3.1. Fischer-Tropsch Synthesis Experiments

The effect of operating conditions (temperature, pressure, and H_2/CO ratio) on the FTS product formation rates, total product selectivities, CH_4 selectivities, olefin/paraffin molar ratios, and ASF α values were investigated for Mo_2C. The effect of temperature on selectivity is shown in Figures 4.3 and 4.4. Increasing temperature caused a decrease in the olefin, alcohol, and higher hydrocarbon selectivities and an increase in CH_4 and CO_2

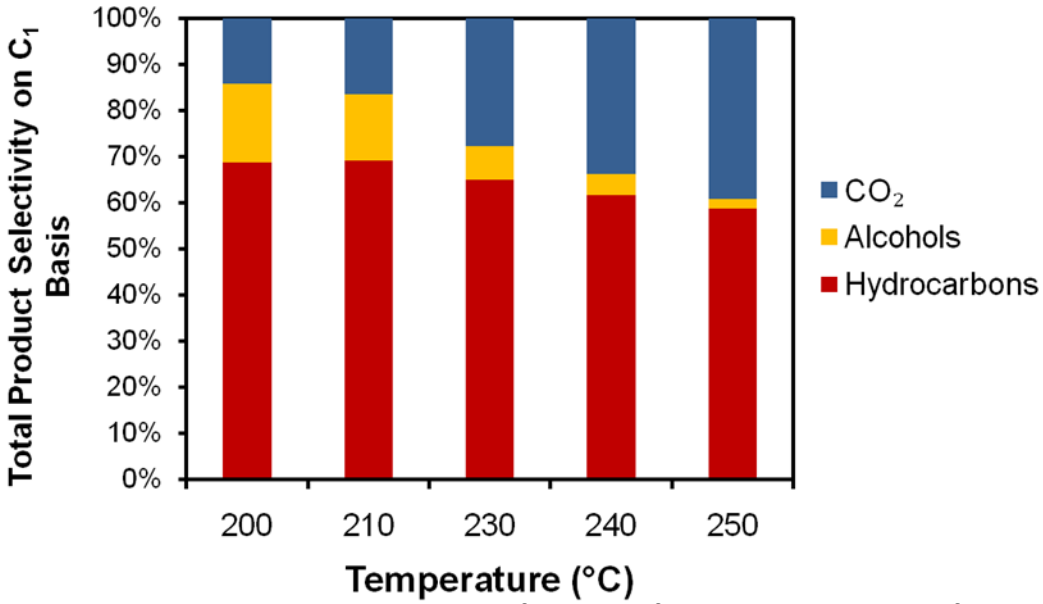

Figure 4.3: Total product selectivity as a function of reaction temperature for Mo_2C. Reaction conditions: 25 bar, H_2/CO = 2.

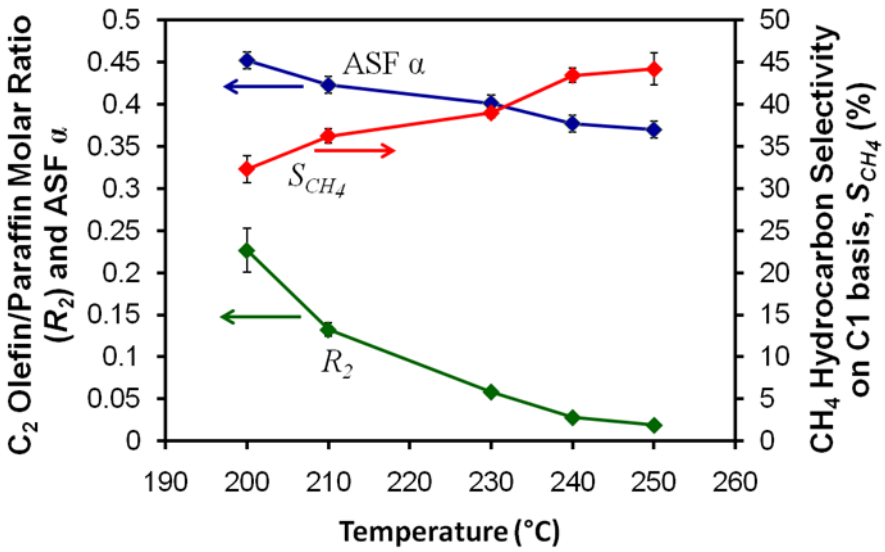

Figure 4.4: C_2 olefin/paraffin molar ratio, ASF α value, and CH_4 hydrocarbon selectivity on C1 basis as a function of reaction temperature for Mo_2C. Reaction conditions: 25 bar, $H_2/CO = 2$.

selectivities. In general, the desired products are the former. The effect of temperature on the rate was described in Chapter 3.

The effect of pressure on the FTS rate and selectivity for Mo_2C is shown in Figures 4.5 – 4.7. The total pressure had the greatest impact on the FTS rates and the

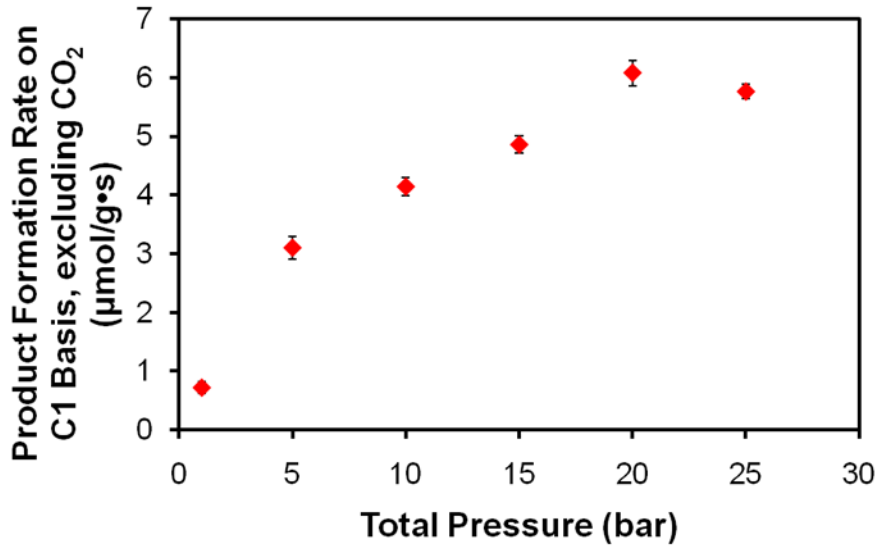

Figure 4.5: FTS product formation rate on C1 basis (excluding CO_2) for Mo_2C as a function of total pressure. Reaction conditions: 240°C, $H_2/CO = 2$.

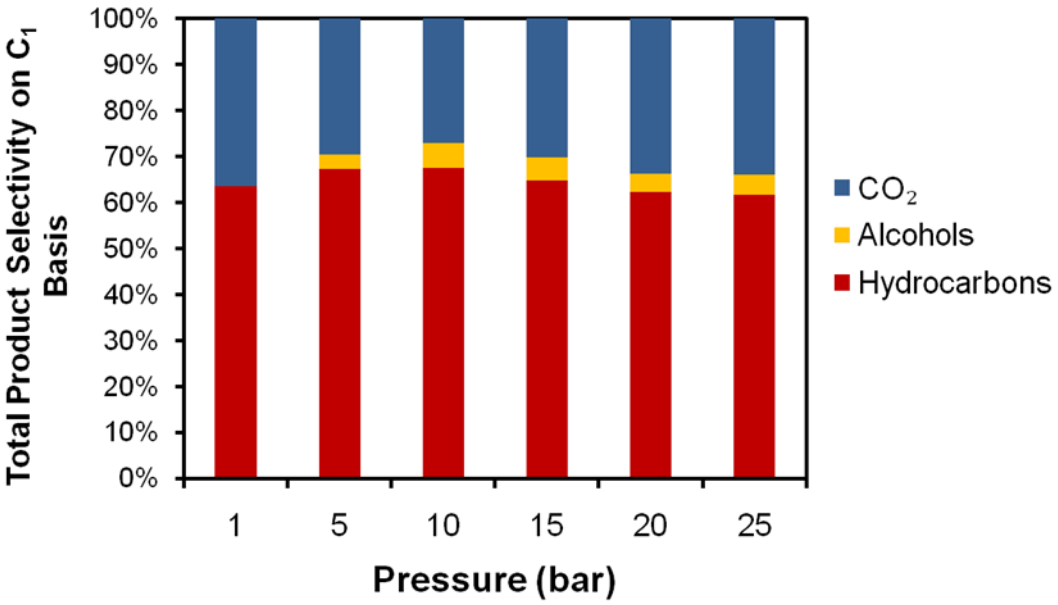

Figure 4.6: Total product selectivity as a function of total pressure for Mo_2C. Reaction conditions: 240°C, $H_2/CO = 2$.

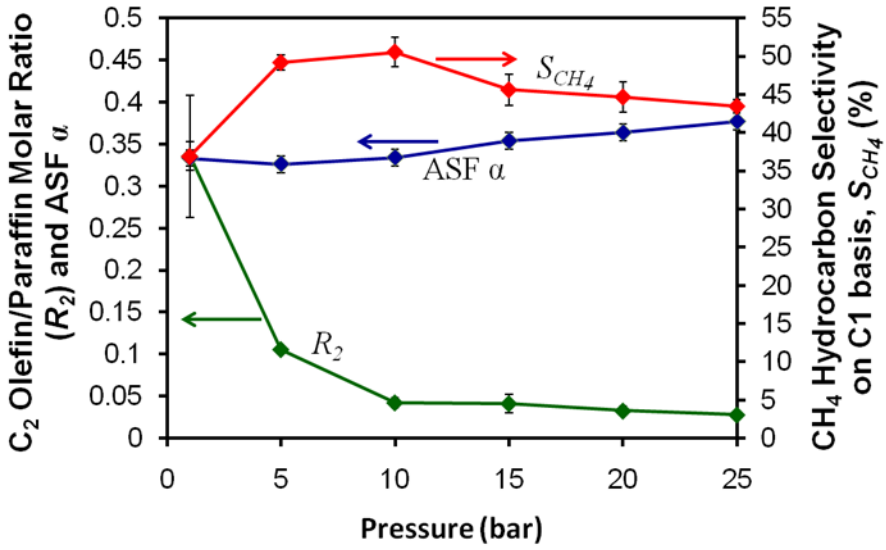

Figure 4.7: C_2 olefin/paraffin molar ratio, ASF α value, and CH_4 hydrocarbon selectivity on C1 basis as a function of total pressure for Mo_2C. Reaction conditions: 240°C, $H_2/CO = 2$.

olefin/paraffin molar ratios. The product formation rates over Mo_2C increased by almost an order of magnitude when the pressure was increased from 1 to 25 bar. Interestingly, the rate increased with total pressure up to 20 bar, but then remained fairly constant. The

olefin/paraffin molar ratios displayed the reverse trend; they decreased by an order of magnitude when the pressure was increased from 1 to 25 bar.

Above 5 bar, the total pressure did not have a significant effect on the total selectivity to hydrocarbons, CO_2, and alcohols. It should be noted that a negligible amount of alcohols was produced at 1 bar. At 5 bar the alcohol selectivity was approximately 3%. The ASF α value increased with increasing pressure, indicating that higher pressures result in higher molecular weight products. Increasing pressure also caused an increase in CH_4 selectivity, but only up to a pressure of 10 bar. Above 10 bar, the CH_4 selectivity decreased. This result suggests a shift in reaction pathway or an increasing probability of chain growth.

The effect of H_2/CO ratio on rate and selectivity is shown in Figures 4.8 – 4.10. The product formation rates increased with increasing H_2/CO ratios. Based on the stoichiometry of the reaction, the ideal H_2/CO ratio for the production of saturated hydrocarbons is approximately 2. The hydrocarbon total selectivity increased slightly

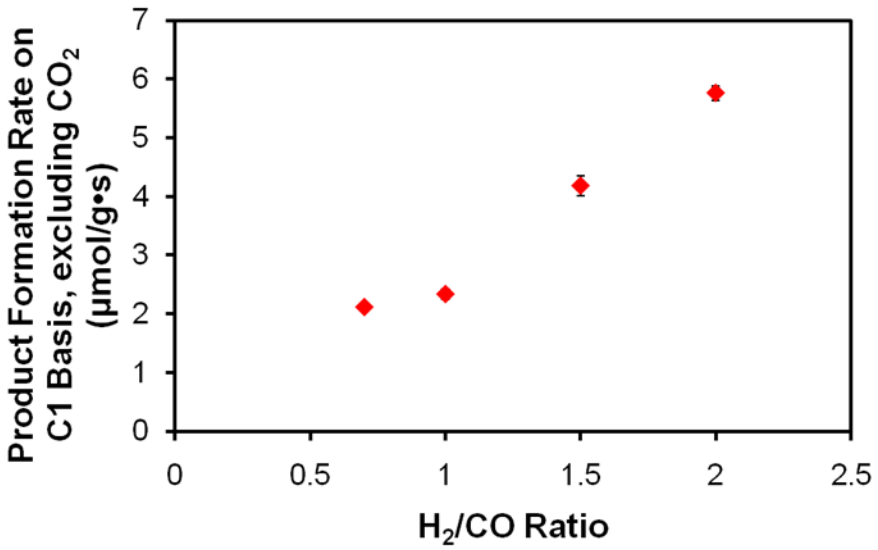

Figure 4.8: FTS product formation rate on C1 basis (excluding CO_2) for Mo_2C as a function of H_2/CO ratio. Reaction conditions: 240°C, 25 bar.

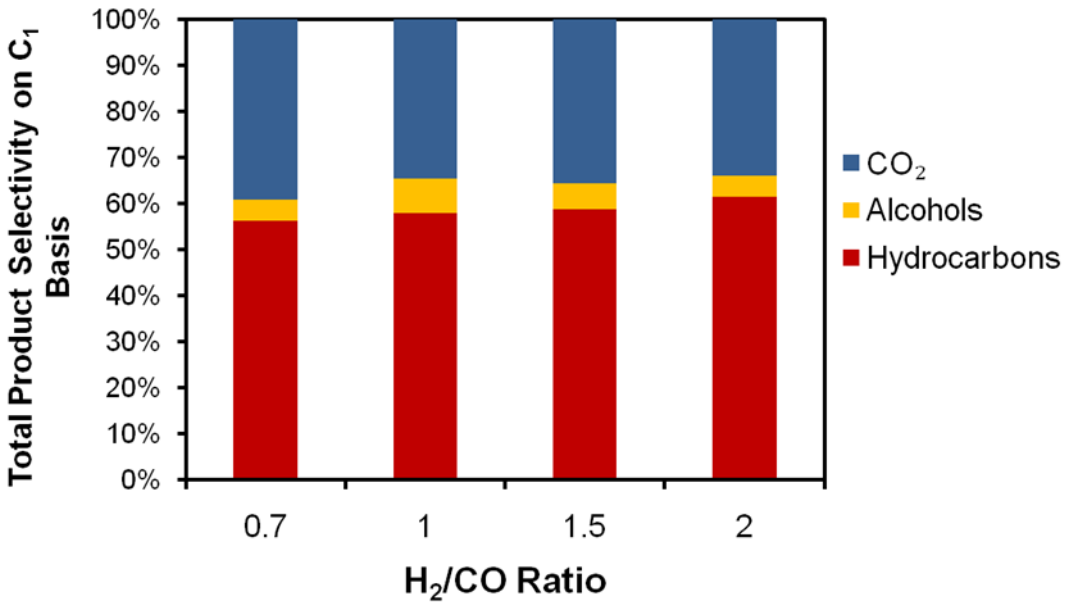

Figure 4.9: Total product selectivity as a function of H_2/CO ratio for Mo_2C. Reaction conditions: 240°C, 25 bar.

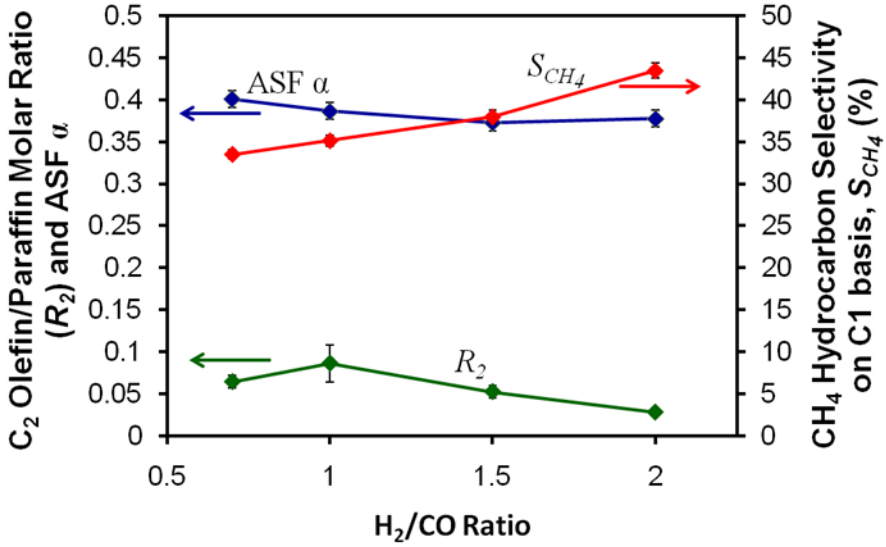

Figure 4.10: C_2 olefin/paraffin molar ratio, ASF α value, and CH_4 hydrocarbon selectivity on C1 basis as a function of H_2/CO ratio for Mo_2C. Reaction conditions: 240°C, 25 bar.

with increasing H_2/CO ratio while the CO_2 selectivity decreased slightly. This result may be due to the higher partial pressure of H_2 which would inhibit the water gas shift reaction (H_2 is a product from WGS) and enhance FTS (H_2 is a reactant for FTS). Increasing the H_2/CO ratio also caused a decrease in α and an increase in CH_4 selectivity.

This result could be due to an increase in the surface concentration (coverage) of adsorbed hydrogen as the H_2/CO ratio was increased. With a higher H_{ads} concentration, carbon on the catalyst surface is more likely to react with adsorbed hydrogen atoms than with other carbon-containing species. Therefore, the probability of chain propagation would decrease. Additionally, with a higher concentration of H_{ads}, the degree of product saturation (hydrogenation) would also increase. This was observed as the olefin/paraffin molar ratio decreased with increasing H_2/CO ratio.

By varying the H_2 and CO feed concentrations, the reaction orders with respect to H_2 and CO were for the Mo_2C catalyst. As shown in Figure 4.11, the FTS

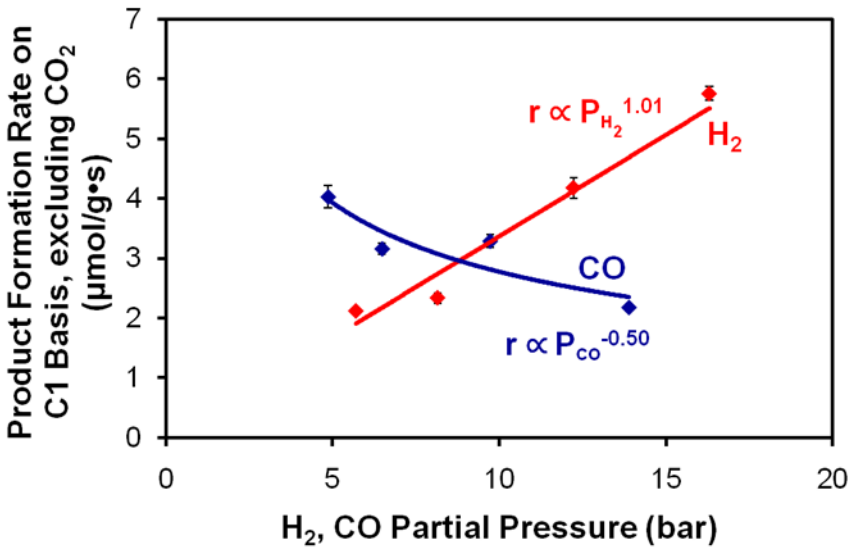

Figure 4.11: Product formation rate on a C1 basis (excluding CO_2) as a function of H_2 (red) or CO (blue) partial pressure. Reaction conditions: 240°C and 25 bar.

product formation rate increased with increasing H_2 partial pressure. The reaction order with respect to H_2 was ~1. Ranhotra et al. also reported a reaction order of 1 with respect to H_2 for CO hydrogenation over Mo_2C at atmospheric pressure [12]. H_2 reaction orders of ~1 have also been reported for Fe and Co FTS catalysts [13, 14]. With regard to CO, the reaction rate for Mo_2C decreased as the partial pressure of CO was increased. The

reaction order with respect to CO was ~ −0.5. Ranhotra et al. reported the CO order for Mo_2C to be approximately 0.3 [12] whereas the CO order for Fe and Co catalysts has been reported in the range of −0.5 to 0.1 [13-15].

In addition to process conditions, the effect of pretreatment conditions on the FTS performance of Mo_2C was explored. The three pretreatment conditions investigated were: N_2 at 200°C for 4 h (labeled as Mo_2C-N_2), H_2 at 400°C for 4 h (labeled as Mo_2C-H_2), and 15% CH_4/H_2 at 590°C for 4 h (labeled as Mo_2C-CH_4/H_2). The effect of these pretreatment conditions on the FTS rate and selectivity for Mo_2C are shown in Figures 4.12 – 4.14. Mo_2C-CH_4/H_2 exhibited the highest FTS product formation rates while Mo_2C-N_2 and Mo_2C-H_2 exhibited similar lower rates. The total selectivities to hydrocarbons, CO_2, and alcohols were similar for all of the Mo_2C samples. The olefin/paraffin molar ratio for Mo_2C-N_2 (0.075) and Mo_2C-H_2 (0.076) was approximately 3 times higher than that for Mo_2C-CH_4/H_2 (0.028). The highest α was observed for

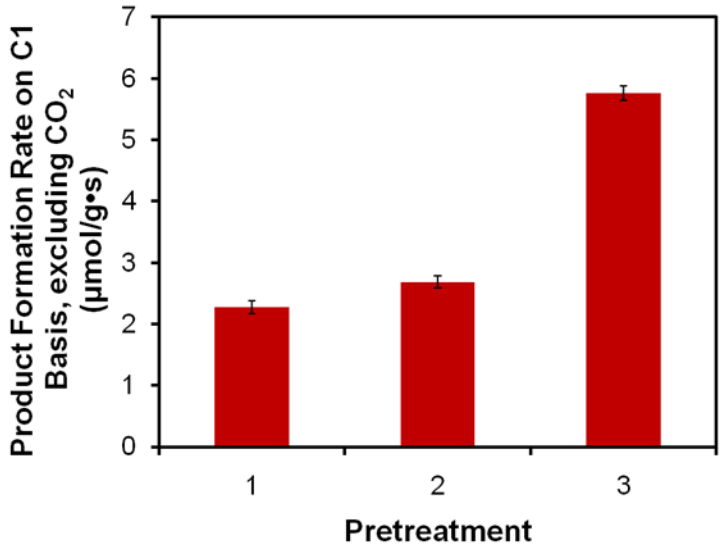

Figure 4.12: FTS product formation rate on C1 basis (excluding CO_2) for Mo_2C after different pretreatment conditions: N_2 at 200°C for 4 h, H_2 at 400°C for 4 h, and 15% CH_4/H_2 at 590°C for 4 h. Reaction conditions: 240°C, 25 bar, $H_2/CO = 2$.

Mo_2C-H_2 (0.39) and the lowest CH_4 selectivities were observed for Mo_2C-H_2 (43.7%) and Mo_2C-CH_4/H_2 (43.5%).

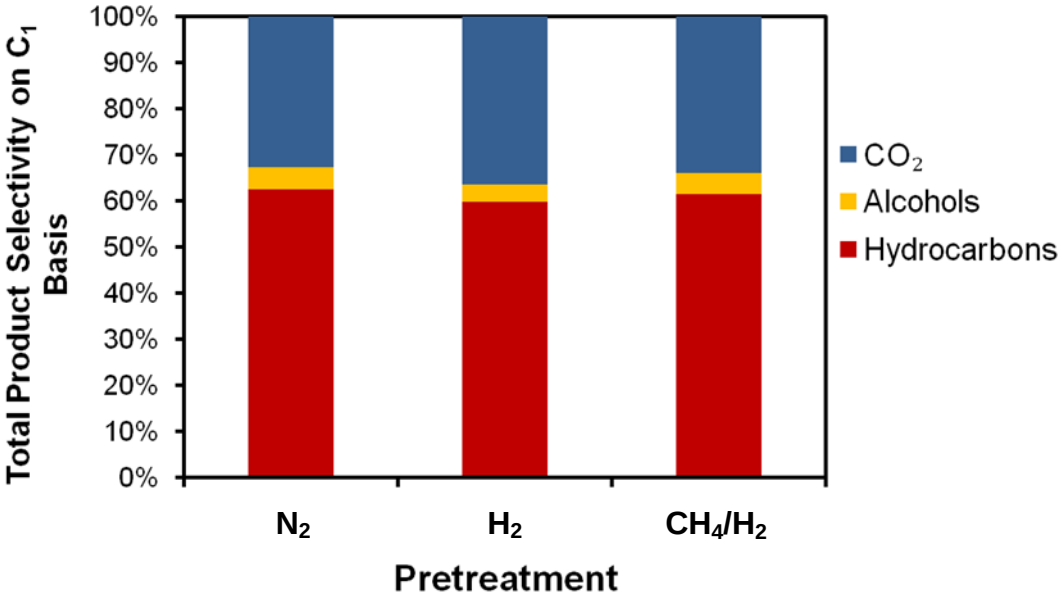

Figure 4.13: Total product selectivity for Mo_2C after different pretreatment conditions: N_2 at 200°C for 4 h, H_2 at 400°C for 4 h, and 15% CH_4/H_2 at 590°C for 4 h. Reaction conditions: 240°C, 25 bar, H_2/CO = 2.

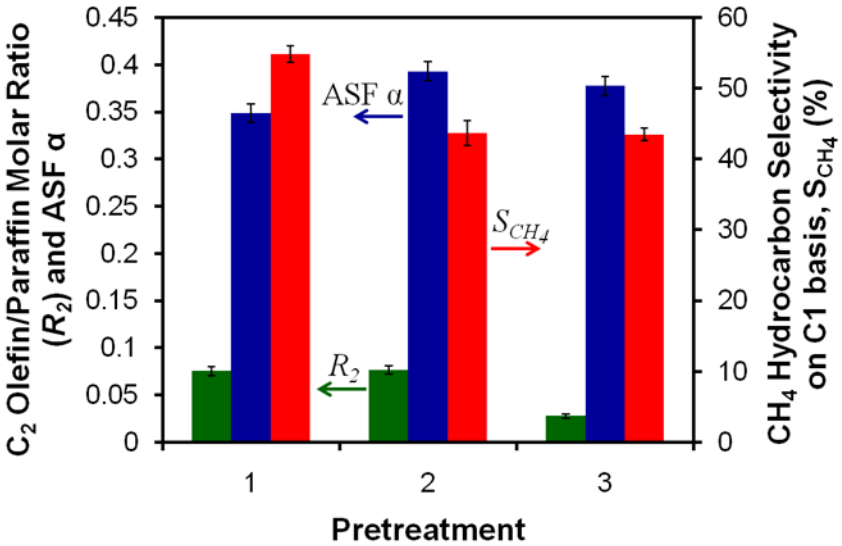

Figure 4.14: C_2 olefin/paraffin molar ratio (green), ASF α value (blue), and CH_4 hydrocarbon selectivity on C1 basis (red) for Mo_2C after different pretreatment conditions: N_2 at 200°C for 4 h, H_2 at 400°C for 4 h, and 15% CH_4/H_2 at 590°C for 4 h. Reaction conditions: 240°C, 25 bar, H_2/CO = 2.

4.3.2. Temperature Programmed Desorption and Reaction Experiments

As discussed in Chapter 3, carbides and nitrides of the same metal exhibited significantly different normalized FTS rates (Figure 3.9). For example, Mo_2C was active for FTS over the entire temperature range (200-320°C) while Mo_2N exhibited negligible activity below 270°C. CO-H_2 pulse chemisorption experiments were performed over the Mo_2C and Mo_2N catalysts at 240°C in the chemisorption analyzer at atmospheric pressure. The MS intensity for m/z = 15 (CH_3 fragments) for these pulse chemisorption experiments is shown in Figure 4.15. After exposing the surface to CO, H_2 pulsing over

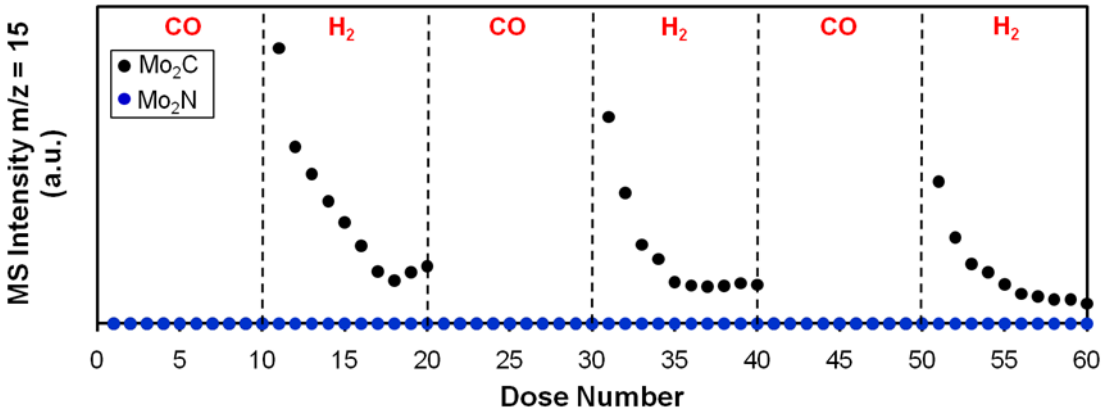

Figure 4.15: MS intensity m/z = 15 for Mo_2C and Mo_2N during CO-H_2 pulse chemisorption experiments. Conditions: 240°C, 1 atm.

the Mo_2C catalyst resulted in the production of CH_4 while no products were observed over the Mo_2N surface. These results agree with the FTS experimental results. For Mo_2C, CH_4 production decreased with each dose of H_2 because carbon on the catalyst surface was being depleted. Additionally, the amount of CH_4 produced decreased from the 1st set of H_2 doses to the 3rd set of H_2 doses. This trend fits with the deactivation observed for Mo_2C during the first 5-10 h of FTS.

The reactivity of the carbide and nitride surface was further explored using a H_2/CO TPRxn (H_2/CO = 4). The MS intensity (m/z = 15, CH_3 fragments) during the

TPRxn is shown in Figure 4.16. The Mo_2C catalyst exhibited a light off temperature for CO hydrogenation at approximately 200°C. The Mo_2N catalyst did not begin to produce CH_4 until 300-350°C. This result suggests that a higher temperature was required for the Mo_2N catalyst to overcome the reaction barrier for CO hydrogenation.

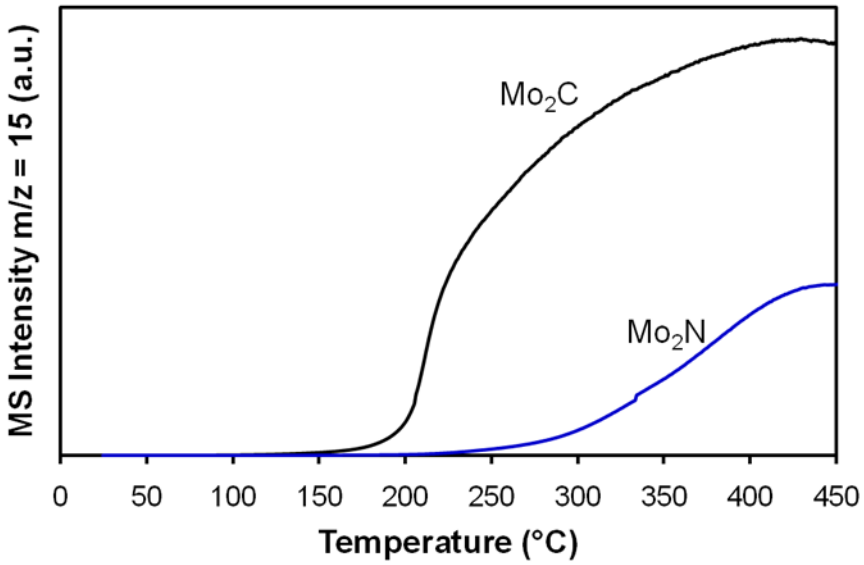

Figure 4.16: Temperature programmed reaction with a 4:1 H_2:CO mixture over Mo_2C and Mo_2N. The heating rate was 10°C/min.

The apparent activation energy for a reaction is governed by the elementary reaction with the slowest forward rate, i.e. the rate-limiting step. The rate-limiting step for FTS is often reported to be adsorption (Equation 4.2) and dissociation (Equation 4.3) of CO or the hydrogenation of carbon species (Equations 4.4 and 4.5) [1-3]. To investigate the first of these proposed rate-limiting steps, CO TPD experiments were performed (see Figure 4.17). Both Mo_2C and Mo_2N exhibited similar CO TPD spectra; there was a broad desorption peak centered at ~100°C. The similarity between the Mo_2C and Mo_2N spectra suggested that the materials possessed similar molecular CO adsorption energies.

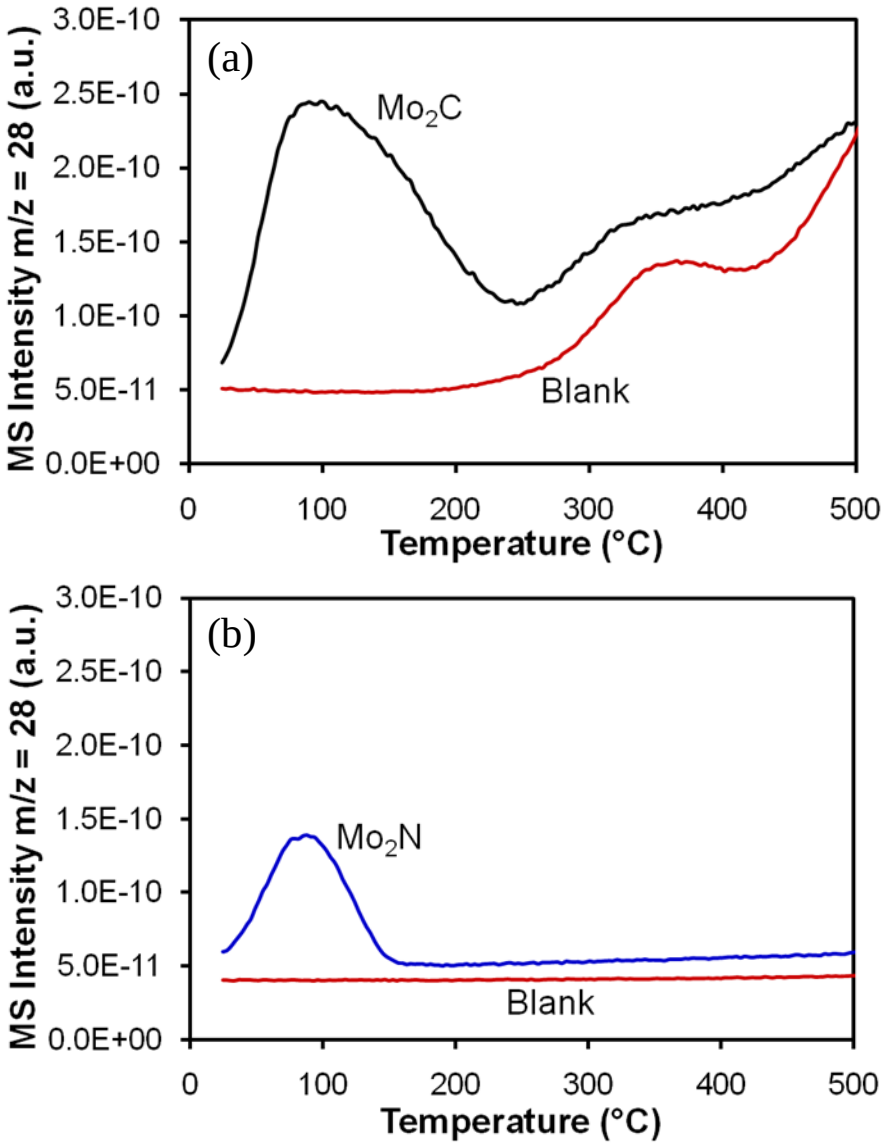

Figure 4.17: CO temperature programmed desorption spectra for (a) Mo_2C and (b) Mo_2N. For blank, catalyst surface was not exposed to CO. Heating rate: 30°C/min.

The molecular CO adsorption energies were experimentally determined for the Mo_2C catalyst using a heating rate variation method [9, 10]. To do so, the broad desorption peak was fit to 4 separate CO desorption peaks. The deconvoluted CO TPD spectra for Mo_2C for the highest (40°C/min) and lowest (4°C/min) heating rates are shown in Figure 4.18. During deconvolution, the relative intensities of the 4 desorption peaks were held constant between spectra with different heating rates. As these runs were

performed over samples from the same batch of Mo_2C, the relative amounts of the different CO adsorption sites on the catalyst surface should remain constant.

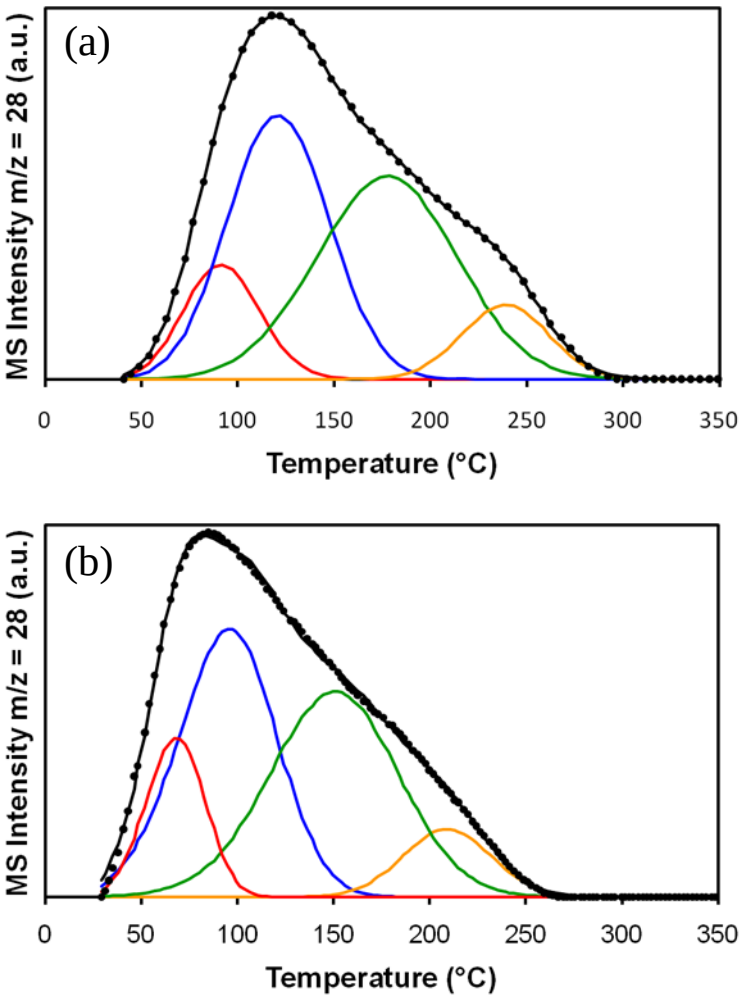

Figure 4.18: Deconvoluted CO TPD spectra for Mo_2C at heating rate of (a) 40°C/min and (b) 4°C/min. Deconvolution performed using CasaXPS. Data (black dots), envelope (black line), peak 1 (red line), peak 2 (blue line), peak 3 (green line), and peak 4 (orange line).

From the plots in Figure 4.18, the temperature at which the maximum desorption rate occurs, T_{max}, was determined for each peak. By plotting $\ln\left(T_{\max}^2/\beta\right)$ vs. $1/T_{max}$ (Figure 4.19), the CO desorption energies related to each peak were determined and are given in Table 4.1. The desorption energies ranged from 90 – 150 kJ/mol. These values are similar

to those reported by St. Clair (93 – 115 kJ/mol), determined via CO TPD from a Mo_2C single crystal [11].

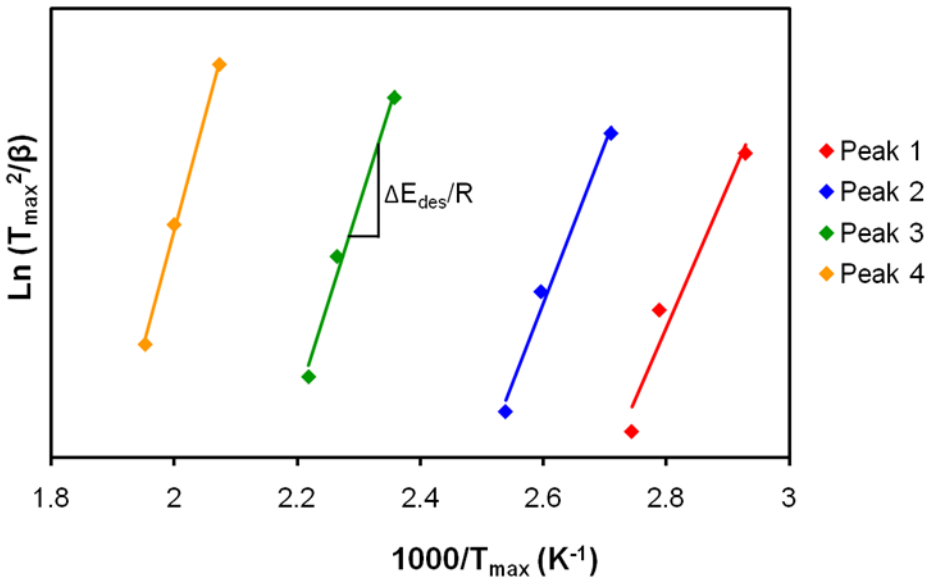

Figure 4.19: Determination of CO desorption energies for Mo_2C using heating rate variation method. Heating rates: 4°C/min, 15°C/min, and 40°C/min.

Table 4.1: CO desorption energies for Mo_2C determined from heating rate variation method.

Peak	**ΔE_{des} (kJ/mol)**
1	91 ± 19
2	103 ± 11
3	126 ± 14
4	148 ± 6

The other proposed rate-limiting steps, CO dissociation and hydrogenation, were investigated over Mo_2C and Mo_2N using the experimental sequence shown in Figure 4.2 (described in Section 4.2.2). Following exposure to CO, an Ar TPD was performed to remove any molecularly adsorbed CO from the catalyst surface. Figure 4.20 shows the MS intensity for CO (m/z = 28) during this TPD step over Mo_2C as a function of the CO exposure temperature. The CO desorption peak observed in Figure 4.17a was again observed for the Mo_2C catalyst exposed to CO at room temperature. As the temperature

of CO exposure increased, the intensity of this peak decreased and the peak shifted to higher temperatures. This shift in intensity and temperature may have been due to CO no longer

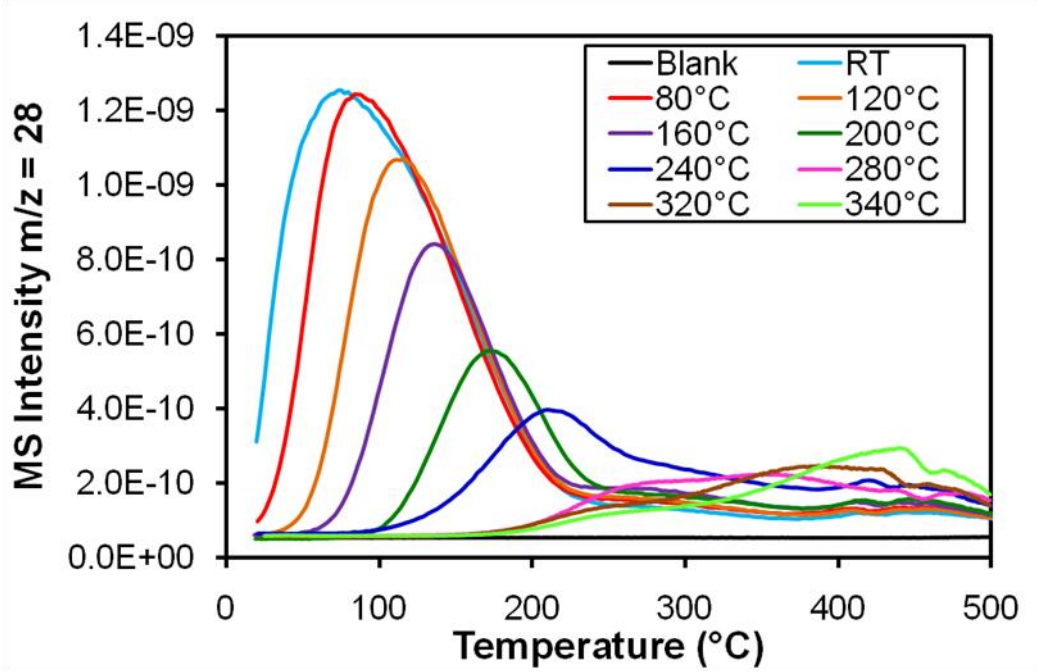

Figure 4.20: CO TPD spectra for Mo_2C as a function of CO exposure temperature. A blank spectrum is also shown in which the Mo_2C catalyst was not exposed to CO.

occupying the adsorption sites with lower binding energies; the temperature for CO exposure was above the temperature at which CO desorbs from these sites. At the highest temperatures for CO exposure (320°C and 340°C), there are CO desorption peaks present at 400-450°C. These peaks may be due to the recombination of adsorbed carbon and oxygen from CO dissociation [11].

Assuming that the Ar TPD step removed molecular CO from the catalyst surface, a subsequent H_2 TPRxn step could be used to hydrogenate adsorbed carbon produced from CO dissociation. Figure 4.21 shows the MS intensity for m/z = 15 (CH_3 fragments) for Mo_2C and Mo_2N as a function of CO exposure temperature. For a CO exposure

temperature of 240°C, a significant amount of CH_4 was produced over the Mo_2C surface compared to the blank (no CO exposure). As the temperature of CO exposure increased, the intensity of CH_4 desorption peak increased. This result suggests that higher

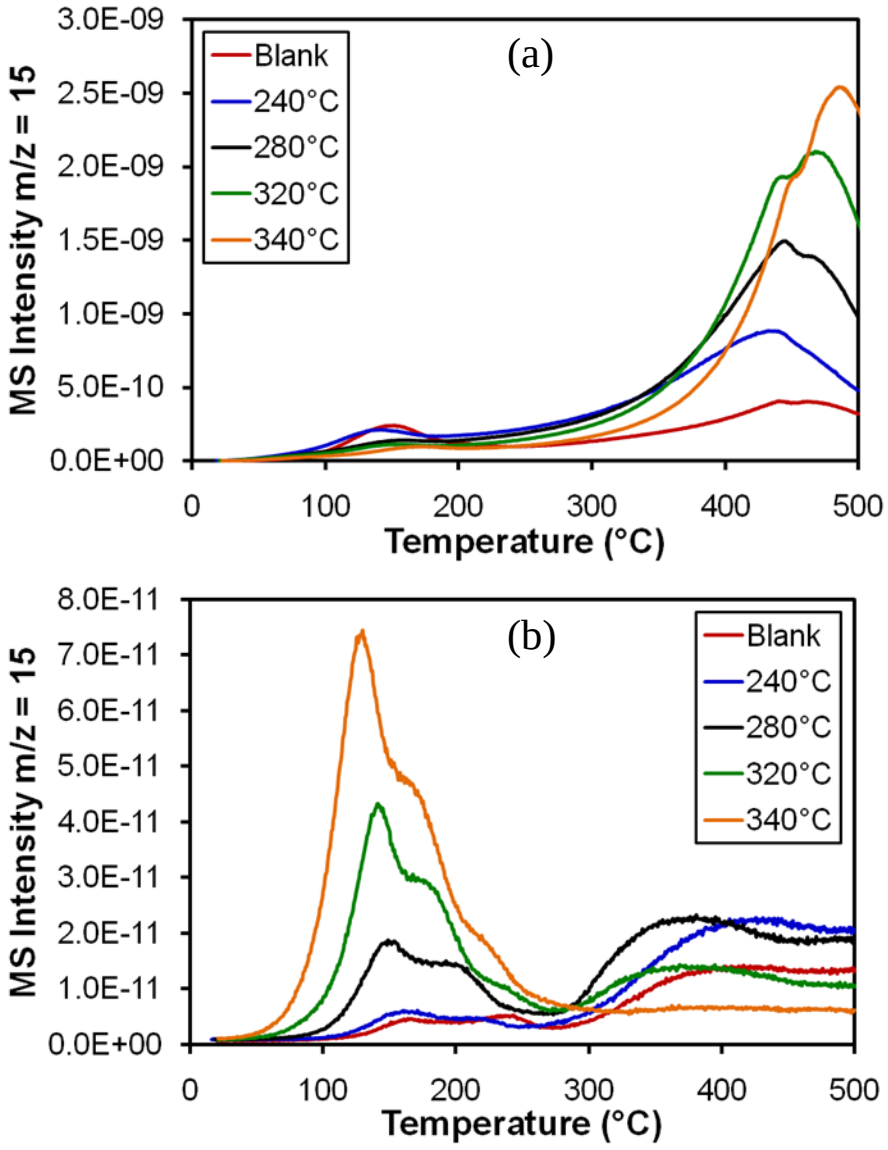

Figure 4.21: H_2 temperature programmed reaction spectra for (a) Mo_2C and (b) Mo_2N as a function of CO exposure temperature. A blank is also shown in which the catalyst was not exposed to CO.

exposure temperatures resulted in a higher concentration of adsorbed carbon from CO dissociation. Additionally, the primary CH_4 desorption peaks were centered at ~450°C. For Mo_2N, the spectra for the sample exposed to CO at 240°C and the blank were similar,

suggesting that CO dissociation did not occur over this surface at 240°C. However, as the temperature for CO exposure was increased, three CH_4 desorption peaks were observed: ~140, ~180, and ~220°C. Similar to Mo_2C, as the temperature of CO exposure was increased, the intensity of the CH_4 desorption peaks increased. Additionally, these peaks shifted towards lower temperatures with increasing CO exposure temperatures. The ratio of intensity of the ~140°C peak to the ~180°C peak also increased with increasing CO exposure temperature. This shift with temperature and the changing intensity ratio are consistent with the carbon surface coverage increasing with increasing CO exposure temperature. Increasing coverage results in weaker binding, thus the desorption peaks would shift to lower temperatures, as was observed. Moreover, at higher CO exposure temperatures, the less reactive sites would be capable of CO dissociation. Therefore, the least reactive sites (lowest desorption temperatures) would be occupied last, thus causing an increase in the intensity ratio for the peak at ~140°C compared to the peak at ~180°C.

During the H_2 TPRxn for Mo_2C and Mo_2N, H_2O formation, due to the hydrogenation of adsorbed oxygen present from CO dissociation, was not observed. H_2O or O_2 also did not desorb during the Ar TPD step. Therefore, adsorbed oxygen from CO dissociation either remained on the catalyst surface throughout the experimental sequence or was removed by reacting with CO to produce CO_2 during the CO exposure step. CO is known to be a good reductant. To probe the removal of adsorbed oxygen by CO, CO pulse experiments were performed while monitoring the production of CO_2 using the MS. Figure 4.22 shows the CO_2 peak areas (MS m/z = 44) for Mo_2C dosed with CO at 240°C and room temperature as well as Mo_2N dosed with CO at 240°C. A significant amount of CO_2 was produced over the Mo_2C surface at 240°C during CO dosing; however, very

little CO_2 was produced over the Mo_2N surface at the same temperature. Based on the previous H_2 TPRxn results, CO dissociation occurred readily

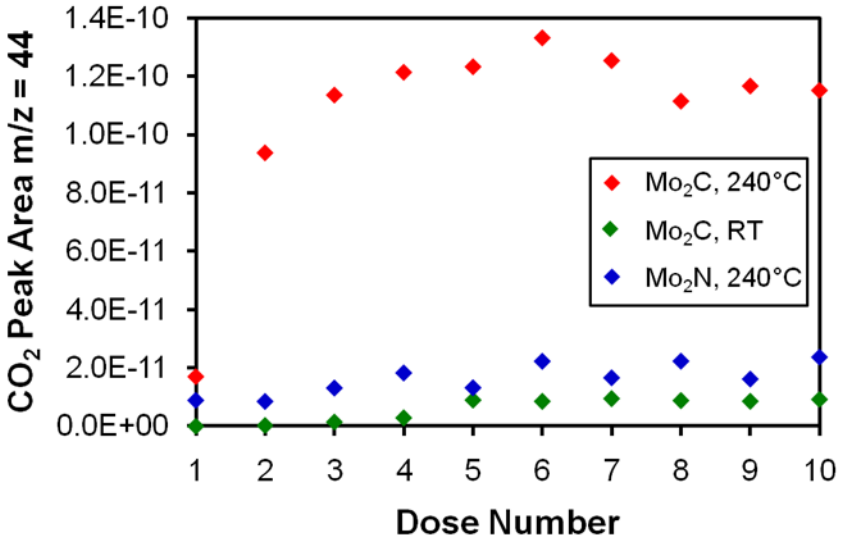

Figure 4.22: CO_2 peak area (MS m/z = 44) during CO dosing experiments for Mo_2C at 240°C and room temperature and Mo_2N at 240°C.

over the Mo_2C surface at 240°C, but did not occur over the Mo_2N surface at 240°C. Therefore, the production of CO_2 over the carbide surface was likely due to the removal of adsorbed oxygen from CO dissociation by reaction with CO. However, it is also possible that some of this CO_2 was produced by reduction of Mo oxides that were not completely reduced during pretreatment. Similar to the Mo_2N surface at 240°C, the Mo_2C surface at room temperature (CO dissociation did not occur) produced very little CO_2 during CO dosing.

In addition to CO dissociation and hydrogenation, the experimental sequence shown in Figure 4.2 allowed for the investigation of the effect of molecular CO vs. dissociated CO on the production of hydrocarbons. Based on the previous results, molecularly adsorbed CO was removed from the catalyst surface during the TPD step. By not performing the TPD step of the sequence (Figure 4.2), molecularly adsorbed CO

remains on the catalyst surface and its impact on hydrocarbon production during the H_2 TPRxn step can be observed. Figure 4.23 shows the MS intensity for m/z = 15 during the H_2 TPRxn step over Mo_2C for which the Ar TPD step was performed and was not performed. Two CO exposure temperatures were tested: 240°C and room temperature.

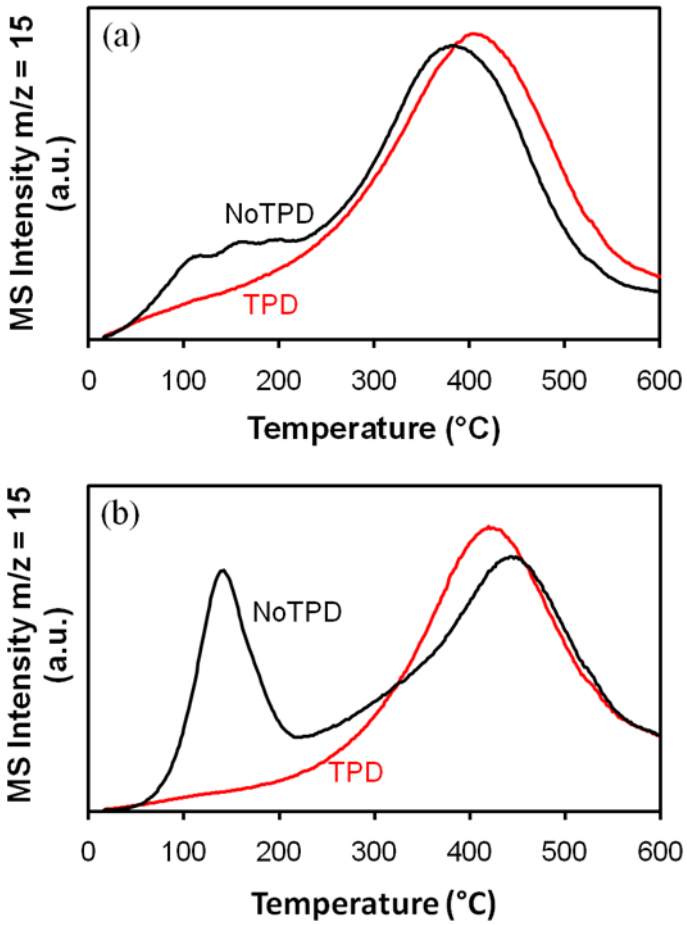

Figure 4.23: H_2 TPRxn spectra (MS intensity m/z = 15) for Mo_2C for which the Ar TPD step was performed and was not performed for CO exposure temperatures of (a) 240°C and (b) room temperature.

For CO exposure at 240°C, an increase in hydrocarbon production was observed over Mo_2C in the temperature range of 100-200°C when the TPD step was not performed. This result was amplified for CO exposure at room temperature. These findings indicate that molecularly adsorbed CO plays a role in hydrocarbon production. Moreover, the

effect of molecularly adsorbed CO on C-C coupling (C_2+ hydrocarbon production) was explored by monitoring m/z = 29 (Figure 4.24). This m/z corresponds to C_2H_5 fragments, which almost all C_2+ hydrocarbons produce. As shown in Figure 4.24,

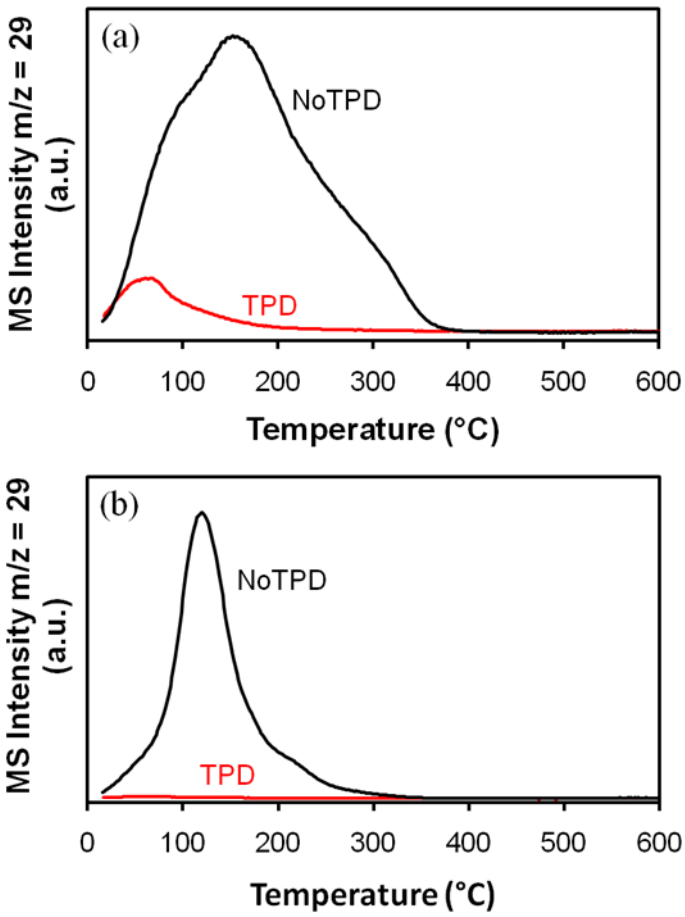

Figure 4.24: H_2 TPRxn spectra (MS intensity m/z = 29, C_2H_5 fragments) for Mo_2C for which the Ar TPD step was performed and was not performed at CO exposure temperatures of (a) 240°C and (b) room temperature.

the presence of molecularly adsorbed CO resulted in a significant increase in the production of C_2+ hydrocarbons, indicating that CO_{ads} plays a key role in C-C coupling.

4.4. Discussion

4.4.1. Effect of FTS Operating Conditions

The effect of temperature, pressure, and H_2/CO ratio on FTS performance of Mo_2C was investigated. The results of this investigation are summarized in Table 4.2 and

compared to the findings reported by Van Der Laan and Beenackers for Fe and Co catalysts [1]. In general, the Mo_2C results agreed with those for Fe and Co catalysts. This similar behavior was likely due to the fact that these relationships are primarily governed by thermodynamics, not by the intrinsic properties of the catalyst. For example, the chain length increased with increasing pressure. Based on Le Chatelier's principle [16], an increase in pressure will result in a reaction shifting to minimize the amount of gas molecules. Therefore, the reaction between H_2 and CO should shift towards consuming a greater number of molecules of H_2 and CO per molecule of hydrocarbon produced. This shift was observed, as a greater concentration of higher hydrocarbons was produced as the pressure was increased.

Table 4.2: Effect of process conditions on FTS performance. ↑ indicates increase with increasing parameter. ↓ indicates decrease with increasing parameter. * indicates a complex relation. Mo_2C (red) and data from Van der Laan and Beenackers (black) [1].

Parameter	Rate	Chain Length (α)	Olefin Selectivity	Alcohol Selectivity	CH_4 Selectivity
Temperature	↑	↓↓	↓*	↓↓	↑↑
Pressure	↑	↑↑	↓*	*↑	*↓
H_2/CO	↑	↓↓	*↓	*↓	↑↑

Although there were no inconsistencies between Mo_2C and the Fe and Co catalysts (i.e. ↑ for Mo_2C vs. ↓ for Fe/Co or vice versa), Mo_2C did exhibit complex relationships for alcohol and CH_4 selectivity with respect to pressure and alcohol and olefin selectivity with respect to H_2/CO ratio. The total alcohol selectivity increased between 1 bar (0%) and 10 bar (5.5%), but then decreased slightly at pressures above 10 bar. The CH_4 selectivity also showed a similar trend with respect to pressure. It increased up to 10 bar, but then decreased slowly at higher pressures (Figure 4.7). One explanation for these two results is that the effect of pressure on the production of higher

hydrocarbons was more significant at pressures above 10 bar. As shown in Figure 4.7, the α value remained fairly constant between 1 and 10 bar, but increased more significantly at pressures above 10 bar. The increased selectivity towards higher hydrocarbons resulted in a decrease in alcohol and CH_4 selectivity (i.e. parallel reaction competition).

The alcohol selectivity also exhibited a complex relationship with H_2/CO ratio. It increased between a H_2/CO ratio of 0.7 and 1, but then decreased with increasing H_2/CO ratio. A similar trend was observed for the olefin/paraffin molar ratio. These local maximums may be due to the ideal surface coverages of H and CO being reached on the Mo_2C surface for production of olefins and alcohols. Since higher H_2/CO ratios favor the production of saturated hydrocarbons (see Equations 1.3 – 1.5), the selectivity towards saturated hydrocarbons increased with increasing H_2/CO ratio and the selectivity towards olefins and alcohols decreased.

With regards to activity, the FTS rate for Mo_2C increased with increasing temperature, pressure, and H_2/CO ratio. The reaction order was 1 with respect to H_2 and −0.5 with respect to CO. These values are in good agreement with those reported for commercial Co and Fe catalysts. The negative CO order indicates that CO has an inhibitive effect on the reaction rate. This negative effect could be due to CO and H_2 competing for the same sites on the Mo_2C surface.

Along with operating conditions, the effect of pretreatment conditions on FTS performance was explored for Mo_2C. The Mo_2C sample pretreated with 15% CH_4/H_2 exhibited product formation rates 2-3 times higher than Mo_2C samples pretreated with N_2 or H_2. Additionally, the N_2 and H_2 pretreated samples exhibited similar rates. Two conclusions can be drawn from these results. First, the Mo_2C surfaces for the N_2 and H_2

pretreated samples were similar under reaction conditions. For Mo_2C-N_2, the pretreatment was only a degassing step; therefore the post-pretreatment Mo_2C surface was likely still covered with oxygen. For Mo_2C-H_2, it has been reported in literature that treatment at 400°C in H_2 was sufficient to reduce the Mo_2C surface [6]. Consequently, the reaction conditions must govern the surface structure of Mo_2C, resulting in similar performance for degassed and reduced samples.

Second, carbon on the Mo_2C surface played a key role in FTS, as the recarburized Mo_2C-CH_4/H_2 sample exhibited the highest rate. The degree of carburization has been shown to influence the activity of Mo_2C for a number of other reactions [8, 17, 18]. Choi and co-workers proposed that the degree of carburization increases the quantity and quality of active sites [17]. For FTS, the degree of carburization also affected the degree of hydrogenation, as Mo_2C-CH_4/H_2 exhibited the lowest selectivity towards olefins (i.e. strongly favored saturated hydrocarbons). It is speculated that the carbon on the Mo_2C surface may provide sites for H_2 adsorption, thus increasing the selectivity towards saturated hydrocarbons. Furthermore, FTS over Mo_2C was first order with respect to H_2, thus an increase in H_2 adsorption sites would result in an increase in rate.

4.4.2. Interactions of CO and H_2 with Mo_2C and Mo_2N Surfaces

The interactions of CO and H_2 with the Mo_2C and Mo_2N surfaces were investigated to explain differences observed in the FTS performance of Mo_2C and Mo_2N as well as shed light on the FTS mechanism over these materials. Through TPD and TPRxn experiments probing the proposed rate-limiting elementary steps (Equations 4.2 – 4.5), it was observed that Mo_2C and Mo_2N adsorb molecular CO with similar binding energies (90-150 kJ/mol). However, CO dissociation occurred readily over the Mo_2C

surface at 240°C while the Mo_2N surface was not capable of dissociating CO at this temperature (Figure 4.21). For temperatures at or above 280°C, Mo_2N was capable of dissociating CO. This result agrees with FTS experiments (Figure 3.8) and H_2/CO TPRxn experiments (Figures 4.15 and 4.16), as Mo_2N did not show any measurable FTS activity below 270°C, suggesting that CO dissociation is a key step in FTS over Mo_2N. Furthermore, since the Mo_2C and Mo_2N surfaces were exposed to CO in the absence of H_2 during the experimental sequence, these materials were capable of direct CO dissociation without the assistance of H_2.

For the H_2 TPRxn experiments (Figure 4.21), as the temperature of CO exposure increased, the intensity of the CH_4 desorption peaks increased for both Mo_2C and Mo_2N. However, these peaks were centered at ~450°C for Mo_2C and ~150°C for Mo_2N. This difference in desorption temperature indicated that the carbon was bound much more strongly to the Mo_2C surface than the Mo_2N surface. This result is in agreement with density functional theory calculations performed for Mo_2C, in which the adsorption energy of carbon was reported to be extremely high, between -630 and -725 kJ/mol depending upon the adsorption site [19].

It is proposed that the activation barrier for CO dissociation is higher over Mo_2N than Mo_2C, and that this difference explains the observed difference in FTS rates. An illustration is shown in Figure 4.25. This higher activation energy for Mo_2N agrees with the difference in light off temperature observed in Figure 4.16. Moreover, based on the Bronsted-Evans-Polanyi relationship, it has been shown that the activation energy for dissociative adsorption of molecules depends linearly on the reaction energy [20-24]. More specifically, the activation energy for CO dissociation is directly related to the

dissociative CO adsorption energy. Therefore, if the activation energy of CO dissociation decreases, the adsorption energy of C and O shifts down in energy (more exothermic,

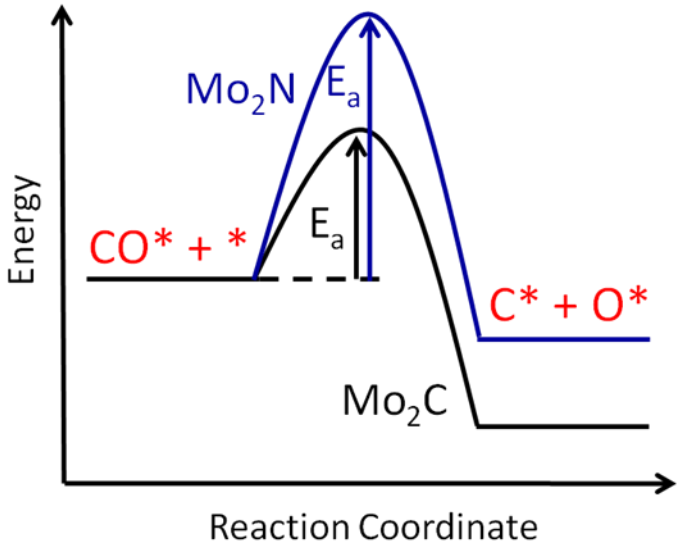

Figure 4.25: Schematic showing the higher activation barrier for CO dissociation over Mo_2N than Mo_2C.

stronger bond). Our findings are in good agreement with this relationship as Mo_2C had a lower CO dissociation activation energy than Mo_2N, and carbon was bound stronger to the Mo_2C surface than the Mo_2N surface. Regarding FTS activity, Bligaard et al. has reported that the dissociative CO adsorption energy is a good descriptor for CO hydrogenation activity (Figure 4.26) [24]. Consequently, materials with different CO dissociation activation energies (Mo_2C vs. Mo_2N) exhibited different activities for CO hydrogenation. It is speculated that Mo_2C (more reactive) lies near the middle of the volcano shown in Figure 4.26, while Mo_2N (less reactive) lies towards the right.

Knowledge regarding the active sites for CO dissociation on the Mo_2C surface can also be elucidated. From Figure 4.21a, the Mo_2C sample produced a significant amount of CH_4 even when the surface was not exposed to CO (blank). This result indicates that surface carbon, present in the carbide structure, was able to be

hydrogenated to CH_4 during the H_2 TPRxn. An example of a carbon-terminated Mo_2C (100) surface is shown in Figure 4.27. One of the surface carbon atoms is circled in red. Based on density function theory calculations, it has been reported that adsorbed carbon

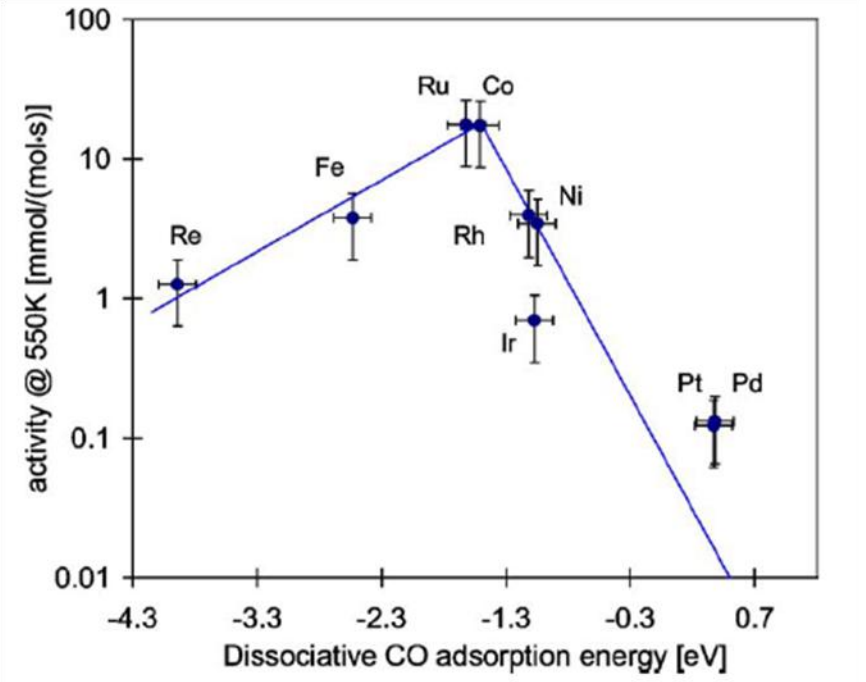

Figure 4.26: CO hydrogenation activities of different supported transition metals as a function of the reaction energy for dissociative CO chemisorption. Taken from [24].

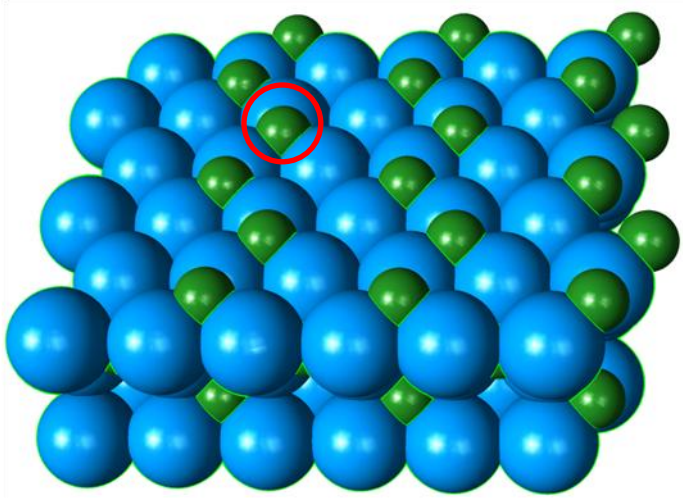

Figure 4.27: Carbon-terminated Mo_2C (100) surface. Carbon (green) and Molybdenum (blue). Image created using CrystalMaker software package.

can occupy the same sites on a Mo_2C surface that carbon normally occupies for a carbon-terminated Mo_2C surface [19]. More specifically, adsorbed carbon from CO dissociation could occupy the site circled in red in Figure 4.27. Additionally, Kitchen et al. reported that adsorption of hydrogen on a carbon-terminated Mo_2C surface resulted in the formation of a stable C-H bond [25]. Based on our results and these reports, it is proposed that the site circled in red in Figure 4.27 is the active site for CO dissociation over Mo_2C. A simplified model of the proposed reaction scheme is shown in Figure 4.28.

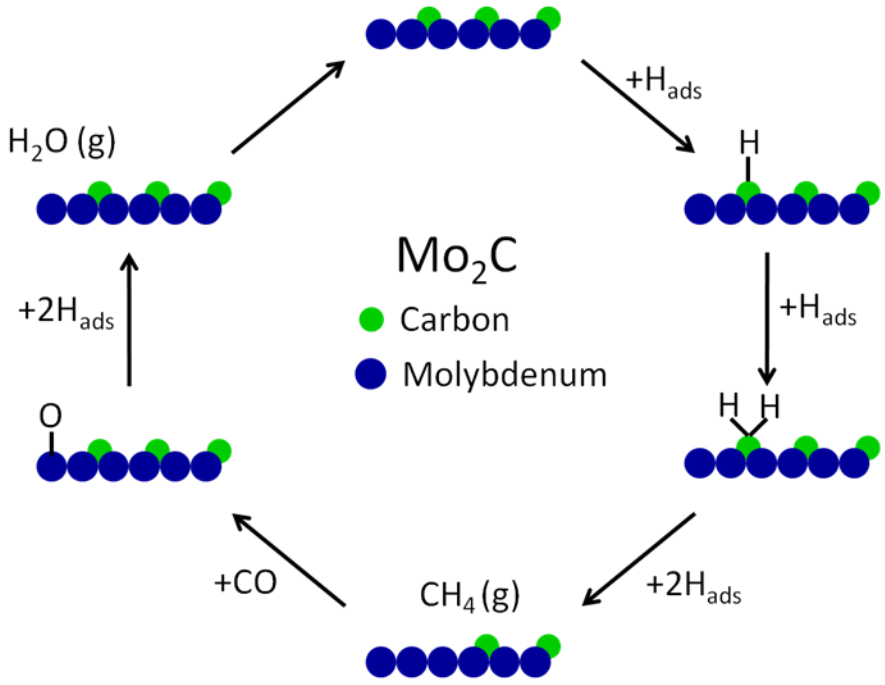

Figure 4.28: Simplified schematic illustrating the proposed reaction cycle for CO dissociation and hydrogenation over Mo_2C.

Since Mo_2C and Mo_2N were active for direct CO dissociation, one might propose that the primary FTS mechanism for these materials was the carbide mechanism (Figure 4.1). However, for Mo_2C, the desorption of CH_4 due to the hydrogenation of adsorbed carbon from CO dissociation primarily occurred at temperatures above 350°C. This temperature is above that of the temperatures employed for the FTS experiments,

suggesting that adsorbed carbon from CO dissociation may remain bound to the Mo_2C surface. Therefore, hydrocarbon formation over Mo_2C is probably not following the carbide mechanism. On the other hand, the CH_4 desorption peaks for Mo_2N were between 100°C and 250°C, within the typical temperature range for FTS. Additionally, FTS activity was not observed for Mo_2N until CO dissociation was favorable. Therefore, it is probable that the carbide mechanism occurs over the Mo_2N surface. Ranhotra et al. speculated that CO dissociation was the critical first step for CO hydrogenation over Mo_2N [12].

Using TPD and TPRxn experiments, the mechanism over Mo_2C was further investigated by exploring the effect of molecularly adsorbed CO vs. dissociatively adsorbed CO on hydrocarbon production. As shown in Figure 4.1, CO dissociation is only required for the carbide mechanism, whereas the oxygenate and CO insertion mechanisms only involve molecular CO adsorption. Figures 4.23 and 4.24 showed that the presence of molecularly adsorbed CO on the Mo_2C surface resulted in an increase in hydrocarbon production as well as C-C coupling (production of C_2+ hydrocarbons). These findings indicate that the dominate mechanism over Mo_2C was either the oxygenate or CO insertion mechanism.

Kojima et al. speculated that the CO hydrogenation mechanism over Mo_2C involved the formation of a CH_xO intermediate [26]. Our results support Kojima's hypothesis as both the oxygenate and CO insertion mechanisms would result in the formation of a CH_xO species. Moreover, as shown in Chapter 3, Mo_2C produced a fair amount of alcohols during FTS. The production of alcohols is expected from the oxygenate and CO insertion mechanisms. Similarly, Fe-based catalysts produce alcohols

and have been reported to follow the oxygenate mechanism [27]. Moreover, these findings suggest that Mo_2C possesses multiple types of catalytic sites: CO dissociation sites and molecular CO adsorption/C-C coupling sites. This is supported by the CO TPD results which showed multiple desorption peaks corresponding to different sites. Based on the results shown in this chapter, it may be possible to improve C-C coupling over Mo_2C by enhancing its ability for associative CO adsorption, i.e. increasing the number of sites for molecular CO adsorption.

For future work, there are a few areas that could be expanded upon for the experiments discussed in this chapter. For the experimental sequence probing CO dissociation and hydrogenation, it would be beneficial to perform a carbon and oxygen balance in order to monitor deposition/removal. Regarding the mechanisms and elementary reactions shown in Figure 4.1, it would be informative to assess the reversibility of the different elementary reactions. The thermodynamics of these steps may govern product selectivity. Additionally, with regards to the product distributions for the carbides and nitrides, it may be necessary to investigate other possible simultaneous reactions (besides CO dissociation, chain initiation, and chain propagation). For example, Mo_2C has been reported to be active for hydrogenolysis [12, 28]. If hydrogenolysis occurs under FTS reaction conditions, it may strongly affect the product distribution.

4.5. Summary

The effect of process conditions on the FTS performance of Mo_2C was explored. In general, the relationships between specific process conditions (temperature, pressure, and H_2/CO ratio) and FTS rate and selectivity for Mo_2C were similar to those reported in literature for Fe- and Co-based catalysts. The FTS rate over Mo_2C was determined to be

first order in H_2 and negative half order in CO. Pretreatment of Mo_2C with 15% CH_4/H_2 resulted in the most active catalyst compared to pretreatment in H_2 or N_2. The increased degree of carburization of the Mo_2C-CH_4/H_2 sample was proposed to be the cause for the increase in activity.

Interactions between H_2 and CO with the Mo_2C and Mo_2N surfaces were probed using temperature programmed desorption and temperature programmed reaction techniques. Both Mo_2C and Mo_2N were capable of direct CO dissociation without H_2 assistance. However, the activation barrier for CO dissociation was much higher over Mo_2N than Mo_2C, thus explaining the difference in observed FTS rates. Mo_2N was proposed to follow the carbide mechanism, while Mo_2C was proposed to follow the oxygenate or CO insertion mechanism. Although CO dissociation occurred over Mo_2C, the carbide mechanism was not feasible as the carbon was bound too strongly to the Mo_2C surface to be removed by hydrogenation under typical FTS reaction conditions. The Mo_2C surface was found to have multiple types of sites: sites active for CO dissociation and sites active for molecular CO adsorption/C-C coupling.

4.6. References

[1] G. P. Van Der Laan, A. A. C. M. Beenackers, Kinetics and Selectivity of the Fischer-Tropsch Synthesis: A Literature Review, *Catalysis Reviews: Science and Engineering* 41 (1999) 255-318.

[2] J. Yang, Y. Liu, J. Chang, Y.-N. Wang, L. Bai, Y.-Y. Xu, H.-W. Xiang, Y.-W. Li, B. Zhong, Detailed Kinetics of Fischer-Tropsch Synthesis on an Industrial Fe-Mn Catalyst, *Industrial Engineering and Chemistry Research* 42 (2003) 5066-5090.

[3] C. G. Visconti, E. Tronconi, L. Lietti, R. Zennaro, P. Forzatti, Development of a Complete Kinetic Model for the Fischer-Tropsch Synthesis over Co/Al_2O_3 Catalysts, *Chemical Engineering Science* 62 (2007) 5338-5343.

[4] B. Davis, Fischer-Tropsch Synthesis: Current Mechanism and Futuristic Needs, *Fuel Processing Technology* 71 (2001) 157-166.

[5] M. Roper, in *Catalysis in C1 Chemistry* (W. Keim, ed.), Reidel, Dordrecht. 1983. Pp. 41-88.

[6] A. Griboval-Constant, J.-M. Giraudon, G. Leclercq, L. Leclercq, Catalytic Behaviour of Cobalt and Ruthenium Supported Molybdenum Carbide Catalysts for FT Reaction, *Applied Catalysis A: General* 260 (2004) 35-45.

[7] J. J. Patt, Carbide and Nitride Catalysts for the Water Gas Shift Reaction, Ph. D. Thesis, University of Michigan, 2003.

[8] T. E. King, Carbide and Nitride Supported Water-Gas Shift Catalysts, Ph. D. Thesis, University of Michigan, 2007.

[9] S. L. M. Schroeder, M. Gottfried, Temperature-Programmed Desorption (TPD) and Thermal Desorption Spectroscopy (TDS), Advanced Physical Chemistry Laboratory, FU Berlin (2002).

[10] P. A. Redhead, Thermal Desorption of Gases, *Vacuum* 12 (1962) 203-211.

[11] T. P. St. Clair, S. T. Oyama, D. F. Cox, CO and O_2 Adsorption on α-Mo_2C(0001), *Surface Science* 468 (2000) 62-76.

[12] G. S. Ranhotra, A. T. Bell, J. A. Reimer, Catalysis over Molybdenum Carbides and Nitrides. II. Studies of CO Hydrogenation and C_2H_6 Hydrogenolysis, *Journal of Catalysis* 108 (1987) 40-49.

[13] M. A. Vannice, Catalytic Synthesis of Hydrocarbons from Hydrogen-Carbon Monoxide Mixtures over the Group VIII metals. I. Specific Activities and Product Distributions of Supported Metals, *Journal of Catalysis* 37 (1975) 449-461.

[14] S. A. Eliason, C. H. Bartholomew, Reaction and Deactivation Kinetics for Fischer-Tropsch Synthesis on Unpromoted and Potassium-Promoted Iron Catalysts, *Applied Catalysis A: General* 186 (1999) 229-243.

[15] W. Ma, G. Jacobs, D. E. Sparks, M. K. Gnanamani, V. R. R. Pendyala, C. H. Yen, J. S. S. Klettlinger, T. M. Tomsik, B. H. Davis, Fischer-Tropsch Synthesis: Support and Cobalt Cluster Size Effects on Kinetics over Co/Al_2O_3 and Co/SiO_2 Catalysts, *Fuel* 90 (2011) 756-765.

[16] S. S. Zumdahl, *Chemical Principles*, 4th ed., Houghton Mifflin Company, Boston, MA, 2002. Pp. 210-216.

[17] J.-S. Choi, G. Bugli, G. Djega-Mariadassou, Influence of the Degree of Carburization on the Density of Sites and Hydrogenating Activity of Molybdenum Carbides, *Journal of Catalysis* 193 (2000) 238-247.

[18] W. Setthapun, Carbide and Nitride Supported Methanol Steam Reforming Catalysts, Ph. D. Thesis, University of Michigan, 2007.

[19] J. Ren, C.-F. Huo, J. Wang, Z. Cao, Y.-W. Li, H. Jiao, Density Functional Theory Study into the Adsorption of CO_2, H and CH_x (x=0-3) as well as C_2H_4 on α-Mo_2C(0001), *Surface Science* 600 (2006) 2329-2337.

[20] J. K. Norskov, T. Bligaard, A. Logadottir, S. Bahn, L. B. Hansen, M. Bollinger, H. Bengaard, B. Hammer, Z. Sljivancanin, M. Mavrikakis, Y. Xu, S. Dahl, C. J. H. Jacobsen, Universality in Heterogeneous Catalysis, *Journal of Catalysis* 209 (2002) 275-278.

[21] V. Pallassana, M. Neurock, Electronic Factors Governing Ethlylene Hydrogenation and Dehydrogenation Activity of Pseudomorphic Pd_{ML}/Re(0001), Pd_{ML}/Ru(0001), Pd(111), and Pd_{ML}/Au(111) Surfaces, *Journal of Catalysis* 191 (2000) 301-317.

[22] Z.-P. Liu, P. Hu, General Trends in CO Dissociation on Transition Metal Surfaces, *Journal of Chemical Physics* 114 (2001) 8244.

[23] A. Logadottir, T. H. Rod, J. K. Norskov, B. Hammer, S. Dahl, C. J. H. Jacobsen, The Bronsted-Evans-Polanyi Relation and the Volcano Plot for Ammonia Synthesis over Transition Metal Catalysts, *Journal of Catalysis* 197 (2001) 229-231.

[24] T. Bligaard, J. K. Norskov, S. Dahl, J. Matthiesen, C. H. Christensen, J. Sehested, The Bronsted-Evans-Polanyi Relation and the Volcano Curve in Heterogeneous Catalysis *Journal of Catalysis* 224 (2004) 206-217.

[25] J. R. Kitchin, J. K. Norskov, M. A. Barteau, J. G. Chen, Trends in the Chemical Properties of Early Transition Metal Carbide Surfaces: A Density Functional Study, *Catalysis Today* 105 (2005) 66-73.

[26] I. Kojima, E. Miyazaki, Catalysis by Transition Metal Carbides. V. Kinetic Measurements of Hydrogenation of CO over TaC, TiC, and Mo_2C Catalysts, *Journal of Catalysis* 89 (1984) 168-171.

[27] B. H. Davis, Fischer-Tropsch Synthesis: Reaction Mechanisms for Iron Catalysts, *Catalysis Today* 141 (2009) 25-33.

[28] J. S. Lee, S. Locatelli, S. T. Oyama, M. Boudart, Molybdenum Carbide Catalysts. 3. Turnover Rates for the Hydrogenolysis of n-Butane *Journal of Catalysis* 125 (1990) 157-170.

CHAPTER 5

Mechanistic Investigation of the Metal Adsorption Process over Mo_2C

5.1. Introduction

For heterogeneous catalysts, the support can have a strong influence on performance [1-9]. For example, a support can interact with a metal in such a way that it induces size and morphology changes, modifies the electronic properties of the metal, and/or participates in the reaction [1, 2]. As such, the preparation of these materials can also influence performance, i.e. the interactions between a metal precursor and a support directly affect the properties of the catalyst including the metal dispersion and particle morphology.

Recently, there has been interest in using early transition metal carbide materials as catalyst supports [10-14]. Carbide-supported metal catalysts have been investigated for Fischer-Tropsch Synthesis [10], hydrodenitrogenation and hydrodesulfurization [11], methanol steam reforming [12], water gas shift [13, 14], and other reactions. In addition, carbides have also been used as supports for electrocatalytic reactions [15-20]. Espositio et al. [15] studied the use of Pt supported on tungsten carbide as an electrocatalyst for the hydrogen evolution reaction, and observed rates comparable to Pt alone.

Although this list is not exhaustive, several different methods have been used to deposit the active metal onto the carbide surface. Esposito et al. [15] deposited Pt onto tungsten carbide thin films in a vacuum environment using thermal evaporation. Griboval-Constant et al. [10] and Lewandowski et al. [11] deposited metal using a wet

impregnation method with a passivated molybdenum carbide (Mo_2C) support. Setthapun et al. [12] and Schweitzer et al. [13] used a modified wet impregnation method to deposit metals directly onto the native carbide surface. In the case of Pt/Mo_2C, depositing Pt directly onto the native Mo_2C surface resulted in the formation of "raft-like" Pt particles [13]. Although there is considerable interest in utilizing early transition metal carbides as supports, there is a lack of knowledge regarding how metals and metal complexes interact with the carbide surface.

The key objective of this chapter is to determine the governing mechanism(s) by which metal deposition onto a native Mo_2C surface occurs, via a wet impregnation method. There are a number of factors that are expected to affect the interaction of the metal complex and support surface: the nature of the support (e.g. the point of zero charge), the solution chemistry (e.g. pH), and the character of the metal complex (e.g. coordination chemistry and ionic strength) [21]. Brunelle was among the first to report that the metal adsorption process may be governed by an electrostatic interaction between the support and the metal complex [21]. This electrostatic adsorption is based on the double layer theory [22] and has recently been investigated in depth by Regalbuto and others [23-26]. Based on this electrostatic theory, the solution pH, the charge of the metal complex in solution, and the point of zero charge (PZC, pH at which the surface of the material has a net zero charge) of the support are the key parameters affecting metal adsorption [21, 23-26].

It has been suggested that by controlling these parameters, metal adsorption via wet impregnation can be optimized. This mechanism has been termed "Strong Electrostatic Adsorption (SEA)" by Regalbuto [23-27]. A schematic illustrating the SEA

process is shown in Figure 5.1. When the solution pH is below the PZC of the support material, the surface of the support becomes protonated, has a net positive charge, and attracts anionic metal complexes (e.g. $[PtCl_6]^{2-}$). For solution pH above the PZC, the

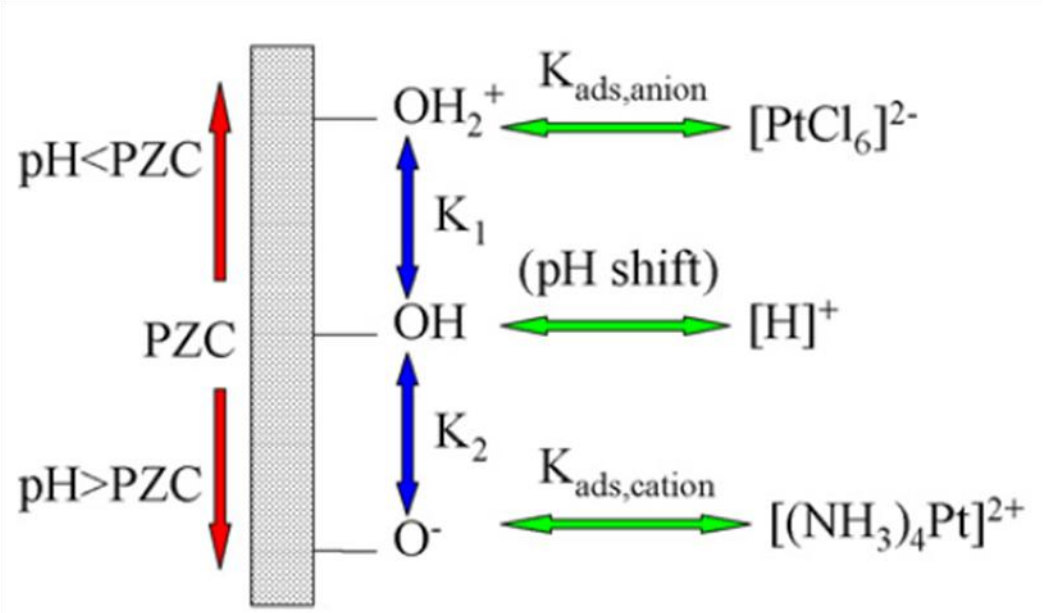

Figure 5.1: Schematic illustrating "strong electrostatic adsorption". Taken from [26].

surface becomes deprotonated, has a net negative charge, and attracts cationic metal complexes ($[(NH_3)_4Pt]^{2+}$). By controlling the pH and selecting the appropriate metal precursor, metal adsorption can be maximized, as shown in Figure 5.2. The adsorption of Pt from the chloroplatinic acid precursor (anionic complex) was maximized at a pH (~2.5) below the PZC (pH 9.4) of the unoxidized carbon xerogels due to the strong electrostatic attraction between the positively charged xerogel surface and the negatively charged Pt complex [25]. The adsorption of Pt is retarded at pH < 2.5 due to the effect of high ionic strength, which effectively diminishes the value of the adsorption equilibrium constant [27].

However, it has been reported that electrostatic binding does not always fully account for metal complex adsorption on oxides [22, 28], so more complex theories have

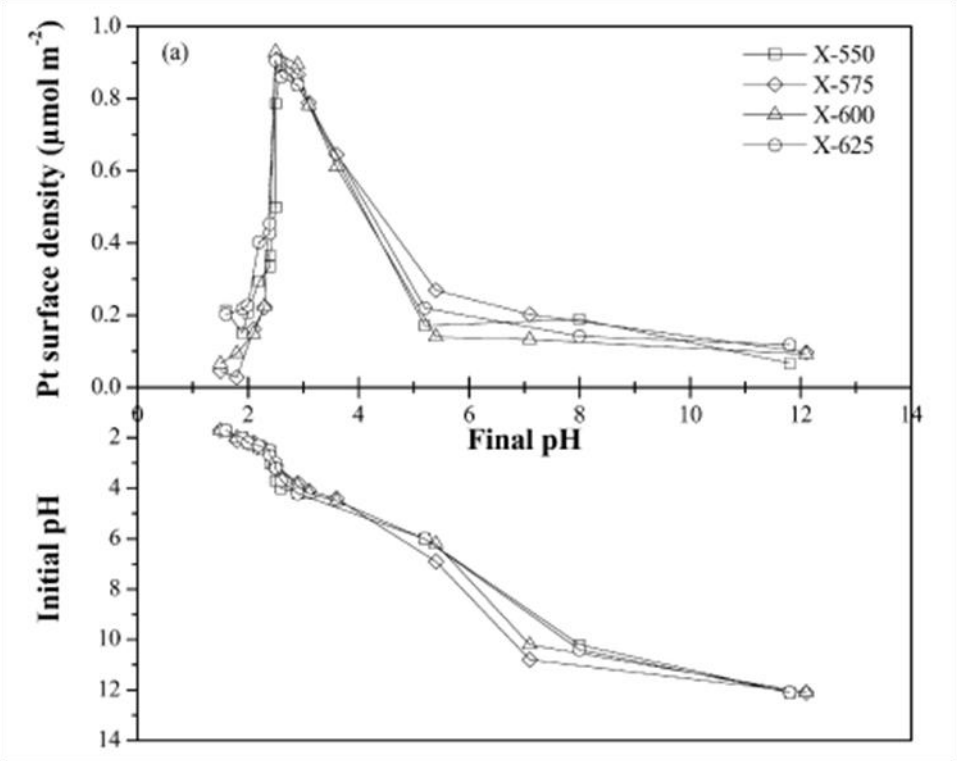

Figure 5.2: Pt uptake as a function of pH for a series of unoxidized carbon xerogels. Taken from [25]. The Pt precursor was chloroplatinic acid, H_2PtCl_6. It forms an anionic complex in aqueous solution. The PZC for the unoxidized carbon xerogels was 9.4.

been developed. These include the triple layer theory, specific site adsorption, and a ligand exchange mechanism [22]. The triple layer theory is a modification of the double layer theory and adds that a part of the adsorbed ions are held at a fixed distance to the surface by some kind of specific site adsorption [22]. Specific site adsorption involves only specific sites on the oxide surface that are capable of interacting with the metal complex. The ligand exchange mechanism involves the replacement of the original ligands of the transition metal in solution with surface groups, thus binding the metal to the surface and forming a covalent bond [22]. Additionally, since transition metal carbides behave more like metals than oxides [29-31], it may be important to consider additional support-precursor interactions that could affect the metal loading mechanism.

For example, a common method for the synthesis of bimetallic metal particles is by a direct red-ox reaction between a parent metal and a second metal in oxidized form [28, 32-33].

For this study, Mo_2C-supported metal (Pt, Pd, Cu, Co, Ni, Fe) catalysts were prepared via wet impregnation. The metal uptake was monitored as a function of time using inductively coupled plasma-optical emission spectroscopy (ICP-OES). The materials were characterized using X-ray diffraction (XRD), X-ray absorption spectroscopy (XAS), and X-ray photoelectron spectroscopy (XPS). Based on the findings, key details regarding the mechanisms governing the metal adsorption process over Mo_2C are discussed and insight regarding catalyst preparation is given.

5.2. Experimental Setup

5.2.1. Catalyst Preparation

The Mo_2C support was synthesized via a temperature programmed reaction as described in Chapter 3 (Section 3.2.1). Upon completion of the temperature program, the material was cooled to room temperature in flowing 15% CH_4/H_2. Metals were loaded onto the support via wet impregnation. The metal precursors were $Pd(NH_3)_4(NO_3)_2$, H_2PtCl_6, $Cu(NO_3)_2$, $CuCl_2$, $Co(NO_3)_2$, $CoCl_2$, $Ni(NO_3)_2$, $NiCl_2$, $Fe(NO_3)_3$, and $FeCl_2$. These metals and precursors were chosen because they include noble and base metals as well as different counter ions. First, 70 mL of deionized water was added to a glass container and bubbled with Ar for 15 min to remove any dissolved oxygen. Next, the desired amount of metal precursor was dissolved in the water. The amount of metal precursor was designed to correspond to ~10% surface coverage of the Mo_2C support, which has a surface area of 120 ± 10 m^2/g. The resulting metal loading solution had a

concentration of 2.27 mmol metal/L. The unpassivated Mo_2C powder (0.75 g) was then transferred under Ar to the solution as bubbling was maintained. The support powder was left in solution for 3 h and periodically stirred. For the concentration vs. time studies, the support powder remained in the precursor solution for up to 45 h with continuous bubbling and samples of the solution were abstracted for elemental analysis via ICP-OES. Finally, the support material was transferred back into the quartz reactor tube under Ar flow.

Depending on the characterization to be performed, the samples were treated in different ways following deposition of the precursor. One set of samples was dried in He flowing at 20 mL/min at room temperature for 24 h. These samples, referred to as "Dried" samples, were then stored in a N_2-filled glove box until analyzed by XAS. Another set of samples was initially dried at 110 °C for 2 h in H_2 and then reduced in H_2 at 450 °C for 4 h. After reduction, these samples, referred to as "Reduced" samples, were also transferred into the glove box until analyzed by XAS. Samples that were not to be characterized via XAS analysis were passivated in 1% O_2/He flowing at 20 mL/min at room temperature for 6 h after the reduction procedure.

5.2.2. Materials Characterization

5.2.2.1.Point-of-Zero Charge Measurements

The PZC of Mo_2C was determined according to the procedure described by Park et al. [34]. First, 18mL of deionized water was bubbled with Ar. This volume of water was chosen to achieve a surface loading of ~5000 m^2/L, similar to the value used in Park et al. [34]. A Fischer-Scientific Accumet Research AR 15 pH meter was submersed in the solution to monitor the pH. Concentrated HCl or NH_4OH were used to adjust the pH of

the solution to a specified value. This initial pH value was recorded. Then, unpassivated Mo_2C (0.75 g), synthesized according to the procedure discussed in Section 5.2.1, was transferred to the solution in Ar. While the solution was continuously stirred and bubbled with Ar, the pH of the solution was recorded as a function of time. Upon stabilization, the final pH was recorded. By plotting the initial pH as a function of the final pH, the PZC of Mo_2C was determined. An example from literature for the unoxidized carbon xerogels discussed earlier is shown in Figure 5.3 [25]. The PZC of the xerogels was 9.4, corresponding to the flat region of the plot.

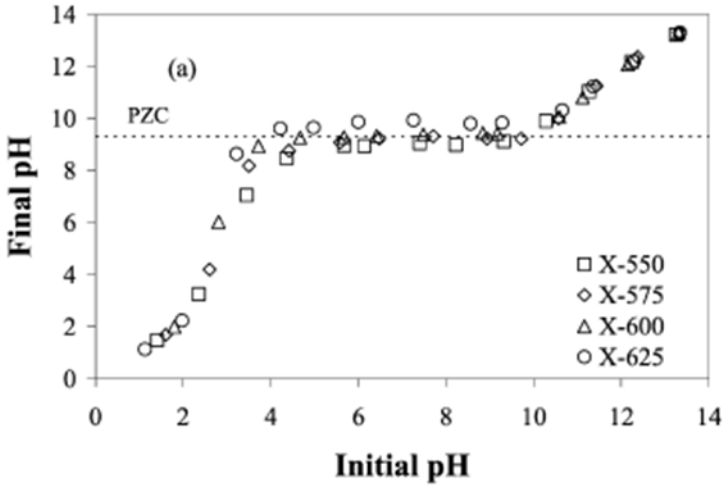

Figure 5.3: Final pH vs. Initial pH for a series of unoxidized carbon xerogels. Taken from [25]. The flat portion of the plot corresponds to the PZC of the materials, which was pH 9.4.

5.2.2.2.Elemental Analysis

Elemental analysis was performed using ICP-OES to monitor the concentration of metal in the loading solution as a function of time as well as to determine the amount of metal uptake on the Mo_2C supports. For the concentration vs. time experiments, 1mL of the precursor solution was diluted with 13mL of deionized water and was analyzed. For direct elemental analysis of the Mo_2C-supported metal catalysts, 15mg of material was

dissolved using 3mL of aqua regia solution (75%vol HCl and 25%vol HNO_3). The solution was allowed to sit for 24 h. Next, 1mL of the aqua regia solution was diluted with 13mL of deionized water and was ready for analysis. All the solutions were analyzed using a Varian 710-ES ICP Optical Emission Spectrometer. For each analysis, quantification was performed by comparing the relative intensities of the catalyst solutions to the relative intensities of several standards of known concentrations.

5.2.2.3.X-ray Diffraction

Diffraction patterns for the Mo_2C-supported metal catalysts were collected using a Rigaku miniflex X-ray diffractometer with a Cu-Kα (λ = 1.54nm) radiation source and a Ni filter. A range of $10° < 2\theta < 90°$ was scanned at a rate of 5°/min with a 0.02° step size.

5.2.2.4.X-ray Absorption Spectroscopy

X-ray absorption spectra were collected at the Argonne National Laboratory Advanced Photon Source beamline MR-CAT 10-ID-B. XAS is an element specific technique that can be used to probe the local atomic coordination and the chemical/oxidation state of the specific element in a compound [35]. The technique is based on the photo-electric effect, in which an x-ray is absorbed by an atom when the energy of the incident x-ray is transferred to a core-level electron (K, L, or M shell) [35]. This transfer of energy leaves the atom in an excited state. Extra energy from the incident x-ray is transferred to an ejected photo-electron. The energy at which the x-ray is absorbed by the atom is element specific and is called the edge energy, E_0. The edges which were collected for this study were the Pt L3 edge (11564 eV), the Pd K edge (24350 eV), the Cu K edge (8979 eV), the Ni K edge (8333 eV) and the Fe K edge (7112 eV).

The data collected during a XAS experiment corresponds to the x-ray absorption coefficient, $\mu(E)$, which is a function of the incident x-ray energy. XAS spectra are typically divided into 2 regimes: X-ray Absorption Near Edge Spectroscopy (XANES) and Extended X-ray Absorption Fine Structure (EXAFS). The XANES region corresponds to the energy region 20 eV below E_0 to 30 eV above E_0, and primarily gives information regarding the oxidation state of the probed element [35]. The EXAFS region corresponds to the energy region 30 eV above E_0 to 800 eV above E_0, and provides information about the local structure around the absorbing atom (i.e. bond distances, coordination numbers, and type of neighbors) [35]. For this study, the XANES region of the XAS spectra will be analyzed to investigate the oxidation state of the metal during the metal adsorption process.

There are primarily two methods for XAS spectra collection: transmission and fluorescence. In transmission mode, the intensity of the incident x-ray and the x-ray transmitted through the sample are compared to determine $\mu(E)$. For fluorescence mode, fluorescent x-rays emitted from the sample due to re-population of the core hole are compared to the incident x-ray to determine $\mu(E)$. Due to the relatively low metal loadings and the strong absorbing nature of Mo_2C, scans for this study were collected in fluorescence mode using Ar ion chambers for detection. Prior to data collection, the samples were crushed and pressed into pellets. All sample preparation was performed in the glove box to ensure that the samples were not exposed to oxygen. The samples were transferred to the beamline for analysis in a sealed quartz tube.

Athena, a free online software for XAS analysis, was used to analyze the resulting XAS data. A standard procedure was followed for each spectrum [36]. First, an energy

shift was applied to the sample spectrum based on a reference (metal foil) spectrum to account for any instrumental drift. Second, a linear pre-edge line (200 to 50 eV before the edge) was subtracted from the sample spectrum. Next, a third order polynomial (normalization line) was fit to the post-edge data (100 to ~400 eV after the edge). The edge step was then determined by taking the difference between the pre-edge and the normalization line. The entire spectrum was then divided by the edge step to normalize the spectrum to 1 x-ray. Finally, the background of the post-edge data was removed using a cubic spline function.

5.2.2.5.X-ray Photoelectron Spectroscopy

The Mo_2C-supported metal catalysts were characterized using XPS to determine the relatieve concentrations of Mo, C, and Cl on the surface. The XPS experiments were performed using a Kratos Axis Ultra x-ray photoelectron spectrometer with an Al anode (K_α radiation at 1486.6 eV) operating at 10 mA and 14 kV. The spectra were analyzed using CasaXPS, a commercially available XPS analysis program. C 1s, Mo 3d, and Cl 2p spectra were collected. The adventitious carbon peak (binding energy = 284.8 eV) was used to reference the other binding energies. The peak areas were normalized using the appropriate atomic sensitivity factors. This normalization allowed comparison of the relative atomic fractions of each species on the catalyst surfaces.

5.3. Results

The PZC of Mo_2C was determined from the plot of final pH vs. initial pH shown in Figure 5.4. The flat region of the curve corresponds to the PZC, which was approximately pH 5. Based on the electrostatic adsorption theory, the surface of Mo_2C

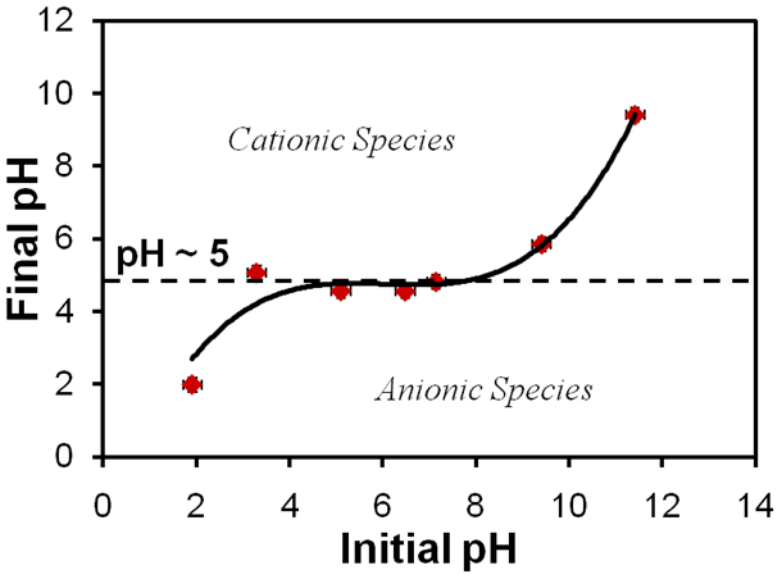

Figure 5.4: Initial pH vs. final pH for aqueous solutions containing Mo_2C at a surface loading of 5000 m^2/L.

becomes protonated and has a net positive charge at a pH below 5, and will adsorb anionic metal complexes [21, 23-27, 34]. At a pH greater than 5, the surface of Mo_2C becomes de-protonated and has a net negative charge, and will adsorb cationic metal complexes.

For each of the metal precursors, the concentration of the metal in the precursor solution was monitored as a function of time, and the results are presented in Figure 5.5. Time zero corresponded to the time at which the Mo_2C support was transferred to the solution. The relative metal loadings achieved after 20 h are given in Table 5.1. The relative metal loading for each sample was determined by ICP-OES analysis of the Mo_2C-supported metal catalyst samples and is defined as:

$$\text{Relative Metal Loading} = \frac{\text{Measured metal wt\%}}{\text{Nominal metal wt\%}} \qquad (5.1)$$

The nominal metal wt% was determined by assuming that 100% of the metal in solution adsorbed to the Mo_2C surface. The Fe precursors, $CoCl_2$ and $NiCl_2$ did not achieve more than 15% relative metal loading even after 20 h, whereas all of the other precursors

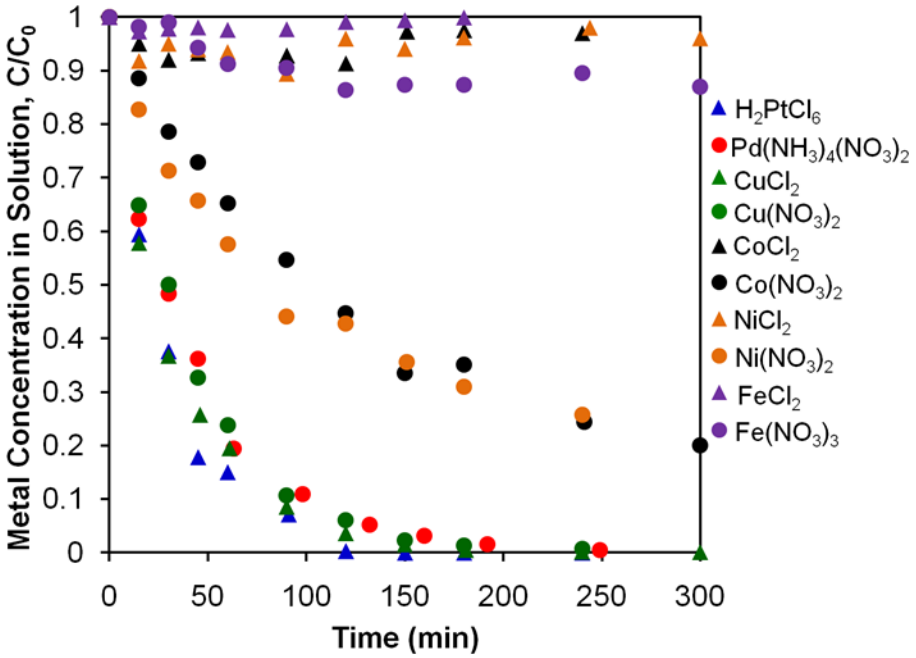

Figure 5.5: Normalized metal concentration (C/C_0) in the precursor solution as a function of time. Metal concentration was measured by ICP-OES.

achieved greater than 90% relative metal loading. It is important to note that the pH of the precursor solution was not adjusted; it was set based on the metal precursor. The initial pH of the precursor solution for each precursor is also given in Table 5.1. Based on the curves in Figure 5.5, the rate of adsorption follows the trend: H_2PtCl_6 ~ $Pd(NH_3)_4(NO_3)_2$ ~ $CuCl_2$ ~ $Cu(NO_3)_2$ > $Co(NO_3)_2$ ~ $Ni(NO_3)_2$ >> $CoCl_2$ ~ $NiCl_2$ ~ $FeCl_2$ ~ $Fe(NO_3)_3$.

The concentration of Mo in the solution during wet impregnation was also monitored using ICP-OES. The Mo concentration as a function of time is shown in Figure 5.6 for the various metal precursors. Additionally, a blank run was performed in which the Mo_2C support was added to 70 mL of deionized, dearated water (no metal precursor was present). The highest concentration of Mo was observed for the Pd precursor, reaching a value of ~0.9 mmol Mo/L after 300 min. In comparison, the concentration of Pd in the initial loading solution was 2.27 mmol/L. During the first 30

min, the Mo concentration for the Pt precursor showed a similar trend to that for Pd, but then decreased sharply. For most of the other metal precursors, the Mo concentration was slightly higher than for the blank run, but significantly below that for Pd. Based on the blank run, very little Mo from Mo_2C dissolved into solution when just deionized water was present.

Table 5.1: Relative metal loadings and precursor solution initial pH for the various metal precursors.

Precursor	Relative Metal Loading[1,2] (%)	Initial Precursor Solution pH
H_2PtCl_6	100	2.5
$Pd(NH_3)_4(NO_3)_2$	100	7.3
$CuCl_2$	100	5.0
$Cu(NO_3)_2$	100	5.1
$CoCl_2$	9	6.2
$Co(NO_3)_2$	91	5.7
$NiCl_2$	11	5.9
$Ni(NO_3)_2$	91	5.7
$FeCl_2$	3	4.7
$Fe(NO_3)_3$	14	2.9

[1] Relative metal loading determined using ICP-OES after 20 h of loading.
[2] Error on relative metal loading was ± 2%.

The metal concentration curves shown in Figure 5.5 were fit to zero-order, first-order, and second-order kinetics based on the following equation [37]:

$$-\frac{dC_i}{dt} = kC_i^n \tag{5.2}$$

where k is the reaction rate constant, t is time, C_i is the concentration of metal in solution, and n is the reaction order (n = 0, 1, or 2). The fit parameters are listed in Table 5.2. The adsorption of H_2PtCl_6, $Pd(NH_3)_4(NO_3)_2$, $CuCl_2$, and $Cu(NO_3)_2$ were best described by first order kinetics whereas the adsorption of $Co(NO_3)_2$ and $Ni(NO_3)_2$ appeared to follow second order kinetics. Second order kinetics typically indicates that two of the reactant

species were involved in the rate limiting step. The difference in the reaction order suggests a different mechanism for these two groups.

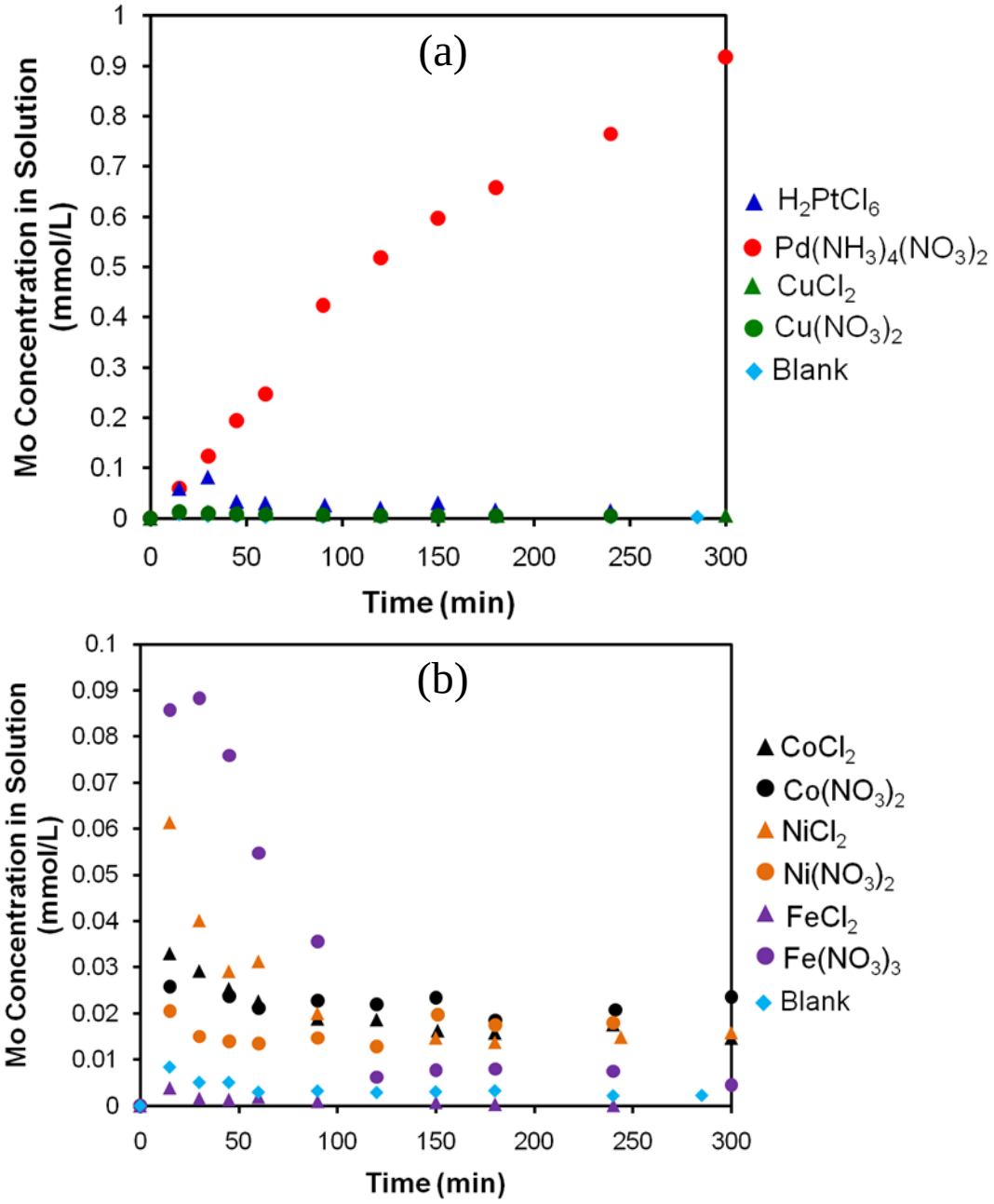

Figure 5.6: Mo concentration in the metal loading solution as a function of time for the (a) Pt, Pd, and Cu precursors and (b) Co, Ni, and Fe precursors. A blank run was also performed in which Mo_2C was added to dearated, deionized water; no metal precursor was present.

Table 5.2: Results from regression of metal concentration data for H_2PtCl_6, $Pd(NH_3)_4(NO_3)_2$, $CuCl_2$, $Cu(NO_3)_2$, $Co(NO_3)_2$, $Ni(NO_3)_2$ to zero order, first order, and second order kinetics.

	Zero Order		First Order		Second Order	
Metal Precursor	k (mol L^{-1} s^{-1})	R^2	k (s^{-1})	R^2	k (L mol^{-1} s^{-1})	R^2
H_2PtCl_6	2.3×10^{-7}	0.76	**6.5×10^{-4}**	**0.90**	1.1	0.89
$Pd(NH_3)_4(NO_3)_2$	1.3×10^{-7}	0.75	**3.7×10^{-4}**	**0.99**	1.9	0.73
$CuCl_2$	1.4×10^{-7}	0.69	**4.7×10^{-4}**	**0.99**	5.2	0.57
$Cu(NO_3)_2$	1.1×10^{-7}	0.68	**3.8×10^{-4}**	**0.98**	3.5	0.74
$Co(NO_3)_2$	8.2×10^{-8}	0.88	9.9×10^{-5}	0.96	**1.1×10^{-1}**	**0.97**
$Ni(NO_3)_2$	6.8×10^{-8}	0.80	9.7×10^{-5}	0.86	**1.1×10^{-1}**	**0.99**

Based on the relative metal loadings shown in Table 5.1, counter ions (Cl^- or NO_3^-) for the Co and Ni precursors may have had an effect on the metal adsorption process. The chloride precursors for Co and Ni achieved approximately 10% relative metal loading while the nitrate precursors achieved greater than 90%. This result suggests that the Cl^- ion may have inhibited metal adsorption. To further investigate this phenomenon, XPS was performed on the Mo_2C-supported metal catalysts synthesized from the chloride precursors. After depositing the metals, the samples were dried at room temperature in 1% O_2/He. The reduction step was not performed to ensure that any Cl that may have been deposited on the Mo_2C surface after metal loading remained on the surface. The Cl 2p spectra for these materials are shown in Figure 5.7. The Pt/Mo_2C and Cu/Mo_2C samples had the most intense Cl 2p peaks. The Cl/Mo atomic ratios for Pt/Mo_2C and Cu/Mo_2C were 0.165 and 0.045, respectively. These materials also had the highest relative metal loadings of all the metal chloride precursors. No clearly discernable Cl 2p peaks were observed for the Co/Mo_2C, Ni/Mo_2C, and Fe/Mo_2C samples. These materials had the lowest relative metal loadings of all the metal chloride precursors. The

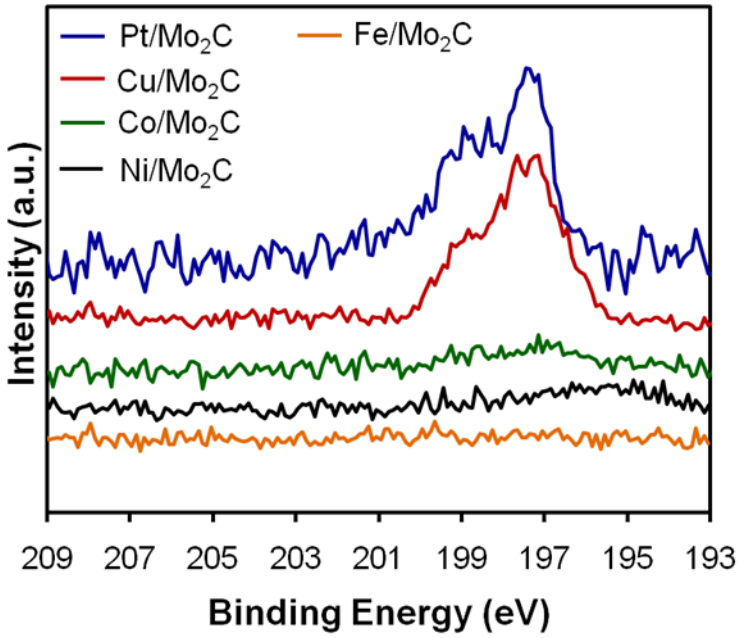

Figure 5.7: Cl 2p XPS spectra for the Pt/Mo_2C, Cu/Mo_2C, Co/Mo_2C, Ni/Mo_2C, and Fe/Mo_2C samples synthesized from the chlorine precursors. After metal loading, the samples were only dried in 1% O_2/He at room temperature; the reduction step was not performed.

chlorine concentration in the precursor solutions was 4.54 mmol/L, except for H_2PtCl_6 which was 13.62 mmol/L. These results suggest that Cl^- did not inhibit deposition.

Diffraction patterns for the Mo_2C and Mo_2C-supported metal catalysts synthesized from the nitrate precursors are shown in Figure 5.8. The patterns contained peaks for β-Mo_2C [38] and α-MoC_{1-x} [39]. No peaks were observed for MoO_2 [40] or MoO_3 [41]. There were also no clearly discernable peaks for the supported metals, indicating that crystallites, if present, were below the detection limit of the X-ray diffractometer. X-ray diffraction patterns for the Mo_2C-supported metal catalysts synthesized from the chloride precursors were similar.

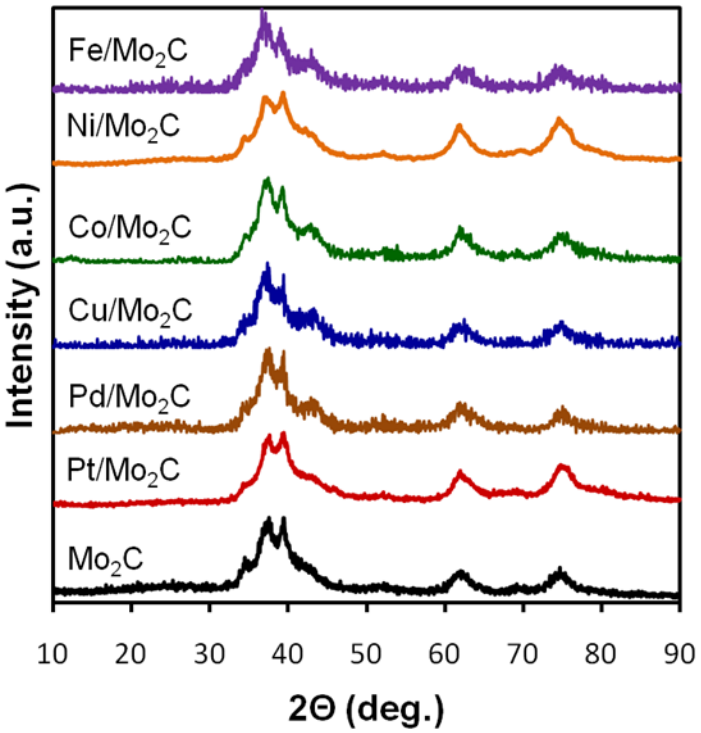

Figure 5.8: X-ray diffraction patterns for Mo_2C and Mo_2C-supported metal catalysts synthesized from the nitrate precursors (except for Pt).

X-ray absorption spectroscopy was used to investigate the oxidation states of the metals during synthesis. Spectra were collected at three different points during the synthesis procedure:

(i) Metal precursor dissolved in the dearated aqueous solution prior to adding Mo_2C. These spectra were labeled "Solution".

(ii) After 3 h of exposure of the precursor solution and Mo_2C, the material was removed from the solution without exposure to air and dried in an inert atmosphere at room temperature. These samples will be labeled as "Dried".

(iii) Instead of being dried in an inert atmosphere as in (ii), the material was removed from the precursor solution without exposure to air and reduced in H_2 at 450 °C. These samples will be labeled as "Reduced".

Spectra for the dried and reduced samples were collected without exposing the materials to air.

Figure 5.9 shows the x-ray absorption near edge structure (XANES) spectra for the precursor solution, dried, and reduced samples produced using the H_2PtCl_6, $Pd(NH_3)_4(NO_3)_2$, $CuCl_2$, $NiCl_2$, and $FeCl_2$ precursors as well as metal foil references (zero valent). For the Pt/Mo_2C material (Figure 5.9a), spectra for the dried and reduced samples resembled the spectrum for the Pt foil. The spectrum for the H_2PtCl_6 in solution had a strong white line indicating that the Pt was in an oxidized state. These results indicate that the Mo_2C support was capable of reducing the $[PtCl_6]^{2-}$ precursor directly to metallic Pt during the metal adsorption process. This type of response is not typically observed for oxide supports such as Al_2O_3, where the Pt remains in an oxidized state upon adsorption and is still complexed with Cl [43-46]. For Pd/Mo_2C (Figure 5.9b) and Cu/Mo_2C (Figure 5.9c), a result similar to that for Pt/Mo_2C was observed. The spectra for the dried and reduced samples resembled that of the metal foil reference. On the other hand, for Ni/Mo_2C (Figure 5.9d) and Fe/Mo_2C (Figure 5.9e), the dried samples closely resembled the precursor solution spectra while the reduced samples closely resembled the foil spectra. In both cases, the dried samples exhibited large white line peaks while the reduced samples did not have distinct peaks. These results indicate that the Mo_2C support can reduce the Pt, Pd, and Cu precursors to a metallic state during the wet impregnation process; however, Mo_2C was unable to reduce the Ni or Fe precursors.

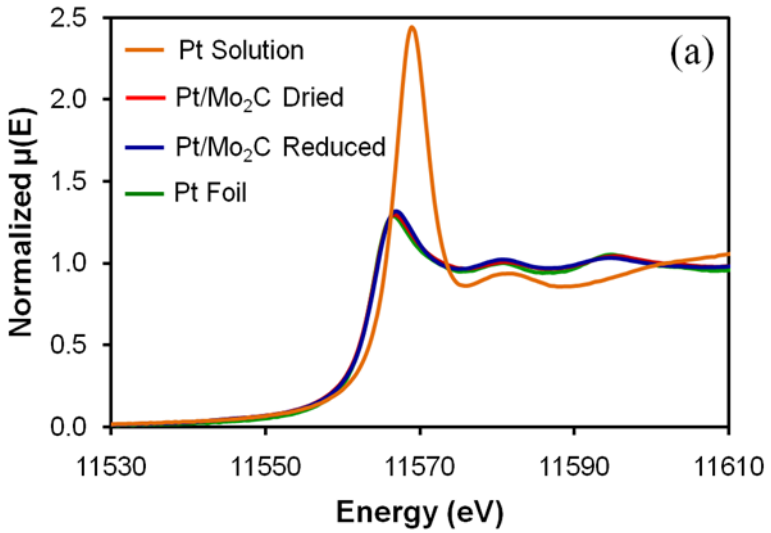
Pt Solution
Pt/Mo2C Dried
Pt/Mo2C Reduced
Pt Foil
(a)
Normalized μ(E)
Energy (eV)
2.5
2.0
1.5
1.0
0.5
0.0
11530
11550
11570
11590
11610

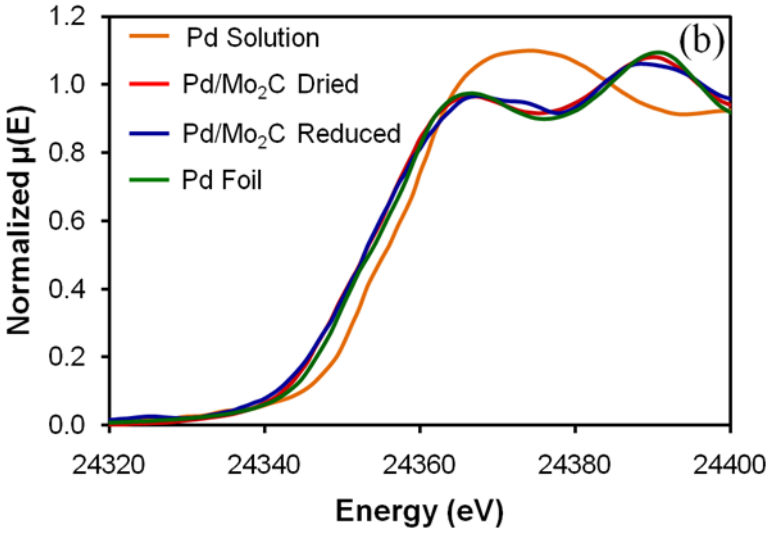
Pd Solution
Pd/Mo2C Dried
Pd/Mo2C Reduced
Pd Foil
(b)
Normalized μ(E)
Energy (eV)
1.2
1.0
0.8
0.6
0.4
0.2
0.0
24320
24340
24360
24380
24400

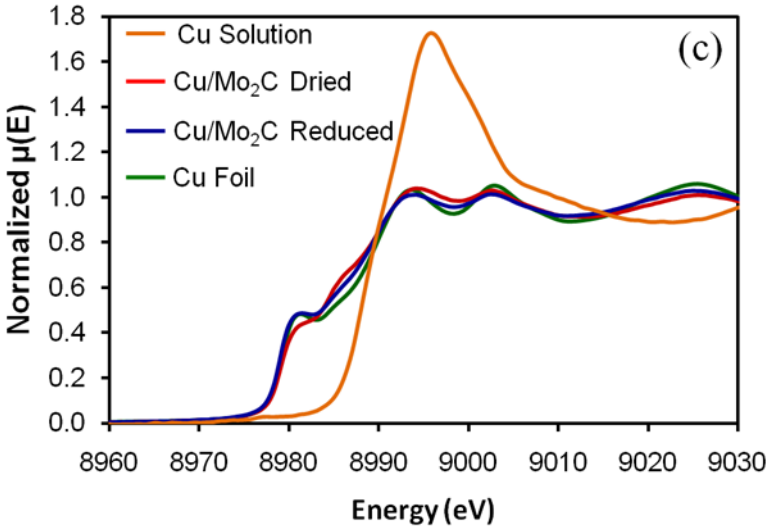
Cu Solution
Cu/Mo2C Dried
Cu/Mo2C Reduced
Cu Foil
(c)
Normalized μ(E)
Energy (eV)
1.8
1.6
1.4
1.2
1.0
0.8
0.6
0.4
0.2
0.0
8960
8970
8980
8990
9000
9010
9020
9030

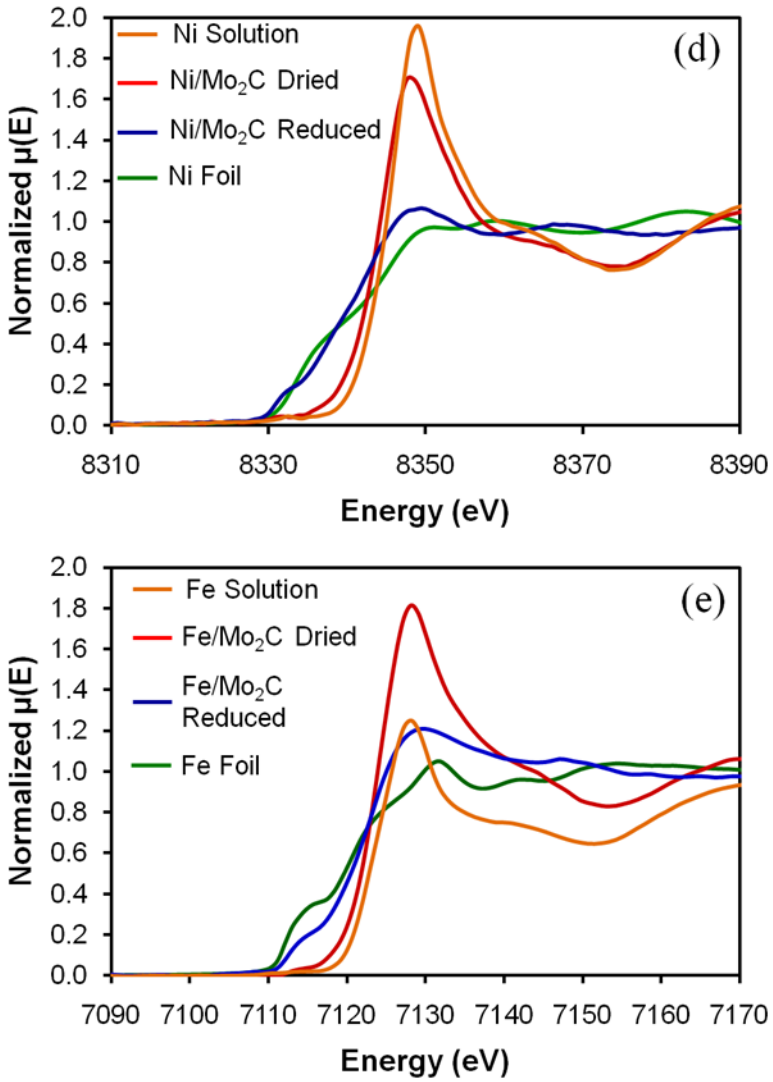

Figure 5.9: X-ray absorption near edge structure (XANES) spectra for the precursor solution, dried, and reduced samples as well as a metal foil reference (zero valent) for (a) H_2PtCl_6 at Pt L3 edge, (b) $Pd(NH_3)_4(NO_3)_2$ at Pd K edge, (c) $CuCl_2$ at Cu K edge, (d) $NiCl_2$ at Ni K edge, and (e) $FeCl_2$ at Fe K edge. Data collected in collaboration with Schweitzer [42].

5.4. Discussion

In this chapter, the interactions between metal precursors and a native Mo_2C surface during wet impregnation have been investigated. During metal deposition, multiple steps have to occur including transport of the metal ion/complex to the support surface, adsorption of the complex, and possibly a surface reaction with the support. This

section will discuss the dominant mechanisms controlling metal adsorption onto a Mo_2C support in regards to these different steps.

One mechanistic step proposed for the adsorption of metals on oxide supports involves electrostatic interactions between the support and the metal ion in solution [21-27]. If electrostatic interactions play a significant role in deposition of the metals onto the Mo_2C surface, one would expect the relative loading of the metals to be a function of the precursor solution pH. For a material like Mo_2C with a PZC of pH 5, the surface should be deprotonated, have a net negative charge, and electrostatically attract cations to the surface in solutions with pH > 5. The surface should be protonated, have a net positive charge, and attract anions in solutions with a pH < 5. Based on the findings of Regalbuto and others [23-27], the electrostatic interactions have the strongest effect on metal adsorption at pH values significantly away from the PZC of the support material. For example, see Figure 5.2 regarding Pt uptake as a function of pH for a series of unoxidized carbon xerogels [25]. The PZC for these materials was pH 9.4, therefore electrostatic attraction should occur between the anionic Pt precursor and the carbon xerogel surface at pH below 9.4. However, significant adsorption of the Pt did not occur until the pH was between 2-5. Therefore, it can be assumed that the electrostatic interactions will have very little effect on metal transport to the surface and adsorption over Mo_2C in the solution pH window of $4 < pH < 6$.

Figure 5.10 shows relative metal loadings for the different metal precursors on the Mo_2C surface as well as the initial pH of the precursor solution (taken from Table 5.1). The red dotted lines indicate the proposed "PZC window" for Mo_2C [40]. Any precursor species that lies outside of the window could be affected by the electrostatic interactions.

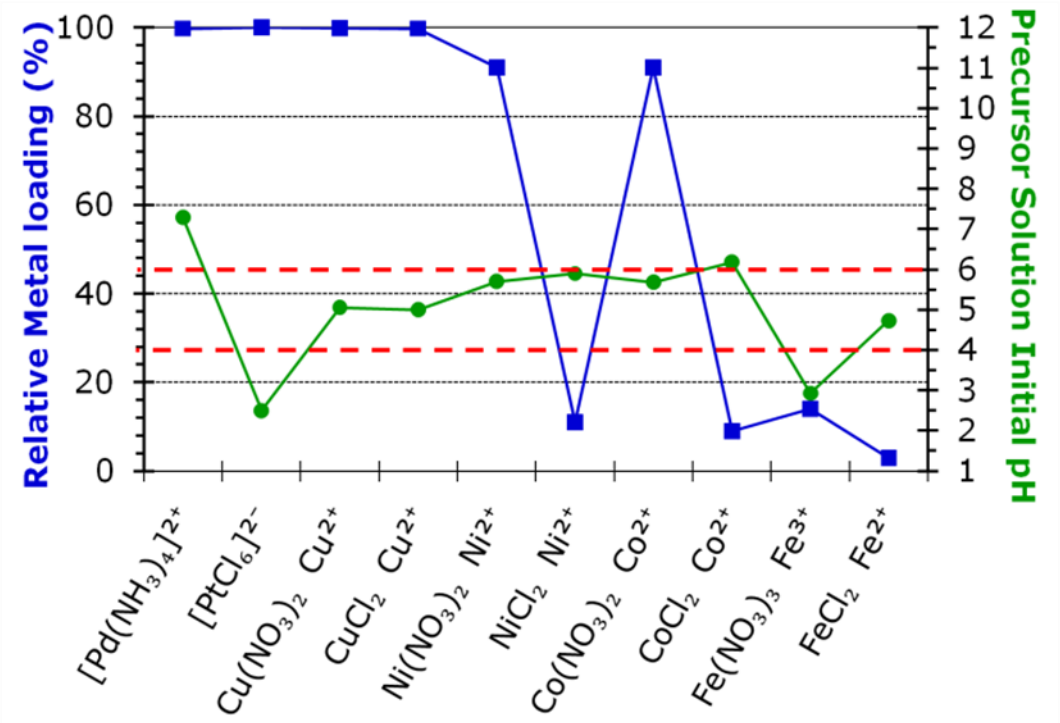

Figure 5.10: Relative metal loading and precursor solution initial pH as a function of metal precursor. The "PZC window" for Mo_2C ($4 < pH < 6$) is given by the red dotted lines. Graph was created in collaboration with Schweitzer [42].

Accordingly, the only species which might be affected are H_2PtCl_6, $Pd(NH_3)_4(NO_3)_2$, and $FeCl_3$. H_2PtCl_6 and $Pd(NH_3)_4(NO_3)_2$ would both benefit from the electrostatic interactions, thus facilitating the transport to the support surface and the adsorption of H_2PtCl_6 and $Pd(NH_3)_4(NO_3)_2$. The pH of the H_2PtCl_6 solution lies below the PZC of Mo_2C and H_2PtCl_6 produces an anionic metal complex, thus the net positive charge on the Mo_2C surface would attract the anionic Pt metal complex. For $Pd(NH_3)_4(NO_3)_2$, the pH lies above the PZC of Mo_2C and the Pd precursor produces a cationic metal species, thus the net negative charge on the Mo_2C surface would attract the cationic Pd metal complex. However, $FeCl_3$ would be inhibited by these electrostatic interactions since its pH is below the PZC of Mo_2C, but produces a metal cation. These electrostatic interactions likely play a role in the transport of the metal complex to the Mo_2C surface

and the coulombic adsorption of the complex; however, electrostatic interactions do not account for all of the observed results. The Cu precursors and Ni and Co nitrate precursors fall within the PZC window for Mo_2C, but exhibit relative loadings greater than 90%.

Another mechanistic step in the metal adsorption process involves a surface reaction between the metal complex and the support. Due to the metallic nature of early transition metal carbides, it is important to explore metal adsorption mechanisms outside of those typically reported for oxides. A surface red-ox reaction has been proposed to explain the synthesis of bimetallic metal particles [28, 32-33]. One example is the modification of Cu catalysts by the addition of Pd [28]. The two half reactions with their standard reduction potentials are given in Equations 5.3 and 5.4.

$$Pd^{2+} + 2e^- \rightarrow Pd \qquad E^0 = 0.99\ V \qquad (5.3)$$

$$Cu^{2+} + 2e^- \rightarrow Cu \qquad E^0 = 0.34\ V \qquad (5.4)$$

The difference in equilibrium potential determines the change in the free energy and the direction of the overall reaction (see Equation 5.5):

$$\Delta G^0 = -nF\left(E_1^0 - E_2^0\right) \qquad (5.5)$$

where n is the number of electrons transferred, F is faraday's constant, and E_i is the standard reduction potential of the respective half cell reaction [28]. For $E_1{}^0 > E_2{}^0$, the Gibb's free energy of the overall reaction will be negative and the reaction will be favorable. Therefore, the overall reaction between Pd and Cu is:

$$Cu + Pd^{2+} \rightarrow Cu^{2+} + Pd \qquad (5.6)$$

because $E^0_{Pd^{2=}/Pd}$ is greater than $E^0_{Cu^{2+}/Cu}$. Since carbides are metal like, it is possible that this phenomenon could occur in metal deposition on carbide surfaces as well.

Figure 5.11 displays the relative metal loadings as a function of the standard reduction potentials of the metal complex ions. Based on Gibb's free energy metal speciation calculations, the metal complex ions shown in Figures

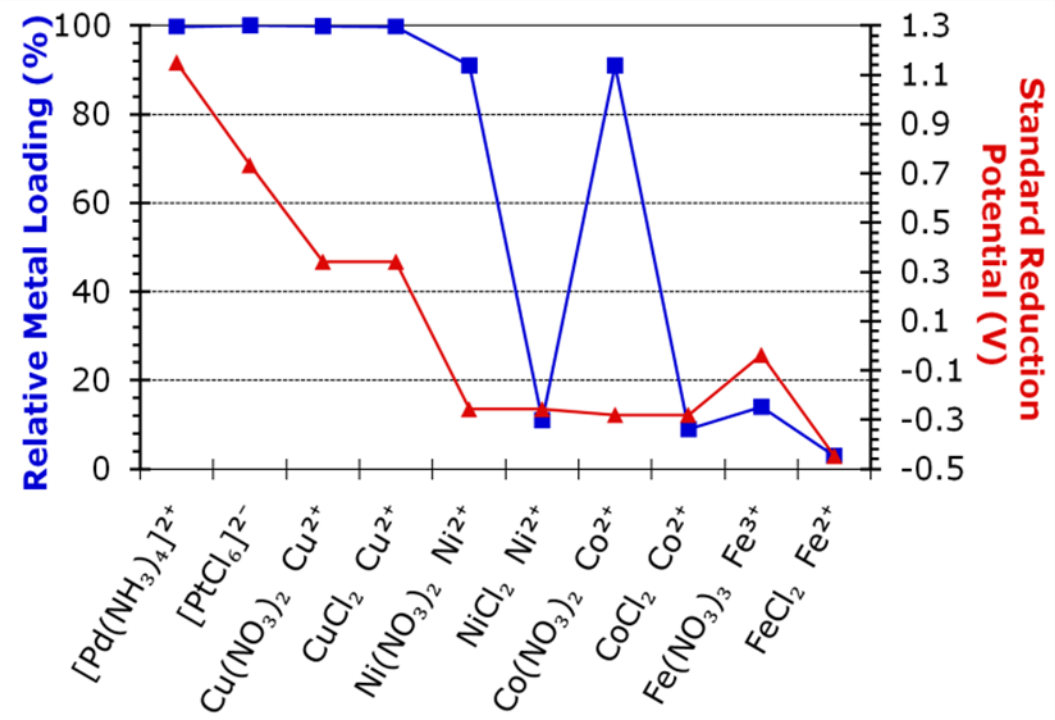

Figure 5.11: Relative metal loading and standard reduction potentials as a function of metal precursor. Standard reduction potentials taken from [47]. Graph was created in collaboration with Schweitzer [42].

5.10 and 5.11 were the most prevalent under the concentrations and conditions used in this study [42]. Generally, precursors that have high standard reduction potentials exhibited high relative loadings. For example, $[PtCl_6]^{2-}$, $[Pd(NH_3)_4]^{2+}$, and Cu^{2+} all have standard reduction potentials greater than 0.3V, and have relative loadings approaching 100%. Based on this observation, we propose that a critical step in the metal adsorption mechanism over Mo_2C involves the reduction of the metal precursor complex by a surface species [42]. This conclusion is supported by the XAS results (Figure 5.9). For the Pt, Pd, and Cu precursors, XANES spectra for the dried samples indicated the

presence of zero-valent metal, even though metal in the precursor solution was oxidized. On the other hand, the dried samples of the Ni and Fe catalysts were oxidized, also resembling the precursor solution. Considering the standard reduction potentials for the Pt, Pd, and Cu precursors, one can deduce that the standard reduction potential of the surface species that is oxidized via the red-ox reaction must be less than 0.3 V (see Equation 5.5). However, it is unclear whether the surface species that interacted with the precursors were Mo, C, or some other unknown species. Although Mo was observed in the solution during metal adsorption (Figure 5.6), a complex relationship existed between the Mo concentration and the metal precursor. For adsorption of all of the metals except Pd, the concentration of Mo was an order of magnitude lower than the initial concentration of metal in the loading solution. Further investigation is needed to determine if the dissolved Mo is present due to the surface redox reaction or some other phenomenon.

Additionally, the driving force for reduction of the metal ions by the Mo_2C surface might be directly related to the difference in reduction potential between the metal ion and the oxidized species. Based on Barbier [28], the extent of metal deposition depends on the red-ox reaction equilibrium constant, K_{eq}, given by Equation 5.7 [28]:

$$\ln K_{eq} = nF\frac{\left(E_1^0 - E_2^0\right)}{RT} \tag{5.7}$$

where R is the ideal gas constant and T is temperature. The Pt, Pd, and Cu precursors had the highest reduction potentials and demonstrated the fastest rates of metal adsorption (see Figure 5.5 and rate constants in Table 5.2). For Co and Ni, the reduction potentials were much lower than those for Pt, Pd, and Cu, and correspondingly the Co and Ni nitrate precursors showed much slower rates of metal adsorption (Table 5.2).

The results also support a conclusion that the nature of the counter ion plays a role in the deposition mechanism. For Ni and Co, the nitrate precursor yielded higher relative loadings than the chloride precursor. This result does not appear to be due to Cl blocking adsorption sites on the Mo_2C surface. XPS results (Figure 5.7) show that very little chlorine was present on the Mo_2C surface after depositing metal from $CoCl_2$, $NiCl_2$, or $FeCl_2$. Moreover, the Cl surface concentration was the highest for the metals with the highest relative metal loadings (H_2PtCl_6 and $CuCl_2$). Based on these findings, we propose two options that may explain these results. First, the NO_3^- counter ion could enhance the metal adsorption process over Mo_2C for the Ni and Co precursors, possibly changing the mechanism for adsorption. For example, the NO_3^- might facilitate oxidation of the Mo_2C surface species involved in the red-ox reaction. This result may be supported by the observation that the Co and Ni nitrate precursors followed second order kinetics while the Pt, Pd, and Cu precursors followed first order kinetics (Table 5.2). Second, Cl^- might form a complex with the metal ion in solution and alter its standard red-ox potential. It has been reported that red-ox properties can be modified by using different ligands [28]. For example, the reduction of Pd^{2+} to Pd metal has a standard reduction potential of 0.99 V whereas the reduction of Pd^{2+} present in the form of $PdCl_4^-$ has a standard reduction potential of 0.62 V. For Co and Ni, complexation with Cl could cause a decrease in the standard reduction potential, possibly lowering it below the standard reduction potential of the Mo_2C surface species. In this case, reduction of the Co and Ni would not be favorable and relative loading would be low. Moreover, this result would suggest that the reduction potential of the Mo_2C surface species would be around that of Co^{2+} and Ni^{2+}.

Finally, it is important to discuss the implications of these findings on further development of carbide-supported metal catalysts. First, the observed direct red-ox reaction between the Pt, Pd, and Cu precursors and the native Mo_2C surface may result in high metal dispersions. Schweitzer et al. reported that the strong interaction between H_2PtCl_6 and Mo_2C resulted in the formation of raft-like particles [13]. Second, the observed red-ox behavior suggests that supporting metals onto the native carbide surface may result in significantly different properties than supporting metals onto an oxidized (i.e. passivated) carbide surface.

5.5. Summary

The metal adsorption process onto a native Mo_2C surface via wet impregnation has been investigated for Pt, Pd, Cu, Co, Ni, and Fe precursors. The adsorption process was primarily governed by the red-ox chemistry of the metal and the Mo_2C support. For metal precursors with high standard reduction potentials (Pt, Pd, and Cu), the target metal loadings were achieved and the Mo_2C support was capable of reducing the metal complexes to a zero-valent state during the adsorption process. Further work is needed to identify the surface species that were oxidized during this red-ox reaction. For metal complexes with low standard reduction potentials, the loadings were ~10% and the metals remained in an oxidized state on the Mo_2C surface. Additionally, the precursor counter ion (Cl^- or NO_3^-) appeared to affect the metal adsorption process; nitrate precursors exhibited higher loadings than chloride precursors. Finally, electrostatic interactions may play a role in the transport process of the metal ion complexes to the Mo_2C support surface. As such, the electrostatic interactions and the red-ox surface reactions might work in tandem.

5.6. Acknowledgements

Elemental analysis and X-ray absorption spectroscopy experiments were performed in collaboration with Neil Schweitzer [42]. We also worked together on the interpretation of these results, as discussed in Section 5.4.

5.7. References

[1] C. H. Bartholomew, R. J. Farrauto, *Fundamentals of Industrial Catalytic Processes*, 2nd ed., John Wiley and Sons, 2006.

[2] G. C. Bond, G. Webb, *Catalysis, Volume 6*, Royal Society of Chemistry, 1983.

[3] A. Boisen, T. V. W. Janssens, N. Schumacher, I. Chorkendorff, S. Dahl, Support Effects and Catalytic Trends for Water Gas Shift Activity of Transition Metals *Journal of Molecular Catalysis A: Chemical* 315 (2010) 163-170.

[4] P. Panagiotopoulou, D. Kondarides, Effect of the Nature of the Support on the Catalytic Performance of Noble Metal Catalysts for the Water-Gas Shift Reaction *Catalysis Today* 112 (2006) 49-52.

[5] P. Panagiotopoulou, D. Kondarides, A Comparative Study of the Water-Gas Shift Activity of Pt Catalysts Supported on Single (MO_x) and Composite (MO_x/Al_2O_3, MO_x/TiO_2) Metal Oxide Carriers *Catalysis Today* 127 (2007) 319-329.

[6] I. D. Gonzalez, R. M. Navarro, W. Wen, N. Marinkovic, J. A. Rodriguez, F. Rosa, J. G. G. Fierro, A Comparative Study of the Water Gas Shift Reaction over Platinum Catalysts Supported on CeO_2, TiO_2, and Ce-modified TiO_2 *Catalysis Today* 149 (2010) 372-379.

[7] H. Iida, A. Igarashi, Characterization of a Pt/TiO_2 (rutile) Catalyst for Water Gas Shift Reaction at Low-Temperature *Applied Catalysis A: General* 298 (2006) 152-160.

[8] A. A. Phatak, N. Koryabkina, S. Rai, J. T. Ratts, W. Ruettinger, R. J. Farrauto, G. E. Blau, W. N. Delgass, F. H. Ribeiro, Kinetics of the Water-Gas Shift Reaction on Pt Catalysts Supported on Alumina and Ceria *Catalysis Today* 123 (2007) 224-234.

[9] K. G. Azzam, I. V. Babich, K. Seshan, L. J. Lefferts, A Bifunctional Catalyst for the Single-Stage Water-Gas Shift Reaction in Fuel Cell Applications. Part 2. Roles of the Support and Promoter on Catalyst Activity and Stability *Journal of Catalysis* 251 (2007) 163-171.

[10] A. Griboval-Constant, J.-M. Giraudon, G. Leclercq, L. Leclercq, Catalytic Behaviour of Cobalt and Ruthenium Supported Molybdenum Carbide Catalysts for FT Reaction, *Applied Catalysis A: General* 260 (2004) 35-45.

[11] M. Lewandowski, A. Szymanska-Kolasa, P. Da Costa, C. Sayag, Catalytic Performances of Platinum Doped Molybdenum Carbide for Simultaneous Hydrodenitrogenation and Hydrodesulfuization, *Catalysis Today* 119 (2007) 31-34.

[12] W. Setthapun, S. K. Bej, L. T. Thompson, Carbide and Nitride Supported Methanol Steam Reforming Catalysts: Parallel Synthesis and High Throughput Screening, *Topics in Catalysis* 49 (2008) 73-80.

[13] N. M. Schweitzer, J. A. Schaidle, O. K. Ezekoye, X. Pan, S. Linic, L. T. Thompson, High Activity Carbide Supported Catalysts for Water Gas Shift, *Journal of the American Chemical Society* 133 (2011) 2378-2381.

[14] J. A. Schaidle, A. C. Lausche, L. T. Thompson, Effects of Sulfur on Mo_2C and Pt/Mo_2C Catalysts: Water Gas Shift Reaction *Journal of Catalysis* 272 (2010) 235-245.

[15] D. V. Esposito, S. T. Hunt, A. L. Stottlemyer, K. D. Dobson, B. E. McCandless, R. W. Birkmire, J. G. Chen, Low-Cost Hydrogen-Evolution Catalysts Based on Monolayer Platinum on Tungsten Monocarbide Substrates *Angewandte Chemie* 49 (2010) 9859-9862.

[16] D. J. Ham, C. Pak, G. H. Bae, S. Han, K. Kwon, S-A. Jin, H. Chang, S. H. Choi, J. S. Lee, Palladium-Nickel Alloys Loaded on Tungsten Carbide as Platinum-Free Anode Electrocatalysts for Polymer Electrolyte Membrane Fuel Cells *Chemical Communications* 47 (2011) 5792-5794.

[17] I. J. Hsu, D. A. Hansgen, B. E. McCandless, B. G. Willis, J. G. Chen, Atomic Layer Deposition of Pt on Tungsten Monocarbide (WC) for the Oxygen Reduction Reaction *Journal of Physical Chemistry C* 115 (2011) 3709-3715.

[18] M. Nie, H. Tang, Z. Wei, S. P. Jiang, P. K. Shen, Highly Efficient AuPd-WC/C Electrocatalyst for Ethanol Oxidation *Electrochemistry Communications* 9 (2007) 2375-2379.

[19] R. Ganesan, J. Dong, J. S. Lee, Platinized Mesoporous Tungsten Carbide for Electrochemical Methanol Oxidation, *Electrochemistry Communications* 9 (2007) 2576-2579.

[20] E. C. Weigert, S. Arisetty, S. G. Advani, A. K. Prasad, J. G. Chen, Electrochemical Evaluation of Tungsten Monocarbide (WC) and Platinum-

modified WC as Alternative DMFC Electrocatalysts *Journal of New Materials for Electrochemical Systems* 11 (2008) 243-251.

[21] J. P. Brunelle, Preparation of Catalysts by Metallic Complex Adsorption on Mineral Oxides *Pure & Appied. Chemistry* 50 (1978) 1211-1229.

[22] J.-F. Lambert, M. Che, The Molecular Approach to Supported Catalysts Synthesis: State of the Art and Future Challenges *Journal of Molecular Catalysis A: Chemical* 162 (2000) 5-18.

[23] K. B. Agashe, J. R. Regalbuto, A Revised Physical Theory for Adsorption of Metal Complexes at Oxide Surfaces *Journal of Colloid and Interface Sci*ence 185 (1997) 174-189.

[24] J. R. Regalbuto, A. Navada, S. Shadid, M. L. Bricker, Q. Chen, An Experimental Verification of the Physical Nature of Pt Adsorption onto Alumina *Journal of Catalysis* 184 (1999) 335-348.

[25] S. Lambert, N. Job, L. D'Souza, M. F. R. Pereira, R. Pirard, B. Heinrichs, J. L. Figueiredo, J.-P. Pirard, J. R. Regalbuto, Synthesis of Very Highly Dispersed Platinum Catalysts Supported on Carbon Xerogels by the Strong Electrostatic Adsorption Method *Journal of Catalysis* 261 (2009) 23-33.

[26] L. Jiao, J. R. Regalbuto, The Synthesis of Highly Dispersed Noble and Base Metals on Silica via Strong Electrostatic Adsorption: I. Amorphous Silica, *Journal of Catalysis* 260 (2008) 329-341.

[27] M. Schreier, J. R. Regalbuto, A Fundametal Study of Pt Tetraammine Impregnation of Silica 1. The Electrostatic Nature of Platinum Adsorption *Journal of Catalysis* 225 (2004) 190-202.

[28] J. Barbier, in: G. Ertl, H. Knozinger, J. Weitkamp (Eds.), *Preparation of Solid Catalysts*, Wiley-VCH, 1999.

[29] J. R. Kitchin, J. K. Norskov, M. A. Barteau, J. G. Chen, Trends in the Chemical Properties of Early Transition Metal Carbide Surfaces: A Density Functional Study, *Catalysis Today* 105 (2005) 66-73.

[30] C. Ruberto, A. Vojvodic, B. I. Lundqvist, Nature of Chemisorption on Titanium Carbide and Nitride *Surface Science* 600 (2006) 1612-1618.

[31] A. Vojvodic, A. Hellman, C. Ruberto, B. I. Lundqvist, From Electronic Structure to Catalytic Activity: A Single Descriptor for Adsorption and Reactivity on Transition-Metal Carbides, *Physical Review Letters* 103 (2009) 146103.

[32] J. Barbier, J. C. Menezo, C. Montassier, J. Naja, Modification of Copper by Redox Reaction: Location of Ru on Cu-Ru Bimetallic Catalysts *Catalysis Letters* 14 (1992) 37-43.

[33] C. Montassier, J. C. Menezo, J. Naja, J. Barbier, J. M. Dominguez, P. Sarrazin, B. Didillon, Preparation and Characterization of Copper Based Bimetallic Catalysts *Journal of Molecular Catalysis* 91 (1994) 107-117.

[34] J. Park, J. R. Regalbuto, A Simple, Accurate Determination of Oxide PZC and the Strong Buffering Effect of Oxide Surfaces at Incipient Wetness *Journal of Colloid and Interface Science* 175 (1995) 239-252.

[35] M. Newville, *X-ray Absorption Fine-Structure Spectroscopy*, 2008 Advanced Photon Source National School on Neutron and X-ray Scattering, Argonne National Laboratory, August 5, 2008.

[36] S. Kelly, *XAS Data Processing*, 2008 Advanced Photon Source National School on Neutron and X-ray Scattering, Argonne National Laboratory, August 5, 2008.

[37] H.S. Fogler, *Elements of Chemical Reaction Engineering*, 3rd ed., Prentice Hall, New Jersey, 1999. p. 235-237.

[38] S. Nagakura, M. Kikuchi, S. Oketani, Electron Diffraction Determination of the Ionization of the Carbon Atom in β-Mo_2C Crystal *Acta Crystallographica* 21 (1966) 1009-1010.

[39] J. C. Schuster, H. Nowotny, Mo- and (Mo,W)-Carbides Within the Temperature Range 600-1600°C *Monatshefte fur Chemie* 110 (1979) 321-332.

[40] M. Ghedira, C. Do-Dinh, M. Marezio, J. Mercier, The Crystal Structure of $Mo_{0.975}Ti_{0.025}O_2$ between 24 and 900°C *Journal of Solid State Chemistry* 59 (1985) 159-167.

[41] J. D. Hanawalt, H. W. Rinn, L. K. Frevel, Chemical Analysis by X-ray Diffraction: Classification and Use of X-ray Diffraction Patterns *Industrial and Engineering Chemistry: Analytical Edition* 10 (1938) 457-512.

[42] N. M Schweitzer, Evaluating the Effect of a Strong Metal-Support Interaction on the Activity of Molybdenum Carbide Supported Platinum Water-Gas Shift Catalysts, Ph. D. Thesis, University of Michigan, 2010.

[43] B. Shelimov, J.-F. Lambert, M. Che, B. Didillon, Initial Steps of the Alumina-Supported Platinum Catalyst Preparation: A Molecular Study by ^{195}Pt NMR, UV-Visible, EXAFS, and Raman Spectroscopy *Journal of Catalysis* 185 (1999) 462-478.

[44] B. N. Shelimov, J.-F. Lambert, M. Che, B. Didillon, Molecular-level Studies of Transition Metal-Support Interactions during the First Steps of Catalysts Preparation: Platinum Speciation in the Hexachloroplatinate/Alumina System *Journal of Molecular Catalysis A: Chemical* 158 (2000) 91.

[45] W. A. Spieker, J. Liu, J. T. Miller, A. J. Kropf, J. R. Regalbuto, An EXAFS Study of the Co-ordination Chemistry of Hydrogen Hexachloroplatinate (IV): 1. Speciation in Aqueous Solution *Applied Catalysis A: General* 232 (2002) 219-235.

[46] W. A. Spieker, J. Liu, X. Hao, J. T. Miller, A. J. Kropf, J. R. Regalbuto, An EXAFS Study of the Coordination Chemistry of Hydrogen Hexachloroplatinate (IV): 2. Speciation of Complexes Adsorbed onto Alumina *Applied Catalysis A: General* 243 (2003) 53-66.

[47] P. Vanysek, *Electrochemical Series*, Handbook of Chemistry and Physics, CRC Press, 2000.

CHAPTER 6

Mo_2C-Supported Metal Catalysts for Fischer-Tropsch Synthesis

6.1. Introduction

In Chapter 3 it was reported that early transition metal carbides and nitrides (e.g. Mo_2C) primarily favored the production of light hydrocarbons (C_1-C_4) during Fischer-Tropsch Synthesis (FTS). Higher hydrocarbons (C_5+), specifically hydrocarbons with chain lengths in the range of those for gasoline (C_7-C_{11}), diesel fuel (C_{10}-C_{19}), and waxes (C_{20}+) are typically the desired products. In an attempt to enhance the performance, metals including Pt, Co, Fe, Ru, Cu, Rh, and Ni were deposited onto the surfaces of Mo_2C. This chapter describes the Fischer-Tropsch Synthesis performance of these Mo_2C-supported metal catalysts.

Mo_2C-supported metal catalysts have been investigated previously by Schweitzer [1, 2], King [3], and Patt [4] for the water gas shift reaction and Griboval-Constant et al. for Fischer-Tropsch Synthesis [5]. Schweitzer and King reported higher water gas shift activities for Pt/Mo_2C catalysts compared to Mo_2C and attributed the enhancement to the bi-functional nature of the Mo_2C-supported Pt catalyst. The Mo_2C sites were proposed to perform H_2O activation while the Pt sites were proposed to adsorb CO [2]. The oxidation of CO was proposed to occur at the interface of the Mo_2C and Pt particles [2]. Free energy diagrams for the water gas shift reaction over an O-terminated Mo_2C surface and an O-terminated Mo_2C surface in which Pt serves as the binding site for CO are shown in Figure 6.1 [2]. The addition of Pt significantly decreased the energy barrier for CO

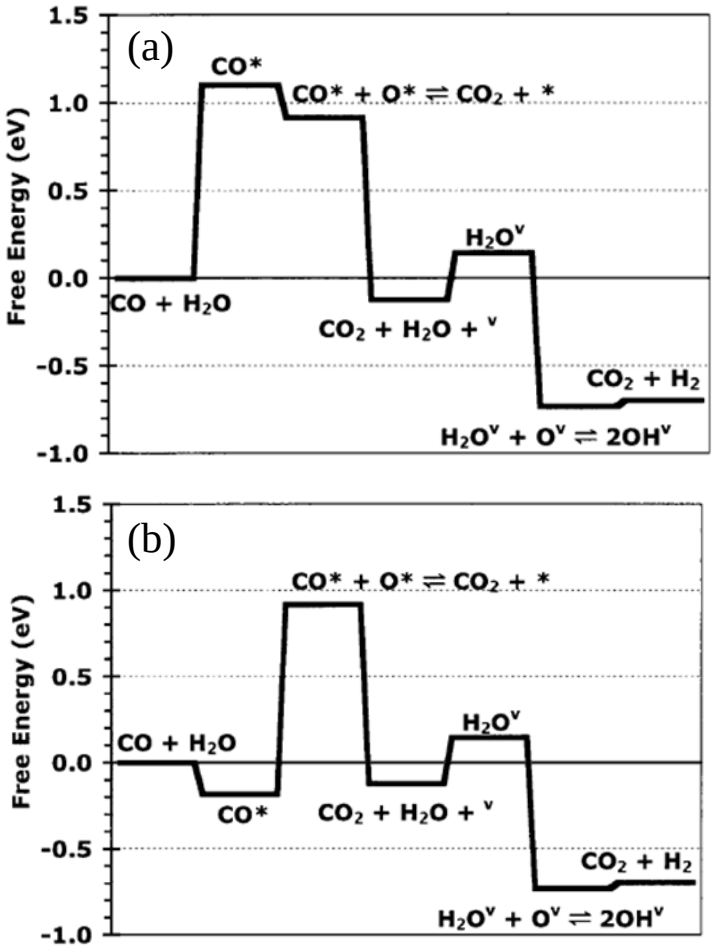

Figure 6.1: Free energy diagrams for the water gas shift reaction mechanism calculated at 240°C using density functional theory over (a) an O-terminated Mo_2C surface and (b) an O-terminated Mo_2C surface in which Pt serves as the binding site for CO. Taken from [2].

adsorption, thereby causing the rate-limiting step for Pt/Mo_2C to be CO oxidation. The bi-functional nature of the catalyst and the presence of "raft-like" Pt particles (which have a high density of $Pt\text{-}Mo_2C$ interface sites on which CO and O can react) resulted in high WGS rates [1, 2].

Griboval-Constant et al. reported that Ru/Mo_2C and Co/Mo_2C exhibited higher FTS rates than Mo_2C [5]. More specifically, Co/Mo_2C exhibited a rate almost 4 times higher than that of Mo_2C at 240°C, 20 bar, and $H_2/CO = 2$. However, no significant change in hydrocarbon selectivity (e.g. C_5+ selectivity and ASF α value) was observed

due to the addition of Ru or Co. For this study, the Mo_2C support surface area was low (~7 m^2/g) and the metal loadings of Ru and Co were 1 wt% [5]. Assuming a site density of $1x10^{19}$ sites/m^2, the surface coverage of Ru and Co was approximately 85% and 150%, respectively. Due to these high surface coverages, the observed FTS performance of Ru/Mo_2C and Co/Mo_2C may have been the result of the innate catalytic properties of the supported metals, and not a combination of the support and the metal. In addition, these materials were synthesized using the passivated Mo_2C support [5]. Therefore, the metal precursors were interacting with an oxidized Mo_2C surface instead of the native Mo_2C surface. Finally, the catalysts were pretreated in pure H_2 to reduce the supported metals, without consideration for recarburizing the Mo_2C support surface.

The objective of research described in this chapter was to evaluate the FTS performance of Mo_2C-supported metal catalysts. The supported metals included Pt, Co, Fe, Ru, Cu, Rh, and Ni. The catalysts were synthesized using the wet impregnation technique discussed in Chapter 5. This method allowed the metal precursor to interact directly with the native Mo_2C surface. The activities and selectivities of the catalysts for FTS were tested in a fixed bed reactor at 270-300°C, 25 bar, and $H_2/CO = 2$. The catalysts were characterized using X-ray diffraction, elemental analysis, CO chemisorption experiments, temperature programmed reduction experiments, and X-ray absorption spectroscopy.

6.2. Experimental Setup

6.2.1. Catalyst Synthesis

The Mo_2C support was synthesized via a temperature programmed reaction as described in Chapter 3 (Section 3.2.1). Upon completion of the temperature program, the

material was cooled to room temperature in flowing 15% CH_4/H_2. Metals were deposited onto the support via wet impregnation. The metals selected for investigation were Pt, Co, Fe, Ru, Cu, Rh, and Ni. Except for Pt, these metals are common catalysts for CO hydrogenation reactions: Co, Fe, and Ru for FTS [6], Cu and Rh for alcohol synthesis [7], and Ni for methanation [8, 9]. Pt was included based on results from Chapter 4, which indicated that Mo_2C primarily followed an oxygenate or CO-insertion mechanism, and Pt might increase the number of sites for molecular CO adsorption on the catalyst surface. Based on the results from Chapter 5, the following metal precursors were selected H_2PtCl_6, $Co(NO_3)_2$, $Fe(NO_3)_3$, $RuCl_3$, $Cu(NO_3)_2$, $Rh(NO_3)_3$, and $Ni(NO_3)_2$.

For the wet impregnation procedure, 70 mL of deionized water was added to a glass container and bubbled with Ar for 15 min to remove any dissolved oxygen. Next, the desired amount of metal precursor was dissolved in the water. The amount of metal precursor added corresponded to ~10% surface coverage of the Mo_2C support, which has a surface area of ~120 m^2/g. The resulting metal loading solution had a concentration of 2.27 mmol metal/L. The unpassivated Mo_2C powder (0.75 g) was then transferred under Ar to the solution as bubbling was maintained. The support powder was left in the solution for varying times depending on the extent of adsorption observed in Chapter 5. The solution was continuously bubbled with Ar and periodically stirred.

Upon completion of metal deposition, the material was transferred back into the quartz reactor tube under Ar flow (no exposure to air). The sample was then dried at room temperature in flowing H_2 for 3 h. After being dried, the sample was exposed to the following reduction procedure in flowing H_2: 110°C for 2 h followed by 450°C for 4

h. The sample was then cooled to room temperature in flowing H_2. Finally, the material was passivated in 1% O_2/He flowing at 20 mL/min at room temperature for 6 h.

The resulting Mo_2C-supported metal catalysts had nominal metal surface loadings of 1.1 atom/nm^2. In addition to this set of catalysts, a Pt-Co/Mo_2C catalyst was also synthesized. This catalyst was investigated because oxide-supported Co catalysts promoted with noble metals have been reported to exhibit high turnover frequencies for FTS [10]. For this catalyst, the Co was deposited first via the method described above. After the reduction treatment (without passivation), the wet impregnation procedure was repeated for Pt deposition. The sample was then reduced and passivated as described above. For the Pt-Co/Mo_2C catalyst, the Co nominal surface loading was 1.1 atom/nm^2 while the Pt nominal surface loading was 0.2 atom/nm^2. Therefore, the atomic ratio of Co:Pt was 5:1.

6.2.2. Catalyst Characterization

6.2.2.1.X-ray Diffraction

X-ray diffraction patterns of the Mo_2C-supported metal catalysts were collected using a Rigaku miniflex X-ray diffractometer with a Cu-Kα (λ = 1.54nm) radiation source and a Ni filter. A range of $10° < 2\theta < 90°$ was scanned at a rate of 5°/min with a 0.02° step size.

6.2.2.2.Elemental Analysis

Elemental analysis of the Mo_2C-supported metal catalysts was performed using Inductively Coupled Plasma-Optical Emission Spectroscopy (ICP-OES). First, 15mg of material was dissolved using 3mL of aqua regia solution (75%vol HCl and 25%vol HNO_3). The solution was left for 24 h. Next, 1mL of the aqua regia solution was diluted

with 13mL of deionized water and was ready for analysis. The solutions were analyzed using a Varian 710-ES ICP Optical Emission Spectrometer. For each analysis, quantification was performed by comparing the relative intensities of the catalyst solutions to the relative intensities of several standards of known concentrations.

6.2.2.3.CO Uptake Measurements

CO pulse chemisorption experiments were performed at room temperature as discussed in Chapter 3 (Section 3.2.2). Prior to analysis, the Mo_2C-supported metal catalysts were pretreated with 15% CH_4/H_2 at 590°C for 4 h, followed by degassing in He at 600°C. During CO pulsing, the effluent stream was analyzed using the thermal conductivity detector (TCD) and the mass spectrometer (MS).

6.2.2.4.Temperature Programmed Reduction Experiments

Temperature Programmed Reduction (TPR) experiments for the Mo_2C-supported metal catalysts were performed in a Micromeritics 2910 AutoChem Chemisorption analyzer. A schematic of the chemisorption analyzer was given in Chapter 2 (Figure 2.2). Approximately 100 mg of passivated catalyst was loaded into a quartz u-tube reactor and supported by a quartz wool plug. The sample was then degassed in flowing Ar at 200°C for 2 h. Following cooling to room temperature in Ar, the sample was exposed to a 10% H_2/Ar mixture flowing at 70 mL/min. The temperature was then linearly increased at 20°C/min to a final temperature of 800°C. The consumption of H_2 was monitored using the TCD.

6.2.2.5.X-ray Absorption Spectroscopy

X-ray absorption spectroscopy (XAS) experiments were performed on a subset of the Mo_2C-supported metal catalysts (Cu/Mo_2C, Co/Mo_2C, and Fe/Mo_2C) to probe the

reduction of the supported metal as a function of pretreatment temperature in 100% H_2 and 15% CH_4/H_2. The experiments were performed as described in Chapter 5 (Section 5.2.2.4). The edges collected were the Cu K edge (8979 eV), the Co K edge (7709 eV), and the Fe K edge (7112 eV). Spectra were collected in fluorescence mode.

Prior to collection of the spectra, the samples were pretreated in a quartz reactor tube in either 100% H_2 or 15% CH_4/H_2 flowing at 100 mL/min. The samples were held at a specified temperature for 1 h (temperatures studied: room temperature, 150°C, 300°C, 450°C, and 590°C). The samples were then cooled to room temperature in the pretreatment gas. The quartz tube was then purged with He and sealed to protect the samples from exposure to air. The samples were then transferred to the beamline and spectra were collected.

XAS spectra were analyzed using Athena as discussed in Chapter 5. However, for this study, the EXAFS region was also explored. R-space data was plotted by first converting the post-edge data into k-space with a k^2 weighting. The photo-electron wavenumber, *k*, is given by Equation 6.1 [11]:

$$k = \sqrt{\frac{2m(E - E_0)}{\hbar^2}} \tag{6.1}$$

where E is the x-ray energy, E_0 is the edge energy, $\hbar$ is Planck's constant, and m is the mass of an electron. Then, using a Fourier transform, the k-space data was converted into R-space. A Hanning window function was used during this conversion. The range of k-space data converted into R-space was selected based on the noise in the data; typically the k-space range was ~2Å^{-1} to ~12Å^{-1}.

6.2.3. Fischer-Tropsch Synthesis Experiments

Fischer-Tropsch Synthesis (FTS) experiments were performed as described in detail in Chapter 3 (Section 3.2.3). The conditions for these experiments were 270-300°C, 25 bar, H_2/CO = 2, and GHSV = 44,000 h^{-1}. Prior to FTS, the Mo_2C-supported metal catalysts were pretreated at atmospheric pressure in 15% CH_4/H_2 at 590°C for 4 h (the same pretreatment used for Mo_2C).

6.3. Results

6.3.1. Catalyst Characterization

X-ray diffraction patterns for the Mo_2C-supported metal catalysts are shown in Figure 6.2. Compared to Mo_2C, the Ru/Mo_2C, Cu/Mo_2C, and Rh/Mo_2C catalysts

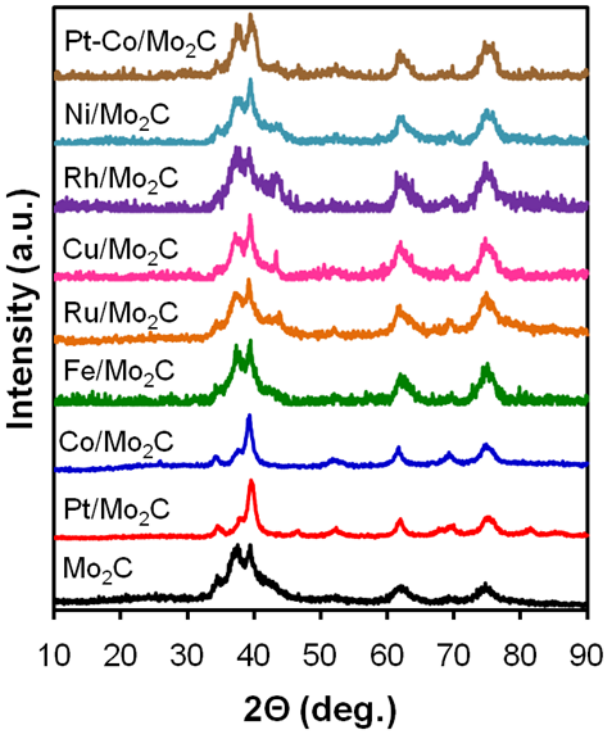

Figure 6.2: X-ray diffraction patterns for Mo_2C and the Mo_2C-supported metal catalysts.

appeared to have an additional peak at ~42°. This peak corresponds to the supported metal for these materials (Ru(101) reflection [12], Cu(111) reflection [13], and Rh(111)

reflection [14]). For the remainder of the Mo_2C-supported metal catalysts, peaks corresponding to the supported metals were not discernable, suggesting high dispersions. The particle size detection limit for the x-ray diffractometer was ~5nm. The nominal and actual metal weight loadings as well as the CO uptakes for the catalysts are given in Table 6.1. With the exception of Fe and Ru, the actual loadings were similar to the nominal loadings. Nominal loadings were based on the assumption that 100% of the metal in solution was deposited on the Mo_2C surface. Recall from Chapter 5 that for Fe, only a small percentage of metal was deposited on Mo_2C even after 20 h in the loading solution. For Ru, it has been reported that it is difficult to dissolve Ru in aqua regia [15], therefore, the low measured metal loading may be due to Ru remaining as a solid and being removed from the solution during filtering prior to ICP-OES analysis. Based on the relatively high reduction potential of Ru ($E^0_{Ru^{2+}/Ru}$ = 0.455 V [16]) and the findings from Chapter 5, it would be expected that Ru could achieve close to 100% relative loading.

Table 6.1: Elemental analysis and CO uptake results for Mo_2C and the Mo_2C-supported metal catalysts.

Catalyst	Nominal Loading (wt. %)	Actual Loading[1] (wt. %)	CO Uptake[2] (μmol/g)
Mo_2C	--	--	268
Pt/Mo_2C	4	4.1 ± 0.1	181
Co/Mo_2C	1.2	0.9 ± 0.1	291
Fe/Mo_2C	1.2	0.3 ± 0.1	354
Ru/Mo_2C	2.1	0.9 ± 0.2	247
Cu/Mo_2C	1.3	1.3 ± 0.1	221
Rh/Mo_2C	2.1	2.0 ± 0.1	290
Ni/Mo_2C	1.2	1.1 ± 0.1	280
$Pt\text{-}Co/Mo_2C$	0.8 Pt 1.2 Co	0.9 ± 0.1 1.1 ± 0.1	283

[1] Determined by ICP-OES.
[2] Determined by room temperature CO chemisorption. The error on CO uptake measurements was ± 10 μmol/g.

The CO uptakes for the catalysts ranged from 181 µmol/g (Pt/Mo_2C) to 354 µmol/g (Fe/Mo_2C). It is interesting that the addition of Pt caused a decrease in the CO uptake compared to Mo_2C, as Pt is known to adsorb CO. One possible explanation is that Pt may be blocking some of the pores of Mo_2C, thus decreasing the overall number of sites for CO adsorption.

Reduction profiles of the passivated Mo_2C-supported metal are shown in Figure 6.3. For Mo_2C, a broad reduction peak was observed around 280°C along with a

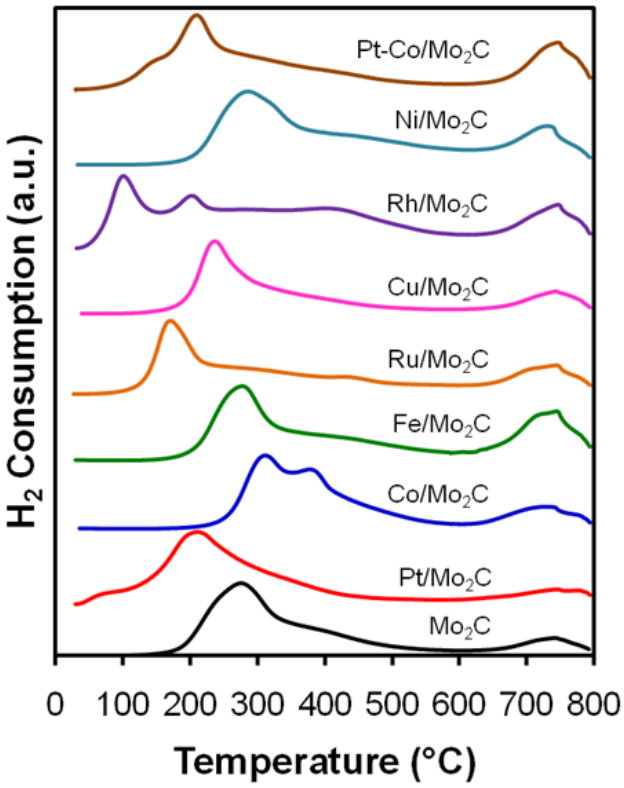

Figure 6.3: H_2 consumption during temperature programmed reduction procedure for Mo_2C and Mo_2C-supported metal catalysts. Conditions: 10% H_2/Ar, ramp rate = 20°C/min.

shoulder at 400°C. These peaks are primarily due to the removal of the passivation layer [4]. The peak at 750°C corresponds to the decomposition of Mo_2C to Mo; the carbon in the catalyst was removed in the form of CH_4 [3, 4]. For the Fe/Mo_2C and Ni/Mo_2C

catalysts, the TPR spectra were similar to that for Mo_2C; no additional peaks or temperature shifts were observed. The addition of metals such as Pt, Ru, Cu, and Rh caused a shift toward lower temperature for the removal of the passivation layer of the Mo_2C support. This shift has been reported previously for Pt/Mo_2C catalysts [17] and could be due to a H_2 spillover effect [18-20]. The addition of Co caused the opposite effect; the peak position for Mo_2C reduction was shifted towards higher temperatures. Additionally, a more-defined peak was observed at 380°C. This peak may be due to the reduction of cobalt oxides (Co_3O_4 and CoO) [21]. It has been reported that Co oxides are often difficult to reduce (require high reduction temperatures) when the Co interacts strongly with the support [21]. To counteract this effect, Co FTS catalysts are often doped with Pt or some other noble metal to facilitate reduction of the Co oxides at lower temperatures [8, 21]. As shown in Figure 6.2, the $Pt\text{-}Co/Mo_2C$ TPR spectrum was similar to that of Pt/Mo_2C, suggesting that the addition of Pt aided in the reduction of the Co oxide. However, it is also possible that the Co oxide particles were completely covered by Pt, thus eliminating the Co oxide reduction peak in the TPR profile.

From the TPR spectra, it is difficult to assign peaks to the reduction of the supported metals. Accordingly, a subset of the catalysts was characterized using XAS. The reduction of Cu/Mo_2C, Co/Mo_2C, and Fe/Mo_2C was monitored as a function of temperature during exposure to 100% H_2 or 15% CH_4/H_2. These three catalysts represent a range of reducibilities with Cu being easier to reduce and Co and Fe more difficult. The XANES spectra for the Cu/Mo_2C catalyst pretreated in H_2 and 15% CH_4/H_2 at various temperatures are shown in Figure 6.4. Without pretreatment, the passivated Cu/Mo_2C sample exhibited a stronger whiteline than the Cu metal reference, suggesting that the Cu

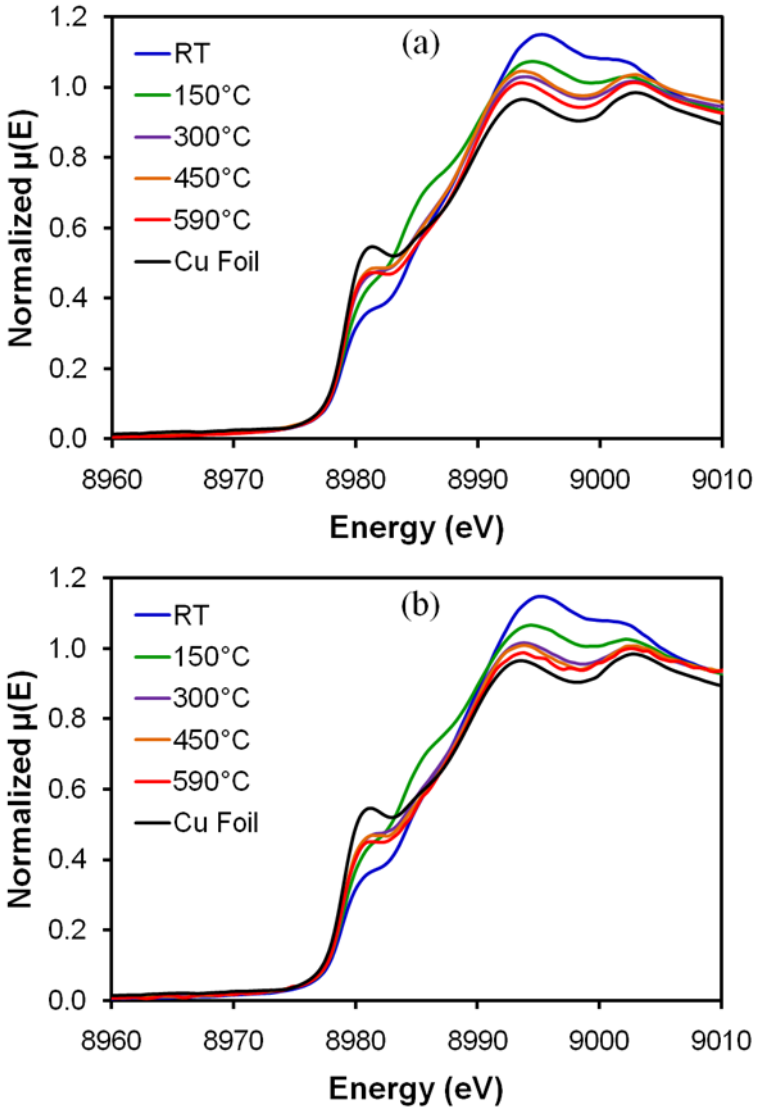

Figure 6.4: Cu K edge XANES spectra for the Cu/Mo_2C catalyst pretreated at various temperatures in (a) 100% H_2 and (b) 15% CH_4/H_2. A spectrum for a Cu foil reference is also shown.

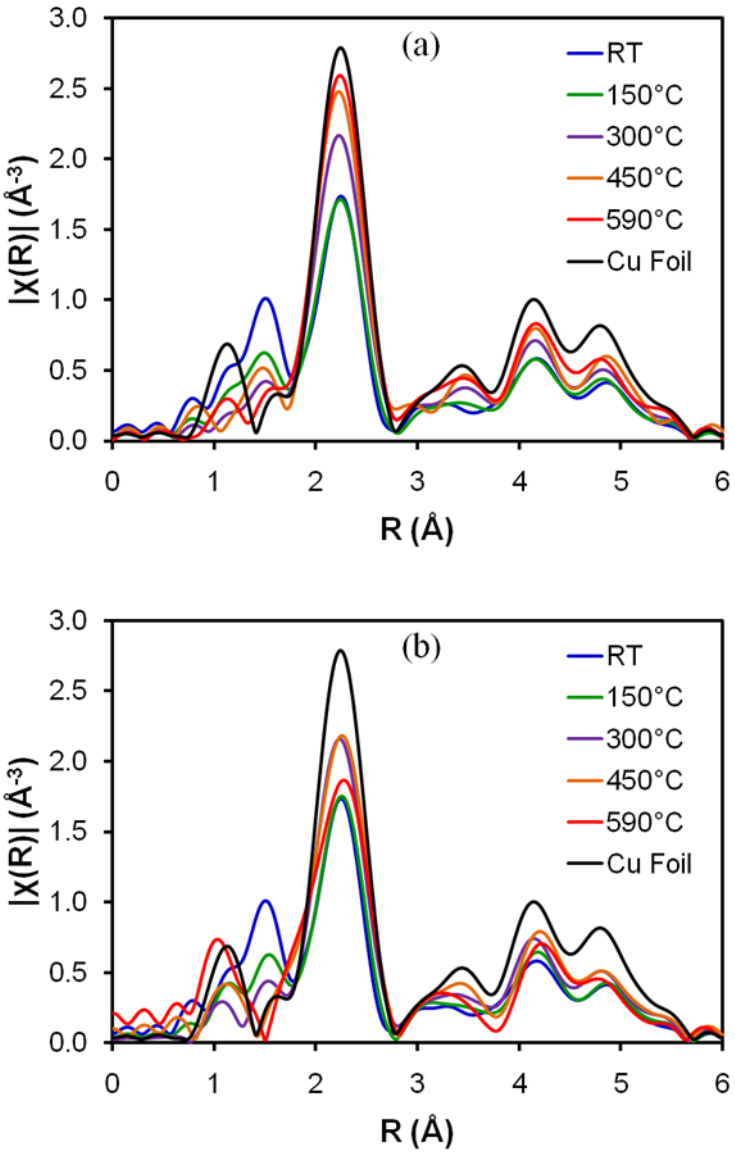

Figure 6.5: Cu K edge EXAFS spectra for the Cu/Mo_2C catalyst pretreated at various temperatures in (a) 100% H_2 and (b) 15% CH_4/H_2. A spectrum for a Cu foil reference is also shown.

was partially oxidized. By 300°C, regardless of the pretreatment gas, the Cu was reduced to the zero-valent state. The EXAFS spectra (Figure 6.5) for the Cu/Mo_2C samples pretreated at temperatures of 300°C and higher clearly resembled that of the Cu metal standard. The strong peak at ~2.2Å corresponds to the first shell Cu-Cu bond. The increase in intensity of this peak with increasing pretreatment temperature suggests that the Cu particles were sintering (increasing in size). The peaks in the range of 4-5Å correspond to the second and third shells. The peak around 1.5Å for the passivated Cu/Mo_2C sample corresponded to the Cu-O bond.

The XANES and EXAFS spectra for the Co/Mo_2C catalyst are shown in Figures 6.6 and 6.7. As the pretreatment temperature was increased, the intensity of the whiteline decreased, indicating that the Co was being reduced. For temperatures of 450°C and 590°C, the Co XANES spectra were similar, suggesting that no further reduction occurred. This result is in agreement with the H_2 TPR data as the reduction peak associated with Co oxides for the Co/Mo_2C catalyst was observed at 380°C. However, even at 590°C in H_2 or 15% CH_4/H_2, the Co was not completely reduced to its zero-valent state (see Co metal standard spectrum). This finding suggests a strong interaction between the Co and the Mo_2C support.

The EXAFS spectra show that the intensity of the peak corresponding to the Co-O bond (R = ~1.5Å [22, 23]) decreased with increasing pretreatment temperature. The peak at ~2.2Å was observed for the Co/Mo_2C catalysts pretreated at 450°C and 590°C, although the peak had fairly low intensity. This peak corresponds to the Co-Co bond in metallic Co (see EXAFS spectrum for Co metal standard). In regards to pretreatment gas, the XANES and EXAFS spectra were similar for Co/Mo_2C pretreated at 590°C in H_2 and

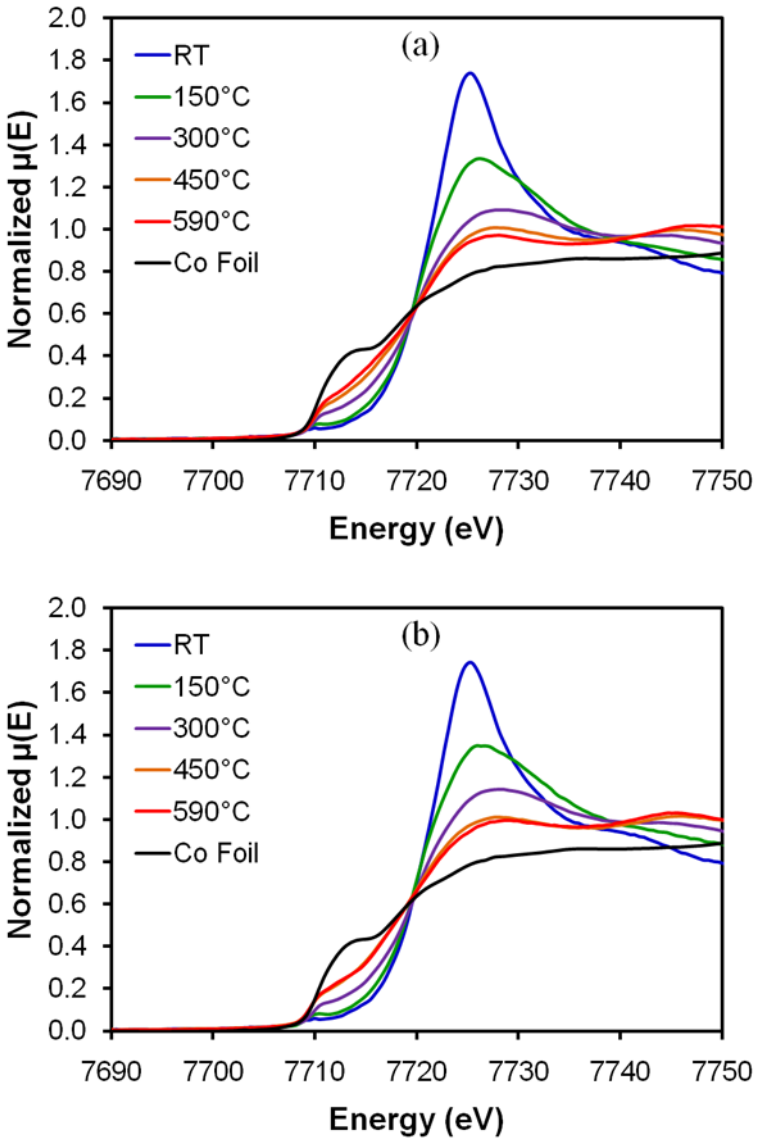

Figure 6.6: Co K edge XANES spectra for the Co/Mo_2C catalyst pretreated at various temperatures in (a) 100% H_2 and (b) 15% CH_4/H_2. A spectrum for a Co foil reference is also shown.

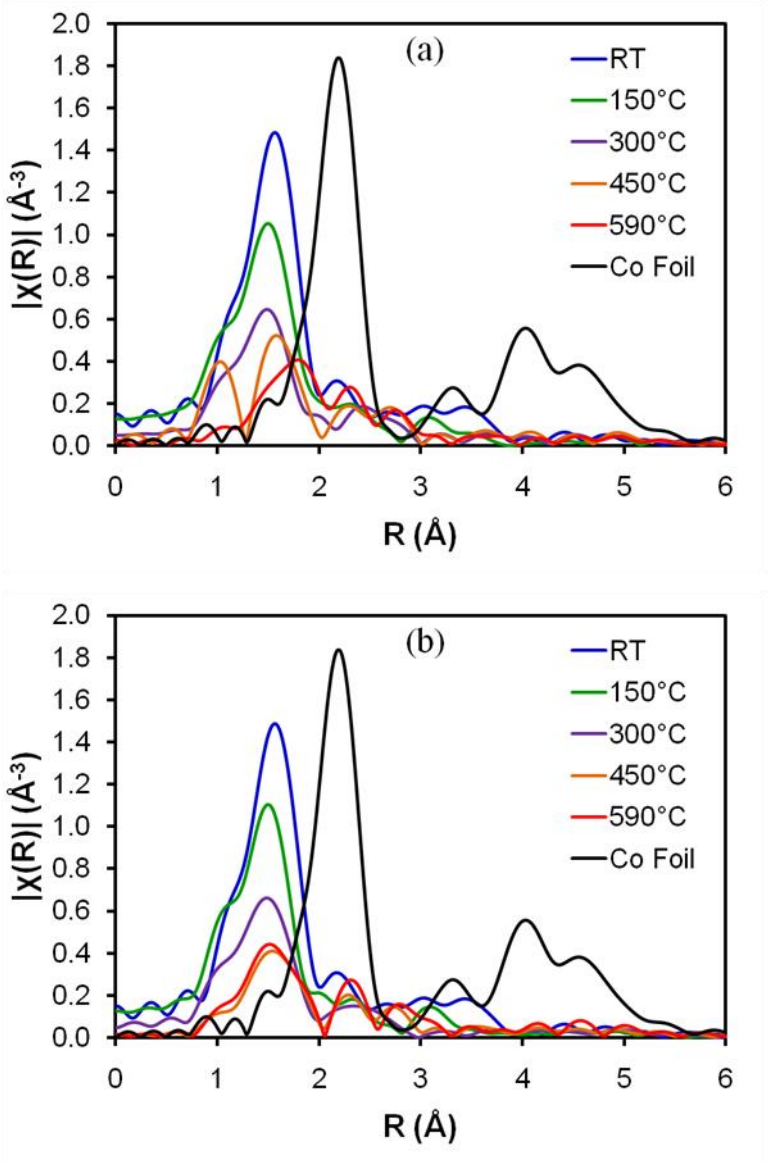

Figure 6.7: Co K edge EXAFS spectra for the Co/Mo_2C catalyst pretreated at various temperatures in (a) 100% H_2 and (b) 15% CH_4/H_2. A spectrum for a Co foil reference is also shown. The intensity of the Co foil spectra was multiplied by 0.4 to put it on the same scale as the Co/Mo_2C catalyst spectra.

pretreated at 590°C in 15% CH_4/H_2, indicating that Co was not carburized by the CH_4/H_2 treatment.

The XANES spectra for the Fe/Mo_2C catalysts are shown in Figure 6.8. Due to the low weight loadings of Fe on the catalyst, the fluorescence intensity was quite low causing a significant amount of noise and requiring extended times for data collection.

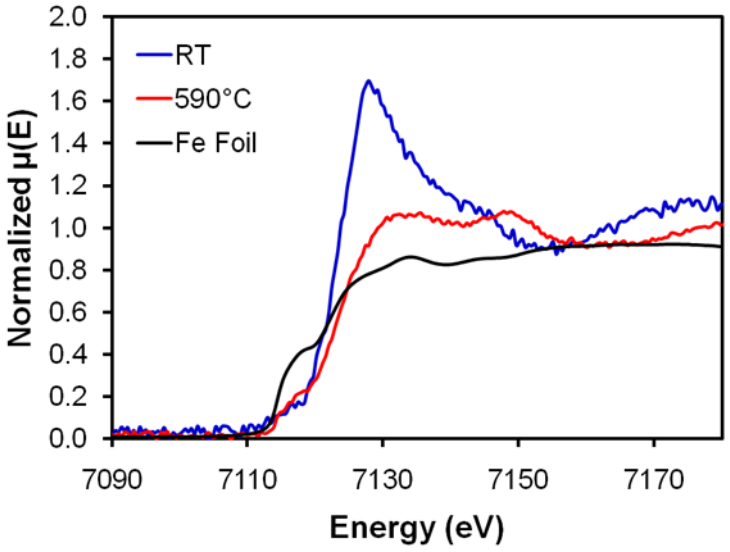

Figure 6.8: Fe K edge XANES spectra for the Fe/Mo_2C catalyst pretreated at various temperatures in 15% CH_4/H_2. A spectrum for a Fe foil reference is also shown.

Therefore, spectra were only collected for the passivated Fe/Mo_2C catalyst at room temperature and the Fe/Mo_2C catalyst pretreated at 590°C in 15% CH_4/H_2. As with Co, the whiteline for the Fe/Mo_2C catalyst decreased significantly after pretreatment, however the Fe was still partially oxidized compared to the metallic Fe standard. Due to the noise in the data, the EXAFS region was not explored.

6.3.2. Fischer-Tropsch Synthesis Performance

Arrhenius plots of the gravimetric FTS product formation rates for the Mo_2C-supported metal catalysts are shown in Figure 6.9. On a gravimetric basis, the Ni/Mo_2C catalyst exhibited the highest FTS rates while the Co/Mo_2C catalyst exhibited the lowest

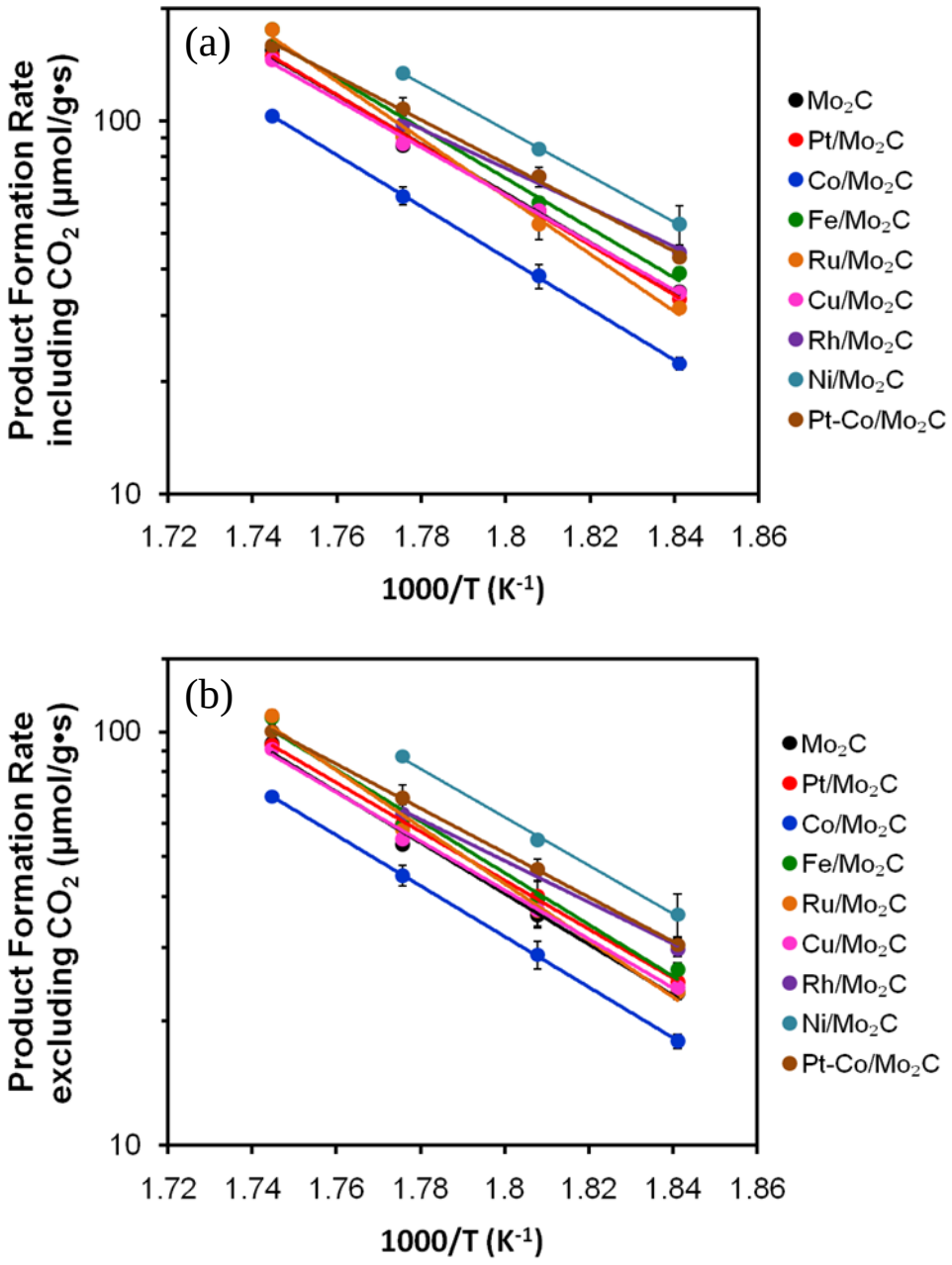

Figure 6.9: Arrhenius plots of the gravimetric product formation rates (a) including CO_2 and (b) excluding CO_2 for Mo_2C and the Mo_2C-supported metal catalysts. Reaction conditions: 25 bar, H_2/CO = 2, 270-300°C, and GHSV = 44000 h^{-1}. Error bars correspond to 95% confidence interval.

rates. Both catalysts had CO uptakes similar to that of Mo_2C (Table 6.1). This decreased rate for Co/Mo_2C compared to Mo_2C was surprising as Co is an active metal for FTS [6, 8] and Co/Mo_2C has been reported to have a higher activity for FTS than Mo_2C [5]. The rate at 300°C for Ni/Mo_2C was not recorded as it became exceedingly difficult to maintain control of the reaction temperature. Except for Ni/Mo_2C and Co/Mo_2C, the Mo_2C-supported metal catalysts exhibited gravimetric rates similar to that of Mo_2C.

The product formation rates normalized by the CO uptakes are shown in Figure 6.10. Again, the Co/Mo_2C catalyst exhibited the lowest normalized FTS rates. The

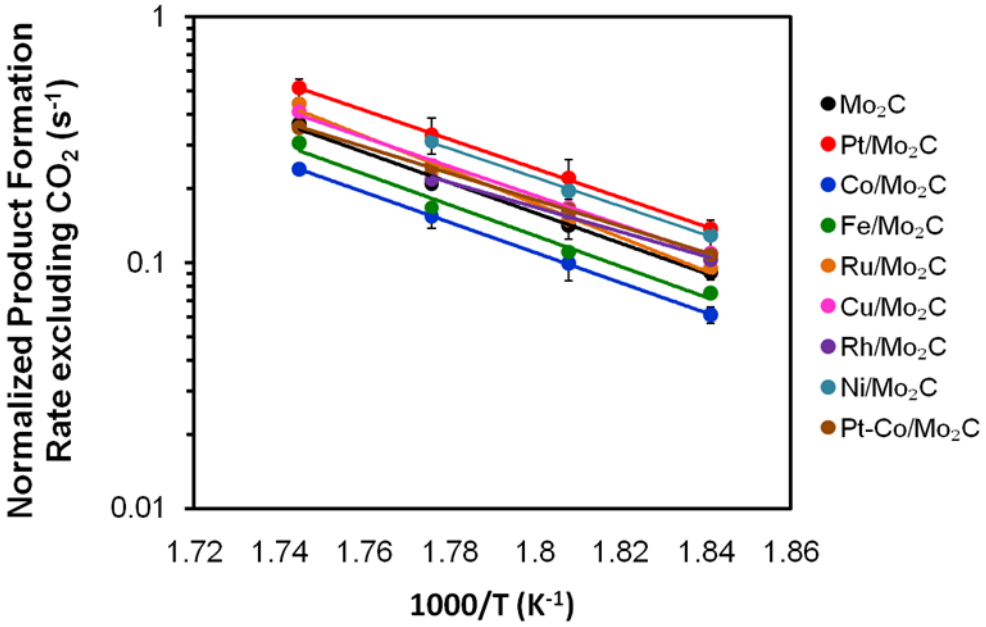

Figure 6.10: Arrhenius plots of the normalized product formation rates excluding CO_2 for Mo_2C and the Mo_2C-supported metal catalysts. Reaction conditions: 25 bar, H_2/CO = 2, 270-300°C, and GHSV = 44000h^{-1}. Error bars correspond to 95% confidence interval.

highest normalized rates were observed for Ni/Mo_2C and Pt/Mo_2C. The shift in relative FTS activity compared to the other catalysts for Pt/Mo_2C was due to its lower CO uptake (181 µmol/g) compared to the other catalysts. Interestingly, the addition of Pt to the Co/Mo_2C catalyst resulted in an increase in FTS rates; however, the rates for $Pt\text{-}Co/Mo_2C$

were not as high as those for Pt/Mo_2C. The activity trend for these materials based on the normalized product formation rates is as follows: Pt/Mo_2C ~ Ni/Mo_2C > Ru/Mo_2C ~ Cu/Mo_2C ~ Rh/Mo_2C ~ $Pt\text{-}Co/Mo_2C$ ~ Mo_2C > Fe/Mo_2C ~ Co/Mo_2C. It should be noted, however, that differences between the most active catalyst (Pt/Mo_2C) and the least active catalyst (Co/Mo_2C) were fairly small. At 290°C, the normalized product formation rates for Pt/Mo_2C and Co/Mo_2C were 0.33 s^{-1} and 0.15 s^{-1}, respectively. Additionally, the apparent activation energies for the Mo_2C-supported metal catalysts were similar to that for Mo_2C, with the exception of Rh/Mo_2C which had a slightly lower activation energy (Table 6.2).

Table 6.2: FTS apparent activation energies for Mo_2C and the Mo_2C-supported metal catalysts.

Catalyst	$E_{a,app}$[1,2] (kJ/mol)
Mo_2C	118 ± 8
Pt/Mo_2C	113 ± 9
Co/Mo_2C	117 ± 6
Fe/Mo_2C	120 ± 11
Ru/Mo_2C	131 ± 10
Cu/Mo_2C	113 ± 5
Rh/Mo_2C	96 ± 9
Ni/Mo_2C	112 ± 5
$Pt\text{-}Co/Mo_2C$	103 ± 4

[1] Calculated from product formation rates excluding CO_2.
[2] Error corresponds to 95% confidence interval.

Although experiments were performed at a series of temperatures, selectivities of the Mo_2C-supported metal catalysts are compared at a temperature of 290°C. As the gravimetric rates were similar for all catalysts, the CO conversions at this temperature were similar allowing for an equitable comparison of selectivities. The total product selectivities for these materials are shown in Figure 6.11. Although the changes were subtle, Co/Mo_2C exhibited an increase in selectivity towards hydrocarbons and alcohols and a decrease in selectivity towards CO_2 compared to Mo_2C. This result is in agreement

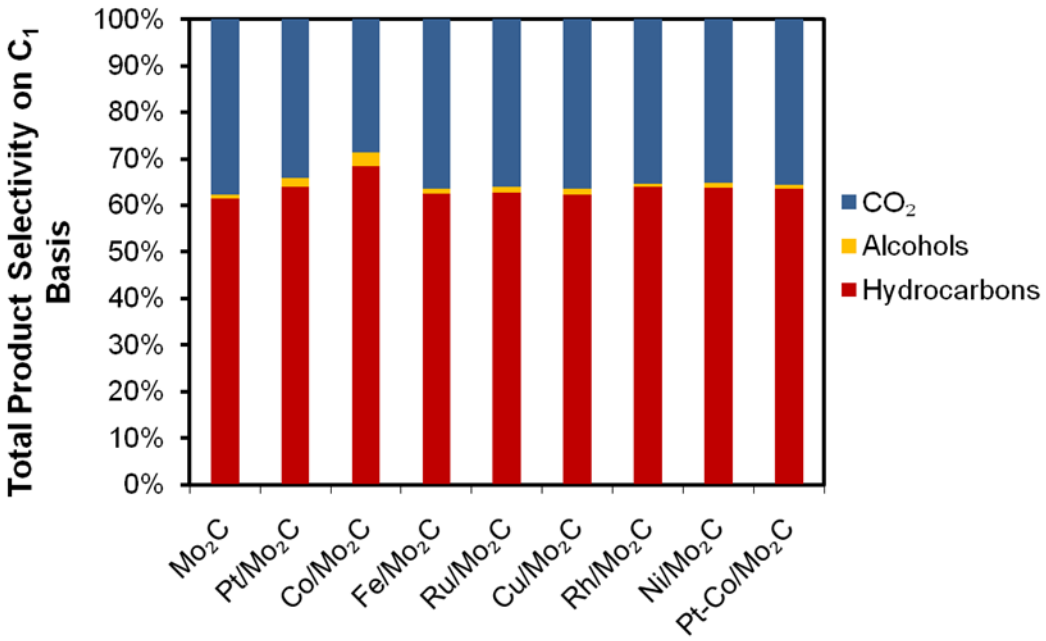

Figure 6.11: Total product selectivity for Mo_2C and the Mo_2C-supported metal catalysts. Reaction conditions: 290°C, 25 bar, $H_2/CO = 2$.

with the observations by King that Co/Mo_2C was less active for the water gas shift reaction (production of CO_2) than Mo_2C [3]. The remainder of the Mo_2C-supported metal catalyst all demonstrated product selectivities similar to that for Mo_2C.

The hydrocarbon selectivity is shown in Figure 6.12. In general, the selectivities for all of the catalysts were similar; there were no large shifts in selectivity due to the addition of metals. However, there were a few subtle changes. The Co/Mo_2C catalyst exhibited a decrease in selectivity towards CH_4 and an increase in selectivity towards C_2-C_4 hydrocarbons compared to Mo_2C. Ni/Mo_2C and Rh/Mo_2C exhibited the opposite trend, an increase in CH_4 selectivity and a decrease in C_2-C_4 selectivity. Pt/Mo_2C and Pt-Co/Mo_2C exhibited similar hydrocarbon selectivities to that of Mo_2C. For further comparison, the gravimetric product formation rates on a C1 basis for the Mo_2C-supported metal catalysts is given in Table 6.3.

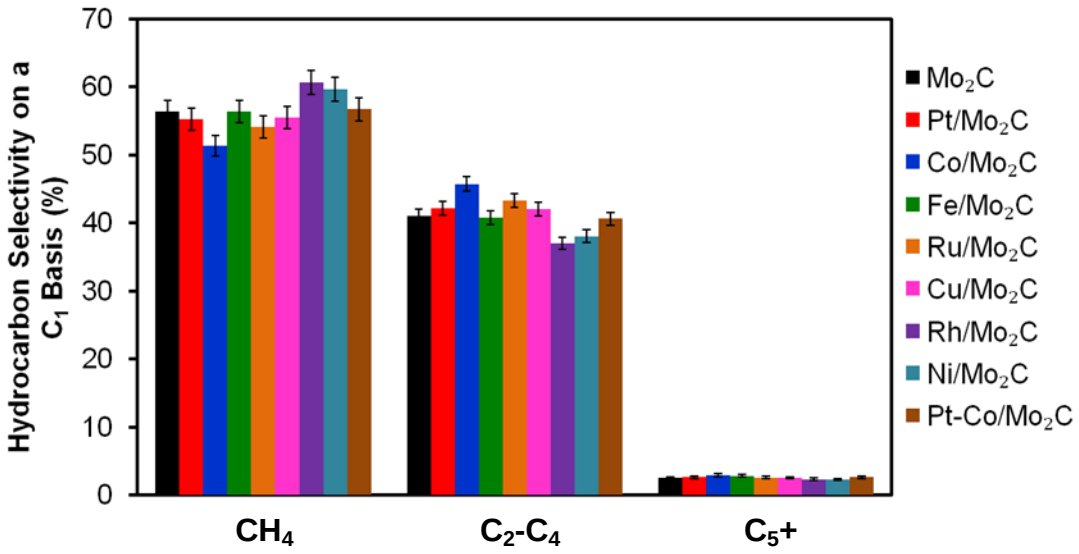

Figure 6.12: Hydrocarbon selectivity for Mo_2C and the Mo_2C-supported metal catalysts. Reaction conditions: 290°C, 25 bar, $H_2/CO = 2$.

Table 6.3: Gravimetric product formation rates on a C1 basis for Mo_2C and Mo_2C-supported metal catalysts. Reaction conditions: 290°C, 25 bar, $H_2/CO = 2$.

	Product Formation Rate on C1 basis (µmol/g•s)				
Catalyst	**CO_2**	**CH_4**	**C_2-C_4**	**C_5+**	**Alcohols**
Mo_2C	34.9	34.0	25.7	1.63	0.66
Pt/Mo_2C	31.1	32.2	24.6	1.55	1.08
Co/Mo_2C	18.1	22.3	19.8	1.27	1.30
Fe/Mo_2C	34.2	33.1	24.0	1.65	0.57
Ru/Mo_2C	32.9	31.0	24.8	1.49	0.69
Cu/Mo_2C	31.6	30.1	22.8	1.38	0.75
Rh/Mo_2C	34.7	38.1	23.3	1.48	0.44
Ni/Mo_2C	47.3	51.3	32.7	1.99	0.91
$Pt\text{-}Co/Mo_2C$	38.4	38.9	27.9	1.83	0.66

Due to the similar hydrocarbon selectivities, the Anderson-Schulz-Flory α values for Mo_2C-supported metal catalysts were also similar (Table 6.4). The highest value was for Co/Mo_2C (0.31) and the lowest value was for Ni/Mo_2C (0.28). However, the error on these measurements was ± 0.01 indicating that all of the α values for the Mo_2C-supported metal catalysts were within error of the value for Mo_2C (0.29).

Table 6.4: ASF α values for Mo_2C and Mo_2C-supported metal catalysts. Reaction conditions: 290°C, 25 bar, $H_2/CO = 2$.

Catalyst	ASF α[1]
Mo_2C	0.31 ± 0.02
Pt/Mo_2C	0.31 ± 0.02
Co/Mo_2C	0.32 ± 0.02
Fe/Mo_2C	0.31 ± 0.02
Ru/Mo_2C	0.31 ± 0.02
Cu/Mo_2C	0.31 ± 0.02
Rh/Mo_2C	0.31 ± 0.02
Ni/Mo_2C	0.30 ± 0.02
$Pt\text{-}Co/Mo_2C$	0.31 ± 0.02

[1] Error calculated from linear regression of ASF plots.

The supported metals appeared to have more of an effect on the olefin/paraffin ratio than on the total product selectivity and hydrocarbon selectivity. The olefin/paraffin ratios for Mo_2C and the Mo_2C-supported metal catalysts are shown in Figure 6.13. The Co/Mo_2C catalyst exhibited an increase in olefin/paraffin ratio compared to Mo_2C while Ni/Mo_2C and Rh/Mo_2C exhibited a decrease in olefin/paraffin ratio. The C_3 olefin/paraffin molar ratios for Mo_2C, Co/Mo_2C, Ni/Mo_2C, and Rh/Mo_2C were 0.20,

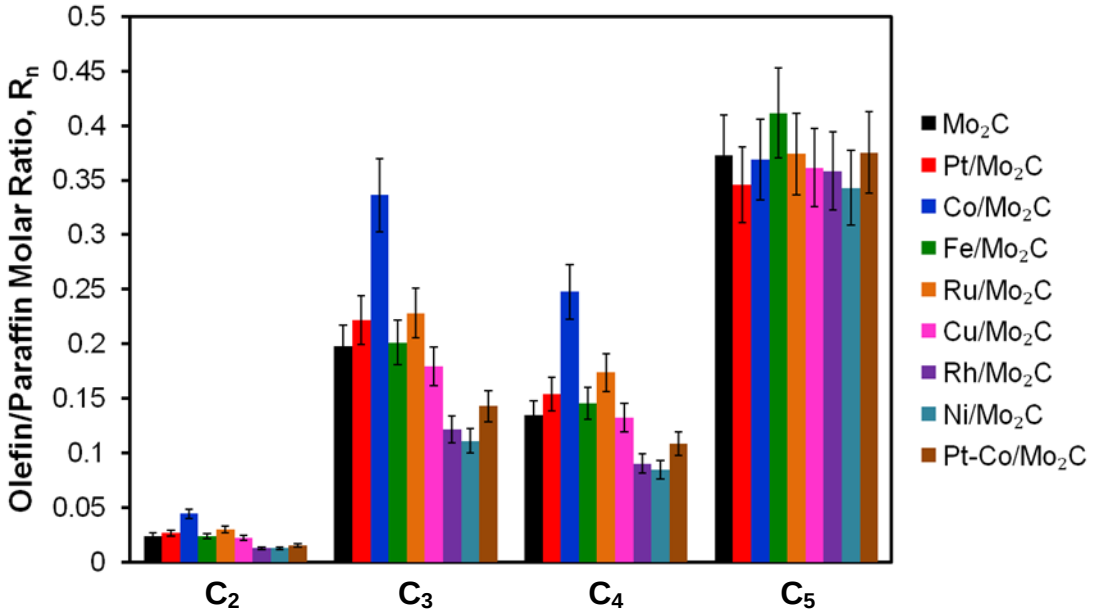

Figure 6.13: Olefin/Paraffin molar ratio for Mo_2C and the Mo_2C-supported metal catalysts. Reaction conditions: 290°C, 25 bar, $H_2/CO = 2$.

0.34, 0.11, and 0.12, respectively. These results suggest that the supported metals affected the hydrogen coverage on the catalyst surface under reaction conditions.

6.4. Discussion

In this chapter, the activities and selectivities of a series of Mo_2C-supported metal catalysts were described for the Fischer-Tropsch Synthesis. Based on the normalized FTS product formation rates (Figure 6.10), the following activity trend was developed: Pt/Mo_2C ~ Ni/Mo_2C > Ru/Mo_2C ~ Cu/Mo_2C ~ Rh/Mo_2C ~ $Pt\text{-}Co/Mo_2C$ ~ Mo_2C > Fe/Mo_2C ~ Co/Mo_2C. Interestingly, the supported metals only caused modest changes in the rates compared to Mo_2C. The most active catalyst, Pt/Mo_2C, exhibited a rate at 290°C that was ~58% higher than that for Mo_2C. Moreover, supporting metals such as Fe, Co, and Ru that are reported to be highly active for FTS [6, 8, 24] resulted in similar or even decreased rates compared to Mo_2C alone.

In regards to selectivity, the Mo_2C-supported metal catalysts behaved similarly to Mo_2C. The most notable exceptions were Co/Mo_2C and Ni/Mo_2C. Although the changes were subtle, Co/Mo_2C exhibited an increase in selectivity towards C_2-C_4 hydrocarbons, alcohols, and olefins and a decrease in selectivity towards CH_4 and CO_2, whereas Ni/Mo_2C exhibited an increase in selectivity towards CH_4 and a decrease in olefin/paraffin ratio and C_2-C_4 hydrocarbon selectivity.

For heterogeneous catalysts, activity and selectivity are sensitive functions of the surface chemistry. The activity and selectivity results for the carbide-supported metal catalysts can be explained based on the individual functions of the supported metal and the Mo_2C support as well as the catalyst pretreatment. The Pt/Mo_2C catalyst exhibited higher normalized FTS rates than Mo_2C, but displayed similar product selectivities (CH_4,

C_2-C_4, and C_5+ selectivity, olefin/paraffin molar ratio, and ASF α). The similar selectivities suggested that similar sites were performing FTS on both the Mo_2C and Pt/Mo_2C surfaces. The higher normalized rates could be attributed to improved quality of the sites or an increase in the number of available sites under reaction conditions. As shown in Figure 6.3, the addition of Pt caused a decrease in the reduction temperature for Mo_2C, indicating that Pt aids in the reduction of Mo_2C. Consequently, it is proposed that the Mo_2C surface is more reduced under reaction conditions in the presence of Pt, resulting in an increase in the number of available sites on the Mo_2C surface to perform FTS. This conclusion is in agreement with the XPS results discussed in Chapter 2. Under water gas shift conditions, the O/Mo atomic ratio for Pt/Mo_2C was lower than that for Mo_2C. For FTS, Pt did not provide sites for the reaction as it is only reported to have negligible activity for FTS [24]; Pt solely aided in maintaining a more reduced Mo_2C surface under reaction conditions.

It is proposed that the subtle changes in activities and selectivities observed for the Ni/Mo_2C and Co/Mo_2C catalysts were due to a combination of the intrinsic catalytic behavior of the supported metal and the Mo_2C support. Ni/Mo_2C favored the production of CH_4 and had a lower α than Mo_2C. These results are in agreement with Ni being an active catalyst for methanation [8, 9]. The Co/Mo_2C catalyst favored the production of higher hydrocarbons, and exhibited lower selectivities towards CH_4 and CO_2. Both of these properties are desirable for a FTS catalyst and are often reported for Co-based catalysts [6, 8, 25]. It is speculated that the primary reason for the activity and selectivity changes being so modest compared to Mo_2C was the low surface coverage of the supported metal. The nominal metal surface coverage of the Mo_2C support for this

investigation was ~10%. Therefore, assuming 100% dispersion and that the supported metal and Mo_2C have similar sites densities and turnover frequencies, the supported metal would only be contributing 10% to the overall activity and selectivity.

Additionally, the pretreatment conditions employed in this study were developed for Mo_2C (15% CH_4/H_2 at 590°C) and were not adjusted based on the supported metal. It is reported that a number of the metals investigated, especially Cu, Co, Fe, and Rh, are sensitive to pretreatment conditions and support effects [21, 26-28]. Copper is known to sinter at temperatures above 300°C [26]. The reduction temperature for Co oxides depends on the strength of interaction with the support [21]. For the Co/Mo_2C catalyst, the Co was not fully reduced after treatment in either 100% H_2 at 590°C or 15% CH_4/H_2 at 590°C (Figure 6.6). This result suggests that Co interacted strongly with the Mo_2C support. As metallic Co is reported to be the active phase for FTS [10], Co oxides remaining on the Mo_2C surface after pretreatment likely affected the activity and selectivity in a negative manner.

Overall, the Mo_2C-supported metal catalysts were not bi-functional in nature for FTS. The reaction appeared to occur on the supported metal sites and Mo_2C sites independently. A synergistic effect, similar to that reported for Pt/Mo_2C for water gas shift [2-4], was not observed. Low metal surface coverages combined with unoptimized pretreatment conditions may have resulted in only modest changes to the activity and selectivity compared to Mo_2C. It should be noted that this study is far from complete. Future work could include investigating the effect of metal weight loading and pretreatment conditions on FTS performance, optimizing the pretreatment conditions using *in-situ* X-ray absorption spectroscopy and temperature programmed reduction

techniques, as well as supporting metals on other carbides or nitrides. Based on this study, the Co/Mo_2C catalyst calls for further investigation, as it shifted the selectivity towards the desired products.

6.5. Summary

The Fischer-Tropsch Synthesis performance of Mo_2C-supported metal (Pt, Co, Fe, Ru, Cu, Rh, and Ni) catalysts was investigated. The Pt/Mo_2C catalyst exhibited the highest normalized rates as the presence of Pt resulted in a more reduced Mo_2C surface under reaction conditions, thus increasing the number of available sites. The addition of Co shifted the selectivity towards the desired products (higher hydrocarbons), and away from the undesired products (CH_4 and CO_2). However, in general, the addition of the supported metal resulted in only minor changes to the activity and selectivity compared to Mo_2C alone. The lack of major changes was primarily due to the metal and the support acting independently and low metal surface coverages.

6.6. References

[1] N. M. Schweitzer, J. A. Schaidle, O. K. Ezekoye, X. Pan, S. Linic, L. T. Thompson, High Activity Carbide Supported Catalysts for Water Gas Shift, *Journal of the American Chemical Society* 133 (2011) 2378-2381.

[2] N. M Schweitzer, Evaluating the Effect of a Strong Metal-Support Interaction on the Activity of Molybdenum Carbide Supported Platinum Water-Gas Shift Catalysts, Ph. D. Thesis, University of Michigan, 2010.

[3] T. E. King, Carbide and Nitride Supported Water-Gas Shift Catalysts, Ph. D. Thesis, University of Michigan, 2007.

[4] J. J. Patt, Carbide and Nitride Catalysts for the Water Gas Shift Reaction, Ph. D. Thesis, University of Michigan, 2003.

[5] A. Griboval-Constant, J.-M. Giraudon, G. Leclercq, L. Leclercq, Catalytic Behaviour of Cobalt and Ruthenium Supported Molybdenum Carbide Catalysts for FT Reaction, *Applied Catalysis A: General* 260 (2004) 35-45.

[6] G. P. Van Der Laan, A. A. C. M. Beenackers, Kinetics and Selectivity of the Fischer-Tropsch Synthesis: A Literature Review, *Catalysis Reviews: Science and Engineering* 41 (1999) 255-318.

[7] M. Gupta, M. L. Smith, J. J. Spivey, Heterogeneous Catalytic Conversion of Dry Syngas to Ethanol and Higher Alcohols on Cu-Based Catalysts *ACS Catalysis* 1 (2011) 641-656.

[8] M. E. Dry, FT Catalysts, *Studies in Surface Science and Catalysis* 152 (2004) 533-600.

[9] G. A. Mills, F. W. Steffgen, Catalytic Methanation, *Catalysis Reviews Science and Engineering* 8 (1974) 159-210.

[10] E. Iglesia, Design, Synthesis, and Use of Cobalt-Based Fischer-Tropsch Synthesis Catalysts, *Applied Catalysis A: General* 161 (1997) 59-78.

[11] M. Newville, *X-ray Absorption Fine-Structure Spectroscopy*, 2008 Advanced Photon Source National School on Neutron and X-ray Scattering, Argonne National Laboratory, August 5, 2008.

[12] S. Gao, J. Zhang, Y.-F. Zhu, C.-M. Che, A Convenient Solvothermal Route to Ruthenium Nanoparticles *New Journal of Chemistry* 24 (2000) 739-740.

[13] M. Chmielova, J. Seidlerova, Z. Weiss, X-ray Diffraction Phase Analysis of Crystalline Copper Corrosion Products after Treatment in Different Chloride Solutions *Corrosion Science* 45 (2003) 883-889.

[14] J. M. Campelo, A. Garcia, D. Luna, J. M. Marinas, $AlPO_4$-Supported Rhodium Catalysts. II. Determination of Metal Dispersion of $Rh/AlPO_4$-SiO_2 Catalysts by Tem and XRD *Colloids and Surfaces* 5 (1982) 227-239.

[15] R. P. Larsen, L. E. Ross, Spectrophotometric Determination of Ruthenium, *Analytical Chemistry* 31 (1959) 176-178.

[16] P. Vanysek, *Electrochemical Series*, Handbook of Chemistry and Physics, CRC Press, 2000.

[17] W. Setthapun, Carbide and Nitride Supported Methanol Steam Reforming Catalysts, Ph. D. Thesis, University of Michigan, 2007.

[18] P. A. Sermon, G. C. Bond, Hydrogen Spillover, *Catalysis Reviews* 8 (1974) 211-239.

[19] V. V. Rozanov, O. V. Krylov, Hydrogen Spillover in Heterogeneous Catalysis, *Russian Chemical Reviews* 66 (1997) 107-119.

[20] S. T. Srinivas, P. K. Rao, Direct Observation of Hydrogen Spillover on Carbon-Supported Platinum and Its Influence on the Hydrogenation of Benzene, *Journal of Catalysis* 148 (1994) 470-477.

[21] G. Jacobs, T. K. Das, Y. Zhang, J. Li, G. Racoillet, B. H. Davis, Fischer-Tropsch Synthesis: Support, Loading, and Promoter Effects on the Reducibility of Cobalt Catalysts, *Applied Catalysis A: General* 233 (2002) 263-281.

[22] A. Y. Khodakov, J. Lynch, D. Bazin, B. Rebours, N. Zanier, B. Moisson, P. Chaumette, Reducibility of Cobalt Species in Silica-Supported Fischer-Tropsch Catalysts *Journal of Catalysis* 168 (1997) 16-25.

[23] B. Ernst, A. Bensaddik, L. Hilaire, P. Chaumette, A. Kiennemann, Study on a Cobalt Silica Catalyst During Reductiong and Fischer-Tropsch Reaction: In Situ EXAFS Compared to XPS and XRD *Catalysis Today* 39 (1998) 329-341.

[24] M. A. Vannice, Catalytic Synthesis of Hydrocarbons from Hydrogen-Carbon Monoxide Mixtures over the Group VIII metals. I. Specific Activities and Product Distributions of Supported Metals, *Journal of Catalysis* 37 (1975) 449-461.

[25] A. Y. Khodakov, W. Chu, P. Fongarland, Advances in the Development of Novel Cobalt Fischer-Tropsch Catalysts for Synthesis of Long-Chain Hydrocarbons and Clean Fuels, *Chemical Reviews* 107 (2007) 1692-1744.

[26] R. Farrauto, S. Hwang, L. Shore, W. Ruettinger, J. Lampert, T. Giroux, Y. Liu, O. Ilinich, New Material Needs for Hydrocarbon Fuel Processing: Generating Hydrogen for the PEM Fuel Cell, *Annual Reviews of Materials Research* 33 (2003) 1-27.

[27] Y. Jin, A. K. Datye, Phase Transformations in Iron Fischer-Tropsch Catalysts during Temperature-Programmed Reduction *Journal of Catalysis* 196 (2000) 8-17.

[28] J. C. Vis, H. F. J. Van't Blik, T. Huizinga, J. Van Grondelle, R. Prins, Reduction and oxidation of Rh/Al_2O_3 and Rh/TiO_2 Catalysts as Studied by Temperature-Programmed Reduction and Oxidation *Journal of Molecular Catalysis* 25 (1984) 367-378.

CHAPTER 7

Summary, Conclusions, and Future Work

7.1. Summary and Conclusions

This work investigated the catalytic properties of early transition metal carbide and nitride based catalysts for (1) the water gas shift reaction in the presence of sulfur and (2) Fischer-Tropsch Synthesis. Regarding water gas shift, the primary goals were to determine the effect of sulfur, present in the form on H_2S, on the structure and water gas shift performance of Mo_2C and Pt/Mo_2C catalysts, and to identify relationships between the deactivation due to sulfur and changes in the catalyst bulk or surface structure. Regarding Fischer-Tropsch Synthesis, the main goals were to evaluate the performance of a series of early transition metal carbide and nitride-based catalysts for Fischer-Tropsch Synthesis, and to develop structure-function relationships that can be used to guide future catalyst development. The series of catalysts explored included carbides and nitrides of Mo, W, V, and Nb as well as Mo_2C-supported metal catalysts. In regards to the Mo_2C-supported metal catalysts, the mechanisms governing metal adsorption onto the native Mo_2C surface during wet impregnation were elucidated.

For water gas shift, the Mo_2C and Pt/Mo_2C catalysts deactivated significantly in the presence of 5ppm H_2S, losing more than 90% of their pre-sulfur exposure hydrogen production rates. Both catalysts were able to be partially regenerated with treatment in 15% CH_4/H_2 at 590°C. Based on rate measurements and XPS and TGA results, the deactivation for Mo_2C was primarily due to conversion of the surface to MoS_2.

Interestingly, the Mo_2C catalyst actually regained some of its lost activity in the presence of sulfur upon conversion of the entire surface to MoS_2; MoS_2 is catalytically active for water gas shift [1]. Moreover, under reaction conditions, Mo_2C possessed a high surface concentration of oxygen, which may have facilitated the formation of MoS_2. As a result, deactivation for Mo_2C could be reduced by controlling the reaction conditions to minimize the concentration of oxygen on the catalyst surface. For Pt/Mo_2C, deactivation was primarily due to irreversible sulfur poisoning of Pt-based sites. Although the addition of Pt improved the activity of the Mo_2C catalyst, it also altered the interaction of sulfur with the catalyst surface resulting in an increased susceptibility to sulfur poisoning.

For Fischer-Tropsch Synthesis, the intrinsic rate trend for these materials was as follows: $Mo_2C \sim W_2C \sim VN \sim NbN > Mo_2N, W_2N >> VC, NbC$. The rates for these materials were a function of both the metal and interstitial element (C or N). Similar to studies that have investigated tuning catalyst performance through alloying, this result suggests that the activity of these materials could be tuned by choice of the parent metal and the interstitial atom. Regarding selectivity, these materials primarily favored light hydrocarbons (C_2-C_4) and exhibited some water gas shift activity. Their selectivity to C_5+ hydrocarbons was much lower than that for Fe or Co-based catalysts. The water gas shift activity imparted a degree of resistance to deactivation under CO-rich feed streams. These results suggest that these materials may be suitable for conversion of biomass-derived syngas, which is typically CO-rich, into fuels. Moreover, the bulk crystal structures of these materials were stable under reaction conditions. However, the catalyst surface was changed under reaction conditions. There was an increase in oxygen and carbon species initially, as well as the deposition of waxy hydrocarbon species over time.

Investigation of the Fischer-Tropsch Synthesis mechanisms over Mo_2N and Mo_2C resulted in the conclusion that both catalysts were capable of direct CO dissociation, but that they followed two different mechanisms. Mo_2N followed the carbide mechanism, which involves CO dissociation followed by hydrogenation of the adsorbed carbon. The activation barrier for CO dissociation over Mo_2C was much lower than over Mo_2N, resulting in carbon being bound much stronger to the Mo_2C surface than the Mo_2N surface. The carbon was bound so strongly to the Mo_2C surface that it could not be removed via hydrogenation under Fischer-Tropsch Synthesis relevant temperatures (200-350°C). Therefore, the predominant mechanism over Mo_2C could not be the carbide mechanism. Using temperature programmed reaction experiments, it was shown that molecularly adsorbed CO played a key role in the production of C_2+ hydrocarbons. Consequently, it was proposed that the dominant mechanism over Mo_2C was either the oxygenate or CO-insertion mechanism. These findings also suggested that there were multiple sites present on the Mo_2C surface: sites for CO dissociation and sites for molecular CO adsorption/C-C coupling.

To explore methods for improving catalyst performance, Mo_2C was utilized as a support for other metals. Prior to kinetic Fischer-Tropsch Synthesis measurements, the metal adsorption process over Mo_2C via wet impregnation was investigated to determine the key mechanisms governing the process. Using X-ray absorption spectroscopy, it was determined that metals such as Pt, Pd, and Cu were reduced to their zero-valent state by the native surface of Mo_2C. These metals possess fairly high reduction potentials and achieved virtually 100% of the targeted metal loading. They also demonstrated the fastest rates of adsorption. Metals such as Ni and Fe were not reduced by the Mo_2C surface.

These metals have lower reduction potentials and did not achieve the targeted loading. It is proposed that the adsorption process is primarily governed by the red-ox chemistry of the metal and the Mo_2C support. Additionally, the precursor counter ion (Cl^- or NO_3^-) affected the metal adsorption process, possibly by modifying the reduction potential of the metal. For metals with low reduction potentials that do not reduce on the Mo_2C surface, electrostatic interactions may need to be exploited to improve loading.

After investigating the adsorption process, Fischer-Tropsch Synthesis kinetic experiments were performed over the Mo_2C-supported metal catalysts to determine the effect of the metal on the catalyst performance. Although previous research regarding Pt/Mo_2C catalysts for water gas shift has shown that these materials are bi-functional in nature and exhibit high rates due to a synergistic effect [2], our findings for Fischer-Tropsch Synthesis indicated that the metal and the Mo_2C were acting independently. In general, only minor changes in performance were observed and the changes followed the intrinsic nature of the supported metals. Ni/Mo_2C exhibited an increase in methane selectivity and Co/Mo_2C exhibited an increase in C_2+ hydrocarbon selectivity and a decrease in water gas shift activity. Both results fit with the reported catalytic properties of these metals. Additionally, Pt/Mo_2C exhibited higher normalized rates because the Pt caused the Mo_2C surface to be more reduced under reaction conditions, thus allowing more sites to be available for the reaction.

7.2. Future Work

7.2.1. Extension of Current Research

Based on the results of this work, there are several areas that warrant future investigation: (1) Fischer-Tropsch Synthesis experiments under more realistic conditions,

(2) further investigation of the Fischer-Tropsch Synthesis mechanism using Infrared spectroscopy and Density Functional Theory calculations, (3) selective poisoning experiments, and (4) development of new catalyst formulations. Regarding (1), Fischer-Tropsch Synthesis experiments in this work were carried out at industrially relevant temperatures and pressures, but at low conversions (<10%). It has been reported that single pass conversion in a Fischer-Tropsch Synthesis reactor for a biomass-to-fuels plant will need to be greater than 60% [3]. Experiments need to be performed at conversions closer to 50%. By running at these high conversions and lower space velocities, more elaborate product analysis will be required. In this work, gas phase products up to C_{10} were analyzed. Future work will need to develop methods for analysis of higher hydrocarbons in the liquid phase. Additionally, catalyst stability is a key issue for industrial Fischer-Tropsch Synthesis catalysts. Future experiments need to be run for extended periods of time (> 50 h) to further explore the stabilities of these early transition metal carbide and nitride based catalysts.

In Chapter 4, it was shown that Mo_2C predominantly followed either the oxygenate or CO-insertion mechanisms, both of which involve the formation of an intermediate via molecular adsorption of CO. Using Diffuse Reflectance Infrared Fourier Transform Spectroscopy, it may be possible to identify these intermediates on the Mo_2C surface under reaction conditions and more conclusively identify the dominant mechanism for Fischer-Tropsch Synthesis. Additionally, it was proposed in Chapter 4 that Mo_2N and Mo_2C followed different Fischer-Tropsch Synthesis mechanisms. Mo_2N was proposed to follow the carbide mechanism, which involves direct CO dissociation and hydrogenation of the adsorbed carbon. Although Mo_2C was also capable of direct CO

dissociation, the carbon was bound too strongly to the surface to be removed via hydrogenation at relevant reaction temperatures, therefore the dominant mechanism was either the oxygenate or CO-insertion mechanism. To further explore the mechanisms over these two catalysts, computational methods based on quantum chemistry, such as Density Functional Theory, could be employed. More specifically, it would be beneficial to investigate the surface termination under relevant reaction conditions, the favorable sites for molecular and dissociative CO adsorption, the routes for C-C coupling, and free energy diagrams for the different Fischer-Tropsch Synthesis mechanisms.

Regarding selective poisoning, it could be explored in two ways: (1) poisoning water gas shift sites and (2) poisoning CO dissociation sites. As shown in Chapter 2, sulfur severely poisoned water gas shift sites on the Mo_2C surface. However, it has been reported that sites on the Mo_2C surface associated with methanol decomposition and methanation were sulfur resistant [4]. Accordingly, it may be possible to selectively poison water gas shift sites with sulfur while leaving sites for CO activation and hydrogenation unchanged. These experiments could shed light on the different types of sites on the Mo_2C surface and allow for modification of the Mo_2C surface to improve its utilization of CO to produce hydrocarbons instead of CO_2. Regarding poisoning of CO dissociation sites, it was shown in Chapter 4 that molecularly adsorbed CO on the Mo_2C surface played a key role in C-C coupling and production of C_2+ hydrocarbons. However, the Mo_2C surface also possessed sites capable of direct CO dissociation. To improve the selectivity of the Mo_2C catalyst towards higher hydrocarbons, the sites capable of direct CO dissociation could be selectively poisoned.

Lastly, the conclusions from this work can guide future catalyst development. As discussed in Chapter 3, the intrinsic Fischer-Tropsch Synthesis activity of the early transition metal carbide and nitride catalysts was a function of the metal and the interstitial atom (C or N). This observation suggests that the activity of the catalyst may be tuned by choice of metal and interstitial atom. Consequently, bimetallic carbide or nitride catalysts (e.g. $Co_xMo_yC_z$) may have improved activities and selectivities. Additionally, although the deposition of other transition metals on Mo_2C resulted in only subtle changes in Fischer-Tropsch Synthesis performance (Chapter 6), promotion of the Mo_2C surface with other elements could be beneficial. For example, promotion of Mo_2C with potassium has been reported to shift the product distribution from hydrocarbons to alcohols [5-7]. In these studies, the potassium was loaded onto the passivated Mo_2C surface via incipient wetness impregnation or physically mixed in a mortar and pestle. It would be interesting to explore the effect of depositing the potassium or other promoters on the native Mo_2C surface, using the method developed in our group.

7.2.2. New Research Thrusts

In addition to the production of fuels from biomass, there is considerable interest in the production of chemicals, especially polymers and plastics, from bio-based feedstocks. One possible route for the production of polymers from biomass involves the gasification of biomass to produce synthesis gas followed by the conversion of synthesis gas to olefins, specifically C_2-C_4 olefins. Current technology first produces methanol, then converts methanol into olefins [8 and references cited therein]. Direct conversion of synthesis gas to olefins eliminates the extra steps involved in this process. Based on the results reported in Chapter 3, the carbide and nitride catalysts favored the production of

light hydrocarbons. Even under conditions that strongly favored only methane production, the carbides and nitrides still produced a fair amount of C_2-C_4 hydrocarbons. Additionally, some of the catalysts, specifically W_2N, exhibited high selectivities towards olefins. Based on these observations, these materials may be promising catalysts for direct conversion of synthesis gas to olefins.

The second research thrust stems from the results of the metal adsorption investigation in Chapter 5. It was proposed that a red-ox reaction occurred between the metal precursor (i.e. for metals with relatively high reduction potentials) and the native Mo_2C surface, resulting in the deposition of zero-valent metal. This type of red-ox chemistry has been exploited to synthesize core-shell electrocatalysts [9-11]. First, a layer of Cu is deposited electrochemically onto the support via underpotential deposition. Then, a monolayer of another metal (with a reduction potential higher than that of Cu) is deposited by displacing the surface Cu atoms, thus forming a core-shell catalyst. This technique requires the use of an electrochemical cell and potentiostat whereas core-shell synthesis with Mo_2C as a core would only require an aqueous solution containing the metal precursor. Based on these findings, Mo_2C and possibly other transition metal carbides and nitrides may be effective core materials for core-shell catalysts.

7.3. References

[1] P. Hou, D. Meeker, H. Wise, Kinetic Studies with a Sulfur-Tolerant Water Gas Shift Catalyst *Journal of Catalysis* 80 (1983) 280-285.

[2] N. M Schweitzer, Evaluating the Effect of a Strong Metal-Support Interaction on the Activity of Molybdenum Carbide Supported Platinum Water-Gas Shift Catalysts, Ph. D. Thesis, University of Michigan, 2010.

[3] M. J. A. Tijmensen, A. P. C. Faaij, C. N. Hamelinck, M. R. M. van Hardeveld, Exploration of the Possibilities for Production of Fischer Tropsch Liquids and Power via Biomass Gasification, *Biomass and Bioenergy* 23 (2002) 129-152.

[4] A. C. Lausche, J. A. Schaidle, L. T. Thompson, Understanding the Effects of Sulfur on Mo_2C and Pt/Mo_2C Catalysts: Methanol Steam Reforming *Applied Catalysis A: General* 401 (2011) 29-36.

[5] H. C. Woo, K. Y. Park, Y. G. Kim, I.-S. Nam, J.-S. Chung, J. S. Lee, Mixed Alcohol Synthesis from Carbon Monoxide and Dihydrogen over Potassium-Promoted Molybdenum Carbide Catalysts *Applied Catalysis* 75 (1991) 267-280.

[6] M. Xiang, D. Li, W. Li, B. Zhong, Y. Sun, Synthesis of Higher Alcohols from Syngas over $K/Co/\beta\text{-}Mo_2C$ Catalysts *Catalysis Communications* 8 (2007) 503-507.

[7] N. Wang, K. Fang, D. Jiang, D. Li, Y. Sun, Iron Carbide Promoted $K/\beta\text{-}Mo_2C$ for Higher Alcohols Synthesis *Catalysis Today* 158 (2010) 241-245.

[8] M. Stocker, Review: Methanol-to-Hydrocarbons: Catalytic Materials and their Behavior *Microporous and Mesoporous Materials* 29 (1999) 3-48.

[9] J. Barbier, in: G. Ertl, H. Knozinger, J. Weitkamp (Eds.), *Preparation of Solid Catalysts*, Wiley-VCH, 1999.

[10] Z. D. Wei, Y. C. Feng, L. Li, M. J. Liao, Y. Fu, C. X. Sun, Z. G. Shao, P. K. Shen, Electrochemically Synthesized Cu/Pt Core-Shell Catalysts on a Porous Carbon Electrode for Polymer Electrolyte Membrane Fuel Cells *Journal of Power Sources* 180 (2008) 84-91.

[11] K. Sasaki, J. X. Wang, H. Naohara, N. Marinkovic, K. More, H. Inada, R. R. Adzic, Recent Advances in Platinum Monolayer Electrocatalysts for Oxygen Reduction Reaction: Scale-up Synthesis, Structure and Activity of Pt Shells on Pd Cores *Electrochimica Acta* 55 (2010) 2645-2652.